The Sumatra Subduction Zone: Seismicity, Velocity Structure and Seismic Anisotropy

Thesis submitted in accordance with the requirements of the University of Liverpool for the degree of Doctor in Philosophy by Rachel Elizabeth Collings.

February 2012

The Sumatra Subduction Zone: Seismicity, Velocity Structure and Seismic Anisotropy

Rachel Collings

On September 12 2007, an M_w 8.4 earthquake occurred within the southern section of the Mentawai segment of the Sumatra subduction zone, where the subduction thrust had previously ruptured in 1833 and 1797. Following the 2007 rupture, a temporary local network was installed in the Mentawai region between December 2007 and October 2008 to record the aftershocks. Additionally, a second network was installed in central Sumatra between April 2008 and February 2009. In this study the data obtained from the Mentawai network were used to determine 2D and 3D *Vp* and *Vp/Vs* models, first motion polarity focal mechanisms and accurate hypocentre locations. In addition to this, shear wave splitting (SWS) measurements from both networks were used to determine the type, amount and location of anisotropy. This has enabled us to obtain a detailed image of the structure of the subduction zone, ascertain the down-dip limit of the seismogenic zone and determine the deformation occurring.

The forearc islands are characterized by a low *Vp* (4.5-5.8 km/s) and a high *Vp/Vs* ratio (>2.0), suggesting that they consist of fluid-saturated sediments. The down-going slab is clearly distinguished by a dipping region of high *Vp* (8.0 km/s), which can be traced to ~50 km depth, with an increased *Vp/Vs* ratio (1.75 to 1.90) beneath the forearc islands and the western side of the forearc basin, suggesting hydrated oceanic crust. Beneath the slab, a ~150 km thick layer of sub-slab anisotropy has developed due to the oceanic asthenosphere being entrained by the subducting slab. Two clusters of seismic activity are found within the ~25-30 km thick overriding crust. The location of the first cluster confirms that the Mentawai Fault is active and may accommodate backthrust movement, while the second cluster suggests a backthrust may be present on the eastern side of the forearc basin. Local SWS measurements suggest that in the overriding plate, adjacent to the Sumatran Fault, a layer of anisotropy has formed from fault-parallel aligned fractures and minerals. Beneath the forearc, a shallow continental Moho of < 30 km depth can be inferred. Within the mantle wedge there is no widespread serpentinization; only localized serpentinization is present at the toe. Beneath the backarc, 2D corner flow is occurring in the continental asthenosphere. The co-seismic slip of the 2007 events, as well as the aftershock distribution, suggests that the down-dip limit to rupture propagation is beneath the slab-Moho intersection at ~50 km depth. Consequently, as the M_w 7.7 Mentawai earthquake on 25 October 2010 showed that the updip limit of the seismogenic zone is at the trench, a potential 200 km wide rupture could take place.

Declaration

I declare than this thesis has been composed solely by myself and, except where otherwise acknowledged, the work presented is entirely my own.

Rachel Elizabeth Collings

February 2012

Contents

Abstract **i**

Declaration **ii**

Contents **iii**

List of Figures **viii**

List of Tables **xii**

1 Introduction **1**

1.1 Thesis Outline 4

2 Geological Setting **7**

2.1 Tectonic Setting 7

2.2 Past Seismicity 11

2.2.1 The 1797 M_w 8.7-8.9 Earthquake 11

2.2.2 The 1833 M_w 8.7-9.1 Earthquake 12

2.2.3 The 1861 M_w 8.5 Earthquake 12

2.2.4 The 2004 M_w 9.3 Sumatra-Andaman Earthquake 13

2.2.5 The 2005 M_w 8.5 Nias Earthquake 16

2.2.6 The 2007 M_w 8.4 Bengkulu Earthquake 20

2.2.7 The 2009 M_w 7.6 Earthquake 21

2.2.8 The 2010 Mw 7.7 Mentawai Earthquake 21

2.3 Rupture Barriers 23

2.4 The Mentawai Region 24

3 The Experiment **26**

3.1 Acquisition of Data and Instrumentation 26

3.1.1 Mentawai Network 27

3.1.2 Central Network 30

3.2 Pre Processing 38

3.3 Event Detection and Phase Picking 38

4 Coupled Hypocentre-Velocity Problem 42

4.1 Linear Inverse Theory 42

4.2 The Minimum 1D Model 46

4.2.1 Requirements of a 1D Minimum Model 46

4.3 3D Tomography 48

4.3.1 Requirements of a Tomography Model 49

4.3.2 Parameters of SIMUL 49

4.4 Resolution 52

4.4.1 Classical Resolution Tests 52

4.4.2 Synthetic Models 55

5 Structure and seismogenic properties of the Mentawai segment of the Sumatra subduction zone revealed by local earthquake travel time tomography 56

5.1 Abstract 56

5.2 Introduction 57

5.3 Tectonic Setting and Seismicity 59

5.4 Data 62

5.5 Velocity Models 64

5.5.1 Minimum 1D Model 64

5.5.2 2D and 3D Tomographic Models 68

5.6 Resolution 71

5.6.1 Model Resolution Matrix 71

5.6.1.1 2D Resolution 73

5.6.1.2 3D Resolution 73

5.6.2 Synthetic Models 74

5.7 Focal Mechanisms 78

5.8 Results and Discussion 79

5.8.1 Forearc Islands 82

5.8.2 Subducting Oceanic Slab 84
5.8.3 Forearc Structure and Continental Crust 89
5.8.4 Continental Mantle 91
5.8.5 Seismogenic Zone 92
5.8.6 Implications for Mentawai Tsunami Earthquake of October 25 2010 96
5.9 Conclusions 98
5.10 Acknowledgments 100

6 Anisotropy 101
6.1 Seismic Anisotropy 101
6.2 Shear Wave Splitting Analysis 103
6.2.1 Minimum Energy Method 103
6.2.2 Eigenvalue Method 103
6.2.3 Rotation Correlation Method 104
6.2.4 Comparing the Different Methods 104
6.2.5 Time Window 105
6.2.6 Null Measurements 106
6.2.7 Shear Wave Splitting Techniques Employed in this Study 107
6.3 Causes of Seismic Anisotropy 107
6.3.1 Lattice Preferred Orientation (LPO) 107
6.3.2 Shape Preferred Orientation (SPO) 109
6.3.3 Anisotropy within the Earth 110
6.3.3.1 Lithosphere 110
6.3.3.2 Upper Mantle Asthenosphere 111
6.3.3.3 Transition Zone and Lower Mantle 113
6.3.4 Observations of Anisotropy within Subduction Zones 114
6.3.4.1 Tonga 115
6.3.4.2 New Zealand 116
6.3.4.3 Ryukyu 117
6.3.4.4 Japan 117

6.3.4.5 Kamchatka 119
6.3.4.6 Aleutian Islands 119
6.3.4.7 Cascadia 120
6.3.4.8 Caribbean 121
6.3.4.9 Central America 121
6.3.4.10 South America 122
6.3.4.11 Sumatra and Java 123
6.3.5 Aims of this Study 127

7 Seismic Anisotropy in the Sumatra Subduction Zone 129
7.1 Abstract 129
7.2 Introduction 130
7.3 Tectonic Setting 135
7.4 Data and Method 137
7.5 Results 138
7.5.1 Teleseismic Results 139
7.5.2 Local Splitting Results 141
7.5.2.1 Forearc Islands 141
7.5.2.2 Forearc 143
7.5.2.3 Sumatran Fault 143
7.5.2.4 Backarc 144
7.6 Discussion of Local S Splitting and Possible Mechanisms 144
7.6.1 Forearc Islands 146
7.6.2 Forearc, Sumatran Fault and Backarc Region 146
7.6.2.1 Trench-Perpendicular Measurements 146
7.6.2.2 Trench/Sumatran Fault Parallel SWS Observations 148
7.6.2.3 Two Layers of Anisotropy 152
7.6.3 Forward Modeling 155
7.7 Teleseismic Splitting and Possible Mechanisms 161
7.7.1 Forward Modeling 166

7.8 Conclusions 169
7.9 Acknowledgments 170

8 The Structure and Seismological Processes Occurring Within the Sumatra Subduction Zone 171
8.1 The Forearc 171
8.2 The Continental Mantle 174
8.3 The Subducting Oceanic Plate 177
8.4 The Seismogenic Zone 178
8.5 Where Will the Next Earthquake Occur? 183

9 Conclusions 186
9.1 Future Work 188

A1 Waveforms 190

A2 Tomography 194

A3 Event Catalogue 209

A4 Shear Wave Splitting Results 220

References 230

Acknowledgments 267

List of Figures

1.1	The Study region	3
2.1	Tectonic map of the Sunda Arc	7
2.2	Sumatra subduction zone and previous large earthquakes	8
2.3	The 2004 rupture	14
2.4	Co-seismic slip distribution of the 2005 event	17
2.5	Co-seismic slip distribution of the 2007 event	19
2.6	Co-seismic slip distribution of the 2010 event	22
2.7	Seismicity distribution within the Mentawai region before 12 September 2007	25
2.8	Seismicity distribution within the Mentawai post 12 September 2007	25
3.1	Amount of obtained station waveform data	27
3.2	The Mentawai network	28
3.3	Log file data	29
3.4	The central Sumatra network	32
3.5	Ocean bottom seismometers	34
3.6	Waveform example for the event on the 25 February 2008	40
3.7	Waveform example for the event on the 19 May 2088	41
5.1	The Sumatra subduction zone	60
5.2	The Mentawai network	63
5.3	The final 1D minimum velocity model	66
5.4	Station and earthquake distribution and ray coverage for tomographic models	69

5.5	Resolution matrix for 2D and 3D models	72
5.6	Checkerboard tests	74
5.7	Restoring resolution tests	77
5.8	2D *Vp* and *Vp/Vs* Model	80
5.9	3D *Vp* and *Vp/Vs* model	81
5.10	Focal mechanisms	83
5.11	Final hypocentre locations	85
5.12	Structure of the Mentawai segment of the Sumatra subduction zone	88
5.13	The M_w 7.7 event on 25 October 2010	95
6.1	Shear wave splitting	101
6.2	Phases to study the sub slab mantle	102
6.3	Lattice preferred orientation of olivine	108
6.4	Retrograde motion model	113
6.5	Shear wave splitting measurements at subduction zones around the world	115
7.1	The west Sumatra subduction zone	134
7.2	Station locations	136
7.3	*SKS* SWS results	140
7.4	Local SWS results	142
7.5	Raypaths of the local events	145
7.6	Source polarization versus fast direction and delay time	154
7.7	Comparison of predicted and observed local SWS	160
7.8	Anisotropy occurring within the Sumatra subduction zone	161
7.9	Comparison of predicted and observed teleseismic SWS	168

8.1	Structure and seismogenic processes occurring within the Sumatra subduction zone	172
8.2	Thermal structure of the Sumatra subduction zone	175
8.3	Updip limit of the seismogenic zone	179
A1.1	*P* pick weight 0	190
A1.2	*P* pick weight 1	190
A1.3	*P* pick weight 2	191
A1.4	*P* pick weight 3	191
A1.5	*S* pick weight 0	192
A1.6	*S* pick weight 1	192
A1.7	*S* pick weight 2	193
A1.8	*S* pick weight 3	193
A2.1	Wadatti diagram of events beneath forearc islands	194
A2.2	Wadatti diagram of events beneath mainland	194
A2.3	Wadatti diagram	196
A2.4	Damping curve for 1D velocity model	196
A2.5	Seismicity distribution following 1D velocity model	197
A2.6	Errors in event hypocentres and *Vp* models after randomly moving hypocentres by up to 10 km	198
A2.7	Errors in event hypocentres and *Vs* models after randomly moving hypocentres by up to 10 km	199
A2.8	Histogram of hypocentre errors after randomly moving hypocentres by up to 10 km and performing joint inversion for *Vp* model	200

A2.9 Histogram of hypocentre errors after randomly moving hypocentres by up to 10 km and performing joint inversion for *Vs* model 200

A2.10 Histogram of hypocentre errors after the bootstrap approach is applied and a joint inversion for hypocentres and *Vp* model is performed 201

A2.11 Histogram of hypocentre errors after the bootstrap approach is applied and a joint inversion for hypocentres and *Vs* model is performed 201

A2.12 Damping curves for 2D models 202

A2.13 Damping curves for 3D models 203

A2.14 Histogram o*f P* residuals for 2D and 3D model 205

A2.15 Histogram of *S*-*P* residuals for 2D and 3D model 206

A2.16 Example of FOCMEC solutions 207

A2.17 Kopp et al.(2001) *P* velocity model 208

A4.1 SKS SWS results for station LAIS 224

A4.2 SKS SWS results for station LAIS 225

A4.3 SKS SWS results for station B50B 226

A4.4 SKS SWS results for station B50B 227

A4.5 Local SWS results for station N50S 228

A4.6 Local SWS results for station A20S 229

List of Tables

3.1	Mentawai network stations	33
3.2	Northern network stations	35
3.3	Picking weights	39
5.1	Focal mechanisms	78
6.1	Shear wave splitting studies at subduction zones around the world	124
7.1	Fresnel Zone Radius	152
7.2	Forward modeling parameters used for station N40S	158
7.3	Forward modeling parameters used for station N20S	158
7.4	Forward modeling parameters used for station A20S	159
7.5	Forward modeling parameters used for station F70S	159
A2.1	Chosen damping values	203
A2.2	Station corrections	204
A3.1	Event catalogue	209
A4.1	Teleseismic shear wave splitting results	220
A4.2	Additional 5 stable teleseismic shear wave splitting results	221
A4.3	Local SWS results of forearc island region	221
A4.4	Local SWS results of forearc region	221
A4.5	Local SWS results of Sumatran Fault region	222
A4.6	Local SWS results of backarc region	223

Chapter 1

Introduction

The largest earthquakes are located along subduction zones, regions of the Earth where two tectonic plates converge and the denser plate sinks into the Earth's mantle (Stern, 2002). Subduction plate interface seismicity accounts for over 90% of the total seismic moment released globally (Pacheco and Sykes, 1992). Generally, large earthquakes manifest as thrust type events and are found at depths less than 50 km, resulting in strong tsunamigenic potential. However, the seismic behaviour of individual subduction zones is highly variable, with some regions generating earthquakes greater than M_w 9 (Chile, Alaska, Sumatra, Japan); while others only have a maximum magnitude of M_w 7 (Mariana-Izu Bonin). The total amount of slip that occurs along the subduction interface fault plane is a combination of both seismic and aseismic slip (e.g. Scholz et al., 1969). The ratio of seismic slip to total slip along the interface, defined as seismic coupling (1=coupled and 0=uncoupled), varies spatially and might also vary in time (Ruff and Kanamori., 1983). During an earthquake the seismic energy released is not uniformly distributed along the megathrust, creating patches of high and low slip. Regions of high slip are interpreted as the areas of greatest coupling and are known as asperities (Lay and Kanamori, 1981). The physical properties of the asperity control the degree of seismic coupling and also the nucleation of large earthquakes. Originally, asperities along the subduction megathrust were attributed primarily to properties of the lower plate, e.g. temperature, age, dip, length, sediment thickness and roughness (e.g. Cross and Pilger, 1982, and references therein). However, more recent studies have noted that deformation occurring within the continental crust and underlying continental mantle is correlated with frictional properties of the interface between the upper and lower plates and thus could affect the seismic behaviour of subduction megathrusts (e.g McCaffrey, 1993); the correlation of forearc basins with seismic asperities is an example of this (Song and Simons, 2003; Wells et al., 2003). This implies that rupture regions along megathrusts

will remain the same for several earthquake cycles. Alternatively, it has been suggested that the controlling factor of earthquake rupture is the stress heterogeneity along the subduction megathrust (Shaw, 2000). This implies that asperities will vary with each earthquake cycle. In the last seven years the Sumatra 2004 (M_w 9.2), Chile 2010 (M_w 8.8), and Japan 2011 (M_w 9.0) megathrust earthquakes have highlighted the hazard posed by subduction zones and the study of their structure, as well as the seismological process occurring within them, is now of particular scientific interest and importance.

The Sumatra subduction zone (Figure 1.1) is an excellent example of a large scale ocean-continent collision zone and is therefore an ideal environment to study the mechanisms of earthquakes generated within a subduction zone. In the last seven years, following the 2004 Boxing day M_w 9.2 earthquake (Figure 1.1) and subsequent tsunami, the northern region of Sumatra has been intensively studied, while the southern and central region have attracted less attention due to their lower levels of seismicity in recent years. However, the Mentawai segment in central and southern Sumatra has previously exhibited strong earthquake and tsunamigenic potential with a M_w 8.5-8.9 and M_w 8.7-8.8 event in 1797 and 1833 respectively (Figure 2.2, Natawidjaja et al., 2006; Newcomb and McCann, 1987). Historical records indicate that the 1833 earthquake ruptured the whole of the Mentawai segment from the Enggano Island in the south to Sipora Island in the north (Natawidjaja et al., 2006; Newcomb and McCann, 1987), generating a devastating tsunami 550 km along the coast (Figure 1.1). Consequently, because of these two large megathrust earthquakes and the occurrence of an M_w 8.4 earthquake on the 12 September 2007 (Figure 1.1, Konca et al., 2008), scientific attention has recently turned to the Mentawai segment of the subduction zone (Figure 1.1). It is currently thought that this segment has the potential to cause a M_w 8.5+ earthquake and the associated tsunami could destroy the city of Padang (Figure 1.1). The risk potential is heightened by the fact that Padang lies only 3 m above sea level, on the east coast of Sumatra, and is home to 800,000 + people.

In this study new data from two local seismic networks installed between December

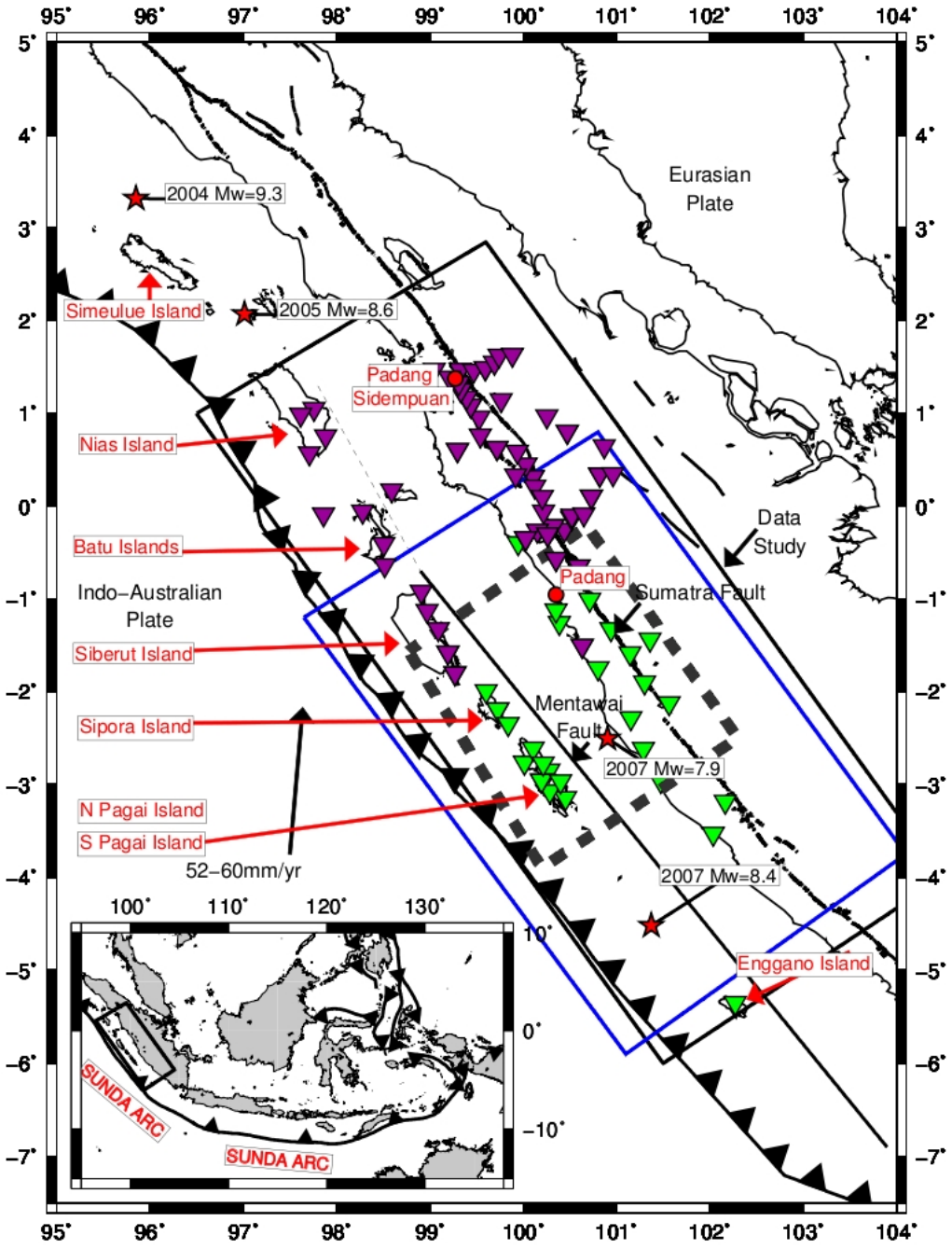

Figure 1.1: The study region in Sumatra. The inset shows the location of the study region in relation to the Sunda Arc. The study region is indicated by the black box. Also shown in main figure are the station locations (inverted green triangles represent the Mentawai network stations and inverted purple triangles represent the central network stations), the hypocentre of recent large events (red stars) and the location of the Sumatran Fault and Mentawai Fault. The blue box indicates the location of Mentawai segment. The dashed grey box indicates the location of the Mentawai region within the Mentawai segment.

2007 and February 2009 within central and southern Sumatra, from 4° S to 2° N (Figure 1.1), reaching from the forearc islands to the backarc, are presented. Local passive seismological networks have been previously used in numerous subduction zones (e.g Cascadia, Japan, Chile, New Zealand, Costa Rica, (Zhao et al., 2001; Zhao et al., 1992; Haberland et al, 2009; Eberhart-Phillips et al., 2005; Deshon et al., 2004) to investigate in detail the structure and associated deformation of subduction. Similarly, the recorded seismicity from our local networks is used to produce tomographic models of seismic velocity and to determine seismic anisotropy. This will enable us to constrain the geometry of the slab, the state of stress in the slab and upper plate, as well as the underlying subduction zone processes.

1.1 Thesis Outline

The tectonic setting of Sumatra and its past seismicity are described in Chapter 2. It includes a detailed description of the geological structure of the region (e.g subduction slab characteristics, Sumatran Fault and Mentawai Fault), a summary of historic earthquakes greater than M_w 8.0 (1797, 1833 and 1861), and recent large events (2004, 2005, 2007, 2009, 2010) that have occurred along the Sumatra subduction zone.

Between December 2007 and February 2009 two seismic networks were installed within central and southern Sumatra, from 4° S to 2° N (Figure 1.1), reaching from the forearc islands to the backarc. The data acquisition and processing, including network set up, event detection and arrival time determination, are described in Chapter 3.

In Chapter 4 the coupled hypocentre-velocity problem is explained. This includes a brief summary of the main aspects of linear inverse theory (Section 4.1) which is used to determine the hypocentre locations, the origin times and the velocity structure of the region the rays pass through, from the observed arrival times. In Section 4.4 a detailed description of the procedure for determining the resolution of the obtained tomographic models from the resolution matrix (Section 4.4.1), as well as a summary of the synthetic resolution tests that were carried out (Section 4.4.2), can be found.

Using a high quality subset of data from the Mentawai network (Figure 1.1), a 1D velocity model was derived and the hypocentres were determined, allowing, for the first time, the structure and geometry of the forearc within the Mentawai region of the Mentawai segment to be revealed (Figure 1.1). The high quality subset of arrival times were then inverted for 2D and 3D velocity models of the region, with special attention paid to the resolution to identify artifacts within the models. The *Vp* models reveal further structural information on the subsurface, suggesting the depth of the continental mantle and thus point of slab/Moho intersection as well as the origin of the forearc islands. The *Vp/Vs* models indicate areas of slab hydration and regions of possible serpentinization can be identified. The tomographic models, along with accurate hypocentre locations and first motion polarity focal mechanisms, are presented and discussed in Chapter 5. This chapter is a paper entitled "Structure and seismogenic properties of the Mentawai segment of the Sumatra subduction zone revealed by local earthquake travel time tomography " which is published in the Journal of Geophysical Research (Collings et al., 2012).

In addition to the tomographic models, the style and geometry of the deformation occurring within Sumatra were further investigated using measurements of seismic anisotropy, through observations of shear wave splitting (SWS). An advantage of performing SWS is that teleseismic phases can be used to determine the seismological processes occurring beneath the subducting slab interface, within the oceanic lithosphere and asthenosphere. Additionally, SWS results from local *S* phases can be used to aid our interpretation of the processes occurring within the mantle wedge and the type of deformation occurring in the overriding crust. In Chapter 6 the different techniques to estimate the SWS parameters are summarized and the causes of seismic anisotropy are discussed.

The teleseismic and local SWS results are presented and discussed in Chapter 7. This is a paper entitled "Seismic Anisotropy in the Sumatra subduction zone" which has been submitted to the Journal of Geophysical Research. The results are compared to a

previous study of seismic anisotropy by Hammond et al., (2010) and global models of mantle flow within the mantle wedge (e.g Ribe, 1989; Long and Silver, 2008) and sub-slab mantle (e.g Long and Silver, 2008, 2009). We also compare our results to other regions where large strike-slip faults have previously been found to cause seismic anisotropy (e.g San Andreas Fault; Alpine Fault/Marlborough region New Zealand). Additionally, forward modeling is used to aid our interpretation of the SWS results.

Lastly, the conclusions are drawn from the tomography images, earthquake source parameters, focal mechanisms and seismic anisotropy. These observations are bought together to produce a comprehensive image of the Mentawai segment of the Sumatra subduction zone and the processes occurring within it (Chapter 8). This includes a detailed discussion of the updip and downdip limits of the seismogenic zone, as well as addressing the question, where will the next rupture occur?

Chapter 2

Geological Setting

The following chapter will give an overview of the tectonic setting of the Sumatra subduction zone, which is located on the Sunda Arc between the Sunda Strait and the Andaman Islands (Figure 2.1), and a detailed description of the previous recent and historical ruptures that have occurred in this section of the Sunda Arc. Also included is a discussion on the apparent segmentation of the Sumatra subduction zone due to possible permanent barriers, as well as a summary about the Mentawai segment (Figure 1.1) which is the focus of our tomography study.

2.1 Tectonic Setting

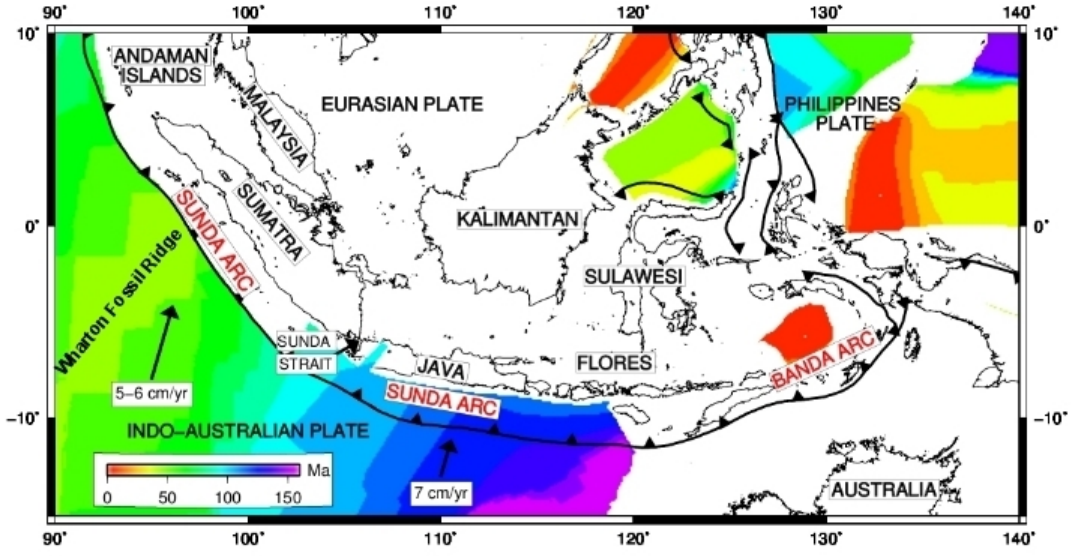

Figure 2.1: Tectonic map of the Sunda Arc showing the age of the oceanic crust (Müller et al., 1997) and plate boundaries (from NOAA, National Geophysical Data Centre). The Sumatra subduction zone is located between on the Sunda Arc between the Sunda Strait and the Andaman Islands.

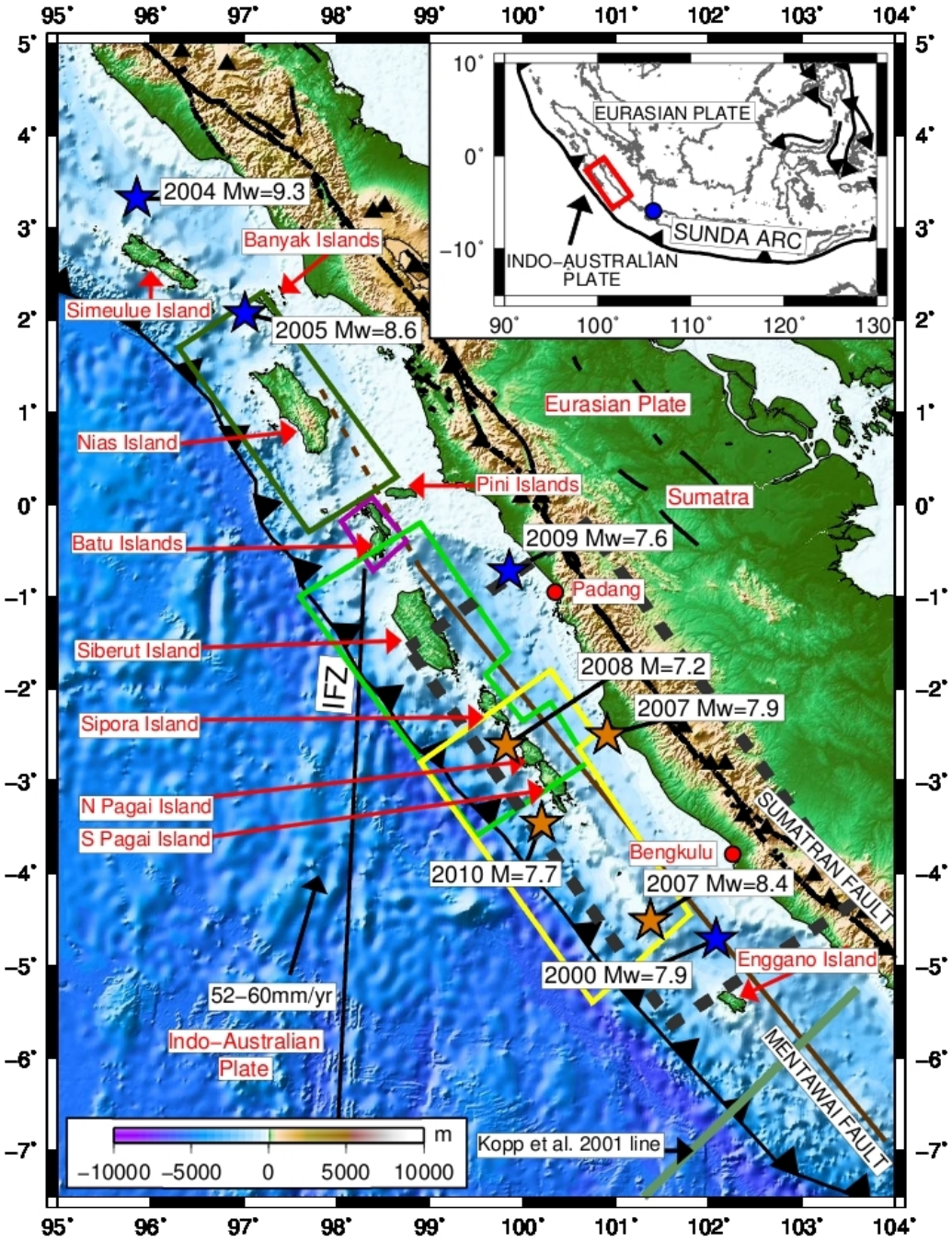

Figure 2.2: Map showing the Sumatra subduction zone and previous large earthquake ruptures taken from Natawidjaja et al. (2006). The Indo-Australian Plate is moving toward the Eurasian Plate forming the Sunda Arc. The blue circle on the inset map of the Sunda Arc marks the position of the Sunda Strait. The Mentawai Fault (Diament et al., 1992) (brown line) and the Sumatran Fault (Sieh and Natawidjaja, 2000) (black line) are also shown. The locations of recent large earthquakes (NEIC catalogue) are indicated by blue and orange stars. The orange stars show the four recent large thrust events that have occurred within the Mentawai segment (M_w 8.4 2007 event, M_w 7.9 2007 event, M_w 7.2 2008 event, M_w 7.7 2010 event). Historic ruptures are indicated by the colored boxes. Light green is the M_w 8.7-8.9 1797 rupture, yellow is the M_w 8.7-8.8 1833 rupture, dark green is the M_w 8.5 1861 rupture and purple is the M_w 7.7 1935 rupture (Rivera et al., 2002). The Investigator Fracture Zone (IFZ) is marked by a black line. The study area for the tomography (outlined by the grey dashed box, red box in inset map) is located in the Mentawai segment of the subduction zone, in the rupture area of the 1797 and 1833 events. The green line at the bottom of the figure shows the location of the refraction line in Kopp et al. (2001). The scale at the bottom left is bathymetry and topography.

The subduction of the Indo-Australian Plate beneath the Eurasian Plate has formed the Sunda Arc which extends for 5,600 km from the Andaman Islands in the northwest to the Banda Arc in the southeast. (Figure 2.1). The island of Sumatra is located on the overriding plate of the Sunda Arc between the Sunda Strait, in the south, and the Andaman Islands, in the north (Figure 2.1 and 2.2). A unique feature of the Sumatra margin is the existence of the forearc islands approximately 75 - 125 km from the deformation front. It has previously been suggested that the forearc islands were part of a former accretionary prism that was uplifted (Hamilton, 1977; Kopp et al., 2001). Singh et al. (2008) proposed that under-plating of sliced ocean crust could have contributed to the uplift of the forearc islands and the presence of ophiolites supports this hypothesis (Samuel et al, 1997). The uplift could then be further enforced by a backthrust on the northeastern side of the forearc islands (Singh et al., 2009).

On the subducting Indo-Australian Plate lies the Wharton Fossil Ridge (Figure 2.1), a bathymetric feature that is left laterally offset by fossil transform faults, which is responsible for the variation in lithospheric age of the oceanic crust along the arc (Deplus et al., 1998). The age of the crust increases from 49-96 Ma beneath Sumatra (where the Wharton Fossil Ridge subducts) to 96-134 Ma beneath Java (Figure 2.1), which is reflected in the dip, temperature and depth of the Wadati Benioff zone (Shapiro et al., 2008). Adjacent to the Wharton Fossil Ridge the subducting lithosphere is significantly more buoyant, warmer and subducting at a shallower angle (average dip 30° determined from relocated earthquakes between 40-200 km depth) than regions further north or south, where the lithosphere is less buoyant, cooler and dipping at 40-50° (Shapiro et al., 2008). In addition to the changing temperature, age and dip of the subducting plate along the Sunda Arc, there is also a variation in the angle of subduction and convergence rate of the Indo-Australian Plate. At the Sunda Strait the subduction angle changes from normal subduction beneath Java to oblique subduction beneath Sumatra (~40° at 2° N) with a convergence rate that decreases from 60 mm/yr at 6° S to 52 mm/yr at 2° N (Prawirodirdjo et al. 2000). The oblique subduction causes strain partitioning of the convergence into strike-slip motion and thrust motion.

Strike-slip motion along the Sumatran margin is accommodated by the Sumatran Fault (Figure 2.2), a large, highly segmented strike-slip fault that extends for 1,900 km from the Sunda Strait to the Andaman Sea across Sumatra, parallel and in close proximity to the volcanic arc (e.g Sieh and Natawidjaja, 2000). Along the Sumatran Fault the slip rate varies from 6 mm/yr at the Sunda Strait to 25 mm/yr at the equator (Bellier and Sebrier, 1994; Bellier and Sebrier, 1995; Genrich et al., 2000). The geological and GPS-derived slip rates correlate very well the seismic slip rates between 0° and 2° S but elsewhere the seismic slip rate is significantly less than geological/GPS-derived slip rate, suggesting that slip may be taken up aseismically along the fault (Lasitha et al., 2006). However, the Sumatran Fault does not account for all of the strike-slip motion along the Sumatran margin (McCaffrey et al., 2000). Approximately two thirds of the margin parallel shear occurs along the Sumatran Fault in northern Sumatra, while within the Mentawai region the Sumatran Fault only accommodates one third of the strike-slip motion. The remaining shear is taken up by the subduction interface or a second fault within the forearc (McCaffrey et al., 2000; Diament et al., 1992). Two models have been proposed to explain the deformation in the forearc caused by the oblique subduction and variation in slip rate along the Sumatran Fault.

McCaffrey (1991, 1992) showed, based on earthquake slip vectors, that the forearc sliver between the Sumatran Fault and the trench is being stretched in a northwesterly direction. His model implies that the forearc is not behaving as a rigid plate as it is being stretched with a uniform strain rate of 1-3 x 10^{-8} mm/yr. The resulting deformation from the stretching is not clearly understood. McCaffrey (1991) has suggested that the forearc will stretch by either normal faulting, which forms forearc basins, or by strike slip faulting, and therefore faults will cross the forearc from the trench to the Sumatran Fault. However, there is no significant evidence for extensional deformation or forearc stretching (Bellier and Sebrier, 1995; Malod and Kemal, 1996).

Alternatively, Diament et al. (1992) proposed that arc-parallel shear is taken up by more than one arc-parallel strike-slip fault within the forearc and such a model was supported by the discovery of the Mentawai Fault (Figure 2.2). The 600 km long Mentawai Fault is

located east of the Mentawai Islands at the boundary between the forearc ridge and the forearc basin. Diament et al. (1992) argued that the linearity and positive flower structures of the Mentawai Fault are characteristic of a large scale strike-slip fault, similar to the Sumatran Fault, explaining the small amount of trench-parallel motion observed along the Sumatran Fault in southern Sumatra. (Figure 2.2). The 600 km long Mentawai Fault is located east of the Mentawai Islands at the boundary between the forearc ridge and forearc basin (Diament et al. 1992). There is however disagreement as to whether the deficit in strike-slip motion on the Sumatran Fault is accommodated on the Mentawai Fault. A more recent study using high resolution seismic reflection and bathymetry data (Singh et al., 2009) did not find any evidence of strike-slip motion. Instead they imaged the Mentawai Fault as a series of southwest dipping backthrusts. This would support Karig et al.'s (1978) original interpretation that the Mentawai Fault is a backthrust with a component of strike-slip motion occurring on it.

2.2 Past Seismicity

Past seismicity within the region indicates that thrust motion along the Sumatran megathrust is primarily accommodated by large thrust earthquakes at the subduction interface. Since 2004, five large thrust earthquakes (2004, 2005, 2007a, 2007b, 2010) have occurred (Figure 2.2). Prior to 2004, three great earthquakes have occurred within the last 300 years (1797, 1833 and 1861), rupturing major segments of the forearc (Figure 2.2).

2.2.1 The 1797 M_w 8.7-8.9 Earthquake

On the 10 February 1797 historical accounts document a large earthquake which caused considerable damage in Padang and resulted in a tsunami that was observed in the mainland ports and at the Batu Islands (Newcomb and McCann, 1987). Analysis of coral heads and forward modeling of the data indicates that the co-seismic slip extended from the trench to 34-40 km depth, rupturing all of the megathrust beneath the Mentawai Islands and yielding a moment magnitude of 8.7-8.9 (Chlieh et al., 2008; Natawidjaja et

al., 2006). The southern limit of the rupture occurred on South Pagai Island, at 3.2° S, within a strongly coupled region of the megathrust, while the northern end of the rupture was near the southern end of the Batu Islands, at the edge of the weakly coupled equatorial patch (Chlieh et al., 2008) (Figure 2.2).

2.2.2 The 1833 M_w 8.7-9.1 Earthquake

The 1833 event is the largest historical earthquake documented in Sumatra. The earthquake originated in southern Sumatra causing a devastating tsunami 550 km along the coast and activity at three nearby volcanoes to increase (Natawidjaja et al., 2006; Newcomb and McCann, 1987). Newcomb and McCann (1987) concluded from the historical accounts and by considering the tectonics of the region that the size of the event was between M_w 8.7-8.8, rupturing the entire plate margin from Enggano Island in the south to the Batu Islands in the north; while Natawidjaja et al. (2006) concluded from the analysis of coral heads and forward modeling that the event was between M_w 8.9-9.1, with the northern limit of the rupture beneath Sipora Island (Figure 2.2). Surrounding the rupture limits of the 1833 event inferred by Newcomb and McCann (1987), beneath the Batu Islands and Enggano Island, low level seismicity is observed and the region is weakly coupled, suggesting that the 1833 event may have ruptured a continuous block of the megathrust (Chlieh et al., 2008). However, the northern rupture limit deduced by Natawidjaja et al. (2006) implies that the rupture stopped within a highly coupled region. Forward modeling (Natawidjaja et al., 2006) suggests that the down-dip end of the rupture shallows from 50 km depth beneath Sipora Island and North Pagai Island to 35 km depth beneath South Pagai Island,while the updip end extends to between 20 km depth and the trench.

2.2.3 The 1861 M_w 8.5 Earthquake

The M_w 8.5 1861 event ruptured 300 km of the plate margin in northern Sumatra between the Banyak Islands and Pini Islands (Figure 2.2), generating a tsunami along 500 km of the arc and uplifting the north and west coast of Nias Island (Newcomb and

McCann, 1987) (Figure 2.2). The northern boundary of the 1861 rupture, the Banyak Islands, lies along a major cross structure associated with vertical faults. This has created a major break in the overriding plate which acts as a barrier, inhibiting rupture propagation (Karig et al., 1980). The southern boundary, the Pini Islands, has tectonic features in both the overriding and the subducting plate that affect the properties of the plate interface. The Pini islands are located on a broad basement arch which is believed to have been stable since the Miocene, causing it to be an anomalous crustal block within the forearc (Beaudry, 1983). In addition to this, within the subducting slab, the Investigator Fracture Zone (Figure 2.2) intersects the forearc and extends beneath the continental margin causing an increase in interplate coupling, stress and deformation (Newcomb and McCann, 1987).

2.2.4 The 2004 M_w 9.3 Sumatra-Andaman Earthquake

The epicentre of the devastating M_w 9.3 earthquake on the 26 December 2004 was northwest of Simeulue Island at 30-40 km depth (Figure 2.2 and 2.3). The rupture propagated north along the plate margin for 1,300 km from Northwest Sumatra to the Andaman Islands, extending to the trench, creating a devastating tsunami (Lay et al., 2005; Ammon et al., 2005). The rupture lasted 600 s and can be divided into three segments (Figure 2.3). It began in the southeast corner of the first segment, the Sumatra segment, initially for the first 50 s with a low energy release and slow rupture rate, before increasing to 2.5 km/s with a large slip of 5-20 m for the next three minutes, generating high frequency radiation. The second and third segments, the Nicobar and Andaman segments, then experienced 5 m of slow slip from 230 s and 600 s respectively, with rapid slip of up to 2 m occurring within the Andaman segment after 350 s. The slow slip continued within these two segments for up to an hour after the rupture began, releasing two thirds of the seismic moment (Lay et al., 2005; Ammon et al., 2005). The contrast in rupture properties of the segments may be due to the variation in age of the oceanic lithosphere (Section 2.1). Within the younger Sumatra segment the buoyant and shallower dipping slab results in the slab being strongly coupled to the overriding plate; while in the older northern Andaman segment, as the subducting

lithosphere is less buoyant, cooler and dipping at steeper angle, there is weaker coupling

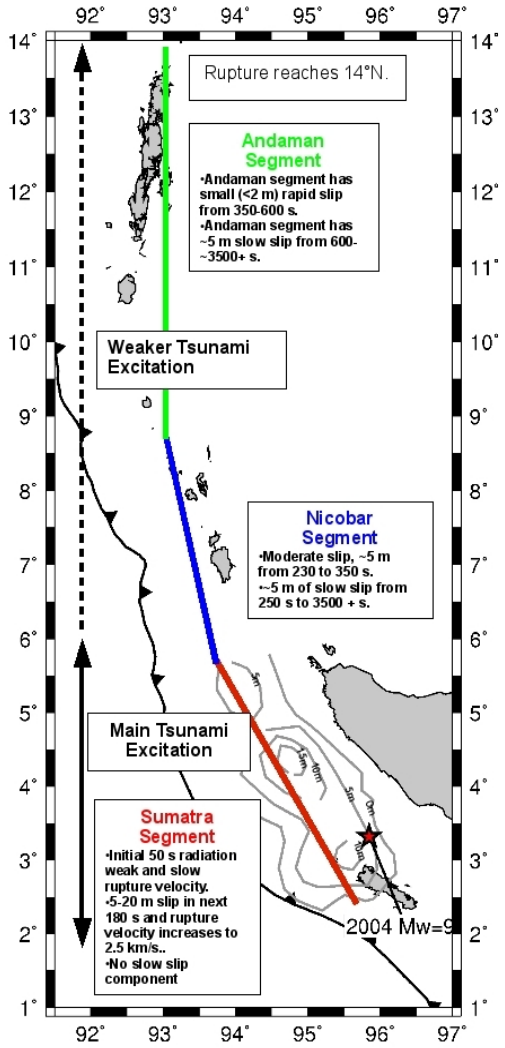

Figure 2.3: The rupture process of the M_w 9.3 earthquake on the 26 December 2004 . Adapted from Lay et al.,(2005). Contours indicate the area of co-seismic slip and are in 5 m intervals.

between it and the overriding plate (Shapiro et al., 2008). Aftershock activity equivalent to a M_w 8.7 earthquake followed the rupture (Subarya et al. 2006), exhibiting a pattern consistent with a 1,300 km long rupture (Engdahl et al., 2007).

The down dip width of the aftershock zone varies from 200 km at the northern end of the rupture, to 275 km at the southern end (Engdahl et al., 2007). Most aftershocks occur at

depths < 35 km. However, in a spatially limited region of the Sumatra segment aftershocks occur at 35-70 km depth (Engdahl et al., 2007). Thermal modeling studies have found that the 350°C to 450°C isotherms are located 214 and 254 km from the trench, at ~34-60 km depth (Hippchen and Hyndman, 2008; Klingelhoefer et al., 2010). Hippchen and Hyndman (2008) conclude that as this depth is beneath the slab-Moho intersection (assumed to be at ~30 km depth) and the slab-Moho intersection coincides approximately with the down dip limit of co-seismic slip and the majority of aftershocks, the down dip limit of the seismogenic zone is the slab-Moho intersection due to the presence of a thin layer of serpentinite in the mantle wedge. However, more recent tomographic models (Dessa et al., 2009; Klingelhoefer et al., 2010) suggest that the continental Moho is very shallow, intersecting the slab at 21-25 km depth. This implies that a significant portion of the rupture, as well as a number of aftershocks, occurred along the interface between the oceanic crust of the down-going plate and forearc mantle. Additionally, the presence of co-seismic slip occurring along the plate interface beneath the forearc mantle suggests that the mantle wedge is not serpentinized.

It has been proposed that the epicentre of the earthquake did not originate at the top of the subducting plate or within the overlying sediments (Singh et al., 2008). A seismic reflection survey of the forearc showed that, within the region of the 2004 earthquake, the subducting crust and oceanic mantle are broken and displaced by landward-dipping thrust ramps, which they argued would inhibit the build up of a large amount of stress at the subduction interface. Instead the authors proposed that the 2004 earthquake initiated below the continental mantle, within the upper mantle of the subducting plate, propagating up to the sea floor via a decollement at the top of the oceanic mantle and crustal thrust faults at the front of the wedge (Singh et al., 2008).

The updip limit of the southern region of the 2004 rupture (Ammon et al., 2005), as well as the aftershock locations (Engdahl et al., 2007), suggest that the updip limit of the seismogenic zone is very close to trench, coinciding approximately with the location of the 100-150°C isotherms (Hippchen and Hyndman, 2008, Klingelhoefer et al., 2010). In addition to this, high resolution bathymetry data of the accretionary prism shows

significant faulting, possibly due to the rupture propagating to the toe of the accretionary prism during the 2004 earthquake (Henstock et al., 2006). These observations all imply that this section of the Sumatra subduction zone is capable of producing shallow megathrust slip.

2.2.5 The 2005 M_w 8.5 Nias Earthquake

On the 28 March 2005 the Sunda megathrust ruptured again, 300 km southeast of the 2004 event at 2.1° N, 97.0° E and 30 km depth, within the same region as the 1861 earthquake (Figure 2.2 and 2.4). The rupture began slowly, propagating at 2.9-3.3 km/s with an average slip of 5.9 m, first initially to the north for 100 km, which would have caused a M_w 8.2 event, and then 40 s later to the southeast for 200 km which resulted in the M_w 8.5 event (Walker et al. 2005, Hsu et al. 2006). The total duration of the rupture was 120 s. The co-seismic slip occurred within a locked area of the megathrust that extends from the trench axis, 150 km landward. The updip edge of the rupture is found at ~10-15 km depth on the western coast of the island belt, with the downdip edge lying at ~48 km depth, east of the island belt (Hsu et al., 2006; Gahalaut and Catherine, 2006).

Afterslip following the 2005 rupture surrounded the region where co-seismic slip occurred, as the rupture increased the stress on this area; 1.4 m and 0.5 m of afterslip occurred within the updip and downdip regions respectively, while an additional 0.5 m of afterslip also occurred south of the co-seismic rupture, at the Batu Islands (Hsu et al., 2006). The amount of afterslip was equivalent to a M_w 8.2 earthquake. However, the sum of co-seismic slip and post-seismic slip from the 2005 rupture is still significantly smaller than the moment deficit of slip accumulated since 1861 (Chlieh et al., 2008).

Following the rupture, on the plate interface at 15-20 km depth, a narrow (20-30 km) band of aftershocks occurred updip of the co-seismic asperities and just down downdip of the updip zone of afterslip modeled by Hsu et al. (2006) (Tilmann et al., 2010). The aftershocks began close to the 500 m bathymetry contour and coincide with the break in forearc slope which marks the transition from outer wedge to inner wedge in the

Coulomb Wedge model (Wang and Hu, 2006). These events also coincide with the 100-150°C isotherms (Grevemeyer and Tiwari, 2006), which at most subduction zones is the temperature at which the updip transition in frictional behaviour of the plate interface is thought to occur (Hyndman et al., 1997). As almost no seismicity is seen between the

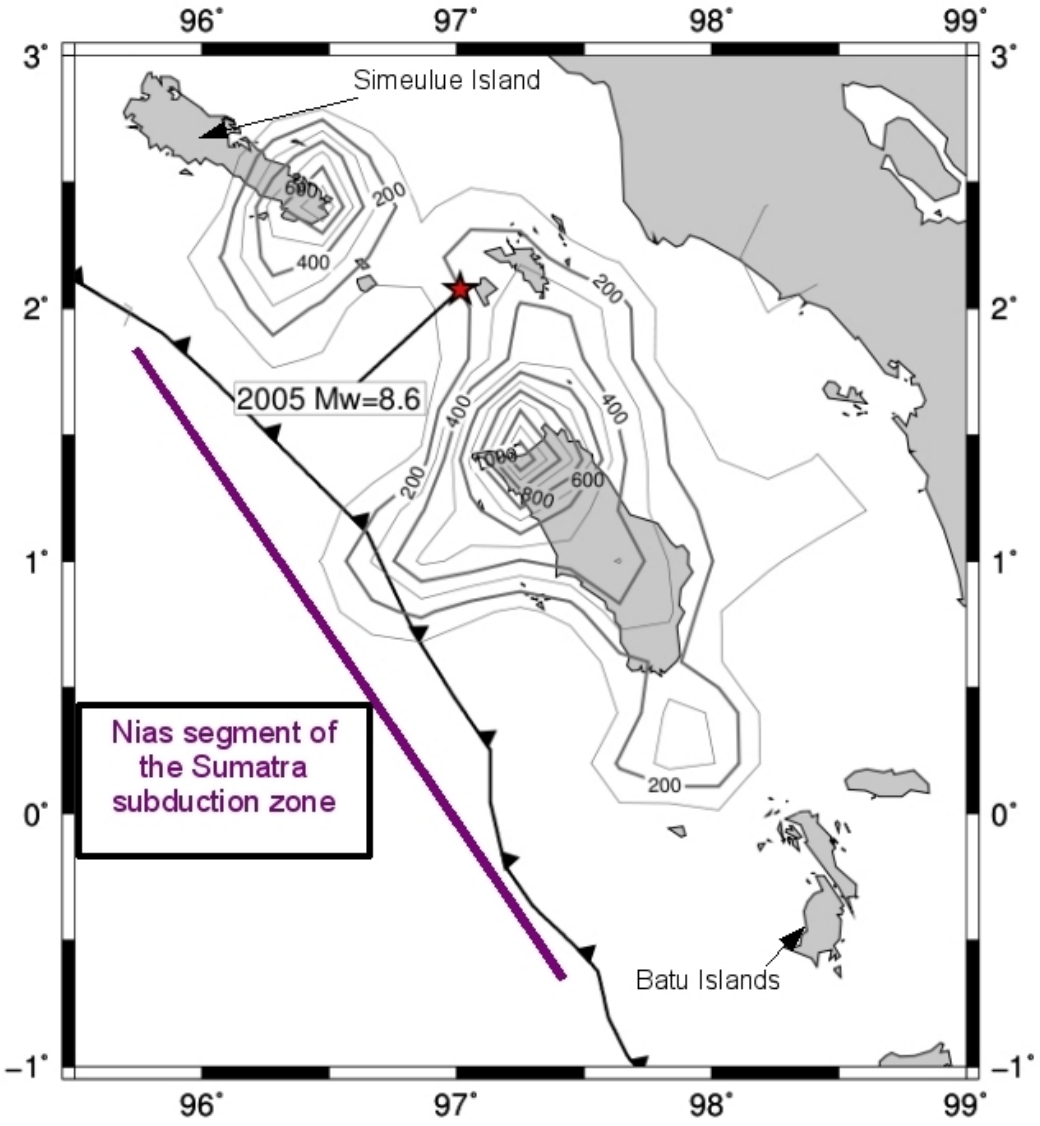

Figure 2.4: The co-seismic distribution for the M_w 8.6 event on the 28 March 2008 (Konca et al., 2007). The co-seismic slip contours are in 100 cm intervals.

trench and the seismic band, the seismic band was thought to mark the transition zone from aseismic behaviour/stable sliding to seismic behaviour/unstable sliding and

therefore the updip extent of seismic rupture (Tilmann et al., 2010). NW of Simeulue Island, in the southern region of the 2004 rupture area where the rupture propagated almost to the trench, the seismic band is missing, the bathymetry never shallows to below 500 m and a number of aftershocks occur close to the trench, suggesting that the updip limit of seismic behaviour in this region is close to the trench (Tilmann et al., 2010). This suggests that there is a sudden transition in the updip limit of the seismogenic zone between the Nias (Figure 2.4) and Sumatra segment (Figure 2.3), possibly due to unusual plate interface properties (i.e. sediment properties or plate temperature) or variations in the amount of sediment entrained (Tilmann et al., 2010, Gulick et al., 2011). However, recently a study has found that on 4 January 1907 a tsunami earthquake occurred within the shallow part of the megathrust in the Nias segment (Figure 2.4), rupturing the frontal section of the interface that did not rupture during the 2005 Nias earthquake (Kanamori et al, 2010). This implies the shallow part of the interface is not aseismic as previously assumed but instead is conditionally stable, and that the updip limit of the seismogenic zone is the trench. The 1907 event may have prevented rupture propagating to the trench during the 2005 rupture because the amount of strain that had accumulated since 1907 on the upper part of the interface was not enough to cause a tsunami earthquake (Briggs et al., 2006; Hsu et al., 2006). This suggests that the upper part of the megathrust (above 15-20 km depth) maybe in a different earthquake cycle to the lower part (below 15-20 km depth) (Briggs et al., 2006).

Similar to the rupture region of the 2004 Sumatra-Andaman segment, the continental Moho in the Nias segment of the Sumatra megathrust (Figure 2.4) is also thought to lie at a shallow depth (<30 km depth, Kieckhefer et al., 1980). Prior to the 2005 M_w 8.5 event, in the Nias segment of the megathrust, the locked fault zone was thought to extend below the slab-mantle intersection into the forearc mantle (Simoes et al., 2004) and indeed the slip model (Konca et al., 2007) and aftershock locations of the Nias earthquake (extend upto 150-170 km from the trench to ~35 km depth, Engdahl et al., 2007) do suggest the seismogenic zone down dip limit is beneath the forearc continental mantle. This implies that the forearc mantle wedge is also not serpentinized in the Nias

segment.

An important conclusion from the 2005 rupture was that it was sparked by the local stresses created by the 2004 rupture despite the increase being only 0.1 bar at its hypocentre (Nalbant et al., 2005). Subsequently the 2005 rupture was found to increase the stress on the megathrust to the south, suggesting that the Mentawai region now posed the greatest seismic threat (Nalbant et al., 2005).

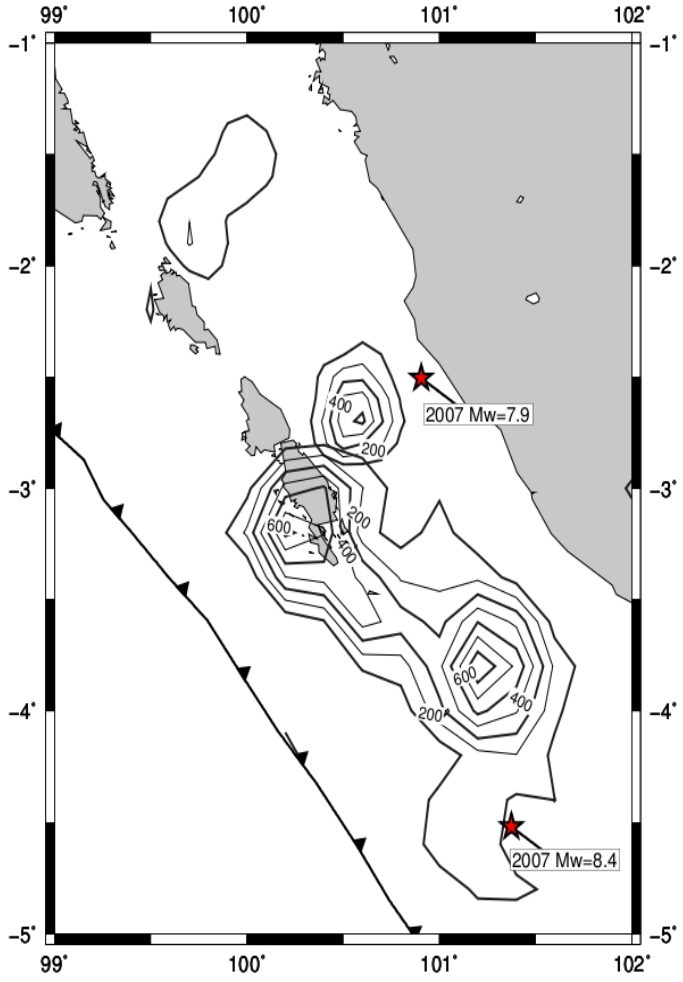

Figure 2.5: The co-seismic slip distribution of the M_w 8.4 and M_w 7.9 earthquakes on the 12 September 2007 (Konca et al., 2008). The co-seismic slip contours are in 100 cm intervals.

2.2.6 The 2007 M_w 8.4 Bengkulu Earthquake

The 12 September 2007 M_w 8.4 earthquake initiated at 4.57° S 101.38° E, within the southern section of the Mentawai segment of the megathrust, 130 km southwest of Bengkulu, within the 1833 rupture area (Figure 2.2 and 2.5, Konca et al., 2008). It should be noted that this rupture did not occur in the rupture region of the 1797 event, a region that was thought to have high Coulomb failure stresses after the 2004 and 2005 events (Wiseman and Bürgmann, 2011). The rupture lasted for approximately 100 s, propagating at 2.1 +/- 0.4 km/s to the northwest with initially low slip (2-3 m) near the hypocentre. The slip then increased to up to 10 m at 3-3.5° S, creating a M_w 8.4 earthquake. The updip limit of rupture propagation was ~15-20 km depth, SW of the island belt, ~50 km from the deformation front; while the down-dip limit was NE of the Mentawai Island ~175 km from the trench, at ~40-50 km depth (Konca et al., 2008). Twelve hours after the main shock a large earthquake, M_w 7.9, occurred near the Sumatra coast, 185 km SSE of Padang (Figure 2.2 and 2.5). This event lasted for 80 s, with the energy released in two pulses, and ruptured the down-dip region of the seismogenic zone (Lorito et al., 2008; Konca et al., 2008).

The 2007 earthquakes appear to have ruptured distinct patches of the fault that were previously strongly locked. Both events took place within the highly coupled rupture area of the 1833 event. However, the pattern and amount of slip between the events are very different. The moment released by the 2007 events was only between 10-70% of the moment released in 1833 and co-seismic uplift was significantly smaller. In 1883 the north coast of South Pagai Island (Figure 2.2) was uplifted by 2.2 m, while in 2007 it was only uplifted by 7 cm, indicating that it acted more like a barrier (Konca et al., 2008). The difference in the amount and location of slip between the two events was due to the fault rupturing in several separate patches because non-permanent barriers had developed from the stress distribution left over from previous earthquakes. As the moment released in 2007 represents only a fraction of the moment released in 1833 and only 25% of the moment that has accumulated since then, the potential for another large megathrust earthquake in the Mentawai region is high (Konca et al., 2008).

2.2.7 The 2009 M_w 7.6 Earthquake

On the 30 September 2009 an M_w 7.6 earthquake occurred on the eastern edge of the Mentawai segment of the megathrust, 60 km west-northwest of Padang, at a depth of 80-90 km, between the 2005 and 2007 events (Figure 2.2). The hypocentre lies within the lower part of the Wadati Benioff zone of the subducting slab, suggesting that it probably ruptured the mantle of the Indo-Australian Plate and not the Sunda megathrust. The focal mechanism for the event suggests oblique thrust motion. Assuming that the event is an intra-plate event, the focal mechanism would indicate a slightly oblique strike-slip event in the slab reference frame. The strike-slip motion aligns with the N-S and E-W fracture zones on the subducting plate, suggesting either right lateral motion along an east-west plane or left lateral motion on a north-south plane. The rupture lasted for only 10 s, creating high frequency energy that produced accelerations greater than other events (McCloskey et al., 2010).

2.2.8 The 2010 Mw 7.7 Mentawai Earthquake

On 25 October 2010 an M_w 7.7 event occurred within the southern Mentawai segment of the megathrust in the updip region of the subduction interface that did not rupture in the 2007 events, despite strong coupling (>50%) in this region (Konca et al., 2008; Chlieh et al., 2008) (Figure 2.2 and 2.6). The rupture initiated updip of the 2007 rupture, possibly triggered by stress changes caused by the 2007 events, and propagated, over ~90 s, updip and northerly for ~100 km with a low velocity rupture of ~1.5 km/s (Lay et al., 2011; Newman et al., 2011). The total slip of the rupture was between 2-4 m, and a 3-9 m tsunami, which devastated Sipora Island, North Pagai Island and South Pagai Island (Figure 2.2), was produced. Low levels of short period seismic wave radiation were produced from the event, resulting in weak ground shaking and the public not being aware of the significant tsunami risk it posed (Lay et al., 2011). It has been suggested that the large tsunami was due to the megathrust rupture arriving at a frontal thrust, which caused the 6 km water column to be uplifted (Singh et al., 2011a).

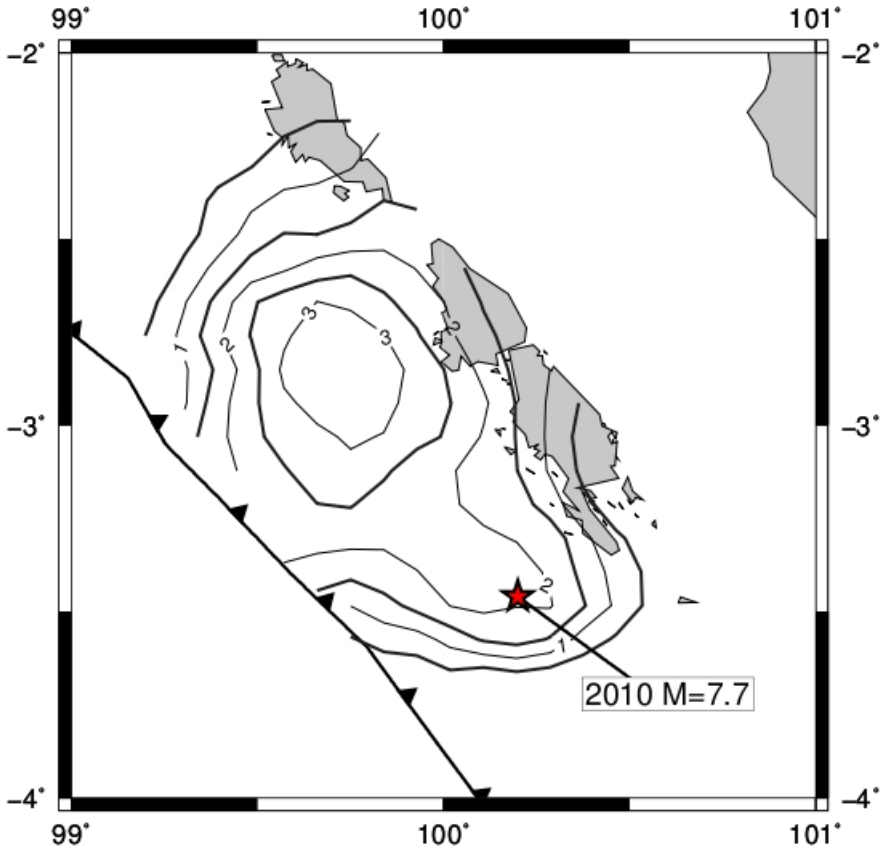

Figure 2.6: The co-seismic slip distribution of the M_w 7.7 event on the 25 October 2010 (Lay et al., 2011). The contours are in 0.5m intervals.

The Mentawai event, similar to to the M_w 7.6 1907 earthquake in the Nias segment (Figure 2.4) (Kanamori et al., 2010), appears to have initiated near the previously assumed updip limit of the seismogenic zone, within the frictionally unstable region of the interface, before propagating updip into the region that was previously assumed to be aseismic (Lay et al., 2011). Aftershocks following the 2010 event nucleate very close to the trench, providing further evidence of a very shallow near-trench rupture, as well as implying that the upper part of the interface can exhibit frictionally unstable behaviour (Bilek et al., 2011; Singh et al., 2011a).

2.3 Rupture Barriers

From analysis of the rupture area of the previous large thrust earthquakes along the Sumatran margin it has been noted that permanent lateral barriers control the rupture pattern of the larger events, for example, the northern boundary of the 2005 rupture coincides with the southern boundary of the 2004 event, and the southern boundary of the 2005 and 1861 events is close to the northern boundary of the 1797 rupture (Lay et al., 2005; Newcomb and McCann, 1987). Several ideas have been suggested for this apparent segmentation of the megathrust, for example, small spatially locked regions of the megathrust (e.g the Batu Islands and Simeulue Island, Figure 2.2) where slip can be released aseismically or in smaller earthquakes, the Simuelue saddle on Simuelue Island (Figure 2.2) (Briggs et al., 2006), variation in pore pressures along the thrust fault (Prawirodirdjo et al., 1997), a lithospheric boundary, e.g Andaman microplate (DeShon et al., 2005) and the subduction of tectonic features on the subducting plate, e.g N-S fracture zones (Franke et al., 2008) which could cause a delay in the onset of seismogenic behaviour and reduce the width of the seismogenic zone (Tilmann et al., 2010).

Non-permanent barriers to earthquake propagation can also develop within a segment of the megathrust. (e.g. Sumatra (Figure 2.3), Nias (Figure 2.4) or Mentawai segment (Figure 1.1)). This is shown by the M_w 8.4 and M_w 7.9 event pair on the 12 September 2007 and the M_w 7.7 event on the 25 October 2010 occurring within the southern Mentawai segment of the megathrust (Figure 1.1), in the rupture area of the 1833 event. The 1833 event, as described in section 2.2.2, originated in southern Sumatra and ruptured the plate margin from Enggano Island in the south to Sipora Island or the Batu Islands in the north, creating a M_w 8.7-9.1 earthquake and tsunami (Figure 2.2, Natawidjaja et al., 2006; Newcomb and McCann, 1987). In contrast, the M_w 8.4 2007 Bengkulu earthquake and subsequent M_w 7.9 earthquake released only 10-70% of the moment released in 1833, with significantly smaller uplift (Konca et al., 2008). The 25 October 2010 M_w 7.7 event occurred southwest of South Pagai Island, within the updip region of the subduction interface that had not ruptured in the 2007 events. The 2007 and

2010 earthquakes demonstrate a change in the behaviour of the southern Mentawai segment: instead of the whole segment rupturing at once in one large earthquake, a number of smaller magnitude events occurred that ruptured smaller portions of the subduction interface.

2.4 The Mentawai Region

The following tomographic study will focus on the Mentawai region within the Mentawai segment of the Sumatra subduction zone (Figure 1.1 and 2.2). The Mentawai segment stretches from 0° to 5° S and includes Siberut Island, Sipora Island, North Pagai Island, South Pagai Island and Enggano Island. As discussed in Section 2.2 and 2.3, large earthquakes have occurred within this region in 1833, 1797, 2007, 2009 and 2010 (Figure 2.2). The rupture areas of the1797 and 1833 earthquakes indicate that a permanent barrier to rupture propagation exists north of the Mentawai segment at the Batu Islands and possibly south at Enggano Island; while the 2007 and 2010 events suggest that non-permanent barriers can also develop within the segment due to the stress distribution left over from previous ruptures. The 2007 M_w 7.9 event ruptured the down-dip region of the megathrust, suggesting that the down-dip limit of the seismogenic zone is NE of the Mentawai Islands, at ~50 km depth; while the rupture area and aftershocks of the 2010 M_w 7.7 event indicate that the updip limit is the trench and not at ~15-20 km depth as previously assumed.

The seismicity within the Mentawai segment (Figure 1.1) between 1833 and 2007 was very low compared to the surrounding segments (Figure 2.7). Post-2007, seismicity significantly increased in the southern part of the Mentawai segment and was substantially higher than adjacent regions of the megathrust (Figure 2.8). However, despite the increase in activity within the last 4 years, the potential for an earthquake greater than M_w 8.5 within the northern part of Mentawai segment, where seismicity is still absent, remains high. Therefore gaining a greater understanding of the subduction zone is vitally important for estimating seismic hazard.

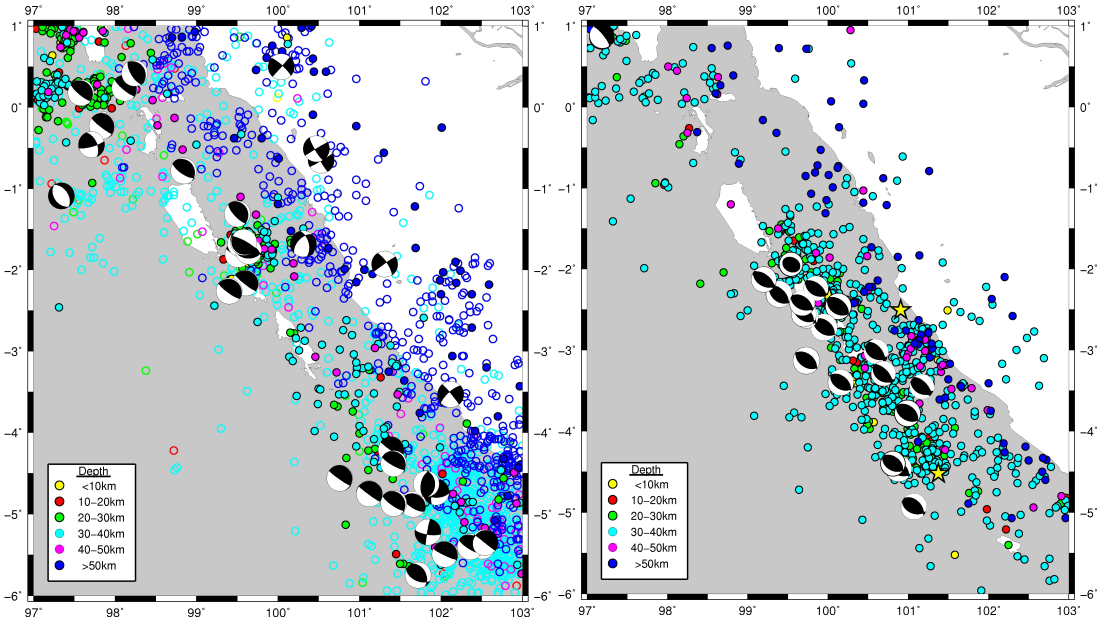

Figure 2.7: Map of past seismicity within the Mentawai segment between 1979 and 12 September 2007. Earthquake locations from the USGS/ NEIC catalogue. Events since the 2004 M_w 9.3 earthquake are indicated by the filled circles while earthquakes between 1979 and 2004 are shown by unfilled circles. Focal mechanisms of events in the gCMT catalogue of Magnitude 6 or greater are shown.

Figure 2.8: Map of seismicity within the Mentawai segment from the 12 September 2007 to December 2010 Earthquake locations from the USGS/ NEIC catalogue. Focal mechanisms from the gCMT catalogue of Magnitude 6 or greater are shown.

Chapter 3

The Experiment

Between December 2007 and February 2009 two seismic networks were installed in southern and central Sumatra, as well as the adjacent Mentawai Islands, Nias Island, Batu Islands and Siberut Island, at two different time periods which overlapped by 6 months (Figure 3.1). The networks were part of the UK Sumatra Consortium project funded by NERC and were installed and maintained by the University of Liverpool (UK), University of Cambridge (UK) and LIPI (Indonesia). A unique feature of the network is that the occurrence of the forearc islands allowed the deployment of seismic land-stations above the shallow part of the thrust fault, and consequently provided high quality locations, as well as tomography and shear wave splitting measurements, for the updip end of the seismogenic zone.

3.1 Acquisition of Data and Instrumentation

The stations were equipped with either CMG-6TD 3 component, Trillium 120P or CMG-3T 120P instruments. The 6TD instruments have the advantage of being robust, easy to deploy, lightweight and have their own integral data storage (8 GB or 16 GB).The CMG-3T and Trillium 120P instruments, despite being more complex to install and service (especially the CMG-3T as requires mass unlocking/locking), are more sensitive, have a wider frequency response (0.0083 to 50 Hz) and produce less noise. Accurate time stamps for the waveforms were received by GPS satellites. Each station was equipped with a photovoltaic system, including a battery charger, 12 V battery (2 x 12 V for broadband stations) and a solar panel (20W for 6TD and either 2 x 20 W or 36 W for broadband stations). Around the sites, fences were erected to protect the stations against animals and to deter thieves. The stations were visited, checked and the data recovered in

cycles of approximately 3 to 4 months. A detailed description of each network is included below.

3.1.1 Mentawai Network

Following the 12 September 2007 M_w 8.4 event and subsequent M_w 7.9 event 12 hours later, a temporary seismic network was installed in the Mentawai region to record the aftershock activity (Figure 3.2, Table 3.1). The network was installed during December

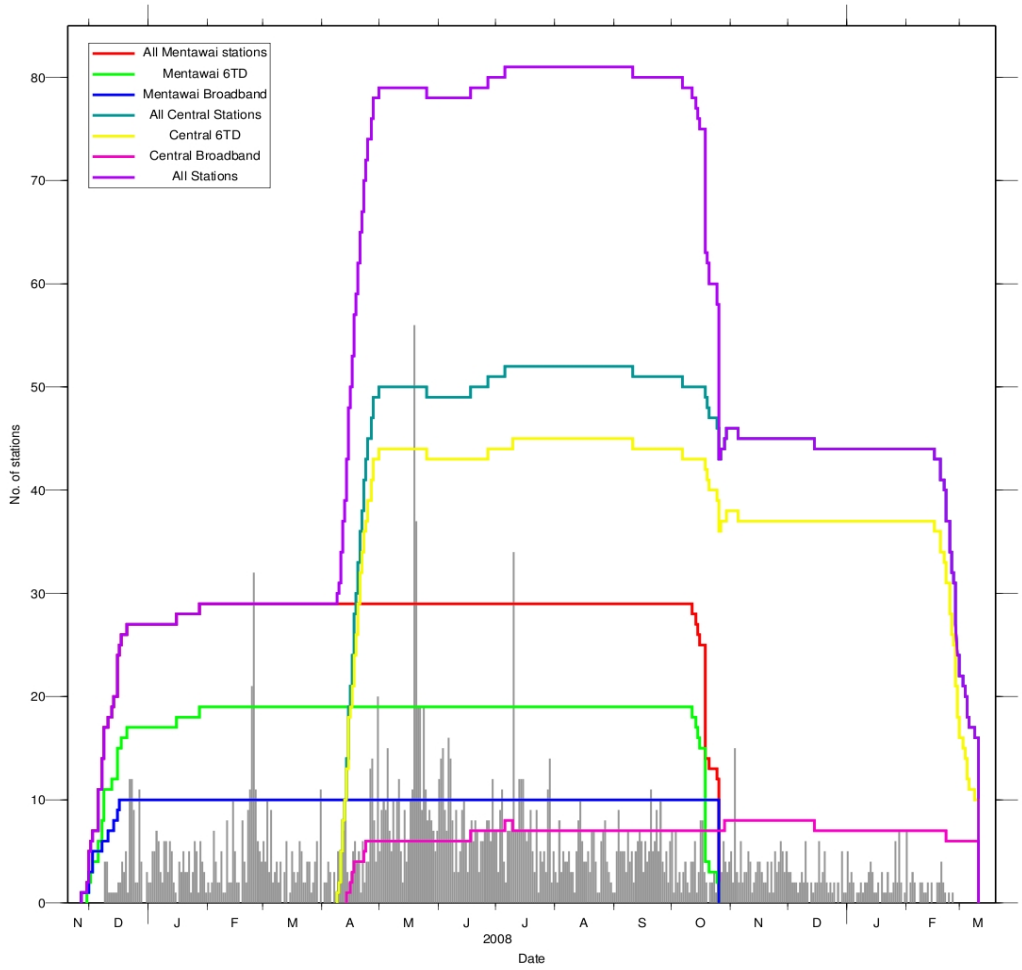

Figure 3.1: The number of stations (6TD and broadband) installed during the deployment of the two networks and the number of events which have been manually picked (grey histogram at bottom of figure). The 6TD stations are represented by the green (Mentawai Network) and yellow (Central Network), while the broadband stations are represented by the blue (Mentawai network) and pink (Central Network) lines.

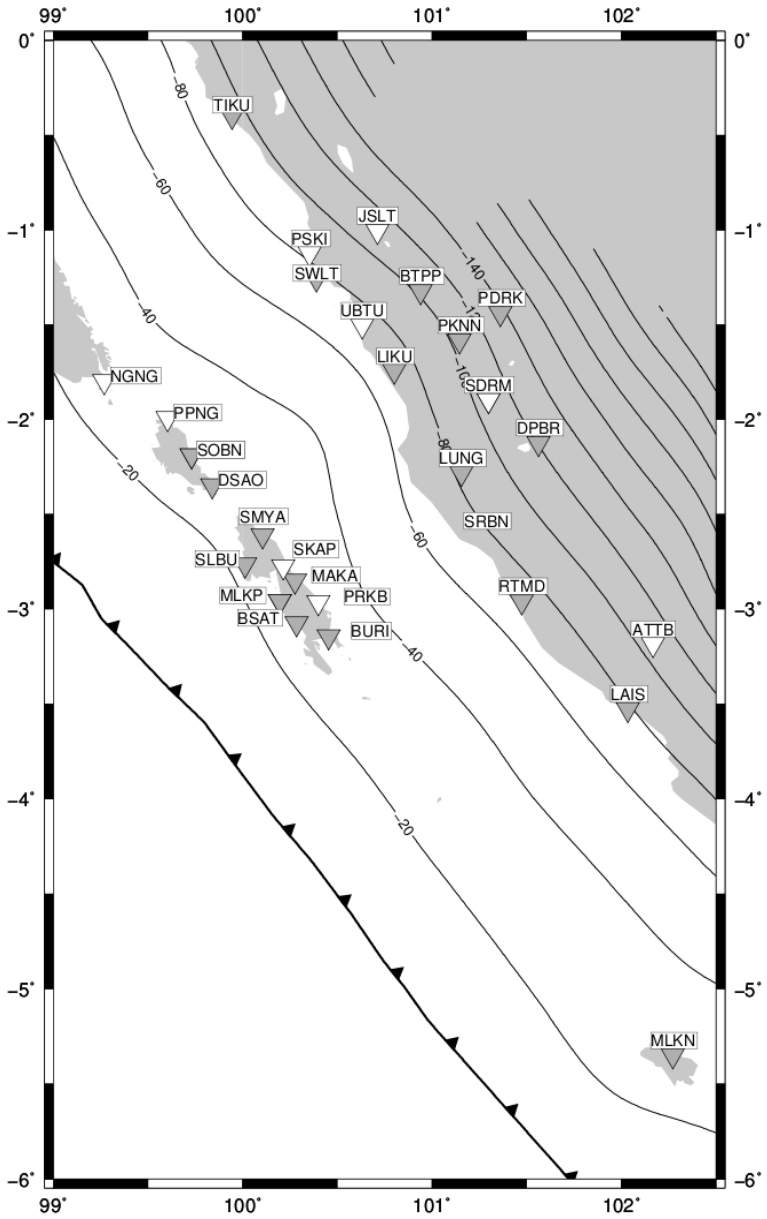

Figure 3.2: The Mentawai network. The 6TD stations are represented by grey inverted triangles and broadband stations are represented by white inverted triangles. The slab contours are shown (SLAB1.0, Hayes and Wald, 2009).

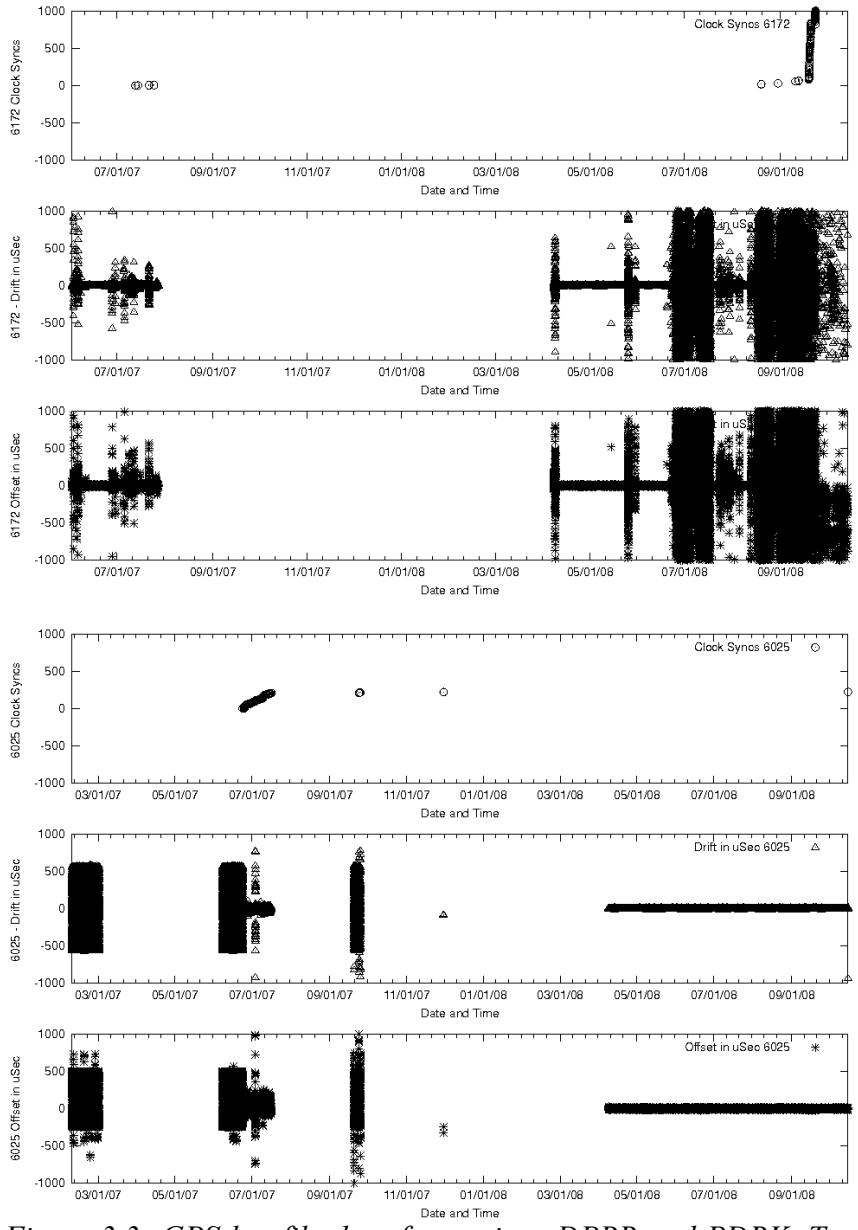

Figure 3.3: GPS log file data for stations DPBR and PDRK. Top: Station DPBR Bottom: Station PDRK. The diagrams for each station indicate when the clock sync occurred (top panel) , the drift (middle panel) and the offset (bottom panel). Both stations have large values for drift and offset.

2007, in western Sumatra between 1° S and 4° S on Enggano Island, the Mentawai Islands and the adjacent mainland (Figure 3.1 and 3he .2). Initially the network consisted of 27 three component stations (17 CMG-6TD and 10 broadband Trillium 120P running at 50 Hz and 100 Hz respectively) but an additional two 6TD stations (TIKU and

MLKN) were installed in January 2008 (Figure 3.1, Table 3.1). The stations were serviced twice, once in April 2008 and then in June/July 2008, before being deinstalled in October 2008. Unfortunately, during the experiment only 17 stations out of the 29 ran without any problems (Table 3.1), which resulted in a significant amount of data loss. Four of the 6TD stations (SOBN, SWLT, LAIS and MLKP) sustained problems with their masses, either becoming stuck or components breaking, while another two stations (PDRK and DPBR) developed GPS problems which resulted in data loss (Figure 3.3). In addition to this, station RTMD recorded largely noise, resulting in most of the data being unusable and station MLKN, on the remote Enggano Island, only recorded 3 months worth of data. Out of the 10 broadband stations (frequency response of 0.0083 to 50 HZ) installed within the region, four (SRBN, PSKI, SDRM and SKAP) suffered power problems, with batteries becoming flooded during the rainy season and even stolen, as well as hard disk issues which resulted in no data being recorded. Data availability for the 6TD and broadband stations was 85% and 58%, respectively (Table 3.1).

3.1.2 Central Network

In addition to the temporary seismic network installed in the Mentawai region between December 2007 and October 2008, a second temporary seismic network (Table 3.2) was installed on the Sumatra mainland between Padang Sidempuan and Padang and on Nias Island, Siberut Island and the Batu Islands to obtain a high quality data set for accurate hypocentre detection and to resolve the structure of the Sumatra subduction zone (Figure 1.1, 3.1, 3.4 and Table 3.2). The dense network was installed in April 2008 (Lange et al., 2010) and comprised 52 continuously-recording three component stations running at 50 Hz and 100 Hz, including 7 broadband stations (Figure 3.1). Thirteen stations (12 6TD and 1 broadband station) were installed on the islands, while the remaining 39 were placed on mainland Sumatra. The network was serviced in June/July 2008 and October 2008, with the network configuration altered during October 2008. The noisy stations (12) were deinstalled and the remaining 6TD stations with 3 GB internal memory were replaced by instruments with 8 GB internal memory from the Mentawai network (13 stations) (Table 3.2). A further three stations (TIKU, NGNS and SWLR) were also

deployed on former sites of the deinstalled Mentawai network, which resulted in 43 stations remaining until the network was deinstalled in February 2009 (Figure 3.2 and 3.4).

Following the June/July service run 90 GB of continuous seismic data were collected. Most of the 6TD stations were running fine, but the broadband station had problems with water penetration into the data logger box and power supply. Data availability for the period between October 2008 and February 2009 for the 6TD and broadband stations was 84% and 70%, respectively. The lower recovery rate from the broadband stations was again due to the broadband station data loggers being more susceptible to water penetration than the 6TD stations. During the deployment, GPS problems occurred at several 6TD stations (B20S, Y10S, Y30S, Y60S, S10R, Z20S and Z35R), as well as at the broadband station A60B. There was also one case of equipment theft at station Y50B.

In order to improve the resolution of the off shore part of the network, 10 three component ocean bottom seismometers with a differential pressure gauge channel, sampling at 100 Hz, were installed in June 2008 for 9 months between the trench and the continental shelf, offshore central Sumatra (Figure 3.5, Lange et al., 2010). In addition to this, for a time span of 14 days between the 25 May and the 10 June 2008, the data from an active experiment comprising 46 OBS (20 stations with hydrophone and Z component and 26 stations with 3 seismometer channels and hydrophone) were included in the study (Figure 3.5).

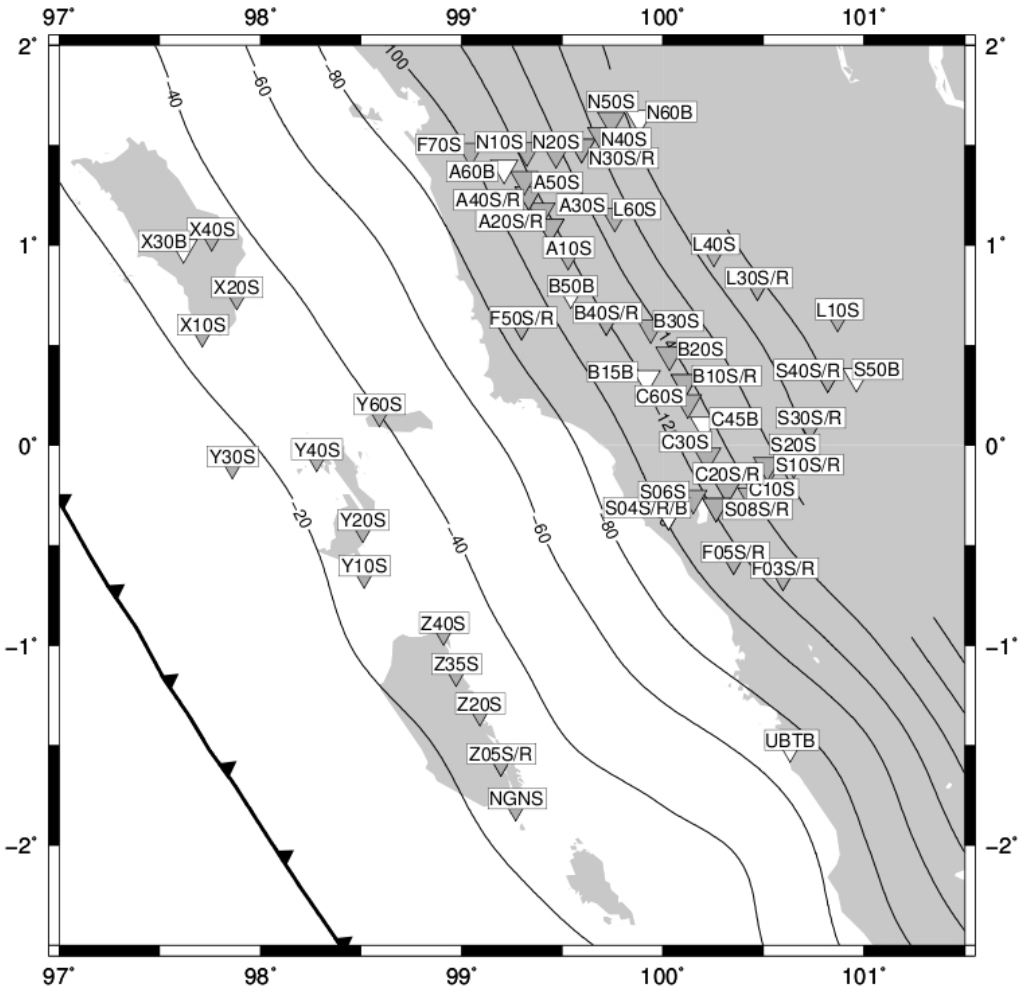

Figure 3.4: The central network. 6TD instruments are represented by grey inverted triangles and broadband instruments are represented by white inverted triangles. Slab contours are shown (SLAB1.0, Hayes and Wald, 2009).

Station Name	Instrument Type	Latitude	Longitude	Elevation (m)	Installation Date	De-installation Date	Sampling Rate (Hz)	Remarks
SOBN	6T	-2.1915	99.7290	29	13/12/07	21/04/08	50	Battery empty and stuck masses. No data.
SOBS	6T	-2.1915	99.7290	29	21/04/08	12/10/08	50	Reoccupied SOBN
SWLT	6T	-1.2589	100.4730	28	01/12/07	21/10/08	50	North component broken. 3 days of missing data.
TIKU	6T	-0.3991	99.9444	34	28/01/08	25/10/08	50/100	Ok
PDRK	6T	-1.4400	101.3596	320	09/12/07	19/10/08	50	Noisy site. Problems with internal GPS resulted in data gaps. Only partly usable.
PKNN	6T	-1.5843	101.1453	925	08/12/07	19/10/08	50	Ok
RTMD	6T	-2.9616	101.4728	39	16/12/07	19/10/08	50	Data unusable, just noise.
BSAT	6T	-3.0766	100.2846	17	09/12/07	16/10/08	50	Ok
BTPP	6T	-1.3251	100.9401	862	02/12/07	19/10/08	50	Ok
BURI	6T	-3.1451	100.4541	35	08/12/07	19/10/08	50	Ok
DPBR	6T	-2.1260	101.5622	815	06/12/07	19/10/08	50	In Dec 07 minor GPS problems.
DSAO	6T	-2.3499	99.8394	43	16/12/07	15/10/08	50	Ok
LAIS	6T	-3.5291	102.0347	29	18/12/07	19/10/08	50	Gap in log files between 24/02/08 and 03/03/08 Z component only and 14 days of data missing between April to Oct 08.
LIKU	6T	-1.7457	100.8003	27	21/12/07	19/10/08	50	Ok
LUNG	6T	-2.2853	101.1556	53	30/11/07	19/10/08	50	Some noise. 4 days of missing data between April and Oct 08.
MAKA	6T	-2.8520	100.2754	19	06/12/07	19/10/08	50	Ok
MLKP	6T	-2.9593	100.1946	22	09/12/07	25/05/08	50	N component stuck but Z and E ok. Sensor changed.
MLKR	6T	2.9593	100.1946	22	25/05/08	14/10/08	50	Reoccupied MLKP
MLKN	6T	-5.3526	102.2715	27	16/01/08	19/10/08	50	Only 3 months of data.
SMYA	6T	-2.6125	100.1051	8	16/12/07	26/10/08	50	Ok
SLBU	6T	-2.7672	100.0110	18	03/12/07	26/10/08	50	Ok

UBTU	TRIL120P	-1.5059	100.6313	40	01/12/07	26/10/08	100	Ok
SRBN	TRIL120P	-2.6157	101.2879	58	14/12/07	26/10/08	100	Hard disk problem. No data collected
ATTB	TRIL120P	-3.1874	102.1672	676	17/12/07	26/10/08	100	Ok
PPNG	TRIL120P	-1.9940	99.6037	52	08/12/07	26/10/08	100	Ok
PRKB	TRIL120P	-2.9666	100.3996	27	06/12/07	26/10/08	100	Ok
PSKI	TRIL120P	-1.1247	100.3535	44	16/12/07	26/10/08	100	In April service disk problem, no data available.
NGNG	TRIL120P	-1.7996	99.2683	65	11/12/07	26/10/08	100	Ok
JSLT	TRIL120P	-1.0064	100.7117	1622	27/11/07	26/10/08	100	Ok
SDRM	TRIL120P	-1.8981	101.2990	989	06/12/07	26/10/08	100	Hard disk problem and Battery stolen in April 08. No data collected.
SKAP	TRIL120P	-2.7762	100.2128	54	01/12/07	26/10/08	100	In April 08 there was a hard disk problem and an empty battery.

Table 3.1: Table showing the location, type of instrument installed, period of installation, the sps setting and if any problems were encountered for the stations in the Mentawai network.

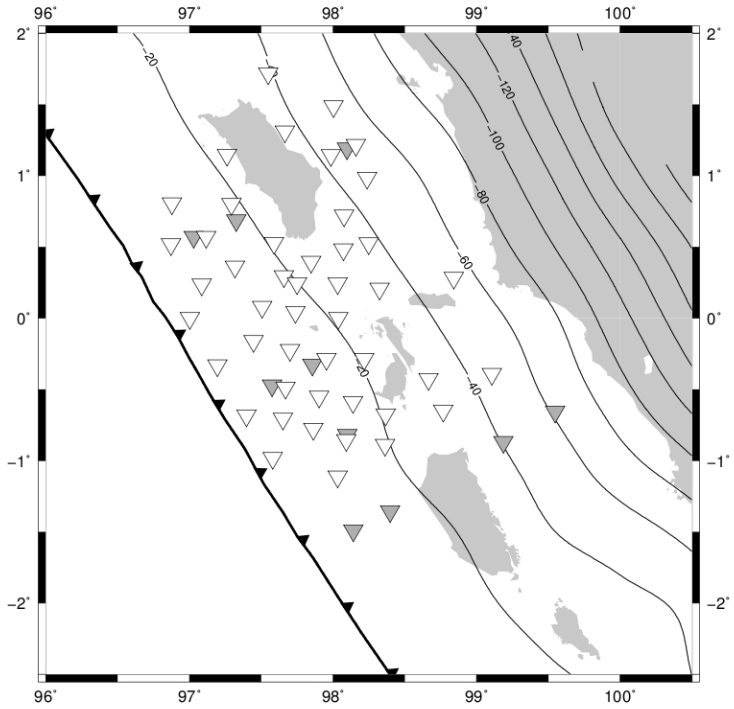

Figure 3.5: Ocean Bottom Seismometers (0BS). Grey inverted triangles indicate the OBS installed between June 2008 and February 2009. White inverted triangles represent the 46 OBS used for the 14 day active experiment.

Station Name	Instrument Type	Latitude	Longitude	Elevation (m)	Installation Date	De-installation Date	Sampling Rate (Hz)	Remarks
A10S	6T	0.9555	99.5295	303	22/04/08	19/10/08	100/50	Ok
A20S	6T	1.0892	99.4405	199	21/04/08	20/10/08	100/50	Noisy Site
A20R	6T	1.0892	99.4405	199	20/10/08	03/03/09	100	Reoccupied Oct, replaced 8Gb 6T Flush Problems in Field
A30S	6T	1.1707	99.3952	296	21/04/08	20/10/08	100/50	Fragmented
A40S	6T	1.2538	99.3323	260	20/04/08	20/10/08	100/50	Fragmented, 12 days of data missing
A40R	6T	1.2538	99.3323	260	20/10/08	11/03/09	100	Reoccupied Oct, replaced 8Gb 6T
A50S	6T	1.3308	99.3100	274	20/04/08	26/10/08	100	After 27/08/08 data becomes unusable.
B10S	6T	0.3142	100.1080	303	15/04/08	22/10/08	100/50	Ok
B10R	6T	0.3142	-100.1080	303	22/10/08	27/02/09	100	Missing 1 day
B20S	6T	0.4502	100.0330	274	16/04/08	26/10/08	100	GPS not working so recovered. Downloaded Leicester
B30S	6T	0.5888	99.9378	499	17/04/08	25/02/09	100	Ok
B40S	6T	0.6285	99.7188	625	18/04/08	21/10/08	100/50	Long Period noise until 27/06/08. 86 days of missing data
B40R	6T	0.6285	99.7188	625	21/10/08	11/03/09	100	Reoccupied Oct, replaced 8Gb 6T. Feb 09 station found dead. Only 17 days of data.
C10S	6T	-0.2535	100.4400	867	28/04/08	21/10/08	100/50	Ok
C20S	6T	-0.2157	100.3200	830	11/04/08	23/10/08	100/50	19 days of missing data on Oct 08 service.
C20R	6T	-0.2157	100.3200	830	23/10/08	11/03/09	100	Ok
C30S	6T	-0.0545	100.2190	600	09/04/08	26/10/08	100/50	Long period noise until 27/06/08
C60S	6T	0.2133	100.1230	383	14/04/08	11/03/09	100/50	ok but noisy site.
F03S	6T	-0.6475	100.5960	551	15/04/08	20/10/08	100/50	Long period noise
F03R	6T	-0.6475	100.5960	551	20/10/08	11/03/09	100	Ok
F05S	6T	-0.5663	100.3500	127	27/06/08	13/10/08	50	Sent to Gurlap in Dec 2008

F05R	6T	-0.5663	100.3500	127	20/10/08	01/03/09	100	overlaps/fragments 14 days missing
F50S	6T	0.6058	99.2973	54	27/04/08	25/10/08	100/50	Ok
F50R	6T	0.6058	99.2973	22	25/10/08	26/02/09	100	Ok
F70S	6T	1.4713	99.0400	82	18/04/08	09/03/09	100	Ok but noisy
L10S	6T	0.6458	100.8670	60	19/04/08	11/03/09	50	Long period noise. 77 days of data missing.
L30S	6T	0.8025	100.4700	72	25/04/08	25/10/08	50	106 days of data missing.
L30R	6T	0.8025	100.4700	72	25/10/08	11/03/09	100	Ok
L40S	6T	0.9710	100.2520	73	25/04/08	21/02/09	50/100	Ok
L60S	6T	1.1455	99.7617	118	24/04/08	28/02/09	50/100	Ok
N10S	6T	1.4735	99.3247	563	19/04/08	11/09/08	100/50	Double tracks
N20S	6T	1.4653	99.4685	188	20/04/08	04/03/09	100	Ok
N30S	6T	1.4900	99.6000	127	21/04/08	29/06/08	100	No logs for all data.
N30R	6T	1.4900	99.6000	127	24/07/08	05/11/08	100/50	No header.
N40S	6T	1.5510	99.6945	134	23/04/08	28/02/09	100	Fragmented after the October service.
N50S	6T	1.6263	99.7430	80	23/04/08	24/02/09	100	5 days of data missing up to October service. Fragmented after the October service.
S04S	6T	-0.3442	100.0270	118	10/07/08	21/10/08	50	Ok
S04R	6T	-0.3442	100.0270	118	20/10/08	19/02/09	100	Fragmented
S06S	6T	-0.2653	100.1500	575	15/04/08	11/03/09	100/200	No Logs.
S08S	6T	-0.3052	100.2640	1178	22/04/08	26/10/08	100/50/100	Ok
S08R	6T	-0.3052	100.2640	1178	25/10/08	16/02/09	100	Missing 1 day.
S10S	6T	-0.1290	100.5190	574	11/04/08	28/06/08	100	No data.
S10R	6T	-0.1290	100.5190	574	21/10/08	01/03/09	100	Fragmented.
S20S	6T	-0.0880	100.6500	579	12/04/08	07/10/08	100/50	Ok
S30S	6T	0.1030	100.7300	129	12/04/08	22/10/08	100/50	Missing 39 days of data.
S30R	6T	0.1000	100.7300	129	18/10/08	22/02/09	100	Missing 4 days.
S40S	6T	0.3435	100.8180	88	13/04/08	22/10/08	100/50	Ok
S40R	6T	0.3435	100.8180	88	22/10/08	27/02/08	100	Missing 1 day. Sometimes Fragmented.
X10S	6T	0.5692	97.7107	98	15/04/08	06/03/09	50/100	Fragmented after October Service.
X20S	6T	0.7565	97.8822	30	14/04/08	05/03/09	50/100	ok

X40S	6T	1.0497	97.7570	30	14/04/08	05/03/09	50/100	22 Days of missing data in October Service.
Y10S	6T	-0.6363	98.5155	50	15/04/08	25/02/09	50/100	Fragmented Data. Noisy Sometimes. GPS out of sync sometimes.
Y20S	6T	-0.4068	98.5078	21	10/04/08	24/02/09	50/100	ok
Y30S	6T	-0.0895	97.8608	12	01/05/08	24/02/09	50	GPS problems
Y40S	6T	-0.0545	98.2800	36	11/04/08	22/02/09	50/100	Ok but slightly noisy
Y60S	6T	-0.1713	98.5903	16	13/04/08	26/10/08	50	No GPS after 26 September 2008
Z05S	6T	-1.5758	99.1937	36	27/04/08	26/05/08	50	Battery Problems.
Z05R	6T	-1.5758	99.1937	36	26/10/08	11/03/09	100	No Data
Z20S	6T	-1.3263	99.0895	44	18/04/08	11/03/09	50/100	GPS problems after October Service
Z35S	6T	-1.1270	98.9727	22	28/04/08	27/02/09	50/100	GPS problems after October Service
Z40S	6T	-0.9223	98.9102	8	17/04/08	27/02/09	50/100	Noisy in daytime
B50B	3T	0.7620	99.5420	488	24/04/08	11/03/09	100	Some small data gaps.
B15B	3T	0.3333	99.9167	809	18/06/08	11/03/09	100	Gap in data between 20/07/08 to 06/09/08
A60B	3T	1.3872	99.2108	431	06/07/08	15/12/08	100	No GPS from October 08 to February 09.
X30B	3T	0.9898	97.6177	526	17/04/08	11/03/09	100	In October station was flooded so no data. In January 2009 it suffered a number of reboots.
UBTB	3T	-1.5058	100.6310	40	29/10/08	11/03/09	100	Data only available 29/10/08 to 18/12/08
S50B	3T	0.3467	100.9620	43	18/04/08	11/03/09	100	Data only available for 5/4/08 to 7/4/08 and 3/10/08 to 21/11/08
C45B	3T	0.1002	100.2050	600	16/04/08	22/02/09	100	Ok
N60B	3T	1.6353	99.8830	60	23/04/08	11/03/09	100	Ok
S04B	3T	-0.3448	100.0270	117	14/04/08	10/07/08	100	

TIKU	6T	-0.3991	99.9444	34	12/04/08	25/10/08	100	
NGNG	6T	-1.7996	99.2683	65	27/10/08	28/02/09	100	New Installation reoccupied, Mentawai Site.
SWLR	6T	-1.2589	100.4730	28	30/10/08	19/02/09	100	New installation, reoccupied Mentawai Site.

Table 3.2: Table showing the location, type of instrument installed, period of installation, the sps setting and if any problems were encountered for the stations in the central Sumatra network.

3.2 Pre-Processing

All available waveforms were preprocessed by Cambridge University. First, the data set was converted to miniseed (MSEED) format before pre-processing techniques such as visual quality control of waveforms and checking of the logfiles took place. Log files in which a GPS offset was larger than 0.5 s were marked untrustworthy. However, stations where GPS problems did occur and the MSEED was fragmented (e.g stations, Y10S, S10R, Z20S, Z35R) often only showed small offsets in their log files, though the absolute timing may not be reliable for these stations.

3.3 Event Detection and Phase Picking

Events were first detected by applying an automatic STA/LTA trigger on the continuous waveforms and possible events were declared based on a coincident triggering approach (Nippress et al., 2010). Subsequently, the waveforms were processed using GIANT (Graphical Interactive Aftershock Network Toolbox, Rietbrock and Scherbaum, 1998) which combines several tools for seismological data processing under an easy to use X-windows based environment. Before the arrival times were manually determined using the interactive processing package PITSA, which is a part of GIANT, a bandpass filter (e.g. 0.1-20 Hz) was applied to the waveforms to improve the signal to noise ratio. Both *P* and *S* arrivals were picked with weights assigned (Table 3.3, Appendix A1). *P* phases for data recorded at the land stations were picked on the vertical component, while the *S* phases were picked on the horizontal components. For the OBS stations the most

pronounced *P* phase onset was found on the hydrophone channel. Therefore the time of the *P* wave onset was generally determined using the hydrophone channel, with the *S* phase, when possible, determined on the horizontal components. Both networks recorded a high amount of seismicity due to a M_w 7.2 earthquake occurring on the 25 February 2008 within the Mentawai region (Figure 3.6) and a M_w 6.0 earthquake occurring on the Sumatran Fault, within the central network, on the 19 May 2008 (Figure 3.7). A total of 877 events with magnitudes M_w 2-7 were manually picked from the Mentawai data and located in a preliminary model, resulting in 12,600 *P* and 6,282 *S* onset times (Figure 3.1); while for the central network 27,077 *P* arrivals and 14,676 *S* arrivals from 1,783 local events were manually picked (Figure 3.1).

Weight	P uncertainty (s)	S uncertainty (s)
0	0.05	0.05
1	0.1	0.15
2	0.2	0.25
3	0.3	0.35
4	0.5	0.5

Table 3.3: Weights used for the P and S phases during manual picking. See Appendix A1 for examples.

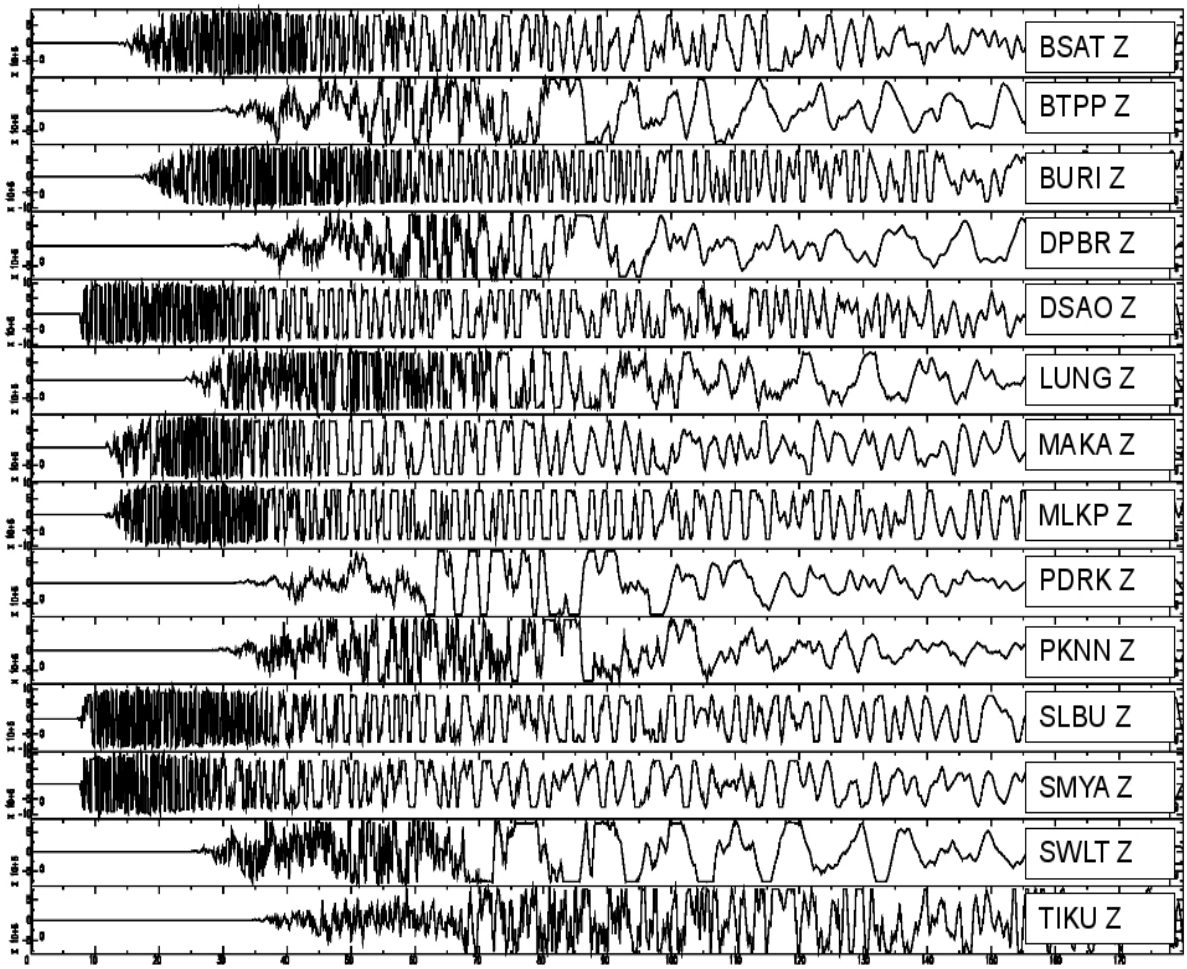

Figure 3.6: The Z component of the Mentawai network 6TD stations recording the M_w 7.2 event on the 25 February 2008 at 08:36:32.

Figure 3.7 (Next page) : The Z component of the central network 6TD stations recording the M_w 6.0 event on the 19 May 2008 at 14:26:44.

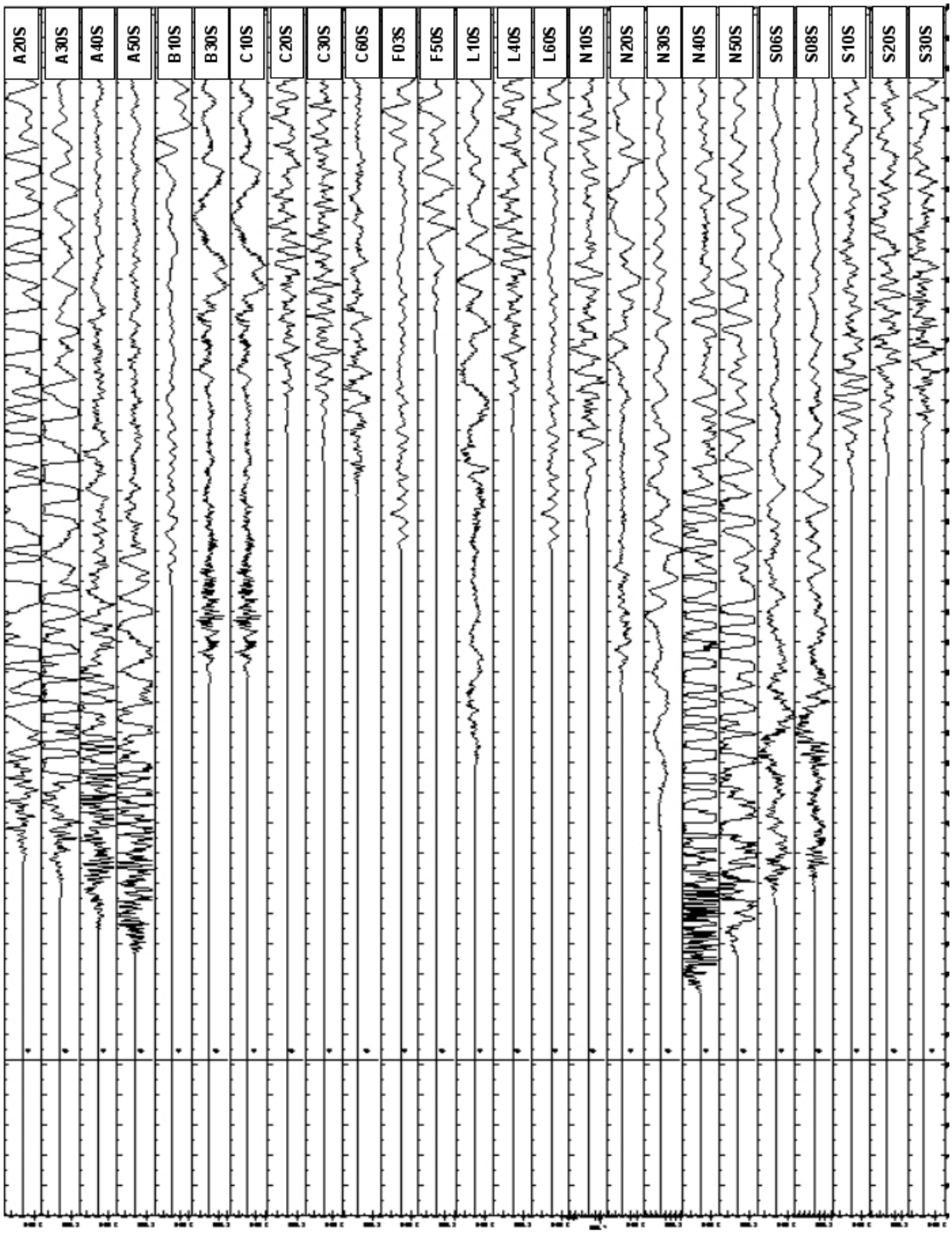
A 20S
A 30S
A 40S
A 50S
B 10S
B 30S
C 10S
C 20S
C 30S
C 60S
F 03S
F 50S
L 10S
L 40S
L 60S
N 10S
N 20S
N 30S
N 40S
N 50S
S06S
S08S
S10S
S20S
S30S

Chapter 4

Coupled Hypocentre-Velocity Problem

In this chapter the methods applied to the data to determine 1D, 2D and 3D velocity models are presented. This includes a summary of the main aspects of linear inverse theory, as well as a detailed description of the procedure to assess the resolution of the obtained tomographic models. Determining reliable velocity models and accurate hypocentre locations is vital to increase our understanding of the processes for aftershock generation.

4.1 Linear Inverse Theory

One of the most important tasks in seismology is locating seismic sources. This requires knowing the hypocentre co-ordinates (x^o, y^o, z^o), origin time (t^o) and velocity structure between the source and station. However, normally these are not known. In this section we will introduce the main aspects of inverse theory which is used to determine the hypocentre locations, origin times and velocity structure of the region the rays pass through, based on observed arrival times.

The body wave travel time (t) from an earthquake (i) to a seismic station (j) is expressed using seismic ray theory as the following path integral (Thurber, 1983)

$$t_{ij}^{s} \int_{source}^{station} u \, ds \qquad (4.1)$$

where u = slowness and ds is an element of the path.

The actual observed arrival times (T_{ij}) are

$$T_{ij} = t_j^o + t_{ij}^s(x_j^o, + y_j^o, + z_j^o, v(s), x, y, z) \qquad (4.2)$$

where t_j^o is the origin time, t_{ij}^s is the travel time of the ray from the source (x_j^o, y_j^o, z_j^o) to the station (x, y, z) and $v(s)$ is the velocity along the path. The only knowns in the local earthquake tomography (LET) problem are the receiver locations (x, y, z) and the observed arrival times $T_{ij,}$. The source coordinates (x_j^o, y_j^o, z_j^o), origin time (t_j^o), ray paths and the velocity parameters ($v(s)$) are the unknowns (the model parameters).

For a given set of arrival times (T_{ij}^{obs}) the predicted travel times (T_{ij}^{pre}) can be calculated using trial origin times and tracing rays from trial hypocentre locations to the receiver locations through an assumed velocity model. The misfit between the observed and predicted arrival times are the travel time residuals (ΔT_{ij}):

$$\Delta T_{ij} = T_{ij}^{obs} - T_{ij}^{pre} \qquad (4.3)$$

The travel time residuals are a function of the differences between the predicted and true origin times, hypocentre locations and velocity structure.

In order to calculate suitable model corrections for the hypocentre (including origin times) and velocity parameters that reduce the travel time residuals, we need to know the dependence of the observed travel times on all of the parameters. The arrival time of a wave generated by an earthquake is a non-linear function of the hypocentre and velocity parameters. However, a linear approximation between the travel time residual and adjustments to the hypocentre and velocity parameters can be obtained by applying a first order Taylor series expansion (Thurber, 1983).

$$\Delta T_{ij} = \Delta t_j^o + \sum_{k=1}^{3} \left[\frac{\partial t_{ij}^s}{\partial x_{kj}^o} \Delta x_{kj}^o\right] + \sum_{l=1}^{L} \left[\frac{\partial t_{ij}^s}{\partial v_l} \Delta v_l\right] \qquad (4.4)$$

Δt_j^o and Δx_{kj}^o are perturbations to the hypocentre parameters in time and space and

Δv_l represents the L parameters of the velocity model (number of parameters in the velocity model). The velocity model partial derivatives ($\frac{\partial t_{ij}^s}{\partial v_l}$) are essentially line integrals along the ray path reflecting the relative influence of each model parameter on a given arrival time datum (Thurber, 1993).

The linearized system of equations can be written in general notation as (Menke, 1989):

$$\mathbf{d} = \mathbf{Gm} \qquad (4.5)$$

where the partial derivatives of travel times with respect to the model parameters are contained in the Jacobi-matrix **G**, **m** is the vector of model adjustments (hypocentre and velocity) and **d** is the vector of travel time residuals ΔT_{ij}.

If the number of observations equals the number of unknowns (model parameters), **G** is square and **m** can be calculated directly by ($\mathbf{m}=\mathbf{G}^{-1}\mathbf{d}$), assuming independent observations. However, as the observed travel times will contain measurement errors, the number of observations used is usually far greater than the number of unknowns, so a reliable estimate of the model corrections can be obtained. The aim is to obtain the best model that fits an "average" of the data. The best model is defined as the model which results in the smallest difference between the observed and predicted data. The misfit (**E**) can be measured using equation 4.6.

$$\mathbf{E} = \mathbf{d}^{\mathbf{obs}} - \mathbf{d}^{\mathbf{pre}} = \mathbf{d}^{\mathbf{obs}} - \mathbf{Gm} \qquad (4.6)$$

where $\mathbf{d}^{\mathbf{obs}}$ are the observed travel time residuals and $\mathbf{d}^{\mathbf{pre}}$ are the predicted travel time residuals using the estimated model corrections.

The inverse problem is designed to find the model perturbations that minimize **E**. The most common way to do this is to write an equation for the squared error and force $\mathbf{E}^2$ to be a minimum by taking the derivative of $\mathbf{E}^2$ with respect to the model parameters and

setting it equal to zero. This leads to the least squares solution (Lay and Wallace, 1995).

$$\mathbf{m}^{est} = (\mathbf{G}^T\mathbf{G})^{-1}\mathbf{G}^T\mathbf{d} \qquad (4.7)$$

where $\mathbf{G}^T$ is the transposed Jacobi matrix and $\mathbf{m}^{est}$ are the estimated model corrections to minimize the error. Equation 4.7 provides the best solution to $\mathbf{m}^{est}$ in a least squares sense, as the squared error is minimized. $\mathbf{G}^T\mathbf{G}$ is a square matrix and symmetrical which means the eigenvalues are real and non-negative (e.g. Lay and Wallace, 1995). However, the irregular distributed data makes the problem under-determined in some regions and over-determined in others, creating a mixed determined problem (Husen et al., 1999). This means that at least some of the model corrections are unable to be resolved independently and a few may never be resolved. In order to avoid small or zero eigenvalues for the under-determined model parameters and to remove strong fluctuations in the model which can be caused by small random errors, damping is introduced to stabilize the numerical solution. By minimizing the solution length and prediction error (Menke, 1989) the solution (damped least squares solution) becomes:

$$\mathbf{m}^{est} = (\mathbf{G}^T\mathbf{G} + \epsilon^2\mathbf{I})^{-1}\mathbf{G}^T\mathbf{d} \qquad (4.8)$$

where $\mathbf{I}$ is the unity matrix and ϵ^2 is the damping parameter that determines the relative importance given to prediction errors and solution length. Damped least squares means that the norm of the model perturbations (more or less the complexity of the model) is weighted and combined with the squared misfit, with the combination minimized at each iteration (Evans et al., 1994).

The linearization of a non-linear problem, as well as the damping, means that the model corrections have to be obtained iteratively. After each iteration the model is updated, the new $\mathbf{d}$ and $\mathbf{G}$ are computed and the equation is solved again. The inversion continues until a stop criterion is reached, e.g. the maximum number of iterations is reached, data improvements are insignificant or the model corrections are below a certain threshold. A stop criterion has to be used as the non-linearity of the original problem and the

subsequent linearization, as well as the errors in the data and the impossibility of truly representing the Earths' structure, prevent $\mathbf{m}^{est}$ ever being the same as $\mathbf{m}^{true}$ (the model corrections that result in zero error) .

The quality of the iterative solution of the linearized problem depends on the quality of the initial estimate of the model parameters, as **E** does not usually have one well-defined minimum. In order to obtain the solution that corresponds to the absolute minimum **E,** the starting guess of the model parameters needs to be close to their true values. How close to the true values the initial estimates need to be depends on the data being used. For data with good azimuth and distance coverage, as well as a large number of observations, the initial locations can be far off the true one and still be well estimated.

The damped least squares solution is employed in the programs SIMUL2000 (Thurber, 1983 and Evans et al., 1994) and VELEST (Kissling et al., 1994), which are used in this study to determine 1D, 2D and 3D velocity models.

4.2 The Minimum 1D Model

In a minimum 1D model inversion the unknowns in the non-linear problem are the origin times, hypocentre locations, station corrections and layer velocities. This creates a coupled hypocentre-velocity problem which will eventually lead to travel time tomography. The complexity and non-linearity of the problem prevents a coupled inversion for hypocentre locations and a 3D velocity model from the beginning; a stepwise approach must be used instead. First a one-dimensional (1D) model is created, then a two-dimensional (2D) and finally a three-dimensional (3D) model. This staggered approach (e.g. Kissling et al., 1994; Haberland et al., 2009) is used to ensure that the velocity values of poorly-sampled nodes do not deviate significantly from the starting model, thus minimizing artifacts in the final 3D model.

4.2.1 Requirements of a Minimum 1D Model

Kissling (1988) defines a minimum 1D model as a 1D velocity model with station corrections that results in the smallest possible uniform location errors, for a large set of events. The 1D minimum model is a product of an iterative simultaneous inversion for hypocentre parameters, station corrections and layer velocities where, when available, a priori information is used to define the layers and initial velocities of the model. If the data set adequately samples the region of interest, the 1D model should drastically improve routine earthquake locations (Kissling et al., 1995).

An important aspect of the 1D model is the station correction terms, since they account for the 3D velocity structure as well as the near surface-geology. One station within the network is set as the reference station, which has a fixed correction. The reference station must be within the centre of the network with a large number of observations, resulting in a good azimuthal coverage. The absolute values of the station correction terms are not resolved as they are coupled to the near-surface geology at the reference station, as well as the upper layers of the 1D minimum velocity model. This is because the ray lengths in the upper layers of the velocity model are similar for all rays to that station, so a change in velocity of the top layers results in a constant shift in the travel time of all the rays, which can be compensated for by correcting the station correction terms. As a result, when analyzing the station correction terms, the absolute value and relative difference between them should be studied and compared to the near-surface geology.

In order for a 1D velocity model to be used to obtain well-resolved hypocentre locations, the following conditions must be met (Kissling et al., 1994).

- The layer velocities are the best average velocities for the cumulated weighted ray lengths within each layer. The true 3D velocity deviations from this model should be evenly distributed with zero mean.
- The depth of the layer boundaries and velocities account for the different phases observed in the data.

- It is possible to locate earthquakes within the area covered by the station array with equal precision.
- The 1D model and station corrections reflect the basic features of surface geology.
- The 1D model should consist of a number of layers to simulate velocity gradients. If too few layers are used there is poor depth control of the events, resulting in large mislocations.

In Chapter 5 results of a 1D coupled inversion for the Mentawai region, using VELEST, are presented.

4.3 3D Tomography

As a first order approximation the Earth's structure is radially symmetrical. Lateral heterogeneities within the Earth's radially symmetrical structure are of second order but are generally a result of tectonic processes. Therefore, imaging of these 3D structures is required to understand the processes taking place within the Earth.

When using a minimum 1D model, the station correction terms incorporate a large part of the 3D structure of the Earth, allowing the hypocentre accuracy to be sufficient for most purposes. However, as discussed in Section 4.2, the coupled hypocentre-velocity problem is the same for a 1D or 3D velocity model, the only difference being that the number of unknowns increases. Therefore, provided enough data are available, a 3D velocity model can be determined from the travel times.

The 3D inversion of travel time residuals in seismology was first introduced by Aki and co-authors in the 1970s, who presented the widely used ACH method (Aki et al., 1977). Since then, numerous papers have been published on the application and theory of the 3D inversion of travel time data, which has become known as seismic tomography (e.g. Kissling, 1988). Different approaches are applied for teleseismic data and local earthquake data, despite the principles being the same. Since we are dealing here only

with local earthquakes, teleseismic tomography is not discussed further.

4.3.1 Requirements of a Tomography Model

In order to obtain a meaningful result from the LET a number of requirements must first be met before the inversions can be carried out.

1) To ensure that earthquakes are locatable, each event must have a large number of observations, small GAP (largest azimuthal distance between two observations) and an initial hypocentre which is close to its true location. This will enable the event to converge to its true location. Initially computing a 1D model minimum model, as described in Section 4.2, will ensure that the data selected are of acceptable quality and the initial hypocentres are close to their true locations.

2) The parameters of the velocity model must be determined before the inversion. The model parameterization must allow accurate ray tracing, be fine enough to image the structural heterogeneities within the study area, but at the same time be coarse enough to allow well-constrained model corrections. In addition to this the initial velocity model, like the initial hypocentre hypocentres, must also be close to the true model.

3) The damping value used in the inversion must be carefully selected. This is done by analyzing damping curves of data variance against model variance for a series of one-step inversions with varying damping values. The damping value chosen is the value that minimizes the data variance at moderate model variance (Eberhart-Phillips, 1986). If the damping is too small, the velocity oscillates from one grid point to the next and large changes in velocity are observed without large reductions in data variance.

4.3.2 Parameters of SIMUL

In 1983 Thurber (Thurber, 1983) introduced the program SIMUL for carrying out seismic tomography based on local earthquake data. Their simultaneous inversion

method of local earthquake arrival time data is similar to that of Aki and Lee (1976), but parameter separation and a 3D approximate ray tracer are included. Throughout the last three decades the SIMUL code has been developed further by Eberhart-Phillips (1986, 1993), Um and Thurber (1987) and Thurber and Atre (1993) and is now one of the most widely used methods for LET. In this study we use a recent version of the SIMUL code (SIMUL2000) that allows *P* and *S* wave travel time data to be used.

SIMUL2000 uses a 3D grid of nodes to represent the Earths' structure, in which the velocity varies continuously in all directions, with linear B-spline interpolation between 8 neighboring grid points (Thurber, 1983). Consequently, only gradual changes in velocity are seen and not sharp discontinuities. Flexible gridding was introduced into SIMUL2000 (Thurber and Eberhart-Phillips, 1999) to allow, instead of just fixed and inverted nodes, values of designated subsets of nodes to be linked, creating master nodes and one or more slave nodes. The linking of nodes in poorer-sampled areas allows a more even distribution of the data which in turn allows a lower damping value to be used as these nodes are no longer under-determined. The node spacing within the velocity model is selected to enable enough ray paths to pass through the central grid points, allowing adequate resolution to be obtained within the centre of the region.

Ray tracing is performed in SIMUL2000 using a two step approach. First, approximate ray tracing (ART) is used in which a number of circular arcs connecting the source and the receiver are constructed and the travel time along the each of the arcs is computed. Arcs of varying radii are examined and the dip of the plane containing the arcs is varied systematically in order to sample the volume of interest. The first arrival path is selected as the path that has the shortest travel time (Thurber, 1983). This path is then perturbed using pseudo-bending (Um and Thurber, 1987), in which ray points are iteratively moved to minimize the travel time on each ray segment.

It is well known that *S* wave onset times are significantly reduced in quality and quantity compared to *P* wave onset times. SIMUL2000 therefore inverts directly for the *Vp/Vs* ratio using the *P* and *S*-*P* travel times (Thurber and Atre, 1993). *P* and *S* wave travel

times are calculated in corresponding velocity models to yield the expected *S-P* travel times dt_{ij}^{Pre}. The *S-P* travel time residuals are related to perturbations to *Vp/Vs* at nodes of the 3D grid (δ(*Vp/Vs*)) using

$$dt_{ij}^{Obs} - dt_{ij}^{Pre} = \int_{path} [\delta (Vp/Vs) - 1] / Vp \, ds \qquad (4.9)$$

where the integration is carried out along the *S* wave path. After the first iteration this equation is an approximation, as the *Vp/Vs* will no longer be constant since the *P* and *S* ray paths will differ. However, extensive testing has shown that the approximation is adequate for rapid and stable convergence. The full system is then inverted for *Vp/Vs* and *Vp*, along with hypocentres. Calculating *Vp/Vs* is preferable to just inverting for *Vp* and *Vs* and taking the ratio of the 3D *Vp* and *Vs* models, as this can lead to severe artifacts where *Vp* is well resolved but *Vs* is not.

The obtained tomography will be a filtered image of the distribution of seismic velocities within the region of the Earth. The filter is a product of the selected travel time data used in the inversion and the method used to construct the 3D model, e.g. ray tracing, model parametrization. The velocity obtained at one location within the model is the average velocity of all the ray path segments, which travel through this location, taking into account each ray's direction and individual weight. To remove any artifacts within the model due to node configuration, additional inversions with horizontally-shifted grids can be carried out and then spatially averaged to obtain a smooth velocity model. This method is used regularly in teleseismic tomography and can be applied to 2D and 3D tomography to provide a smooth and robust final model, as well as accurately imaging dipping structures (Haberland et al., 2009).

Finally, previous work by various authors evaluating different aspects of LET (e.g. model parameterization (Toomey and Foulger, 1989); the influence of the initial velocity (Kissling et al., 1994); the coupled problem (Thurber, 1992) and the ray-tracing method (Le Meur et al., 1997), has found that reliable results can be produced using SIMUL2000 that agree with information collected from alternative methods. However, this is

providing the model is carefully set up, there is a good understanding of the data set and the inherent effects of a linearized solution to a highly non-linear problem are taken into account. Therefore as long as these criteria are met, LET allows us to directly obtain information on the 3D velocity structure of the Earth from the travel time arrivals of local earthquakes.

In Chapter 5, LET of the Mentawai region using SIMUL2000 is presented.

4.4 Resolution

The geometry of the study region, as well as the locations of earthquakes and receivers, results in a subsurface structure being resolved with spatially varying quality. For any geological interpretation of the obtained tomographic image it is necessary to quantify which regions of the model are resolved and which are not. The well-resolved regions of a tomographic inversion can be determined by classical resolution measures, e.g. hit count, derivative weighted sum (DWS) and resolution diagonal elements (RDE) (Toomey and Foulger, 1989), as well as synthetic tests such as checkerboard tests (Spakman and Nolet, 1988) and restoring resolution tests (Zhao et al., 1992).

4.4.1 Classical Resolution Tests

The numbers of rays that travel though the region of influence around each of the velocity nodes is defined by the hit count. However, the hit count does not take into account the ray path length, direction or observed weight. An improvement on the hit count is the derivative weighted sum (DWS), which provides an average relative measure of the density of the seismic rays near a given velocity node (Toomey and Foulger, 1989). This measure of ray distribution is sensitive to the spatial separation of the rays from a node location and the ray segment length. The *DWS* of the n^{th} velocity parameter (α_n) is defined as

$$DWS(\alpha_n) = N \sum_i \sum_j \left[\int_{P_{ij}} \omega_n(x)\, ds \right] \quad (4.10)$$

where *i* and *j* are the event and station indices, ω is the weights used in the linear

interpolation and depends on the coordinate position, P_{ij} is the raypath between i and j, and N is the normalization factor that takes into the account the volume influenced by α_n . Poorly-sampled nodes are marked by relatively small values for the DWS. Nevertheless, neither the hit count nor the DWS account for the directionality in the used ray distribution. This results in the hit count/DWS for a node sampled by sub-parallel rays being the same as for a node which is sampled by ray directions which are evenly distributed (Toomey and Foulger, 1989).

How well-constrained the velocity is at each grid point and how much 'smearing' occurs from adjacent nodes is indicated by the resolution matrix (**R**). The model resolution can be defined as

$$\mathbf{m}^{\mathbf{est}} = (\mathbf{G}^{\mathbf{T}}\mathbf{G} + \epsilon^2\mathbf{I})^{-1}\mathbf{G}^{\mathbf{T}}\mathbf{d} = (\mathbf{G}^{\mathbf{T}}\mathbf{G} + \epsilon^2\mathbf{I})^{-1}\mathbf{G}^{\mathbf{T}}\mathbf{G}\mathbf{m}^{\mathbf{true}} = \mathbf{R}\mathbf{m}^{\mathbf{true}} \quad (4.11)$$

where $\mathbf{m}^{\mathbf{est}}$ are the estimated model corrections and $\mathbf{m}^{\mathbf{true}}$ are the model corrections which would solve equation 4.5 (Refer to page 45 for definition of other variables). Therefore **R** represents the filter through which the estimated model corrections are obtained from the true model corrections (Thurber, 1993).

Each row of the resolution matrix is an averaging vector for a single model parameter which results in the row describing the dependence of an individual model parameter on all the other model parameters (Menke, 1984). The averaging vector of a model parameter can be both pictorially and quantitatively examined. One method of pictorial examination is to plot the averaging vector for a single model parameter in the 3D space of the study volume. Interpreting the full resolution matrix would require one 3D image per model parameter and therefore is not practical. Instead, for a first-order diagnostic tool, the diagonal elements are used. Well-resolved nodes have large diagonal elements (close to 1) and small off-diagonal elements. However, the diagonal element only provides a relative estimate of resolution as its magnitude depends on the damping value used, as well as the number/density of the model parameters.

Smearing can be visualized by contouring each row of the resolution matrix, which as described above is the averaging vector for a single model parameters (Reyners et al., 1998). The surface around the model parameter where the value of the averaging vector decays below a certain value, say 70%, is shown for each node. The shape and spatial extent of the contours is interpreted as a measure of the spatial smearing, with close contour lines indicating a well-resolved node. Nevertheless, the resolution contours only provide a 2D view of smearing as no information about smearing in the perpendicular direction can be deduced.

A quantitative view of resolution can also be provided using the spread function, which summarises the information contained in a single averaging vector or row of the full resolution matrix (Toomey and Foulger, 1989). The spread function (S) for a single averaging vector is defined as

$$S(\mathbf{r}_p) = \|\mathbf{r}_p\|^{-1} \sum_{q=1}^{m} \Omega(p,q)\mathbf{R}_{p,q}^2 \quad (4.12)$$

where $\mathbf{r}_p$ is the averaging vector of the p^{th} parameter, $\mathbf{R}_{pq}$ is an element of the resolution matrix, $\Omega(p,q)$ is a weighting function defined as the distance between the p^{th} and q^{th} nodes and m is the number of parameters. For a peaked resolution (low smearing and considerably larger diagonal element than off-diagonal element) the spread value is low, but there is no universal value to define what is acceptable, as the spread value depends on the damping and grid node spacing.

In order to obtain a reliable assessment of the quality of the inversion result, all of the above methods need to be implemented to obtain a complete picture of the properties of the resolution matrix. Using only one method to evaluate the resolution matrix would result in some information being disregarded.

In Chapter 5 the resolution matrices of the 2D and 3D tomographic models are evaluated.

4.4.2 Synthetic Models

The above methods only evaluate the quality of the obtained models following the inversion. Synthetic tests can be implemented to determine useful information about model parameterization and the resolution capability of the actual data. Checkerboard tests are commonly used to assess the image blurring (Spakman and Nolet, 1988) but do not assess the capacity of the data to resolve the geometry and amplitude of the velocity structure. This can be done with restoring resolution tests (Zhao et al., 1992; Haslinger et al., 1999). In restoring resolution tests a synthetic model is constructed which has the same characteristics (amplitude and dimensions) of the inversion result based on the real data but with a different geometry and a different sign of the velocity variations. Low resolution regions will be highlighted, as the input structure will not be resolved in these regions. A synthetic structure that is very close to the inversion result is not used as its solution will lie in the same local minimum, which can lead to a stable solution in areas of low resolution.

Checkerboard and resolution tests were performed using the same hypocentre and station locations as the real data and the model parameters used in the 2D and 3D inversions. The results of the synthetic tests are presented in Chapter 5.

Chapter 5

In this chapter a paper is presented which describes how the 2D and 3D velocity structure of the Mentawai segment of the Sumatra subduction was obtained, using the data recorded from the Mentawai network. It includes data selection, computation of 1D Minimum Model, 2D velocity model and 3D velocity model, analysis of the resolution matrix for the 2D and 3D models and results of synthetic tests. The tomographic models, along with accurate hypocentre locations and first motion polarity focal mechanisms which are also presented in the paper, result in an integrated picture of the Sumatra subduction zone along the Mentawai segment.

Structure and seismogenic properties of the Mentawai segment of the Sumatra subduction zone revealed by local earthquake travel-time tomography.

R. Collings[(1)] (rachel.collings@liverpool.ac.uk), D. Lange[(2,6)], A.Rietbrock[(1)], F. Tilmann[(3)], D. Natawidjaja[(4)],B. Suwargadi[(4)], M. Miller[(5)] and J. Saul[(3)]

[(1)] University of Liverpool, 4 Brownlow street, Liverpool, L69 3GP, UK

[(2)]Institute of Earth and Environmental Science, University of Potsdam, Potsdam-Golm, Germany

[(3)]GFZ German Research Centre for Geosciences, Potsdam, Germany

[(4)]LabEarth, Indonesian Institute of Sciences (LIPI), Bandung, Indonesia

[(5)]Universidad de Concepción, Concepción, Chile

[(6)] Bullard Laboratories, Dept of Earth Science, University of Cambridge, Uk

Journal of Geophysical Research, 117, B01312, (2012)

5.1 Abstract

On September 12 2007, an M_w 8.4 earthquake occurred within the southern section of the Mentawai segment of the Sumatra subduction zone, where the subduction thrust had

previously ruptured in 1833 and 1797. Travel time data obtained from a temporary local seismic network, deployed between December 2007 and October 2008 to record the aftershocks of the 2007 event, was used to determine two-dimensional (2D) and three-dimensional (3D) velocity models of the Mentawai segment. The seismicity distribution reveals significant activity along the subduction interface and within two clusters in the overriding plate either side of the forearc basin. The down-going slab is clearly distinguished by a dipping region of high *Vp* (8.0 km/s), which can be a traced to ~50 km depth, with an increased *Vp/Vs* ratio (1.75 to 1.90) beneath the islands and the western side of the forearc basin, suggesting hydrated oceanic crust. Above the slab, a shallow continental Moho of less than 30 km depth can be inferred, suggesting that the intersection of the continental mantle with the subducting slab is much shallower than the downdip limit of the seismogenic zone despite localized serpentinization being present at the toe of the mantle wedge. The outer arc islands are characterized by low *Vp* (4.5-5.8 km/s) and high *Vp/Vs* (greater than 2.0), suggesting that they consist of fluid-saturated sediments. The very low rigidity of the outer forearc contributed to the slow rupture of the M_w 7.7 Mentawai tsunami earthquake on 25 October 2010.

5.2 Introduction

Subduction zones host the world's largest earthquakes, greater than M_w 9 (Chile, Alaska, Sumatra, Japan), although the seismic behaviour of individual subduction zones is highly variable (Stern, 2002). Most large earthquakes manifest as thrust type events along the interface, at depths of less than 50 km (Ruff, 1996). The total amount of slip that occurs along the subduction interface fault plane is a combination of both seismic and aseismic slip. The ratio of seismic slip to total slip along the interface is defined as seismic coupling. During an earthquake, seismic slip is not uniformly distributed, creating patches of high and low slip along the interface. Regions of high slip are interpreted as the areas of greatest coupling and are known as asperities (Lay and Kanamori, 1981). The physical properties of the asperity control the degree of seismic coupling and also the nucleation of large earthquakes. Originally asperities along subduction megathrusts were attributed primarily to properties of the lower plate, e.g. temperature, age, dip,

length, sediment thickness and roughness (e.g. Cross and Pilger, 1982, and references therein). However, more recent studies have noted that the deformation occurring within the continental crust and underlying continental mantle is correlated with frictional properties of the interface between the upper and lower plates and thus could affect the seismic behaviour of subduction megathrusts (e.g. McCaffrey, 1993). The correlation of forearc basins with seismic asperities is an example of this (Song and Simons, 2003; Wells et al., 2003).

The region of the subduction interface that ruptures by seismic slip during large earthquakes is known as the seismogenic zone (Oleskevich et al., 1999). In regions shallower and deeper than the seismogenic zone, aseismic portions that are dominated by aseismic slip are found. The transition from seismic to aseismic slip at depth is suggested to be either thermally controlled by the depth at which the temperature at the plate interface reaches 350°C to 450°C, or where the overriding plate Moho intersects the subducting plate (Hyndman et al., 1997). An analysis of global subduction zone earthquakes indicates that the average downdip limit occurs at 40 +/-5 km (Pacheco et al., 1993), which could correspond to either the thermal or the compositional control, depending on the geometry and lithology of each individual subduction zone (Tichelaar and Ruff, 1993). Exceptions occur though, with deeper limits at the Hokkaido trench junction (Tichelaar and Ruff, 1993) and in central Chile (Tichelaar and Ruff, 1991), and shallower limits in Mexico (Currie et al., 2002) and Cascadia (Hyndman and Wang, 1995).

Local passive seismological networks have been used in numerous subduction zones (Cascadia, Japan, Chile, New Zealand and Costa Rica) to investigate in detail the structure and associated deformation of subduction (Zhao et al., 2001; Zhao et al., 1992; Haberland et al, 2009; Eberhart-Phillips et al., 2005; Deshon et al., 2004). In this paper we present the results of a simultaneous inversion of *Vp* and *Vp/Vs* ratio and hypocentre parameters using the aftershocks of the M_w 8.4 Bengkulu earthquake (Figure 5.1). The experiment has allowed us to determine a detailed image of the structure of the

subduction zone. The study is complemented by an analysis of focal mechanisms, enabling us to investigate the depth extent of the seismogenic zone as well as determining the deformation occurring in the upper plate.

5.3 Tectonic Setting and Seismicity

The study area for the present work is located within the Mentawai segment of the Sumatran subduction zone, which is the region of the megathrust between the Batu Islands and Enggano Island (Figure 1.1 and 5.1). The Sumatra subduction zone is part of the Sunda Arc, which extends for 5600 km from the Andaman Islands in the northwest to the Banda Arc in the southeast. A unique feature of the Sumatra subduction zone is the non-volcanic forearc ridge that is situated above sea level between the trench and the mainland, forming within the Mentawai segment Siberut Island, Sipora Island, North Pagai Island and South Pagai Island (Figure 5.1).

In Sumatra, the Indo-Australian Plate subducts beneath the Eurasian Plate at an oblique angle (~40° at 2°N) with a convergence rate that varies along the trench from 60 mm/yr at 6°S to 52 mm/yr at 2°N (Prawirodirdjo et al., 2000). The oblique subduction results in strain partitioning of the convergence into strike-slip and thrust motion. Strike-slip motion along the Sumatran margin is accommodated by the Sumatran Fault (Figure 5.1), a large highly segmented strike-slip fault that extends for 1900 km from the Sunda Strait to the Andaman Sea, parallel and in close proximity to the volcanic arc (Sieh and Natawidjaja, 2000). Along the Sumatran Fault, the slip rate varies from 6 mm/yr at the Sunda Strait to 25 mm/yr at the equator (Bellier and Sebrier, 1994; Bellier and Sebrier, 1995; Genrich et al., 2000). In the Mentawai region the Sumatran Fault only accommodates a third of the strike-slip motion, with two-thirds taken up by the subduction interface or a fault within the forearc (Sieh and Natawidjaja, 2000). Diament et al. (1992) proposed that arc-parallel shear is taken up by more than one strike-slip fault within the forearc and such a model was supported by the discovery of the Mentawai Fault. The 600 km long Mentawai Fault is located east of the Mentawai Islands at the boundary between the forearc ridge and the forearc basin (Figure 5.1).

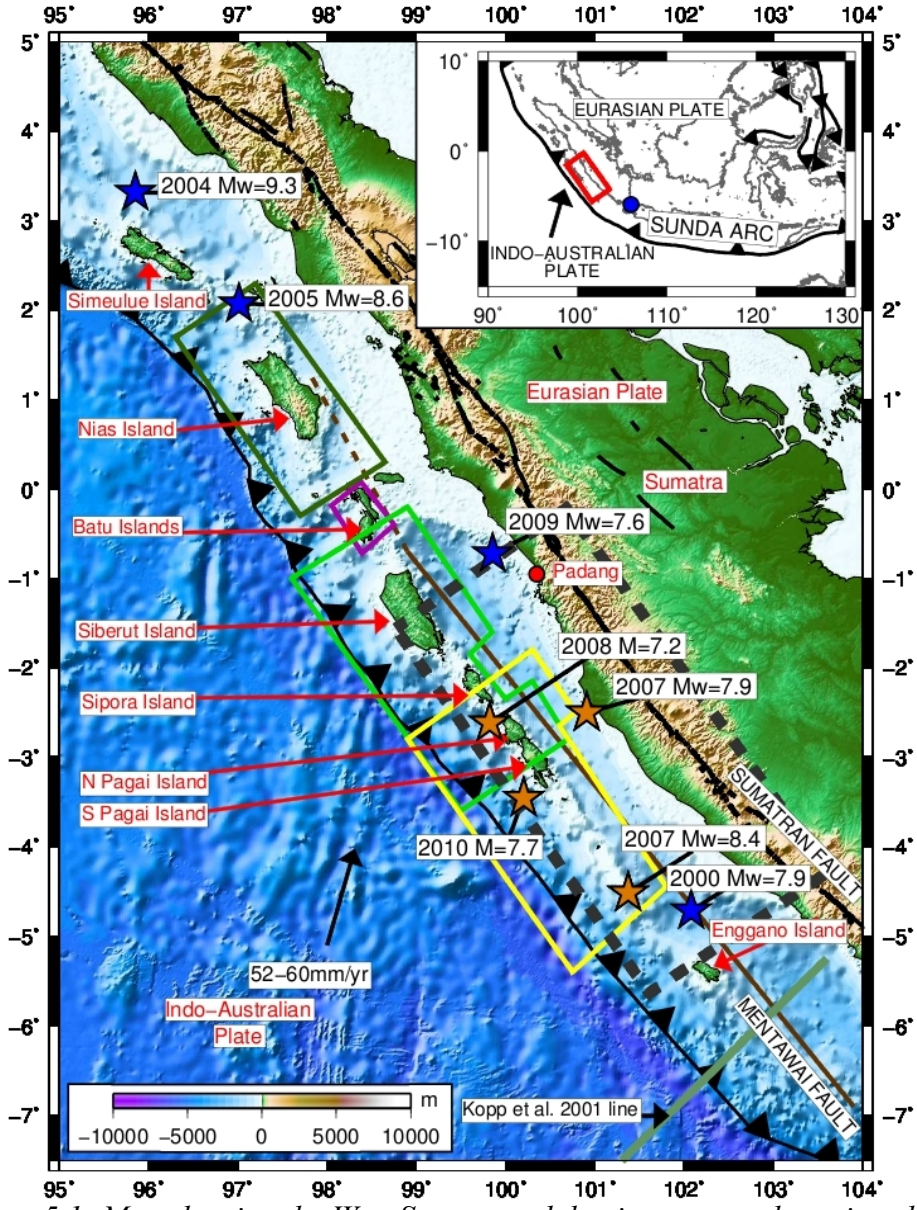

Figure 5.1: Map showing the West Sumatra subduction zone and previous large earthquake ruptures taken from Natawidjaja et al. (2006). The Indo-Australian Plate is moving toward the Eurasian Plate forming the Sunda Trench. The blue circles on the inset map of the Sunda Arc marks the position of the Sunda Strait. The Mentawai Fault (Diament et al., 1992) (brown line) and the Sumatran Fault (Sieh and Natawidjaja, 2000) (black line) are also shown. The locations of recent large earthquakes (NEIC catalogue) are indicated by blue and orange stars. The orange stars show the four recent large thrust events that have occurred within the Mentawai segment (M_w 8.4 2007 event, M_w 7.9 2007 event, M_w 7.2 2008 event, M_w 7.7 2010 event). The Mentawai segment is the region of the megathrust between the Batu Islands and Enggano Island. Historic ruptures are indicated by the coloured boxes (Natawidjaja et al., 2006). Light green is the M_w 8.7-8.9 1797 rupture, yellow is the M_w 8.7-8.8 1833 rupture, dark green is the M_w 8.5 1861 rupture and purple is the M_w 7.7 1935 rupture. The study area (outlined by the grey dashed box, red box in inset) is located in the Mentawai region, in the rupture area of the 1797 and 1833 events. The green line at the bottom of the figure shows the location of the refraction line in Kopp et al. (2001). The scale at the bottom left is bathymetry and topography.

Diament et al. (1992) argued that the linearity and positive flower structures of the Mentawai Fault are characteristic of a large scale strike-slip fault, similar to the Sumatran Fault, explaining the small amount of trench-parallel motion observed along the Sumatran Fault in Southern Sumatra. However, there is disagreement as to whether the deficit in strike-slip motion on the Sumatran Fault is accommodated on the Mentawai Fault. A more recent study using high resolution seismic reflection and bathymetry data (Singh et al., 2009) imaged the Mentawai Fault as a series of southwest dipping backthrusts with no evidence for strike-slip motion.

Past seismicity within the region indicates that thrust motion along the Sumatran margin is primarily accommodated by large thrust earthquakes at the subduction interface. Since 2004, three large thrust earthquakes greater then $M_w > 8$ (2004, 2005 and 2007) have occurred (Figure 5.1). Prior to 2004, three great earthquakes occurred within the last 300 years (1797, 1833 and 1861), rupturing major segments of the forearc (Newcomb and McCann, 1987). It has been noted that permanent lateral barriers control the rupture pattern of these large events, causing the megathrust to rupture in segments, e.g. the northern boundary of the 2005 and 1861 ruptures coincides with the southern boundary of the 2004 event (Briggs et al., 2006) and the southern boundary of the 2005 and 1861 event is close to the northern boundary of the 1797 rupture (Newcomb and McCann, 1987; Lay et al., 2005). Several hypotheses have been suggested for the underlying causes of this apparently stable segmentation, for example, variations in pore pressure (Prawirodirdjo et al., 1997), the Andaman microplate boundary (DeShon et al., 2005) and tectonic features on the subducting plate (Franke et al., 2008). Non-permanent barriers to earthquake propagation can also develop within a segment. This is shown by the M_w 8.4 and M_w 7.9 event pair on 12 September 2007 (Konca et al., 2008) and the M_w 7.7 event on 25 October 2010 (Lay et al., 2011; Newman et al., 2011) occurring within the southern Mentawai segment of the megathrust, in the rupture area of the 1833 event (orange stars, Figure 5.1). The 1833 earthquake originated in southern Sumatra and ruptured the plate margin from Enggano Island in the south to Sipora Island in the north (Figure 5.1), creating an M_w 8.7-8.8 earthquake and tsunami that was observed 550 km along the coast (Newcomb and McCann, 1987; Natawidjaja et al., 2006). In contrast, the

M_w 8.4 2007 Bengkulu earthquake and subsequent M_w 7.9 earthquake released only 10-70% of the moment released in 1833, with significantly smaller co-seismic uplift (Konca et al., 2008). The 2010 M_w 7.7 earthquake occurred southwest of South Pagai Island, within the updip region of the subduction interface that had not ruptured in the 2007 events. The 2007 and 2010 earthquakes suggest a change in the rupture behaviour of the southern Mentawai segment; instead of the whole segment rupturing at once in one large earthquake, a number of smaller magnitude events occur that rupture smaller portions of the subduction interface.

On September 30, 2009 an M_w 7.6 earthquake occurred on the northern edge of the Mentawai segment, 60 km northwest of Padang at a depth of 80-90 km. The hypocentre lies within the lower part of the Wadati Benioff zone of the subducting slab, probably rupturing the mantle of the subducting Indo-Australian Plate (McCloskey et al., 2010; Lange et al., 2010). Consequently, as the 2007 and 2010 events ruptured only the southern section of the Mentawai segment and the displacement was not sufficient to account for the 55-60 mm/yr convergence that had been accumulating since 1797/1833 (Konca et al., 2008), the potential for a large megathrust earthquake to occur on the subduction interface below the northern section of the Mentawai segment (e.g. Siberut Island), within the area of the 1797 rupture, remains high.

5.4 Data

Between December 2007 and October 2008 a temporary seismic array of 27 three component stations (18 CMG-6TD and 9 broadband Trillium 120P) was installed in western Sumatra between 1°S and 4°S on the Mentawai Islands and the adjacent mainland (Figure 5.2). Each station was equipped with a photovoltaic system that consisted of a battery charger, 12 V battery (2 x 12 V for broadband stations) and solar panels. In order to prevent flooding the batteries were placed in plastic boxes and half buried. Stations were located in quiet areas, away from roads, with fences erected around them to protect against animals and deter thieves. During the deployment the 6TD and broadband stations recorded continuously with a sampling rate of 50 Hz and 100 Hz,

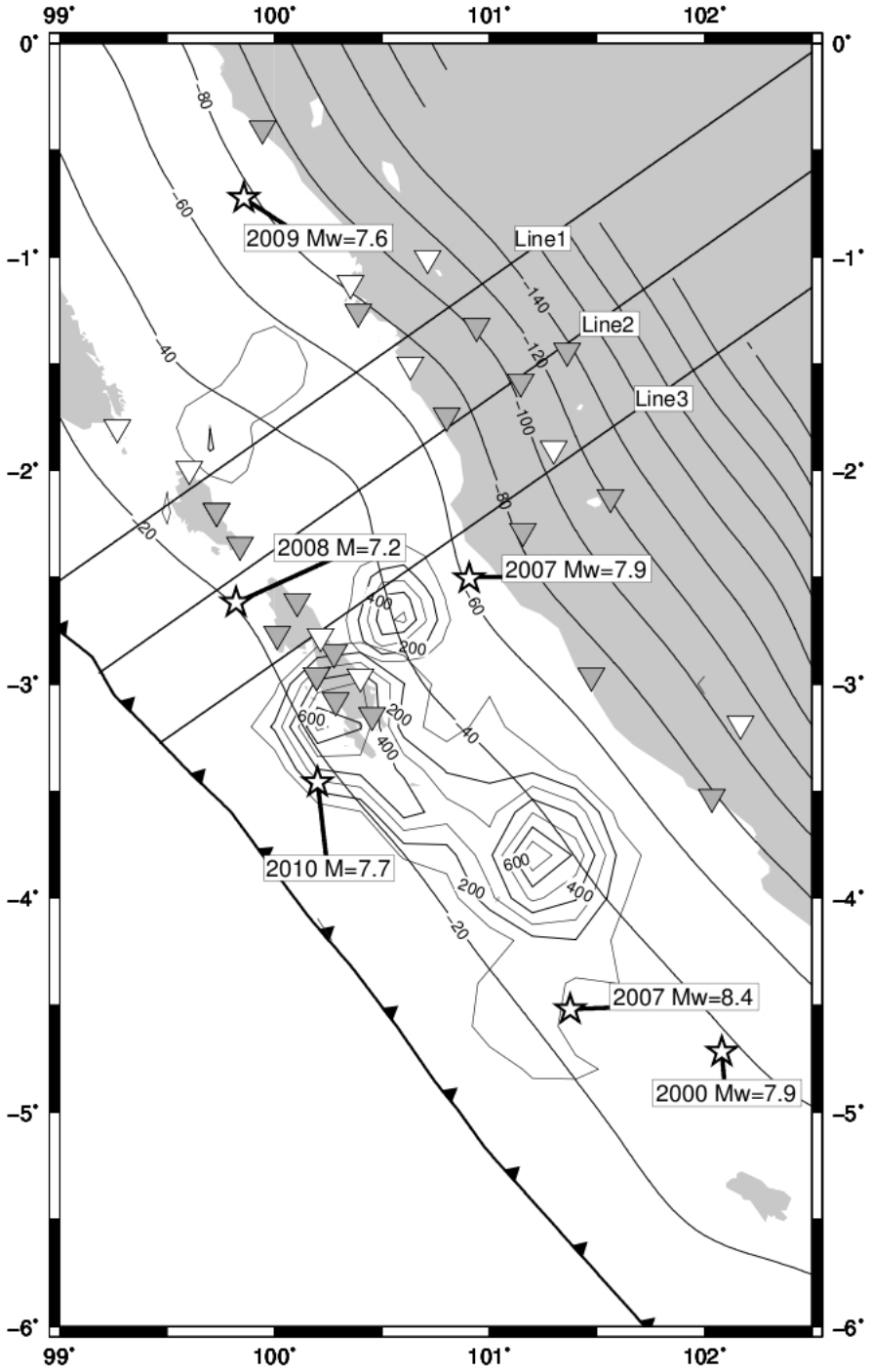

Figure 5.2: Map showing station locations. Dark grey triangles are the 6TD instruments and white triangles are broadband instruments. Black contours indicate the depth of the subducting slab (SLAB1.0, Hayes and Wald, 2009). The co-seismic slip distributions of the M_w 8.4 and M_w 7.9 earthquakes on 12 September 2007 are also shown (Konca et al. 2008). The units of slip is cm. The stars represent the large earthquakes which occurred within the region, see Figure 5.1 for more details. The locations of the cross sections in the 3D tomography are shown.

respectively. Data availability for the 6TD stations was 85%. Due to power problems and microdrive disk failures the broadband stations had a recovery rate of 58%.

Events were detected by applying an automatic STA/LTA trigger on the continuous waveforms and possible events were declared based on a coincident triggering approach (Nippress et al., 2010). Subsequently, arrival times of the *P* and *S* waves were manually determined using the GIANT/PITSA software program (Rietbrock and Scherbaum, 1998). In total, 877 events with magnitudes M_w 2-7 were manually picked and located in a preliminary model from Tilmann et al. (2010), resulting in 12,600 *P* and 6,282 *S* onset times.

5.5 Velocity Models

To obtain tomographic models for the region a staggered inversion scheme was applied, beginning with a one-dimensional (1D) model, followed by a two-dimensional (2D) coarse inversion for *Vp*, fine inversion for *Vp*, inversion for *Vp/Vs* and finally a three-dimensional (3D) model. This staggered approach (Kissling et al., 1994; Haberland et al., 2009) was chosen to ensure that the velocity values of poorly sampled nodes had values in the regional context, thus minimizing artifacts in the final 3D model.

5.5.1 Minimum 1D Model

A high quality subset of 312 events (A2.5) with an azimuthal gap (GAP) of less than 180°, 10 or more *P* arrivals and 4 or more *S* arrivals were selected for a simultaneous inversion for accurate hypocentres, 1D velocity model and station corrections (VELEST, Kissling et al., 1994). In total 4706 *P* and 2724 *S* onset times were used for this inversion step. During the initial manual location step it became apparent, based on *S* wave residuals, that the *Vp/Vs* ratio showed substantial variability perpendicular to the trench (Figure A2.1 and A2.2). Events located beneath and on the southwesterly side of the Mentawai islands required a *Vp/Vs* of 1.80 to 1.90 to accommodate the observed *S* wave arrival times. For events located in other parts of the forearc a *Vp/Vs* ratio of 1.73 to 1.80

was used.

First, we inverted for a 1D *Vp* model using a wide range of initial starting *P* wave velocity models with different velocity values and a varying number of layers. A *Vp/Vs* ratio of 1.80, determined from Wadati diagrams (Figure A2.3), was used during the inversions. Station corrections were included to account for the shallow lateral variation in the subsurface geology and to accommodate a substantial part of the 2D/3D velocity structure. The damping for the velocities was chosen based on analysis of data variance against model complexity (Eberhart-Phillips, 1986) and a damping value of 100 was selected (Figure A2.4). A trial and error process was used to determine the damping value for the station corrections, again balancing data variance and model complexity (station correction amplitudes). This resulted in a damping value of 450. Inversions to obtain the *Vs* model were subsequently run by keeping the *Vp* model fixed. Damping parameters for the station corrections and velocity model (here *Vs)* remained at 450 and 100 respectively.

The final minimum 1D velocity model is shown in Figure 5.3. At the surface a *Vp* of 5.53 km/s is observed, increasing to 6.20 km/s at 5 km depth. Numerous geological and geophysical studies have taken place on and around Nias Island (e.g Hamilton, 1977; Kieckhefer et al., 1980), north of our study area, and also around Enggano Island, south of our study area (Kopp et al., 2001, Figure A2.17). From these studies the authors concluded that the forearc islands were formed from uplifted accreted sediment that has a low velocity of 5-5.8 km/s (Hamilton, 1977; Karig et al., 1979; Kopp et al., 2001) and the forearc basins, landward of the islands, are underlain by a thick layer of continental crust that has velocities of 6-6.5 km/s (Kieckhefer et al., 1980; Kopp et al., 2001). These observations are in agreement with our derived velocities and can be attributed to both low velocity consolidated sediment beneath the islands and continental crust beneath the forearc basin and mainland Sumatra. In our model we do not observe the 1.4-3.3 km thick layer of low velocity sediment (1.5-2.7 km/s) imaged within the Nias forearc basin by Kieckhefer et al. (1980) as the ray paths do not sample this shallow region of the marine forearc. At 20 km depth, the gradient of *Vp* increases sharply, with velocities

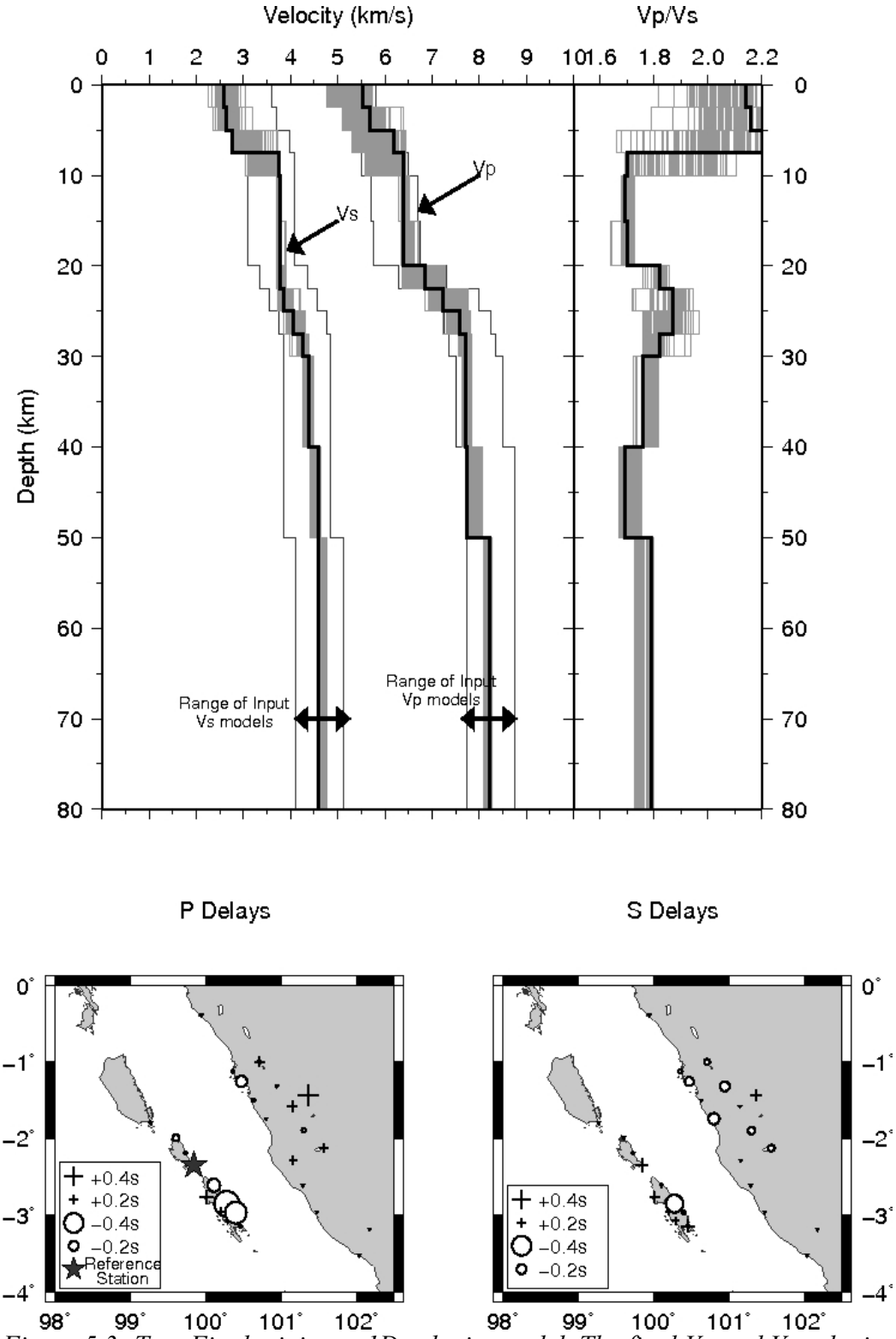

Figure 5.3: Top: Final minimum 1D velocity model. The final Vp and Vs velocity model and Vp/Vs ratio are shown with thick black lines. All models with a RMS within 5% of the final model are indicated by the grey lines. The range of input models for Vp and Vs are indicated by the thin black lines. Bottom Left: P wave station corrections. The reference station is shown with a star. Bottom Right: S wave station corrections.

increasing from 6.39 km/s at 20 km depth to 7.72 km/s at 28 km depth, marking the transition into the subducting slab (Figure A2.17, Kopp et al., 2001; Klingelhoefer et al., 2010). At 50 km depth mantle *Vp* velocities of 8.20 km/s are found; similar velocities were observed in the oceanic mantle in a wide-angle profile southeast of Enggano Island (Figure A2.17, Kopp et al., 2001; see Figure 5.1 for location of line). The modeled *Vp/Vs* ratio (Figure 5.3) is very high (greater than 2.0) down to a depth of 7.5 km, before dropping to values of about 1.70. A second increase of the *Vp/Vs* ratio is observed between 20-30 km depth, which coincides with the depth range of the top of the subducting slab, in the area of most seismicity (Figure A2.5) and therefore possibly indicates a hydrated slab.

P and *S* wave station delays are similar for nearby stations (Figure 5.3). Stations on the eastern side of the forearc islands and at the coast of the mainland are characterized by negative *P* wave station delay terms while stations on the western side of the forearc islands and further inland on mainland Sumatra show positive delays.

The robustness and stability of the 1D minimum model was assessed using two different methods. In the first test the hypocentre positions were randomly moved by 6-10 km in latitude, longitude and depth and a joint inversion was performed using the previously determined 1D model as the starting model. This process was repeated 100 times and the resulting velocity models and hypocentre locations were then compared to the final hypocentre locations and 1D minimum velocity model. The standard deviation for latitude and longitude is typically less than 1.0 km and 3.0 km for depths (Figure A2.6, A2.7, A2.8 and A2.9). The velocity model obtained does not change significantly from the final 1D minimum model (<2% *Vp* (A2.6) and <3% *Vs* (A2.7)), and the prominent *Vp* velocity discontinuities are still evident at 5-8 km depth and 20-23 km depth.

As a further test of the accuracy of the hypocentres and the velocity model a bootstrap approach (Langer et al., 2007) was applied to the data set. This method involves re-sampling the dataset by selecting only a proportion of the picks for each event, before carrying out a 1D inversion. The previously-determined minimum 1D velocity model

was used as the starting model and 100 runs were carried out for both the *P* wave and *S* wave velocity model. Re-sampling of the onset times for each event was carried out using the replacement strategy which means that we did not change the absolute number of onset times, but the GAP could vary. For the *P* wave and *S* wave model we randomly selected 14 (*P* waves only) and 18 onset times (random mixture of *P* and *S* waves), respectively, from the catalogue. The hypocentre locations again showed differences in latitude and longitude, with standard deviations of less than 2.0 km in horizontal direction and 5.0 km in depth (Figure A2.10 and A2.11). The velocity models obtained are close to the final minimum 1D model with deviations in *Vp* and *Vs* of less than 2% and 4.5%, respectively.

5.5.2 2D and 3D Tomographic Models

The inversion program SIMUL2000 (Thurber, 1983, 1993; Eberhart-Phillips, 1986 and Eberhart-Phillips and Michael, 1998) was used to determine the 2D and 3D velocity structure. This method involves an iterative simultaneous inversion for velocity structure and hypocentres from the observed travel times incorporating an approximate 3D ray tracer (Um and Thurber, 1987). A grid of nodes is used to represent the velocity structure, in which the velocity varies continuously in all directions using linear B-spline interpolation between 8 neighbouring grid points. It is well known that the quality and quantity of *S* wave onset times is significantly reduced in comparison to *P* wave data. SIMUL2000 therefore inverts for *Vp/Vs* ratio instead of an independent *Vs* model, using the fact that *Vp/V* is spatially more homogeneous (Thurber, 1993). However, the obtained velocity model will only represent an approximation to the true structure due to he inherent smoothing constraints of the inversion. While the degree of the heterogeneity that can be imaged depends primarily on ray density, sharp interfaces will not be recovered. Spacing within the velocity grid was selected to enable enough ray paths to pass through the central grid points, allowing adequate resolution to be obtained within the centre of the model.

For the tomographic inversions the same events selected for the 1D inversion were

included. Additionally, 29 events beneath Sipora Island, North Pagai Island and South Pagai Island with a GAP of 180° to 270°, 10 or more *P* picks and 4 or more *S* picks were included to improve resolution within the updip area of the subduction zone. A total of

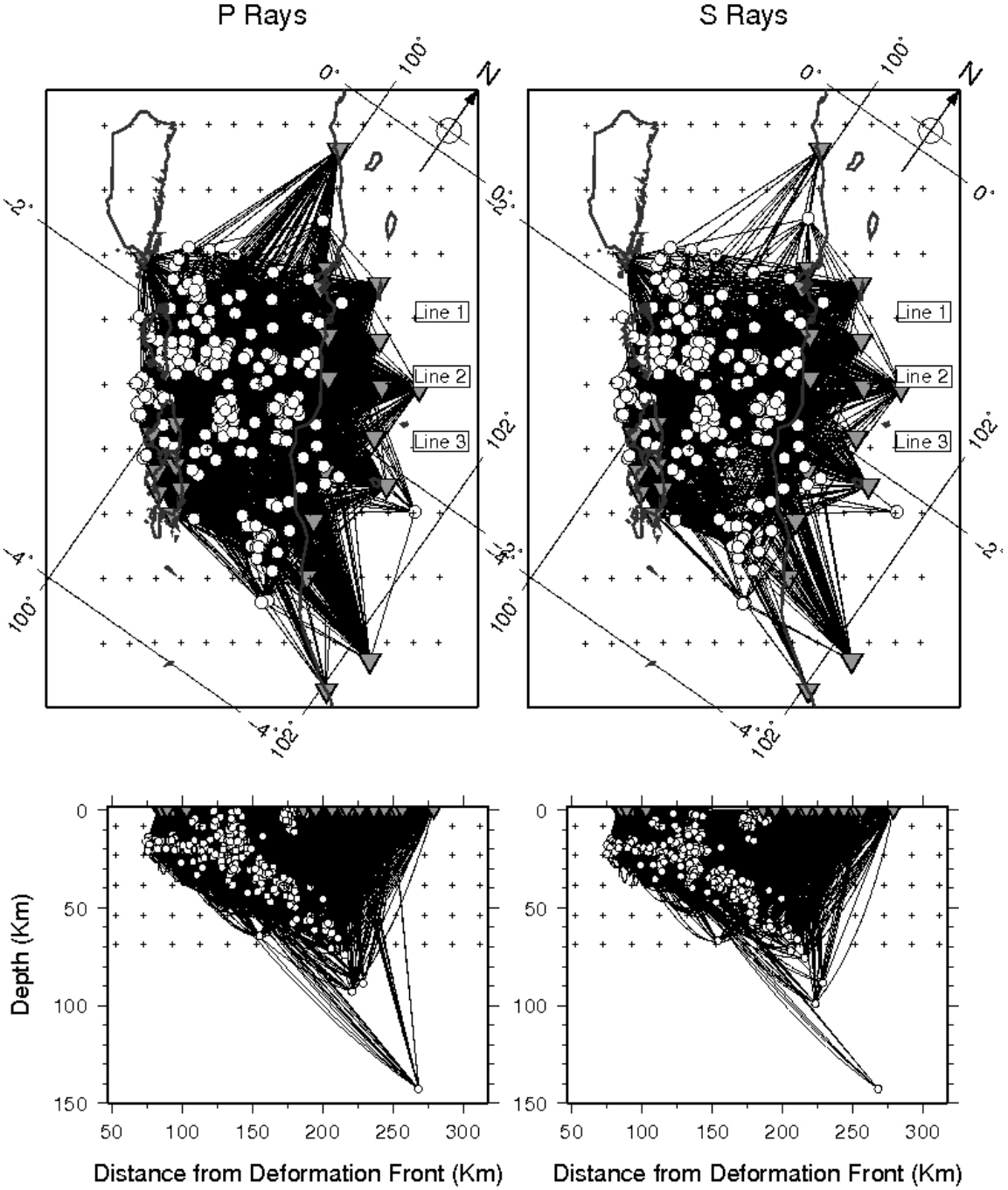

Figure 5.4: Station (grey triangles) and earthquake (white circles) distribution and ray coverage (black lines). Crosses represent the nodes of the final 3D tomographic model. Left: P wave ray paths. Right: S wave ray paths.

5,121 *P* picks and 2,934 *S* picks were used for the inversions (Figure 5.4). Arrival times with initial residuals up to 2.5 s were accepted. The starting model for the coarse 2D inversion was the previously-calculated 1D minimum model for *Vp* and a constant value of 1.80 for *Vp/Vs,* based on Wadati diagrams. In subsequent inversions for fine 2D *Vp* and *Vp/Vs* models as well as 3D models, the previously-calculated *Vp* and *Vp/Vs* models were used as starting models. At each stage of the inversion the hypocentres were relocated with the updated velocity model. The final hypocentres for 538 events which have 6 or more P picks and 4 or more S picks, and were computed using the final 3D *Vp* and *Vp/Vs* model, can be found in A3.

The coarse 2D model has a horizontal grid spacing of 30 km in the centre of the network (SW to NE) and 15 km spacing in the vertical direction to a depth of 70 km, with additional nodes at 150 km and 200 km depth. The fine grid has a horizontal spacing of 20 km, and again 15 km spacing in the vertical direction (Figure 5.4). The 3D model has the same spacing as the fine model in depth and SW to NE direction but a node spacing of 50 km was used in the NW-SE direction. The node spacing was determined after extensive tests to determine a reasonable resolution given the available data set. Within a subduction zone we are expecting to image dipping structures, e.g. the subducting slab. In order to image the dipping structure using a regular rectangular grid, additional inversions were carried out with horizontally shifted grids (5, 10, 15, 20 and 25 km for the coarse inversion and 5, 10 and 15 km for the finer inversion) and spatially averaged to obtain a smooth velocity model. This method is used regularly in teleseismic tomography and can also be applied to 2D and 3D local earthquake tomography to provide a smooth and robust final model (Haberland et al., 2009).

Damping values in each stage of the inversion were calculated using trade-off curves from one-step inversions (Eberhart-Phillips, 1986, Figure A2.12 and A2.13, Table A2.1). The damping value for the station corrections was set to a high value (1000) for each of the inversions to ensure we did not underestimate the lateral heterogeneity within the region. In the final inversion, station corrections were included to account for velocity inhomogeneities caused by near-surface structures (e.g weathering, sedimentation, and

others) which can produce very large velocity variations in the shallowest 100 m or so (Table A2.2). For all the inversions we used the same reference station (DSAO) as in the 1D case (Figure 5.3).

5.6 Resolution

The geometry of the subduction zone as well as the location of earthquakes and receivers results in a subsurface structure being resolved with spatially varying quality. For any geological interpretation of the obtained tomographic image it is necessary to quantify which regions of the model are well resolved and which are not. We used the model resolution matrix, synthetic checkerboard tests and also restoring resolution tests to determine the well resolved regions in our model.

5.6.1 Model Resolution Matrix

The resolution matrix indicates to what degree the velocity at each grid point can be determined independently of its neighbours, i.e., how much 'smearing' occurs from adjacent nodes. Each row of the resolution matrix is an averaging vector for a single model parameter; it describes how the estimate for an individual model parameter depends on the values of all other model parameters (Menke, 1984). The resolution diagonal elements (RDE) describe the independence of one model parameter in the solution. Well-resolved nodes have large diagonal elements (close to 1) and small off-diagonal elements. Smearing can be visualized by contouring the averaging vector. The surface around the model parameter where the value of the averaging vector decays below 70% of the diagonal value is shown for each node (Figure 5.5). The shape and spatial extent of the contours is interpreted as a measure of smearing, with close contour lines indicating a well resolved node. A synoptic view of resolution can be provided using the spread function (Toomey and Foulger, 1989) which summarizes the information contained in a single averaging vector or row of the full resolution matrix. For a peaked resolution (low smearing and considerably larger diagonal element than off-diagonal elements) the spread value is low but there is no universal value to define

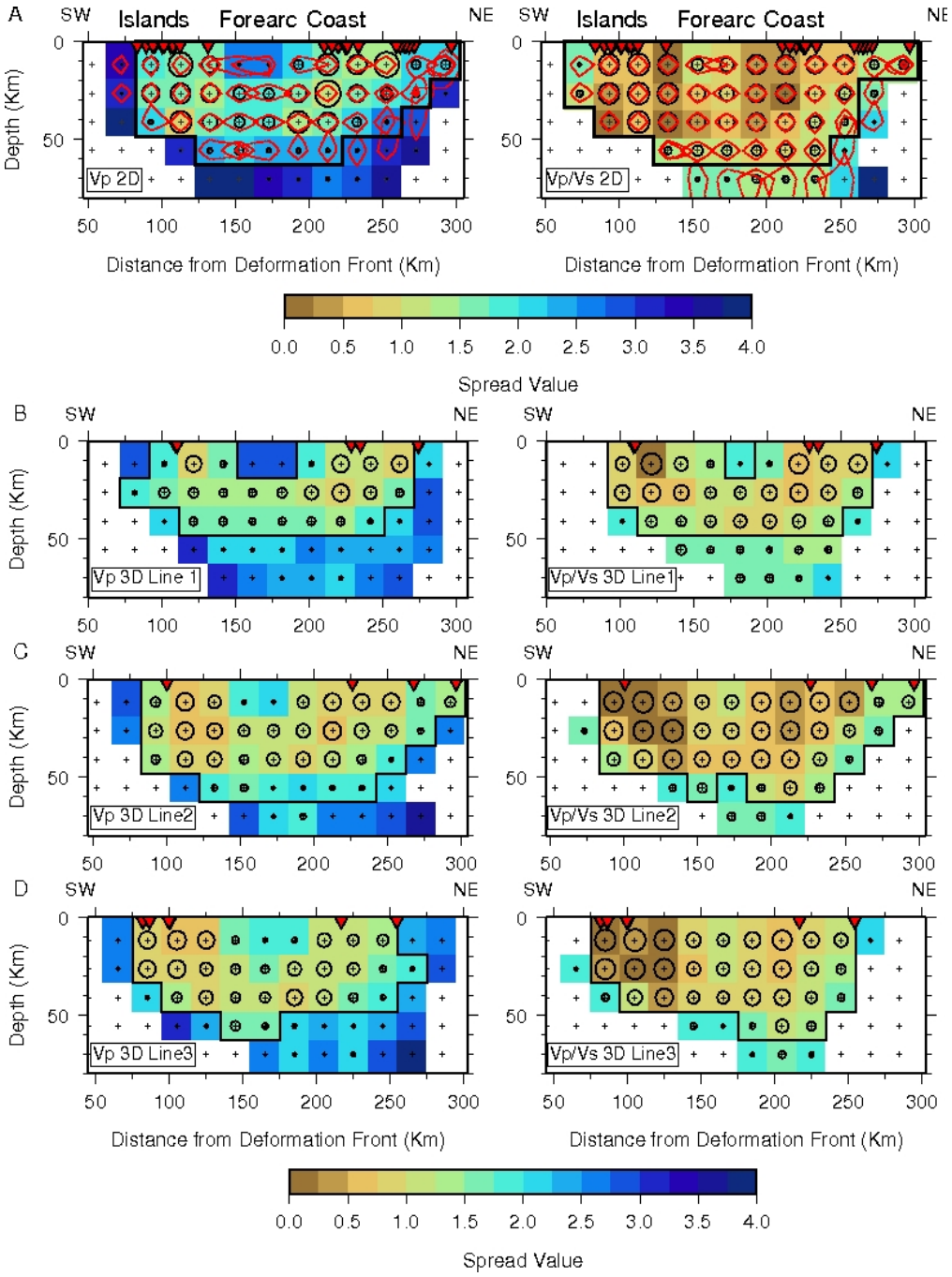

Figure 5.5: Resolution estimates for 2D and 3D models based on the analysis of the model resolution matrix for the fine 2D and 3D tomographic inversions. Left: Vp model. Right: Vp/Vs model. Spread values are shown by different colours, diagonal elements are shown by black circles of varying size and the 70% contour lines of the resolution kernel are shown by red contours. Regions of good resolution are within the thick black line. Station locations are represented by red triangles. A: 2D model. B: 3D model line 1. C: 3D model line 2. D: 3D model line 3. See Figure 5.2 for location of lines.

what an acceptable spread value is, as this value depends on the damping and grid node spacing.

5.6.1.1 2D Resolution

Large diagonal elements of the *Vp* model, a small extent of the 70% kernel and spread values of less than 2.5 are observed for a large proportion of the nodes across the forearc within the centre of our network, indicating that this region of the velocity model is well resolved (Figure 5.5A). The ability to have stations on the forearc islands along the Sumatra subduction zone results in good resolution of the updip region of the subduction zone. Low resolution is observed beneath the centre of the forearc basin due to little seismic activity and hence fewer rays traveling though this region. This can be seen by small diagonal elements, large spread values and significant horizontal smearing as indicated by the 70% kernels. Small diagonal elements, larger radius of the 70% kernel and spread values of above 2.5 are found for depths greater than 60 km and at the edge of the network, indicating diminishing resolution (Figure 5.5A).

The spread values of the *Vp/Vs* model (generally <2.5, Figure 5.5A) are lower than for the *Vp* model (upto 4) due to the lower damping value used for the *Vp/Vs* inversion. Inspection of the diagonal elements and 70% kernel implies that a spread value of 1.5 or less indicates well-resolved areas. Smearing is still observed in the upper layers beneath the forearc basin.

5.6.1.2 3D Resolution

The spread values and RDE for three cross sections in the 3D model are shown in Figure 5.5B, 5.5C and 5.5D. In Figure 5.5B analysis of the RDE for Vp implies that a spread value of 2 and below shows areas of acceptable resolution can be found from 90 km and up to 270 km from the deformation front, down to a depth of 50 km. However, the large spread values of greater than 3.0 for the two nodes at 10 km depth in the forearc basin indicate that resolution is very poor in this region. A similar pattern of resolution is

observed for *Vp/Vs*. Within the centre of the region (Figure 5.5C) *Vp* resolution is acceptable for up to 300 km from the deformation front at shallow depths and down to 60 km depth for a large proportion of the forearc. Resolution for *Vp/Vs* is also acceptable in most regions from 140 to 240 km from the trench until a depth of 60 km. In line 3 (Figure 5.5D) resolution for *Vp* and *Vp/Vs* is still satisfactory beneath the forearc and islands but a smaller proportion extends to 60 km depth.

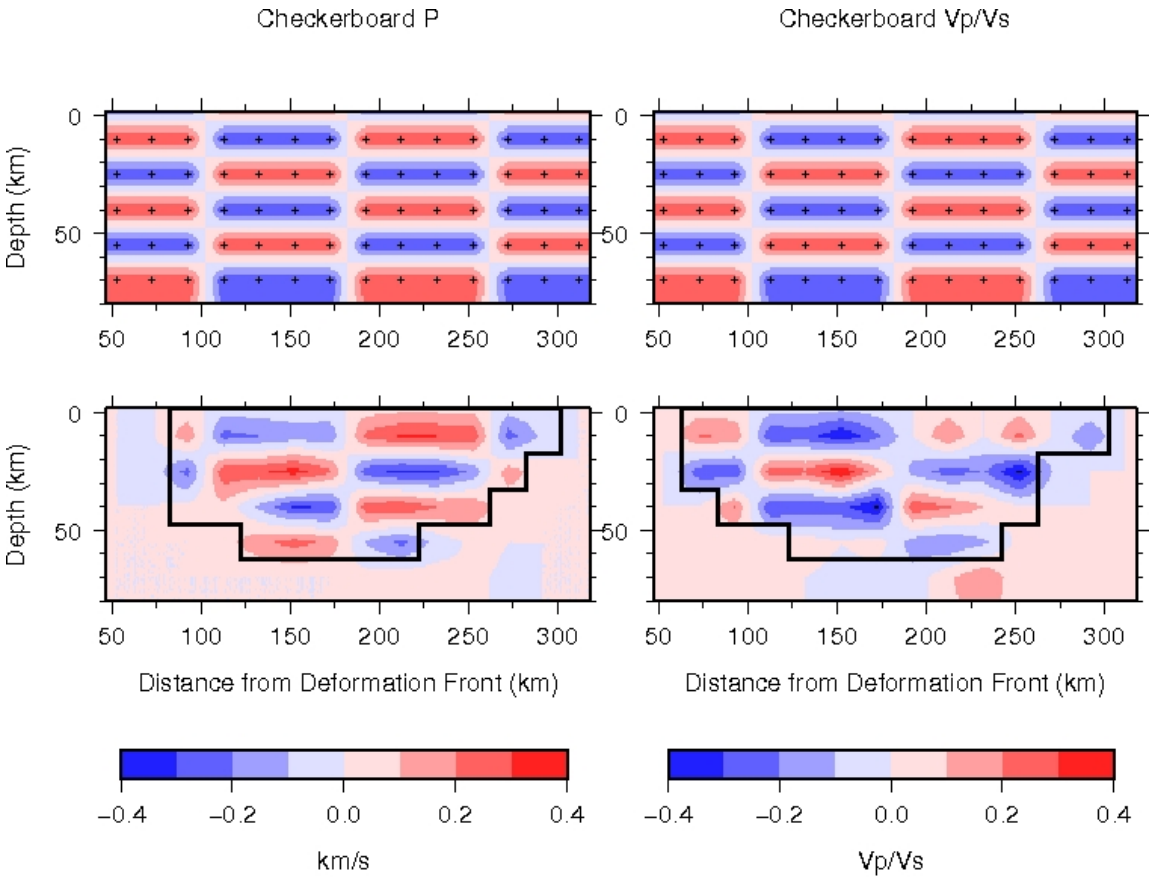

Figure 5.6: Top: Synthetic 2D models for Vp (left) and Vp/Vs (right) checkerboard tests. Bottom: Inversion result for Vp (left) and Vp/Vs (right). Crosses represent nodes used in the inversion.

5.6.2 Synthetic Models

The quality of the velocity model was also evaluated using checkerboard and restoring resolution tests. Checkerboard tests estimate the degree of smearing between nodes. A

synthetic model with a checkerboard pattern of ±0.3 km/s *Vp* or ±0.3 *Vp/Vs* variations from the original model was created. Synthetic travel times using the same hypocentre and station locations as the real data were calculated with normally-distributed random noise added to reflect the quality associated with each real observation. For the highest quality readings (weight 0) random noise with a standard deviation of 0.05 s was added, increasing to 0.20 s for phases of lowest quality (weight 3). The synthetic travel times were then inverted using the same parameters used for the actual inversion and the resulting model compared to the synthetic one. The 2D *Vp* model (Figure 5.6) shows that little smearing occurs within the centre of the network down to a depth of 60 km. For the *Vp/Vs* inversion (Figure 5.6) the amplitude of the anomalies are generally well recovered but at depths greater than 50 km and between 0 and 20 km depth, 200 to 250 km from the deformation front, recovered amplitudes are smaller than the input model. However, the checkerboard pattern is still recovered within the centre of the network down to 60 km depth.

Restoring resolution tests (Zhao et al., 1992) were used to estimate the capacity of the data to resolve geometry and amplitude of features. A synthetic velocity model was constructed with similar characteristics (amplitude and dimensions) as the inversion result based on the real data. Instead of using a synthetic model with the same grid spacing as used in the tomographic inversion, finer models with a horizontal spacing of 15 km and 5 km in the vertical direction were created. The finer node spacing allowed us to assess the ability of our tomographic inversions to image small, thin and inclined structures and strong velocity gradients. The hypocentre and station locations were used to compute the synthetic travel times with normally distributed random noise added to reflect the quality of the real data using the same parameters as described above for the checkerboard tests. The synthetic *Vp* model (Figure 5.7A) based on a subducting slab is very well recovered within the regions of good resolution mentioned above and has no significant artifacts introduced in the less resolved areas. The absolute values of *Vp* for continental crust and continental Moho are reproduced well. However, within the centre of the subducting slab, above 60 km depth, in the region with good resolution, the absolute recovered *Vp* values are 4% higher than in the input model. Large scale *Vp/Vs*

anomalies of 1.85 within the subducting slab (Figure 5.7B) are resolved with small localized regions showing elevated amplitudes (~3%) of 1.9. Below 50 km, significant smearing into adjacent nodes occurs (as has been seen in the formal resolution tests), but above this depth variations in the *Vp/Vs* ratio along the subducting slab can be distinguished reasonably well (Figure 5.7C). In the forearc crust and beneath the islands, anomalies in *Vp/Vs* (Figure 5.7D) are recovered with little smearing. Beneath the islands, in localized regions, the *Vp/Vs* is elevated by ~10% from 2.0 to 2.2, while in contrast, small patches beneath the forearc basin show a reduced Vp/Vs of 1.7 from the input model of 1.75. However, the mean *Vp/Vs* ratio within these two regions is approximately equal to the input model.

The spread values, diagonal elements, checkerboard and restoring resolution tests shows that for both *Vp* and *Vp/Vs,* reasonably good resolution is obtained within the centre of our network until depths of 50-60 km depth. At greater depths and at the edge of the network the lack of earthquakes and seismic stations causes significant smearing between adjacent nodes and the resolution diminishes.

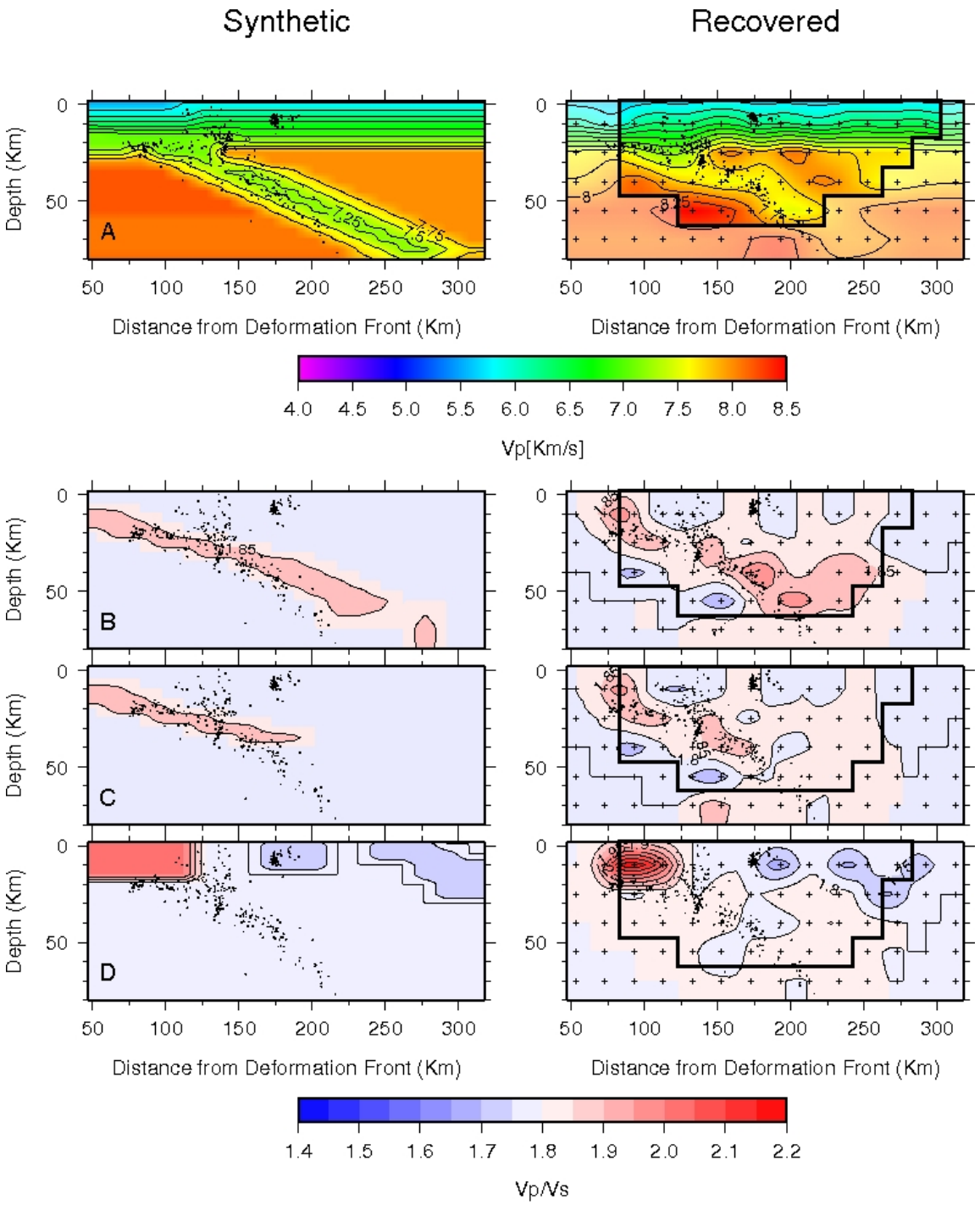

Figure 5.7: (Left) Synthetic 2D models and (right) corresponding inversion results for the restoring resolution tests. Small black dots represent local events used in the inversion. Regions of good resolution are within the thick black line. (A) Synthetic Vp model representing a subduction zone. (B) Synthetic Vp/Vs model with a high positive anomaly in the slab to represent altered and hydrated oceanic crust and mantle. (C) As B except a depth limit is given to the high positive anomaly within the slab. (D) Vp/Vs model with anomalies in the overriding plate.

5.7 Focal Mechanisms

Focal mechanisms for 32 events (Figure 5.10), which have at least 15 *P* wave onsets with clear first motion polarity, were determined using the FOCMEC algorithm (Snoke et al., 1984) (Table 5.1, A2.16). The events are located within the crust, subducting slab and at the plate interface. Take-off angles and azimuths were computed in the final 3D velocity model. Only focal mechanisms that have a well-constrained solution and no

Event (ddmmyy)	Lat (Deg)	Long (Deg)	Depth (km)	No. Polarities	Strike	Dip	Slip	CMT	Lat Diff (km)	Long Diff (km)	Depth (Diff)	CMT Strike	CMT Dip	CMT Slip
191207	-2.3352	100.3103	32	17	141	75	-85	NO	-	-	-	-	-	-
201207	-2.3347	100.3403	31	19	290	18	-81	NO	-	-	-	-	-	-
221207	-2.1405	100.6180	8	20	140	32	71	NO	-	-	-	-	-	-
271207	-1.9410	100.2447	39	20	265	16	71	NO	-	-	-	-	-	-
40108	-2.8900	100.8300	27	20	265	36	54	YES	-22	-16	19	323	27	102
60108	-2.1902	100.0482	14	16	34	41	75	NO	-	-	-	-	-	-
80108	-2.2475	99.8832	24	20	91	85	75	NO	-	-	-	-	-	-
90108	-2.3782	100.3381	36	17	321	14	45	NO	-	-	-	-	-	-
230108	-2.9796	101.0340	32	19	268	34	49	YES	-28	-5	23	302	27	86
280108	-2.3625	100.3440	32	20	138	70	-79	NO	-	-	-	-	-	-
60208	-1.9712	99.6137	24	15	104	44	61	NO	-	-	-	-	-	-
140208	-2.1677	100.0703	25	16	85	75	53	NO	-	-	-	-	-	-
230208	-2.0905	100.6310	44	26	106	85	80	NO	-	-	-	-	-	-
240208	-2.5512	99.8242	19	20	120	76	75	NO	-	-	-	-	-	-
250208	-2.3773	100.3051	40	19	150	34	-67	NO	-	-	-	-	-	-
250208	-2.4665	99.7913	19	19	122	74	85	YES	-12	-7	-4	125	84	89
250208	-2.3929	99.7254	20	20	162	61	76	YES	-8	-3	-3	124	82	88
260208	-2.6717	100.0511	19	16	109	75	80	NO	-	-	-	-	-	-
270208	-2.5047	99.9832	21	20	253	77	-64	NO	-	-	-	-	-	-
10308	-2.0652	100.9141	62	18	216	85	-85	NO	-	-	-	-	-	-
90408	-2.5058	100.4512	10	15	358	59	66	NO	-	-	-	-	-	-
90408	-1.3720	100.0558	59	16	5	25	79	NO	-	-	-	-	-	-
270408	-3.2720	101.3378	42	17	269	21	44	YES	-30	-18	9	316	32	98
30508	-3.0814	101.1937	46	20	277	17	44	YES	-22	-12	9	322	29	109
50508	-2.2883	100.7296	44	18	260	26	11	NO	-	-	-	-	-	-
140508	-2.5457	99.7128	22	17	260	51	-53	NO	-	-	-	-	-	-
240608	-3.2716	101.2711	45	16	272	70	78	YES	-13	-26	-2	321	31	107
300608	-2.2725	101.2549	75	17	145	18	33	NO	-	-	-	-	-	-
100708	-2.1432	100.6238	9	16	166	21	76	NO	-	-	-	-	-	-
290808	-2.1377	100.6196	10	15	88	79	-45	NO	-	-	-	-	-	-
80908	-2.3223	100.3045	30	15	320	23	-84	YES	-11	-7	-10	327	43	-58

Table 5.1: Focal mechanisms with one well constrained solution, at least 15 P polarities and no more than two wrong polarities. CMT stands for global Centroid Moment Tensor (www.globalcmt.org).

more than 2 wrong polarities are included in this study (A2.16). The data set includes 8 events with published gCMT solutions (www.globalcmt.org), allowing us to bench-mark our results based on the local network data.

The gCMT locations are shifted up to 40 km seaward and are generally at deeper depths (Table 5.1). A similar observation was made in northern Sumatra (Tilmann et al., 2010) and the epicentre shift at subduction zones has been reported to occur globally (Engdahl et al., 1998). This is because the gCMT events are relocated using a global 1D velocity model which does not include the sbducting slab velocities. The eight focal mechanisms we obtained all agree with the type of faulting inferred from the gCMT solutions. However, there is an average difference of 35° between the strike of the focal mechanisms determined in this study and the strike of the gCMT solutions. The largest difference, 58°, is observed for the event on the 4 January 2008 with a strike of 265° in our study and a strike of 323° in the gCMT catalogue. The dip angles of both catalogues are similar, with a mean difference of 16°. The largest difference is found for the event on the 24 June 2008. A dip angle of 70° is determined from our focal mechanisms, which is 39° larger than the dip angle given by the gCMT solution (31°). The slip angle of the obtained focal mechanisms agrees with the gCMT solutions with regards to the direction of motion of the hanging wall. However, for seven events the slip angle determined from our focal mechanisms is more oblique than the slip angle from the gCMT catalogue; on average there is a 37° difference. The only exception to this pattern for the slip angle is the one normal fault event on 8 September 2008. Here, we determined a slip angle of -084° from the focal mechanisms, which is 26° larger than the slip angle determined from the gCMT solutions (-058°), suggesting that the actual slip angle is not as oblique as previously suggested by the gCMT solutions.

5.8 Results and Discussion

The resulting 2D velocity models, 3D velocity models and hypocentre locations are presented in Figures 5.8, 5.9 and 5.11, respectively, while the focal mechanisms are shown in Figure 5.10. In the following sections they are used to determine the structure

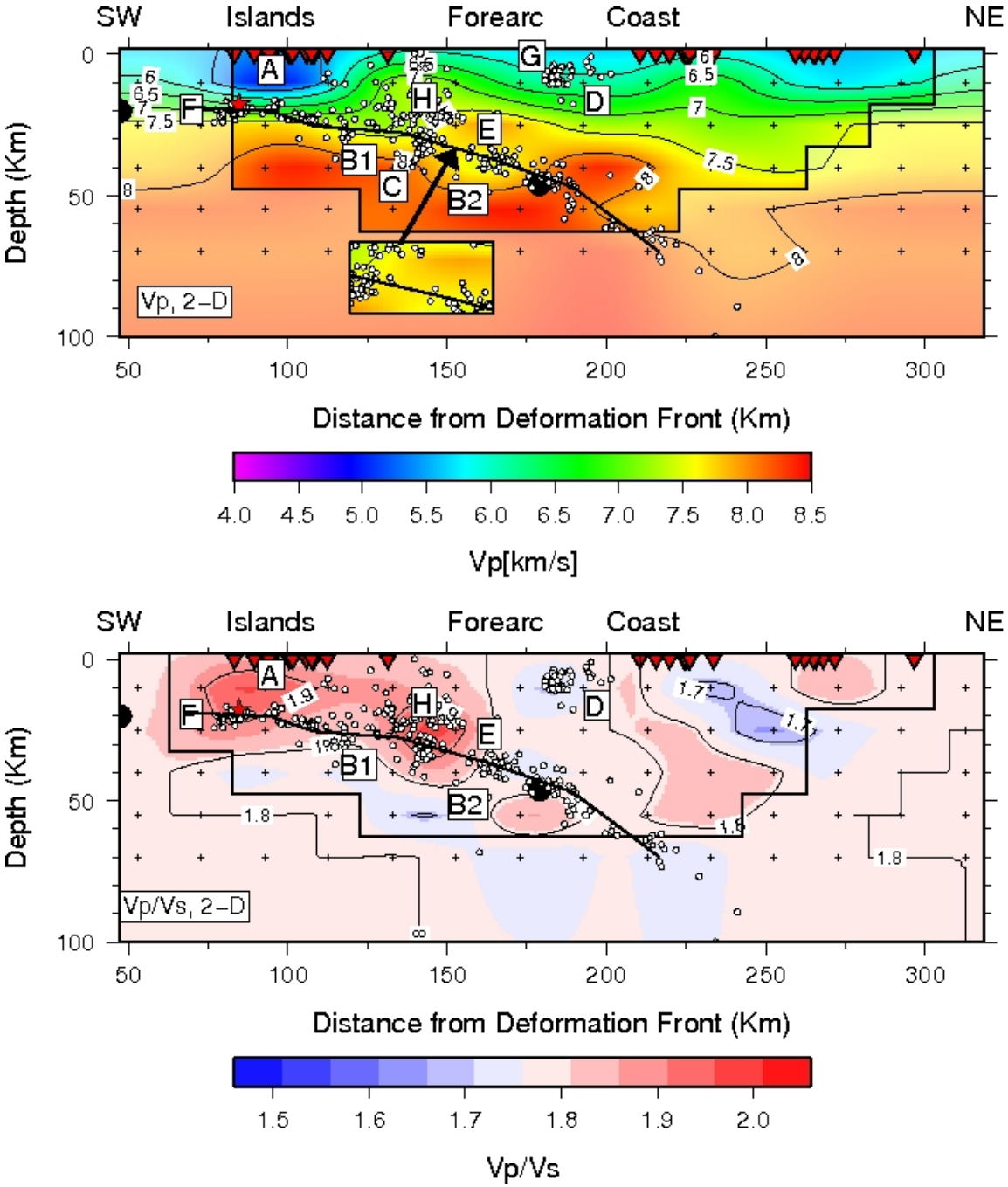

Figure 5.8: 2D velocity model of Vp (top) and Vp/Vs (bottom). Velocities and Vp/Vs ratios are colour coded. Regions which are well resolved are within the thick black line (Figure 5.5). The hypocentres of all earthquakes used in the inversion are represented by white circles and grid nodes are indicated by crosses. The red star is the hypocentre of the M_w 7.2 February 25, 2008 event determined from our data. The region of slip during the M_w 8.4 and M_w 7.9 event on 12 September 2007 (beneath forearc basin/islands) (Konca et al., 2008) are indicated by the black circles. The inferred plate interface is shown by the black line. A=Forearc Islands, B1=Subducting slab above 30 km depth, B2=Subducting slab beneath 30 km depth, C=Cluster of seismicity within the subducting slab, D=Continental crust, E=Mantle wedge, F=Region of intense aftershock activity, G=Cluster of seismicity on eastern side of the forearc basin, H=Mentawai Fault. On the top figure the inset figure of seismicity shows the 10 km gap in seismicity on the plate interface, 150-160 km from the deformation front.

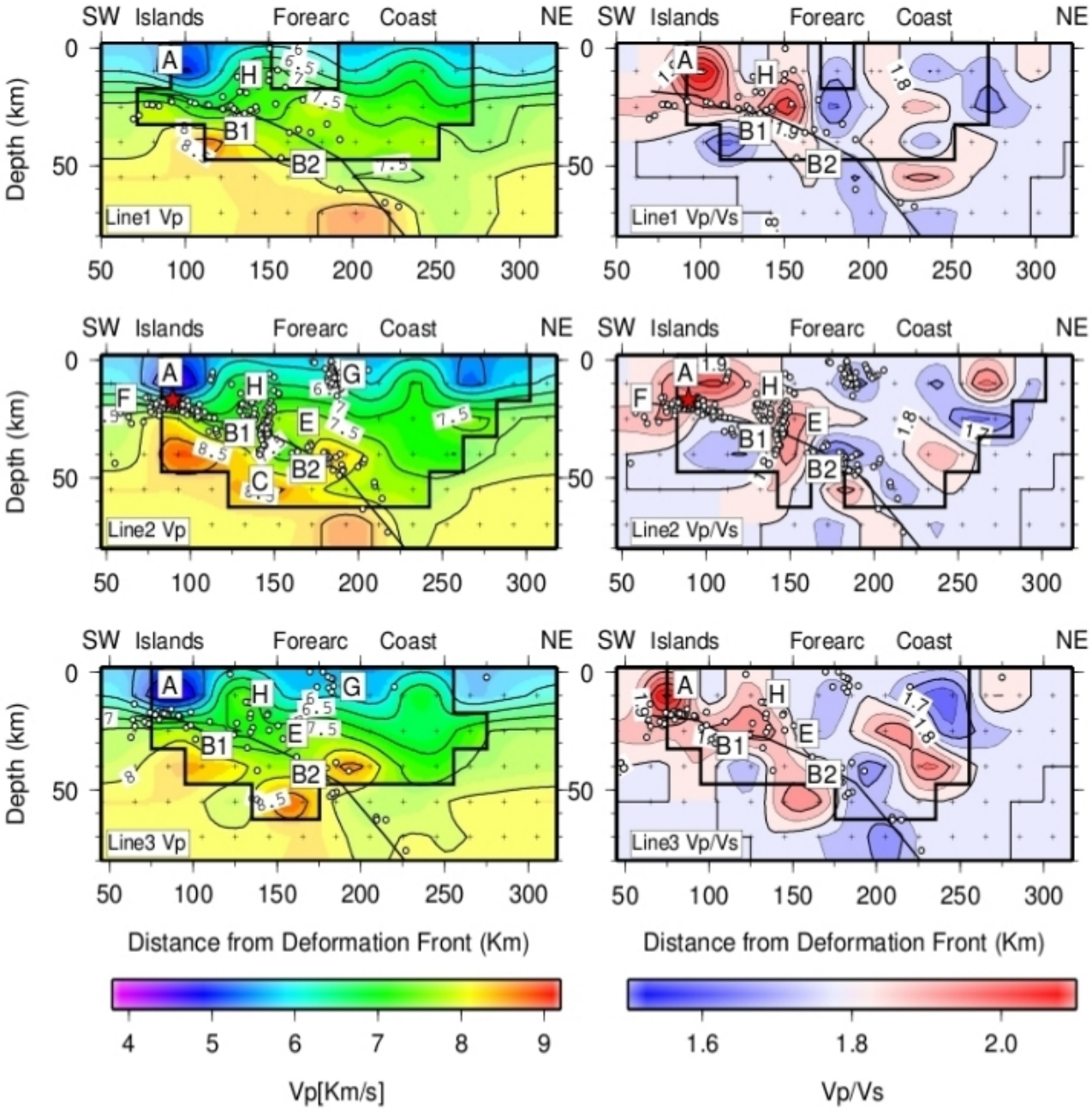

Figure 5.9: Cross sections along three SW to NE trending lines through the final three dimensional velocity model. See Figure 5.11 for location of cross sections. Left: Vp model. Right: Vp/Vs model. Regions which are well resolved are within the thick black line. Earthquakes within a 50 km wide corridor around each section which have at least 6 P and 4 S picks are represented by white circles. Grid nodes are indicated by crosses. The red star is the hypocentre M_w 7.2 of the 25 February 2008 event determined from our data. The inferred plate interface is shown by the black line. See Figure 5.8 and text for explanation of characters.

and seismogenic properties of the Mentawai segment of the Sumatra subduction zone.

5.8.1 Forearc Islands

Beneath the forearc islands (Figure 5.8, area A) low *Vp* of 4.5 km/s at shallow depths, increasing to 5.8 km/s at 15 km depth, and high *Vp/Vs* ratios of greater than 2.0 are observed. Amplitudes elevated by up to 10% in the restoring resolution test (Figure 5.7D) suggest that the true *Vp/Vs* may be slightly lower than the *Vp/Vs* obtained. However, even taking this into account, the *Vp/Vs* is significantly higher than the average *Vp/Vs* for the region (~1.80). The islands are imaged as a continuous region of low *Vp* and elevated *Vp/Vs* along the subduction zone in the 3D model (Figure 5.9, area A). No seismicity is present within this shallow region of the forearc. Kopp et al. (2001), based on wide-angle refraction data, observed similar *P* wave velocities down to a depth of 15 km (Figure A2.17), which they interpreted as sediments possibly metamorphosed near the basement. The low velocities, which are indicative of sediments, suggest that the islands were part of a former accretionary prism which has been uplifted (Kopp et al., 2001). This agrees with Hamilton's (1977) and Karig et al.'s (1979) conclusion that the forearc islands were formed from a large wedge of uplifted sediment. The high *Vp/Vs* ratios most likely indicate that the sediments contain free water within their pore spaces, which is expelled during compaction (Hyndman and Peacock, 2003). Similar *Vp/Vs* ratios above the subducting slab have previously been imaged in Chile and New Zealand (Eberhart-Phillips et al., 2005; Haberland et al., 2009) and were interpreted as fluid-saturated over-pressured sediments. In both studies the sediments are located at depths shallower than 20 km, above the subducting interface and within the frontal part of the forearc, similar to the location in this study.

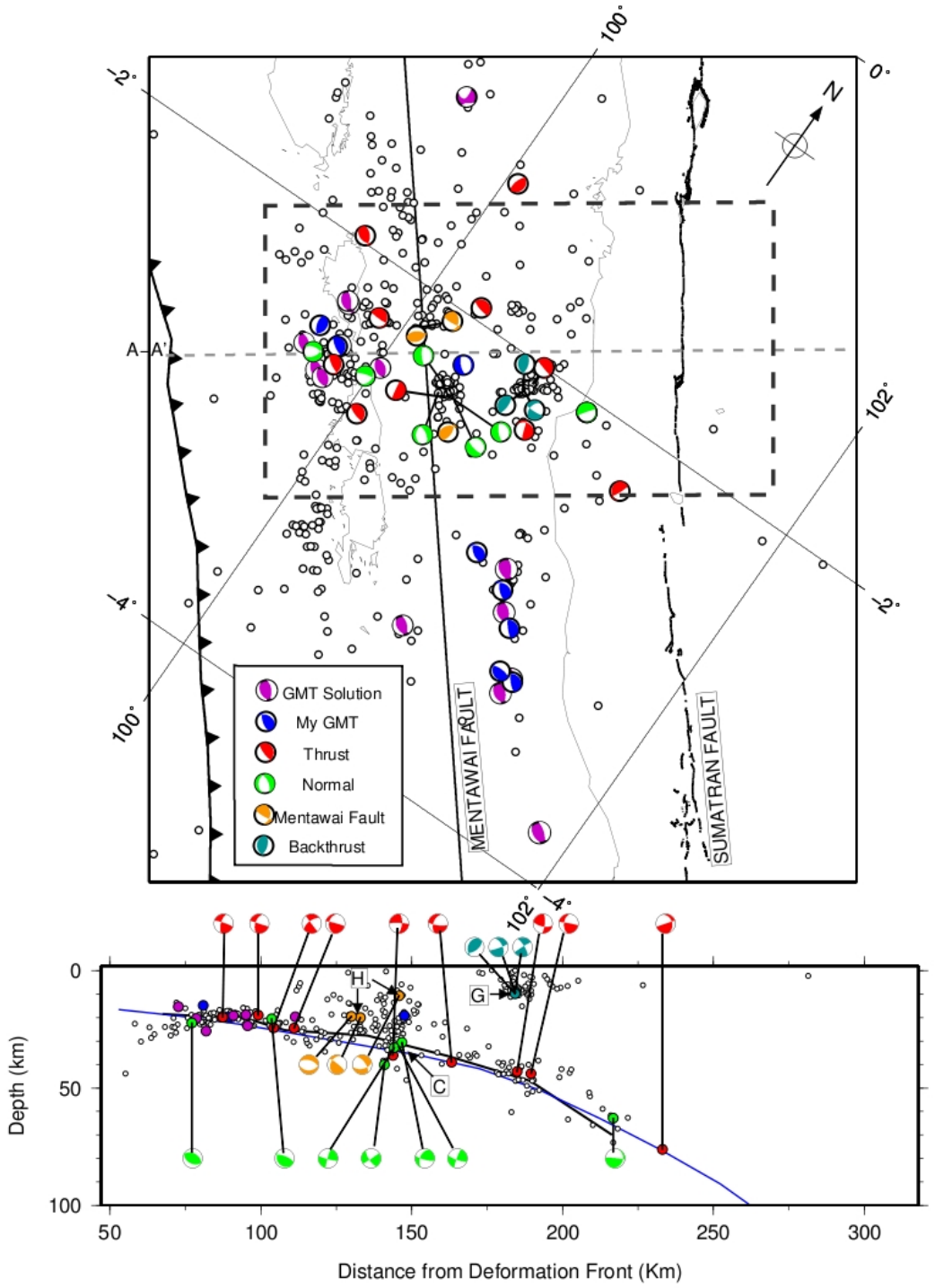

Figure 5.10: Focal Mechanisms of 32 events. See Table 5.1 for values. gCMT events are represented by purple and blue. All events from the gCMT catalogue are plotted at the locations obtained from this study. Blue are focal mechanisms for the gCMT events obtained in this study and purple are the gCMT focal mechanisms (no focal mechanisms based on our data were determined for these events). Green represents normal faults and red represents thrust events at the subduction interface and within the slab. Orange indicates events at the Mentawai Fault. Turquoise indicates events within the shallow cluster on the eastern side of the forearc basin. Top: Map view. Bottom: Cross section view in which all events within the centre of the network are projected on to line A-A' with focal mechanisms in cross section indicated. Black line is the plate interface position derived from our results. Blue line is the plate interface position from SLAB1.0 (Hayes and Wald, 2009). See Figure 5.8 and text for explanation of characters.

5.8.2 Subducting Oceanic Slab

The plate interface was inferred from the seismicity distribution (Figure 5.8 and 5.9) by calculating probability density functions (PDF) of the event depths at 0.05° (~5km) intervals along a profile perpendicular to the trench (line 2, Figure 5.11). Thus, at each location the depth which has the highest probability of an event occurring is found. An inclined plane is then drawn through the peak of the PDF at each location to determine the plate interface. The slab lies at 20 km depth below the forearc islands, dipping gently at ~13° to reach 30 km depth beneath the western side of the forearc basin. The increase in slab dip to ~35° at distances greater than 150 km from the deformation front results in the slab lying at 60 km depth below the Sumatra coast. Seismicity is most intense between ~15 and 25 km depth (75-110 km from the deformation front) but can be traced down to ~50 km depth (180 km from the deformation front) and is particularly visible along the central profile (Figure 5.9, line 2 area B1). Along the southern and northern profiles (Figure 5.9, line 1 and line 3, area B1) seismicity is mainly present on the shallow part of the plate interface (75 km to 110 km from the trench); at greater depth it is predominantly absent, with the exception of a small cluster of activity that is observed on line 3, 175 km from the trench (Figure 5.9). Along the central profile, a 10 km wide gap in seismicity along the subduction interface is observed beneath the forearc basin, 150-160 km from the trench (inset Figure 5.8). Adjacent to this gap in seismicity, ~140 km from the trench, a large cluster of activity extends for 10 km from the subduction interface into the slab (Figure 5.8, 5.9 and 5.10, area C). Mechanisms indicate that faulting is predominantly extensional within this cluster (green events and focal mechanisms (Figure 5.10)). Focal mechanisms for six events located on the plate interface (down to 50 km depth) indicate thrust faulting with the strike of the fault plane orientated approximately parallel to the strike of the trench (red focal mechanisms and events, Figure 5.10). At distances >180 km from the deformation front (Figure 5.8 and 5.9, area F and B2) seismicity is still present along the subduction interface in the central profile (Figure 5.9, line 2) but has significantly decreased. The sparse activity is dispersed within the slab or on the interface with focal mechanisms still indicating thrust faulting; however, the fault plane is no longer orientated parallel to the strike of the

trench (red focal mechanisms and events, Figure 5.10). Throughout the forearc the *Vp* velocity at the top of the slab (20 km depth), beneath the forearc islands, is ~7.0 to 7.2 km/s, increasing to 8.0 km/s at ~30 km depth which is indicative of the underlying mantle (Figure 5.8 and 5.9, area F to B1). Within this region, and continuing laterally until ~150 km from the deformation front, an increased *Vp/Vs* ratio of 1.75 to 1.90 is found (Figure 5.8 and 5.9, area F to B1). In the central and southern profiles (Figure 5.9, line 2 and line 3) the *Vp* at the top of the slab increases as distance from the deformation front increases, reaching 8 km/s at 50 km depth (Figure 5.8 and 5.9, area B2). In these two profiles (line 2 and line 3), at 45-55 km depth, velocities of ~ 8 km/s are also present above the Wadati-Benioff zone, possibly indicating the position of the continental mantle (Figure 5.8 and 5.9, area B2). Line 1 (Figure 5.9) however, does not show a significant increase in *Vp;* within the slab it remains between 7.5-8 km/s 180 km from the deformation front, and above the Wadati-Benioff zone velocities of 8 km/s are not present, suggesting that there may be a variation in the properties of the continental mantle and subducting slab along the arc.

P wave velocities of ~7.0 km/s for the subducting slab beneath the islands (Figure 5.8 and 5.9) agree with velocities obtained previously from a marine refraction survey in southern Sumatra (Figure 5.1 and A2.17, Kopp et al., 2001). Beneath the islands the region of increased *Vp/Vs* (1.75-1.90) within the slab can be explained by altered oceanic crust that contains hydrous minerals such as chlorite, serpentinite, amphibole and prehnite that form from hydrothermal circulation and metamorphism under high temperatures and low pressures (Peacock, 1990). Similar *Vp/Vs* ratios within the subducting oceanic crust have been observed at other subduction zones around the world and attributed to hydration of the slab (e.g Haberland et al., 2009; Shelly et al., 2006). Hydrated alkali basalts have also been found in the basement rock of a core from the Indo-Australian Plate a few hundred kilometres south of the study region at 9° 46.53' S 102° 41.95' E (Hekinian, 1974), implying that the plate is hydrated at the ridge.

The seismicity distribution indicates that the subducting slab lies at ~20 km depth beneath the forearc islands which is in agreement with Kopp et al. (2001) who observed

the slab at 19 km beneath the outer arc high and 21 km beneath the forearc basin (Figure A2.17). A significant proportion of the events beneath the Mentawai Islands are foreshocks and aftershocks of the M_w 7.2 event on 25 February 2008 (Figure 5.8, 5.9 and 5.11, area F).

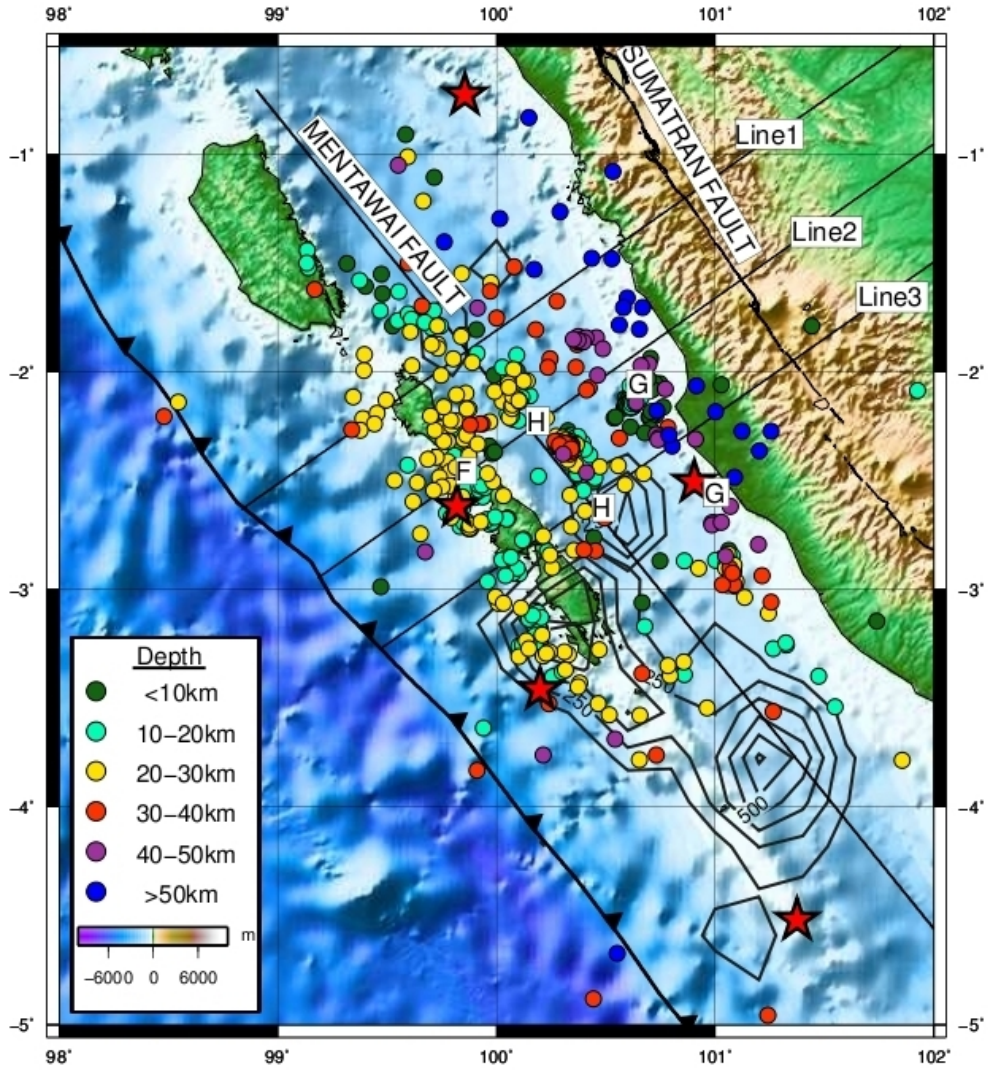

Figure 5.11: Final hypocentre location of 538 earthquakes that had 6 or more P picks and 4 or more S picks, located using the final 3D Vp and Vp/Vs model (Locations can be found in A3). The locations of the cross sections shown in Figure 5.9 are indicated. The locations of recent large earthquakes (NEIC catalogue) are indicated by red stars and the slip distributions for the 2007 earthquakes are indicated by the grey contours (Konca et al, 2008). See Figure 5.8 and text for explanation of characters.

The aftershock region is not only constrained to the plate interface, but extends into the oceanic crust. Focal mechanisms indicate thrust faulting along the plate interface while extensional faulting is observed within the oceanic crust (Figure 5.10). In northern Sumatra near Simeulue Island the aftershocks of the 2005 Nias and 2004 Aceh-Andaman earthquakes were found to be updip of the co-seismic rupture asperities but downdip of the afterslip (Hsu et al., 2006; Tilmann et al., 2010). A preliminary afterslip model indicates afterslip both updip and downdip of the rupture zone of the M_w 8.4 event (J.-P. Avouac, pers. comm, 2011). In our seismicity distribution we find a NW-SE trending group of aftershocks immediately updip of the peak slip region in the northern asperity of the first earthquake on the 12 September 2007 (M_w 8.4) (Figure 5.11). Updip of the second earthquake (M_W 7.9) even more intense aftershock activity is recorded. Despite this earthquake only rupturing the deeper part of the subduction zone, the aftershocks extend updip to a point, such that their seaward limit coincides approximately with the 1,000 m bathymetry contour, ~75 km from the deformation front. However, the majority of aftershocks, including the M_w 7.2 event on 25 February 2008, are found further along strike, NW of North Pagai Island, between the main co-seismic rupture asperities of the M_w 8.4 and M_w 7.9 events and the secondary (northwestern) asperity of the M_w 7.9 event, located at 2° S (Figure 5.11, area F). This region appears not to have ruptured during the two events but experiences a large proportion of the aftershocks we recorded in our network.

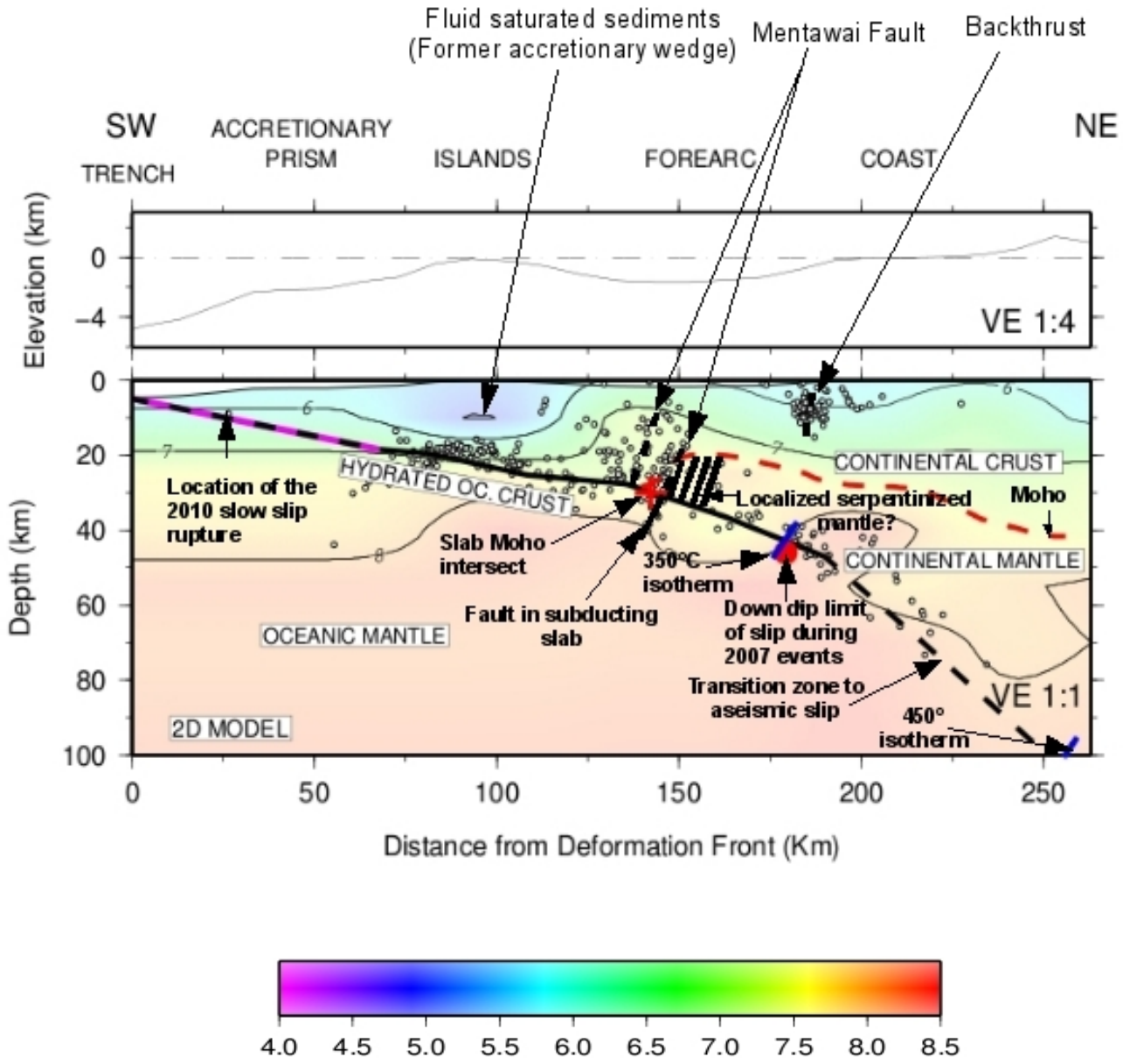

Figure 5.12: Cross section centred on 100.5°E, 2.0° S, running SW to NE, summarizing the main results of this study. The hypocentres of earthquakes used in this study are shown by white circles. The thick black line represents the seismogenic zone based on the hypocentre distribution and the dashed black line represents the transition zone between seismic slip to aseismic slip. The purple line beneath the dashed black line in the shallow region of the plate interface shows the rupture area of the earthquake on 25 October 2010.

The cluster of normal faulting within the subducting slab, 140 km from the trench (Figure 5.8 and 5.9, area C), may result from either dehydration reactions within the slab (e.g Meade and Jeanloz, 1991; Rietbrock and Waldhauser, 2004); faulting related to bending or unbending (Kawakatsu, 1986); downdip tensional stresses from slab pull (Lay et al., 1989) or the reactivation of old faults formed on the oceanic plate prior to subduction (e.g Savage, 1969; Ranero et al., 2003). A geophysical survey by Deplus et al. (1998) found active deformation within the eastern part of the Indian Oceanic Plate prior to its subduction at the trench. East of the Wharton Fossil Ridge (Figure 2.1), which is where our study area is located, long (greater than 1000 km) left lateral, north-south orientated strike-slip faults are reactivating fossil fracture zones. The 4 June 2000 M_w 7.9 Enggano earthquake (Figure 5.1) initiated as a N-S striking, left lateral strike-slip fault within the subducting plate, which was interpreted as a reactivated fracture zone (Abercrombie et al., 2003). The focal mechanisms from our events within the slab exhibit N W-SE-striking normal faulting (Figure 5.10, area C), which differs from the regional fabric inferred by Deplus et al. (1998), suggesting that they do not originate from the reactivation of transform faults. The strike direction of the events would be consistent with bending-related faulting but at this depth it is not clear whether the change in curvature of the slab would be sufficient to generate bending-related faulting. Therefore tensional stresses within the slab are the most likely scenario producing the observed normal faulting found within the slab.

5.8.3 Forearc Structure and Continental Crust

A cluster of activity is observed at the Mentawai Fault, extending from ~5 km depth to the subduction interface at ~25 km depth, within a ~25 km thick layer with *Vp* velocities of 6 km/s to 7.5 km/s (Figure 5.8, 5.9 and 5.11, area H). In the centre of the study area the cluster of activity can be split into two clusters whereas the surrounding segments show a more diffuse seismicity distribution (Figure 5.9, line 2, area H). Focal mechanisms from three events located at the Mentawai Fault indicate thrust faulting (Figure 5.10, orange events and focal mechanisms). However, the orientation of the fault planes is not consistent with the strike of the Mentawai Fault, varying from N-S to W-E.

This region coincides with a high *Vp/Vs* ratio of 1.8 to 1.9 and elevated *Vp* of 7.2 km/s at 15-20 km depth. The 25 km thick layer with *P* wave velocities of 6.0 km/s to 7.5 km/s continues beneath the forearc basin to mainland Sumatra, where it increases in thickness to 30 km (Figure 5.8, area D). On the eastern side of the forearc basin a large shallow cluster of activity is found at 5-15 km depth (Figure 5.8, 5.9 and 5.11, area G). The cluster of seismicity is prominent in the centre of the study region (Figure 5.9, line 2, area G, Figure 10).

P wave velocities of 6 km/s to about 7.5 km/s are indicative of continental crust which suggests that the crust is 25 km thick at the Mentawai Fault, increasing to 30 km thick beneath the mainland. The thickness of the continental crust beneath the forearc basin is similar to that observed by Klingelhoefer et al. (2010) in a refraction profile to the northwest of Simeulue Island, in northern Sumatra at a distance of 170 km from the trench. This indicates that the forearc basins along the whole length of Sumatra are underlain by continental crust, as was suggested previously for central Sumatra based on refraction profiles near Nias Island (Kieckhefer et al., 1980).

Despite the focal mechanisms determined within the overriding crust at the Mentawai Fault not being orientated parallel to the strike of the Mentawai Fault, the observed thrust faulting at the Mentawai Fault (Figure 5.10) would support Singh et al.'s (2009) conclusion that the Mentawai Fault consists of two backthrusts, a main backthrust and a frontal backthrust (Figure 5.12). The backthrust could act as a pathway for fluids released within the slab from dehydration reactions, and potentially expelled into the upper plate postseismically (Singh et al., 2011). Such a process could also explain the high *Vp/Vs* ratio (1.9 to 2.0) imaged in region H. Post seismic fluid release could play a role which is characterized by an increased *Vp/V*s ratio and has previously been inferred in the Antofagasta area of northern Chile following the 1995 M_w 8.0 Antofagasta earthquake by Husen et al. (2000) and Nippress and Rietbrock (2007).

On the eastern side of the forearc basin, within the continental crust, the hypocentres of the large shallow cluster of activity (Figure 5.8 and 5.9, area G) are located in a region

where no large scale linear faults like the Sumatran Fault and Mentawai Fault have been previously mapped. However, the existence of earthquakes, as well as the focal mechanisms, suggests the possible presence of an additional backthrust structure at this position, on the eastern edge of the forearc basin within the centre and southern part of our study region (Figure 5.12).

5.8.4 Continental Mantle

Landward of the Mentawai Fault (> 140 km from the deformation front), above the plate interface at ~25 km depth, the *Vp* velocity increases to 7.5-8 km/s and the *Vp/Vs* ratio remains above 1.8 (Figure 5.8 and 5.9, trenchward of area E). The *Vp/Vs* ratio decreases to values below 1.8, 165 km from the deformation front, while the *Vp* velocity remains between 7.5-8 km/s (Figure 5.8 and 5.9, landward of E). A significant increase in the *Vp* velocity to 8-8.20 km/s is observed along the central and southern profiles, above the plate interface, ~175 km from the deformation front (Figure 5.9, line 2 and 3). Within this region the *Vp/Vs* ratio remains between 1.7 and 1.8. However, line 1 does not show an increase in *Vp* and remains below 8 km/s with *Vp/Vs* ratios of 1.7 to 1.8 (Figure 5.9, line 1).

Previous gravity surveys and wide angle refraction surveys, within the rupture area of the 2004 and 2005 event have suggested that the continental Moho intersects the subducting slab at shallow depths of less than 30 km (Kieckhefer et al., 1980; Simoes et al., 2004; Dessa et al., 2009; and Klingelhoefer et al., 2010). This, as well as the preliminary results of receiver function studies on mainland Sumatra which suggest that the Moho lies at a depth of ~30 km, reaching 40 km depth below the active volcanic arc (MacPherson et al., 2010; Gunawan et al., 2011), lead us to interpret the 7.5 km/s contour as the Moho (Figure 5.8, 5.9 and 5.12). The 7.5 km/s contour intersects the subducting slab ~140 km from the deformation at ~25 km depth, thus implying a similar geometry of the Moho/plate-interface intersection in the study region as described for northern and central Sumatra (Figure 5.8, 5.9, trenchward of E and Figure 5.12). The presence of an average reduced seismic *Vp* of 7.70 km/s and high *Vp/Vs* > 1.85 at the toe

of the mantle wedge (Figure 5.8 and 5.9, trenchward of area E) implies that a very localized part of the mantle, adjacent to the subducting slab, may be hydrated from aqueous fluids (Hyndman and Peacock, 2003). A *Vp* of 7.70 km/s suggests an increase in serpentinite content of the mantle of up to 12%, corresponding to an increase of ~2% of the water content (Carlson and Miller, 2003).

In the 2D velocity model and also in lines 2 and 3 of the 3D model (Figure 5.8 and 5.9), beneath mainland Sumatra, 175-200 km from the trench and at ~ 40 km depth, below the inferred Moho, an area with *Vp* velocities typical of unaltered mantle (8.0-8.2 km/s) is found. The areas to the west and east, as well as the continental mantle of the northern profile (Figure 5.9, line 1), exhibit lower velocities (7.7 km/s) indicating possible localized mantle serpentinization. However, a *Vp/Vs* of less than 1.85 in these regions beneath the inferred Moho (7.5 km/s) (Figure 5.8 and 5.9, landward of area E) suggests that wide spread serpentinization of the continental mantle, which has been postulated at several subduction zones around the world including central Chile (Graeber and Asch, 1999), Cascadia (Zhao et al., 2001), Costa Rica (DeShon and Schwartz, 2004) and Japan (Seno et al., 2001), does not occur here. Our findings are more in agreement with recent studies in southern Chile in the nucleation area of the 1960 Chile event (Haberland et al., 2009), which also did not find widespread mantle serpentinization in the forearc.

5.8.5 Seismogenic Zone

At subduction zones the downdip limit of the locked fault zone is thought to correspond to either a thermal (Oleskevich et al., 1999) or a compositional control (Hyndman et al., 1997). If the plate interface does not reach temperatures of 350°C- 450°C before its intersection with the continental Moho, the downdip limit is thought to occur there due to the presence of aseismic hydrous minerals (serpentinite) in the overlying mantle that allow stable sliding. If the critical temperatures are reached before the Moho/subduction thrust intersection aseismic slip occurs due to the stable sliding of quartzo-feldspathic rocks. In the Mentawai segment based on the 7.5 km/s contour the subduction interface intersects the continental Moho ~140 km from the trench at a shallow depth of ~25 km

(Figure 5.12). The hypocentre of the M_w 7.9 event on the 12 September 2007 (Figure 5.1) and the slip models of both the M_w 8.4 and M_w 7.9 2007 events (Figure 5.2, 5.8, 5.11 and 5.12) as well as geodetic data indicate that the seismogenic zone extends beyond this point until at least ~185 km from the trench (Chlieh et al., 2008; Konca et al., 2008). This agrees with the seismicity distribution we obtain, as seismicity is present almost continuously along the subduction interface until ~50 km depth, 180 km from the trench (Figure 5.8, 5.9 and 5.12) but beyond this, it is diffuse and not observed beyond 225 km from the trench. Therefore, the Moho inferred from the velocity model is shallower than the observed downdip limit of the seismogenic zone (Figure 5.12), which contradicts the hypothesis that the continental Moho-slab interface intersection is the downdip limit, if the critical temperature is not already reached at shallower depths. This parallels the findings of Dessa et al. (2009) and Klingelhoefer et al. (2010) who suggest that the deeper part of the 2004 rupture also occurred on the interface between the forearc mantle and down-going plate. Seismogenic zone earthquakes which rupture the forearc mantle have also been observed in NE Japan where the rupture of a magnitude M_w 7.7 earthquake continued until 50 km depth in a region where the upper plate Moho is located at 20 km depth (Hino et al., 2000).

Hippchen and Hyndman (2008) produced thermal models for the Batu Islands, where the plate age is ~44 Ma, indicating that the 350°C to 450°C isotherms are reached 156 to 230 km from the trench, respectively. The plate age at the Mentawai segment is ~60 Ma (Sdrolias and Müller, 2006), which would move the thermal limits ~ 20 km landward to 176 and 250 km respectively (Hippchen and Hyndman, 2008, Figure 5.12) where the subducting slab is beneath the continental Moho. This indicates that the subducting plate is too cool to allow stable sliding of quartzo-feldspathic rocks (Blanpied et al., 1991, 1995) above the Moho/subduction thrust intersection. The inferred downdip limit for the seismogenic zone from our seismicity distribution and the slip models for the 2007 events lies between the 350°C and 450°C isotherms (Figure 5.12). This temperature is well below the temperature needed for ductile flow of mafic rocks and crust. A possible explanation for the downdip zone to be deeper than the Moho intersection is that the forearc mantle is not serpentinized. In this study we do not observe widespread

serpentinization but we do observe a small amount at the toe of the mantle wedge, adjacent to the subduction interface. A serpentinized toe of the mantle wedge has been observed off Fukushima, Japan, where the locked fault zone is thought to extend below the 20 km deep Moho (Miura et al., 2003). The region of localized serpentinization (Figure 5.8, 5.9, trenchward of area E and Figure 5.12) coincides with the gap in aftershock activity on the subduction interface (~150 km from the deformation front). Despite the absence of aftershock activity, this region of the interface did experience co-seismic slip during the M_w 8.4 and M_w 7.9 2007 events. It has previously been proposed by DeShon et al (2006) that in Costa Rica, where the mantle wedge is serpentinized, rupture during a large earthquake may not initiate along the subduction interface where there is serpentinization, but is still able to propagate along it. This may be similar to our findings for the Mentawai region, as the 2007 events ruptured along the region of partial serpentinization but due to the possible weaker coupling in this region, aftershocks are unable to initiate.

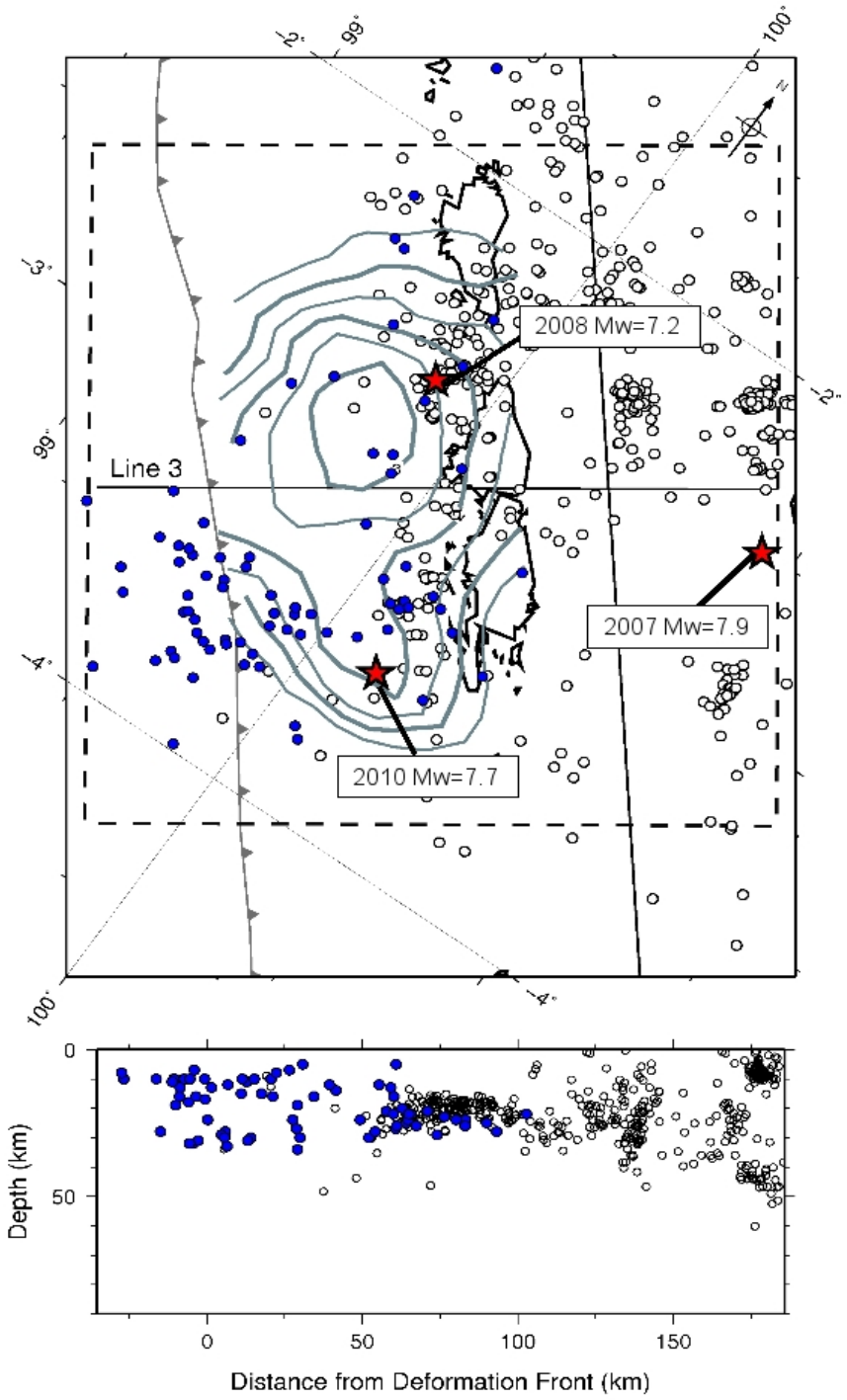

Figure 5.13: Aftershock distribution of the M_w 7.7 event on 25 October 2010. Top: Map view. The co-seismic slip distribution for the M_w 7.7 event is shown (Lay et al., 2011) (grey lines, the contour interval is 50cm). The red stars represent the epicenters of the M_w 7.7 event on the 25 October 2010, M_w 7.2 event on the 25 February 2008 and M_w 7.9 event on 12 September 2007. Blue circles represent the aftershock locations of the M_w 7.7 event from GEOFON and the white circles are the location of the aftershocks following the 2007 events (this study). Cross section: Trench-perpendicular cross section (line 3 in Figure 5.2). The majority of these aftershocks are constrained by depth phases (although seafloor topography is not taken into account in the localization procedure).

5.8.6. Implications for Mentawai Tsunami Earthquake of October 25 2010

Within the study region but two years after completion of our deployment, the M_w 7.7 Mentawai earthquake occurred on 25 October 2010 to the southwest of South Pagai Island. This event nucleated within a known aftershock cluster along the plate interface (southernmost red star in Figure 5.13) and propagated to the northwest and updip, probably all the way to the trench into a zone that was nearly aseismic during our temporary experiment: only a handful of events were located there and the depths of all but one of them, though poorly constrained, indicate hypocentres well within the down-going plate (Figure 5.13, cross section). Approximately 10 minutes after the origin time, a tsunami with runups in excess of 7 m hit the shores of North Pagai Island and South Pagai Island (Satake et al., 2011). The full rupture duration of this event was ~115 s with peak moment rates lasting for about 60 s, long for an event of this magnitude. Furthermore, the event was characterized by an unusually slow rupture velocity of 1.2-1.5 km/s (Newman et al., 2011; Lay et al., 2011). The aftershocks of this event map out an area of ~55 km in width and 95 km along strike. Aftershocks occur within the pre-existing cluster just seaward of North Pagai Island and South Pagai Island, but also along the whole width of the rupture as well as near and seaward of the trench.

The long rupture duration, low excitation of higher frequencies and the tsunami, disproportionately large for the given magnitude, marks this event out as a tsunami earthquake as defined by Kanamori (1972). As moment M_0 is related to slip d and area A via $M_0=\mu Ad$, it is necessary to know the shear modulus μ when estimating the slip from seismic data. The main rupture area lies outside the resolvable region of our tomographic model but extrapolating the *Vp/Vs* ratio and *Vp* found to the southwest of the forearc islands and considering *Vp* velocities within the accretionary wedge and decollement reported for the Kopp et al. (2001) refraction line (Figure 5.1), we estimate μ~15-25 GPa. The higher bound assumes that the plate interface does not sample the lowest velocities in the accretionary wedge, justified by the observation that the interface seismicity at 75 km distance to the trench occurs where *Vp* is approximately 6 km/s, not within the region of the lowest forearc velocities. The lower bound assumes the

properties within the accretionary wedge; this estimate is more consistent with the very low rupture velocity, if we consider that rupture velocities are usually 70-80% of *Vs* (Shearer, 1999). Using μ=25 GPa and the aftershock area and moment, we obtain an average of slip of ~5 m. Alternatively, scaling the USGS finite-fault solution to correct for the lower value of μ (15 GPa) we obtain a peak slip of 7 m and average slip of ~3.50 m. These slip estimates are a little higher than the models from Lay et al. (2011, peak slips 2-4 m) but lower than the preferred model of Newman et al. (2011, peak slip 9.60 m). No observations from the SuGaR GPS station on North Pagai Island have yet been published but the slip and rupture area as described above are approximately consistent with the trenchward horizontal motion (~50 cm) and minor subsidence (<5 cm) inferred from integration of a strong-motion record on the southwest coast of North Pagai Island (Muzli et al., 2011). The peak slip of the Mentawai event thus seems comparable to that of the M_w 8.4 great megathrust earthquake in 2007 (Konca et al., 2008).

To first order, the Mentawai event seems to follow the model of Bilek and Lay (2002) which proposes that rupture initiates within a frictionally unstable part of the plate interface and then ruptures in the updip direction into the conditionally stable zone where no rupture can nucleate, but can rupture when perturbed externally. However, some of the aftershocks landward of the trench occur at depths shallow enough to have occurred on the plate interface (Figure 5.13, cross section). If so, then at least small patches of the plate interface exhibit frictionally unstable behaviour all the way to the trench.

Nearly all previous tsunami earthquakes have occurred at erosive margins (Bilek, 2010). The Sumatran margin is classed as accretionary (Clift and Vannucchi, 2004; Kopp et al., 2008) but locally features of frontal erosion can be identified, such as re-entrants related to seamount subduction (Kopp et al. 2008). The unusual case of a tsunami earthquake rupturing directly updip of a megathrust rupture, and with comparable peak and average slip values, raises the question whether the margin usually breaks in this mode (which might additionally include separate rupture of the downdip end as occurred in the form of the second event (M_w 7.9) on 12 September 2007), or whether great megathrust

earthquakes more commonly break the whole width from the trench to the downdip end of the seismogenic zone. No definitive answer is possible but we note that the updip ends of the megathrust ruptures and aftershock series of both the Nias and Bengkulu earthquakes appear to be correlated with forearc morphology as predicted by dynamic Coulomb wedge theory (i.e the slope break marks the transition between velocity strengthening behaviour up-dip of it and velocity weakening behaviour down-dip of it, Wang and Hu, 2006), suggesting that at least the boundary between the great earthquake rupture and the tsunami earthquake is not specific to the current sequence but a long-standing feature of the margin. A historical event in north Sumatra in 1907 has recently been shown to have occurred within the shallow part of the Simeulue-Nias segment (Kanamori et al., 2010), notably within an area that has also experienced significant afterslip after the 2005 megathrust earthquake (Hsu et al., 2006). Therefore, the separate rupture of a conditionally stable shallow plate interface in tsunami earthquakes and a deep frictionally unstable part in great megathrust earthquakes is not unprecedented, and the potential for tsunami earthquakes, either following a great megathrust rupture or in the interseismic period, probably exists for a large part of the Sunda Margin, and by implication in other subduction zones worldwide. Alternatively, these regions may rupture in one go, which in the Padang region has the potential to create a M_w 8.5 earthquake (assuming an average slip value of 10m).

5.9 Conclusions

Using local seismic data from a temporary seismic network we have imaged the structure of the subduction zone within the Mentawai region by inverting for 2D and 3D velocity models and accurately relocating aftershocks following the 12 September 2007 M_w 8.4 earthquake. Our main findings are as follows:

- The forearc islands are underlain by high *Vp/Vs* material, probably fluid saturated sediments which were part of a former accretionary prism.

- Clustered seismic activity is found for distances of ~75-180 km from the trench and

to a depth of ~50 km, but sparse activity associated with the slab can be traced down to depths of 100 km. However, no significant local seismicity is located below the downdip end of the M_w 8.4 Bengkulu earthquake on 12 September 2007.

•Beneath the Mentawai Islands the plate interface lies at ~20 km depth. Further landward at ~30 km depth we found a cluster of normal faulting events below the plate interface, which are thought to initiate from tensional stresses within the slab.

•The continental Moho is less than 30 km deep at the point of intersection with the subduction thrust. Lower *P* wave velocities of around 7.5 to 7.7 km/s and high *Vp/Vs* ratios of 1.8 to 1.9 in the toe of the mantle wedge indicate a modest degree of mantle serpentinization. In spite of this, the downdip limit of the seismogenic zone is not the intersection of the megathrust with the continental Moho. Instead, it lies deeper and is attributed to a change in the physical properties of the plate interface. At the subduction interface, adjacent to the region of modest serpentinization, there are no aftershocks despite this region rupturing during the 2007 events, suggesting that there is weaker coupling in this area.

•Two clusters of activity are found within the ~25 to 30 km thick overriding crust. The location of the first cluster confirms that the Mentawai Fault is active and may act as a path way for fluid migration. Focal mechanisms suggest that the Mentawai Fault may accommodate backthrust movement. The second cluster on the eastern side of the forearc basin exhibits thrust motion and could be interpreted as a second backthrust, assuming a fault is aligned with the NE dipping seismicity cluster.

•The M_w 7.7 Mentawai earthquake on 25 October 2010 initiated at the southeastern limit of the aftershock region of the 2007 events. It propagated northwest and updip, all the way to the trench, in a zone that was nearly aseismic during the temporary seismic experiment two years before. The peak slip of the event is comparable to the M_w 8.4 megathrust event in 2007. Shallow aftershocks of the 2010 event suggest that patches of frictionally unstable behaviour can occur all the way to the trench.

- The co-seismic slip of the 2007 events, as well as the aftershock distribution, allows us to conclude that the downdip limit of rupture propagation is ~175-200 km from the trench, while the 2010 event and its aftershocks have shown that the updip limit of the seismogenic zone is defined by the trench. Although in the 2007-2010 sequence of aftershocks in south Sumatra the shallow part of the interface has ruptured separately, a 200 km wide rupture could potentially take place along the interface and therefore should be taken into consideration when determining hazard models for this region. Based on these findings a reevaluation of the seismic and tsunami hazard for other subduction zones, where the updip limit is thought to be far from the trench, is necessary.

5.10 Acknowledgments

The project was funded by NERC (NE/D002575/1 and NE/F012209/1). We thank the SeisUK facility in Leicester for the provision of the 6TD instruments and Liverpool University for providing the broadband instruments. We also thank the Earth Observatory Singapore for funding part of the fieldwork and letting us co-occupy sites of the SuGAr GPS array. We acknowledge the support of colleagues at Geotek-LIPI and the whole field crew which made this possible. We gratefully acknowledge the cooperation of many Sumatran landowners for allowing us to install the seismic stations on their property. Furthermore we thank the captain and crew of the Andalas and the field crews for their excellent work under difficult conditions.

Chapter 6

Anisotropy

At subduction zones many geodynamic questions still remain unanswered, including the pattern of flow within the mantle wedge and beneath the slab. An important tool in understanding the style and geometry of deformation occurring within a subduction zone is the measurement of seismic anisotropy through observations of shear wave splitting (SWS).

This chapter different methods for SWS analysis are explained and evaluated. Following this, an overview of anisotropy including the causes and results obtained from previous studies at subduction zones around the world, is presented.

6.1 Seismic Anisotropy

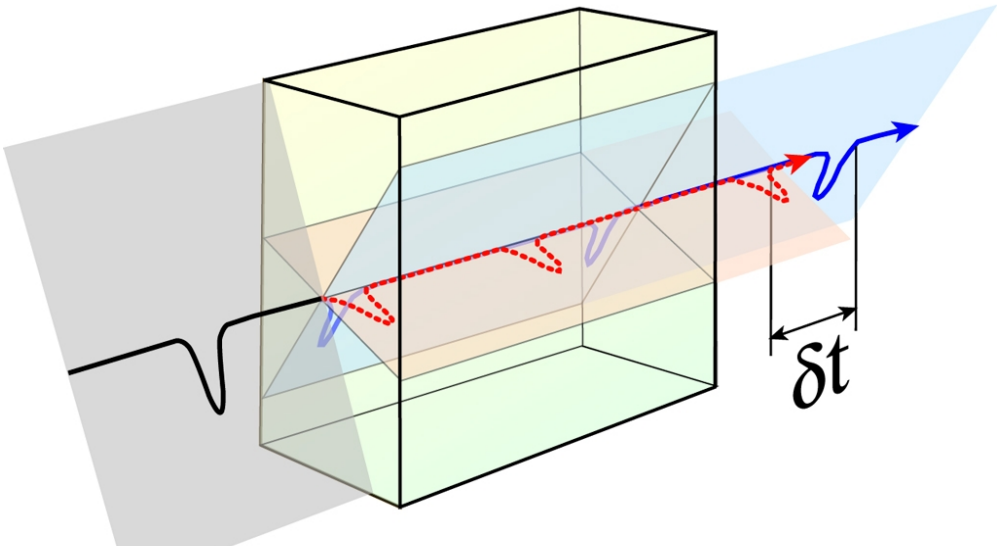

Figure 6.1: SWS. When a shear wave travels through an anisotropic medium it is split into two waves, qS_1 and qS_2, that are separated by a delay time and have polarizations parallel and perpendicular to the fast direction. The orientation of the fast shear wave (blue) and the delay time between the fast and slow wave are measured by seismologists. Figure courtesy of Ed Garnero (http://garnero.asu.edu/research_images).

Anisotropy is the dependence of seismic velocity on direction which can be measured in *P, S* and surface waves. When a shear wave propagates through an anisotropic medium it is split into two independent waves that have polarizations perpendicular to each other and that travel at different velocities (Figure 6.1, Savage, 1999). The component that is polarized parallel to the direction of fast seismic velocity travels faster than the orthogonal component, causing SWS. Two parameters are measured, the orientation of the fast shear wave (Φ) and the delay time between the two arrivals (δt). The fast direction corresponds with the anisotropic symmetry axis and the time lag between the two arrivals provides information on the magnitude of anisotropy. Seismic anisotropy is often reported as the percentage difference between the velocities corresponding to the fast and slow orientations.

$$Anisotropy\,(\%) = 100\,((V_{max} - V_{min})/V_{average}) \qquad (6.1)$$

A variety of seismic phases are suitable to determine anisotropy, depending on which region of the subduction zone is under study. Core phases, e.g. *SKS, SKKS* and *PKS*, sample the sub-slab mantle, slab, mantle wedge and overriding plate (Figure 6.2), while local *S* phases only sample the slab, mantle wedge and overriding plate.

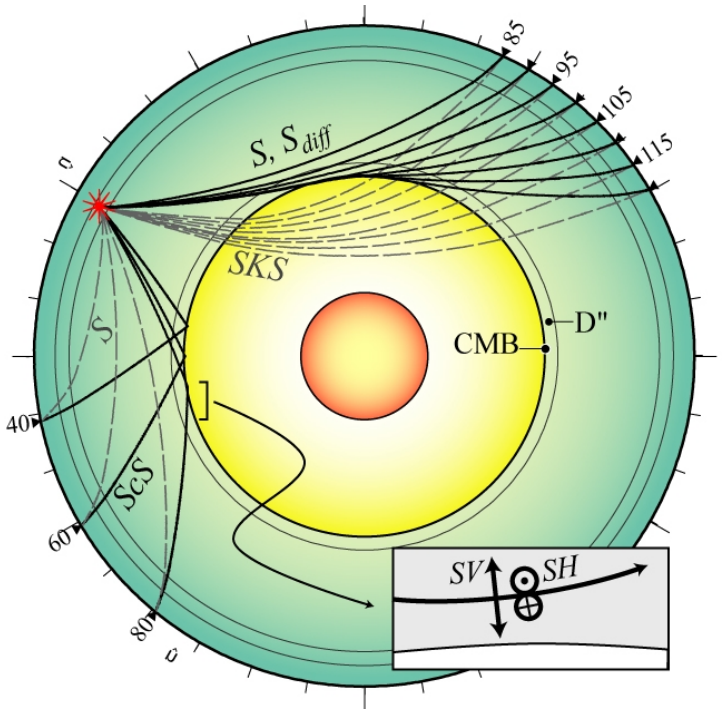

Figure 6.2: The most commonly used phases to study sub-slab mantle anisotropy. Figure courtesy of Ed Garnero (http://garnero.asu.edu/research_images)

6.2 Shear Wave Splitting Analysis

Two techniques have been developed for estimating the splitting parameters Φ and δt. The first type is a multi-event technique which utilizes simultaneously a set of records from different azimuths (e.g. Vinnik et al., 1989; Chevrot, 2000), while the second type determines the splitting parameters on a per event basis (Bowman and Ando, 1987; Silver and Chan, 1991). In this study splitting parameters will be determined for teleseismic (*SKS*) phases and local *S* phases using the per event technique. In this method a grid search is performed to determine the splitting parameters which best remove the effect of the splitting. Different methods for the 'best removal' exist and are discussed in the following section.

6.2.1 Minimum Energy Method

The most popular method of SWS analysis is to determine the minimum energy on the transverse component (Silver and Chan, 1991). This method is based on the principle that in the absence of anisotropy the shear wave is linearly polarized but when it passes through an anisotropic medium significant energy is produced on the transverse component. This means it can only be applied to phases such as *SKS* and *SKKS* phases, as it is assumed the initial wave has linear particle motion, has not undergone splitting due to anisotropy, and is polarized in the ray plane. In this technique a grid search is performed over all possible values of Φ and δt, the horizontal components are rotated and time shifted appropriately and the amount of the energy on the transverse component is measured. The best fitting parameters correspond to the Φ and δt values that minimize the energy on the transverse component, and therefore remove the effect of anisotropy.

$$E_{trans} = \int_{\alpha}^{\alpha} \tilde{U}_T^2(t)\,dt \quad (6.2)$$

where U_T is the displacement on the transverse component with respect to time t.

6.2.2 Eigenvalue method

A slight variation on the energy minimizing method is the eigenvalue method (Silver and

Chan, 1991). Instead of of minimizing the energy on the transverse component, the horizontal seismograms are corrected for a range of possible lag times and fast directions, and the eigenvalues of the covariance matrix are calculated. The best fitting Φ and δt correspond to the pair of values that result in the smallest second eigenvalue of the covariance matrix, These parameters linearize the ellipticity of the particle motion the best. In contrast to the energy minimizing method, the eigenvalue method is able to be used when the source polarization is unknown, as it does not assume the rays are polarized in the ray path plane. Therefore it can be used for local *S* phases.

6.2.3 Rotation Correlation Method

This method used in studies by Fukao (1984), Bowman and Ando (1987) and others, assumes that after a shear wave propagates through an anisotropic medium it is split into orthogonally polarized fast and slow components with identical pulse shapes. A grid search is performed to identify the best fitting parameters by rotating and time shifting the horizontal components. As the fast and slow components are assumed to have identical pulse shapes this method seeks to maximize the cross correlation between the corrected horizontal components. This technique can be visualized as searching for the splitting parameters that maximize the similarities in the pulse shapes of the two corrected seismogram components.

6.2.4 Comparing the Different Methods

The three methods described above have been tested on *SKS* and *SKKS* waveforms by Vecsey et al. (2008) to determine which method performs best. The authors concluded that the minimum energy method appears to be robust, regardless of the level of noise, the shape of the signal and the ellipticity of the particle motion. In seismograms with a signal to noise ratio of less than 6:1, the rotation correlation method was found to obtain a stable but false minimum which can deviate by up to 45° from the fast axis. Similarly, cycle skipping was found to occur when using the eigenvalue method for seismograms with a signal to noise ratio of 3:1 or less, resulting in very large δt . However, the

minimum energy method does have the disadvantage of only being able to be used for shear waves polarized in the ray path plane (i.e. core mantle refracted waves), whereas the rotation correlation and eigenvalue method can be used for shear waves that are polarized out of the ray path plane and therefore can be used for local *S* phases.

These methods have also been tested in regions of simple and complex anisotropy (Long and Van der Hilst, 2005). When a single layer of anisotropy is present with a horizontal axis of symmetry and no lateral heterogeneity, all measurements should yield usable measurements which agree inside the error bars. However, in regions of complex anisotropy, which is a more realistic situation, the different techniques often disagree, with the minimum energy method seeming to be more affected (Long and Van der Hilst, 2005).

The different splitting techniques also perform differently when the source polarization (equivalent to backazimuth for *SKS* events) is close to the fast or slow direction (null direction, see Section 6.2.6). When back azimuths are sufficiently far away from the fast or slow direction the rotation correlation and minimum energy method both give correct values. However when the backazimuth is near the null direction the value of δt in the rotation correlation method dramatically reduces and the Φ exhibit deviations of +/- ~45° (Wüstefeld and Bokelmann, 2007). In contrast, the measurements obtained using the minimum energy method are quite stable until the backazimuth is very close to the null direction, in which case the fast axis will deviate by +/- ~90° and the delay times will often reach the maximum search value (Wüstefeld and Bokelmann, 2007).

It is evident from the above discussion that each of the methods has pros and cons and in practice a combination of methods should be implemented to increase the confidence that each individual measurement is robust and no questionable measurements have been included.

6.2.5 Time Window

An important part of SWS analysis is the selection of an appropriate time window (Vecsey et al., 2008). Usually the start time is not as important as the end time because only noise should be present before the phase. However, when selecting the end time you have to balance the need to have a sufficient length of the signal analysed and not analyzing a signal contaminated by other phases. Consequently, in manual selection, determining the length of a time window must be done very carefully and as the result should also be stable over several different sized shear wave windows, it is very time-consuming. To improve time efficiency and to estimate error bounds, automated SWS analysis has been developed (Teanby et al., 2004). This enables Φ and δt to be calculated for a range of windows within an initially manually selected range, and then the optimum Φ and δt values are found using cluster analysis (Teanby et al., 2004). The resulting Φ and δt are not necessarily the results that produce the smallest error bars but are the results that are stable over various size analysis windows.

6.2.6 Null Measurements

A shear wave which has not been split is often referred to as a null measurement. Null measurements obtained, despite the wave propagating through anisotropic medium, do not constrain the delay times, and the spol (source polarization) corresponds to either the actual fast or slow axis (e.g. Savage, 1999). In contrast, the estimated fast axis from null measurements of waves which have passed through an isotropic medium simply reflects the source polarization, which for *SKS* phases equals the backazimuth (e.g. Savage, 199). Typically null measurements are identified visually by using criteria such as little or no energy on the uncorrected transverse components and particle motion that is linear before correction. However, more recently, a numerical criterion has been developed for the identification of null measurements in teleseismic phases (Wüstefeld and Bokelmann, 2007). This method uses the difference in fast direction and ratio in delay time of the splitting measurements obtained from the rotation correlation and the minimum energy method. These two techniques have different characteristics when close to the null direction (Section 6.2.4), which can be used to detect null, near null and non null measurements. A teleseismic measurement can be classed as null if the ratio of

delay time from the two techniques is between 0-0.2 and the difference in fast axis estimates between the two different techniques is between 37° and 53° (Wüstefeld and Bokelmann, 2007).

6.2.7 Shear Wave Splitting Techniques Employed in this Study

For local SWS analysis, SHEBA (Teanby et al., 2004), which is based on the eigenvalue methodology of Silver and Chan (1991), will be used. SHEBA is chosen as the eigenvalue technique is able to be used when the source polarization is unknown, which is the case for local *S* waves. For teleseismic phases, both SHEBA (Teanby et al., 2004) and SplitLab (Wüstefeld et al., 2008) will be used. The advantage of using SplitLab for SWS analysis is that Φ and δt estimates are determined using three independent methods: eigenvalue (Silver and Chan, 1991), rotation correlation (Bowman and Ando, 1987) and minimum energy (Silver and Chan, 1991). SplitLab is able to be implemented for teleseismic phases as the ray is polarized in the ray plane, so the spol is known, as it is the backazimuth. Only shear wave measurements that produce similar Φ and δt estimates in all techniques (difference in $\Phi < 20°$ and $\delta t < 0.3$) will be used in this study, as this will indicate a stable and reliable result.

6.3 Causes of Seismic Anisotropy

Seismic anisotropy usually results from either the lattice preferred orientation (LPO) of mantle minerals (Figure 6.3) or shape preferred orientation (SPO) of cracks/fractures or melt in either the crust or mantle.

6.3.1 Lattice Preferred Orientation (LPO)

It is widely accepted that seismic anisotropy generated in the upper mantle is dominated by LPO of the most abundant mineral olivine, which has a significant single-crystal shear wave anisotropy of 18 % (Mainprice, 2007). The minerals are initially orientated randomly but deformation leads to a preferred orientation of the mineral, under certain

temperature and pressure conditions.

The main mechanism for the development of LPO is dislocation slip (Nicolas and Christensen, 1987). Dislocation slip occurs at high stress levels or when large grain sizes are present (usually until 200-300 km depth); the motion of crystalline dislocation within the grains causes preferred mineral alignment (i.e. LPO) and therefore, anisotropy (e.g. Savage, 1999; Karato and Wu, 1993). In the upper mantle there is also a second mechanism for deformation, diffusion creep (Karato and Wu, 1993). However, diffusion creep occurs at low stresses and small grain sizes and is the solid state diffusion between grain boundaries or across crystal lattices, which results in no mineral alignment and hence an isotropic medium.

LPO measured in naturally deformed peridotite rocks (Christensen, 1984; Nicolas and Christensen, 1987) and in samples deformed in the laboratory (Zhang and Karato, 1995) suggest that the fast axis of olivine (a-axis) tends to align with the maximum shear direction or mantle flow direction (Babuska and Cara, 1991; Mainprice et al., 2000; Mainprice, 2007), producing A-type olivine fabric. These experimental observations and the fact that SWS fast polarization directions are shown to align with relative plate motion (e.g. Hall et al., 2000) allow seismologists to gain direct information about dynamic processes, such as mantle flow.

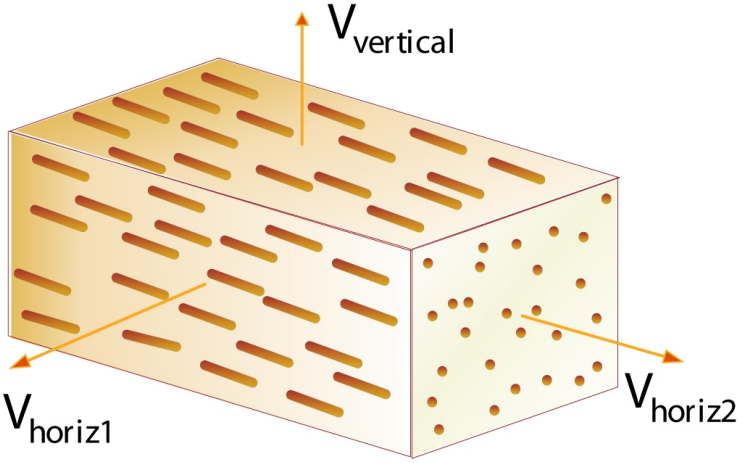

Figure 6.3: The LPO of olivine. Figure courtesy of Ed Garnero.

However, over the last decade, a series of experiments (Jung and Karato, 2001; Katayama et al., 2004; Jung et al., 2006; and Katayama and Karato, 2006) have shown that the orientation of the fast axis of olivine does not always align with the maximum shear direction, but is dependent upon stress, temperature, pressure and water content. So there are now in fact 5 different types of olivine LPO and fast axes: the original A-type plus B-, C-, D-, and E-types.

An increase in temperature and pressure only has a small affect on the shear wave velocity but significantly affects the preferred orientation. At higher temperatures, diffusion and grain boundary mobility enhances the preferred orientation. Below 900°C, the critical temperature, the grains are not easily reorientated and the anisotropy is frozen (e.g Savage, 1999). Partial melt can reduce anisotropy by promoting the transition from dislocation creep to diffusion creep, which prevents the formation of a preferred mineral orientation (Kendall, 1994). However, aligned partial melt can also enhance the degree of anisotropy (e.g Savage, 1999).

The presence of water affects the type of olivine fabric that forms. At high differential stresses, hydrous conditions, and at temperatures of 1470 K, B-type olivine fabric develops with the a-axis orthogonal to the shear direction, not parallel to the shear direction like in A-type olivine fabric (Jung and Karato, 2001); this results in the fast direction of the shear wave being orientated perpendicular to the direction of mantle flow. At the Ryukyu subduction zone, the addition of water creates B-type olivine fabric with the fast axis aligned perpendicular to the flow direction (Long and van der Hilst, 2006). Lassak et al. (2006) modeled a synthetic seismic profile over a subduction zone and found that at the boundary between anhydrous and hydrous mantle a rotation in Φ from trench-normal to trench-parallel occurs within 75 km of where the transition occurs.

6.3.2 Shape Preferred Orientation (SPO)

SPO occurs when orientated cracks in the crust, faults, fractures, melt filled inclusions,

compositional layering or lenses within the mantle make an otherwise homogeneous medium anisotropic for wavelengths larger than the space interval of the structure (Backus, 1962). The SPO results in the fast axis being polarized along the strike of the cracks, faults, etc. Within the different layers of the earth, SPO is caused by different sources. In the lower crust, SPO is mainly due to fluid-filled cracks (Crampin and Lovell, 1991; Crampin, 1994) while in the mantle SPO is predominantly caused by melt-filled cracks or lenses or compositional lamellae (Mainprice, 1997; Kendall, 1994; Kendall, 2000; Vauchez et al., 2000; Walker et al., 2004).

6.3.3 Anisotropy within the Earth

Seismic anisotropy has been observed in many regions of the Earth's interior, including the crust, upper mantle and the transition zone (e.g Savage, 1999, Long and Silver, 2009). As deformation in the Earth leads to anisotropy through SPO and LPO (Section 6.3.1 and 6.3.2), the characterization and interpretation of anisotropy within these different layers allows us to obtain direct constraints on the dynamic processes occurring.

6.3.3.1 Lithosphere

All phases that are used for shear wave splitting (e.g. local S, S, SKS) travel through the crust. However, in order to identify the crustal component of anisotropy it is helpful to obtain SWS measurements from shallow events as the splitting caused by the crust is in general small (0.04-0.2 s, Long and Silver, 2009) and is therefore usually masked by the splitting from anisotropic layers deeper within the Earth. Crustal anisotropy in the overriding plate at subduction zones is caused by cracks and micro-cracks in the upper 10-15 km of the crust, which results in the fast direction being aligned with the direction of maximum stress (Crampin, 1994). However, in active fault zone regions, where the cracks that have developed parallel to the maximum stress contain fluids at high pore pressures, a 90° flip in the fast polarization direction is observed (Zatsepin and Crampin, 1997; Crampin et al., 2002). Beneath 10 - 15 km depth, where the pressure is 200-300

MPa, anisotropy is usually no longer present due to the closure of cracks (Savage, 1999). If anisotropy is present, it is attributed to other factors, such as minerals aligned during ductile flow. Anisotropy in regions which contain large structural features, e.g strike slip faults, has also been suggested to develop from preferential mineral alignment and orientated cracks and fractures (Kaneshima, 1990; Gledhill and Stuart, 1996; Savage, 1999).

At subduction zones, anisotropy can also be found within the subducting slab which is sampled by core phases (e.g. *SKS*) and partially by local *S* phases. Anisotropy can occur from the preferred orientation of highly anisotropic hydrous minerals formed along steeply dipping faults and the large scale vertical layering of dry and hydrated crust-oceanic mantle sections, whose spacing is several times smaller than the teleseismic wavelength (Faccenda et al., 2008). It has also been suggested that brittle crack damage, caused by dehydration reactions in the subducting slab, can induce intra-slab anisotropy (Healy et al., 2009). In addition to these two mechanisms, fossilized anisotropy could occur in the down-going subducting slab. As oceanic lithosphere is formed and moves over the asthenosphere it accumulates a large anisotropic signature (e.g. at the East Pacific Rise Wolfe and Solomon, 1998; Harmon et al., 2004) in the direction of plate motion. This anisotropic structure is then frozen into the lithosphere, and may remain present in the subducted slab. However, it is unclear what portion of the slab is capable of retaining this fossilized deformation - the whole slab or just the centre core that is a sufficient distance away from the edges that are being deformed as the slab subducts.

6.3.3.2 Upper Mantle Asthenosphere

The upper mantle is composed of three anisotropic and volumetrically important phases, olivine, orthopyroxene and clinopyroxene. When flow occurs due to simple shear, the a-axis of the predominant mineral olivine aligns parallel to the direction of flow (Mainprice et al., 2000). As the fast direction of the *S* wave and the orientation of the a-axis are the same, the flow direction of the mantle can be inferred (Park and Levin, 2002; Silver and Chan, 1991).

Core phases (e.g. *SKS*, *SKKS* and *PKS*) are popular phases to study the upper mantle as the phase's polarization is controlled by the *P* to *S* conversion at the core mantle boundary (CMB), which means the observed splitting is due to anisotropic structure on the receiver side and the phase propagates nearly vertically through the upper mantle, ensuring that the incidence angle is well within the shear wave window (phases with incidence angles larger than ~35° at the surface are distorted by post-critical *S* to *P* reflections (Evans, 1984; Booth and Crampin,1985)). In addition to the core phases, other shear phases (e.g. direct *S*, converted phases such as *P660s* and reflected phases such as *SS* and *sS*) are useful for identifying anisotropy. At subduction zones, the splitting of local direct *S* phases originating within the subducting slab is effective in characterizing the anisotropy within the mantle wedge.

In a subduction zone setting, the subducting slab experiences two components of motion, longitudinal (downdip) and retrograde (roll back or advance) (Buttles and Olson, 1998). Purely downdip motion results in the olivine a-axis aligning perpendicular to the trench. Above the slab, in the mantle wedge, corner flow is produced, while beneath the slab, entrained flow is occurring, producing a 2D flow (Long and Silver, 2008). Retrograde motion (i.e. trench migration) causes trench-parallel flow and consequently trench-parallel fast directions, which is the dominant fast direction observed for teleseismic phases at subduction zones (Long and Silver, 2008). Long and Silver (2008) attribute these trench-parallel SWS observations to trench migration with a model where the slab is decoupled from the subslab mantle, causing the primary influence on mantle flow to be from slab motion normal to the slab surface, which could move the slab towards or away from the overriding plate, despite the plates converging (Figure 6.4). The resulting induced flow is three dimensional with a trench-parallel component. A barrier to sub-slab flow (possibly at the top or base of the transition zone) as well as a distant horizontal barrier will force lateral flow in the trench-parallel direction (Russo and Silver, 1994). As the retrograde motion increases, the splitting time increases due to fast moving trenches setting up a more coherent, larger scale return flow beneath the slab, creating a larger region of lattice preferred orientation. The migration of the trench could also be

responsible for trench-parallel splitting observations seen within the mantle wedge, since as in the subslab case, it creates a 3D flow field. However, within the mantle wedge a 2D corner flow is also induced by the viscous coupling between the subducting slab and overlying continental mantle (Ribe, 1989). The relative importance of these two flow fields is controlled by the relative magnitudes of trench migration and convergence (Long and Silver, 2008). If the flow field is dominated by 2D corner flow, the anisotropy is trench-perpendicular whereas if trench migration is rapid compared to down-dip motion, the wedge is dominated by trench-parallel flow. For subduction zones where the rate of migration and convergence are similar, the two flows are competing and the resulting flow field is less coherent which prevents a strong LPO from developing and δt is small (Long and Silver, 2008). 3D flow in the supra mantle can also develop when the geometry of the slab changes due to variable slab dip, curved trench or oblique subduction (Kneller and van Keken, 2008).

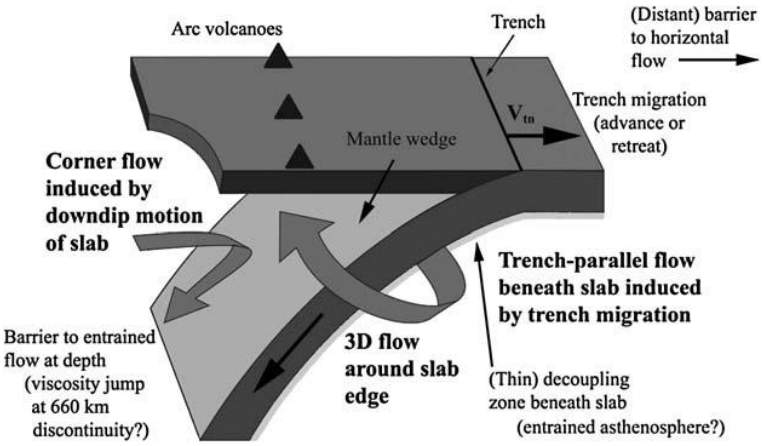

Figure 6.4: The model of Long and Silver (2008) showing the dominance of 3D flow beneath the slab and the competing influence of 2D and 3D flow fields in the mantle wedge. Figure from Long and Silver (2008).

Within the wedge, trench-parallel fast directions may also be evident due to the development of B-type olivine fabric when water is present, despite 2D corner flow still dominating (see Section 6.3.1, Jung and Karato, 2001), and melt filled cracks and networks beneath localized regions of melting (Kneller and van Keken, 2008).

6.3.3.3 Transition Zone and Lower Mantle

A number of shear phases (*SKS* and *SKKS*) can be used to investigate the transition zone and lower mantle, in addition to the upper mantle. Evidence for anisotropy in this region can be found from discrepancies in the splitting measurements between *SKS* and *SKKS* phases, since these two phases have very similar raypaths within the upper mantle and their paths only diverge in the lower mantle. Globally, studies of differential *SKS* and *SKKS* splitting have demonstrated that in 95 % of cases the measured splitting parameters for *SKS* and *SKKS* agree (Niu and Perez, 2004), suggesting little anisotropy exists in the transition zone and lower mantle. This is because 410 km depth is a major seismic discontinuity which marks the phase transition from olivine to wadsleyite. At this point anisotropy becomes weaker with depth due to the increase in isotropic phases such as garnet, majorite and ringwoodite in the transition zone (Mainprice et al., 2000). A few studies however have found evidence of anisotropy beneath the upper mantle e.g. Iidaka and Niu, (1998); Wookey et al., (2002); Niu and Perez (2004); Restivo and Helffrich (2006); and Long and Silver (2009). Weak anisotropy, observed between 600-1000 km depth at subduction zones, has been attributed to the subducting slab encountering viscosity at the top of the 660 km discontinuity. This impedes the movement of the slab and consequently produces large stresses in the top of the lower mantle, causing mineral alignment and anisotropy (Nippress et al., 2004).

6.3.4 Observations of Anisotropy within Subduction Zones

Since the early observations of SWS (Ando et al., 1983; Fukao, 1984), subduction zones have been among the most popular targets for SWS studies. An astonishing diversity in SWS patterns (e.g. Greve et al., 2008; Hammond et al., 2010; Long and van der Hilst, 2005b) have been identified in different regions from local *S* phases and teleseismic phases such as *SKS*, including both trench-parallel and trench-perpendicular fast polarization directions (with some oblique directions as well) and widely variable delay time values (Figure 6.5 and Table 6.1). In fact, it is common for SWS observations to vary along a single subduction zone. This variation in SWS observations highlights the complex structure of subduction zones, with contributions to splitting coming from

various parts of the subducting system: the sub-slab mantle, the subducting slab, the mantle wedge and the overlying continental crust. The following section summarises the SWS observations from subduction zones around the world.

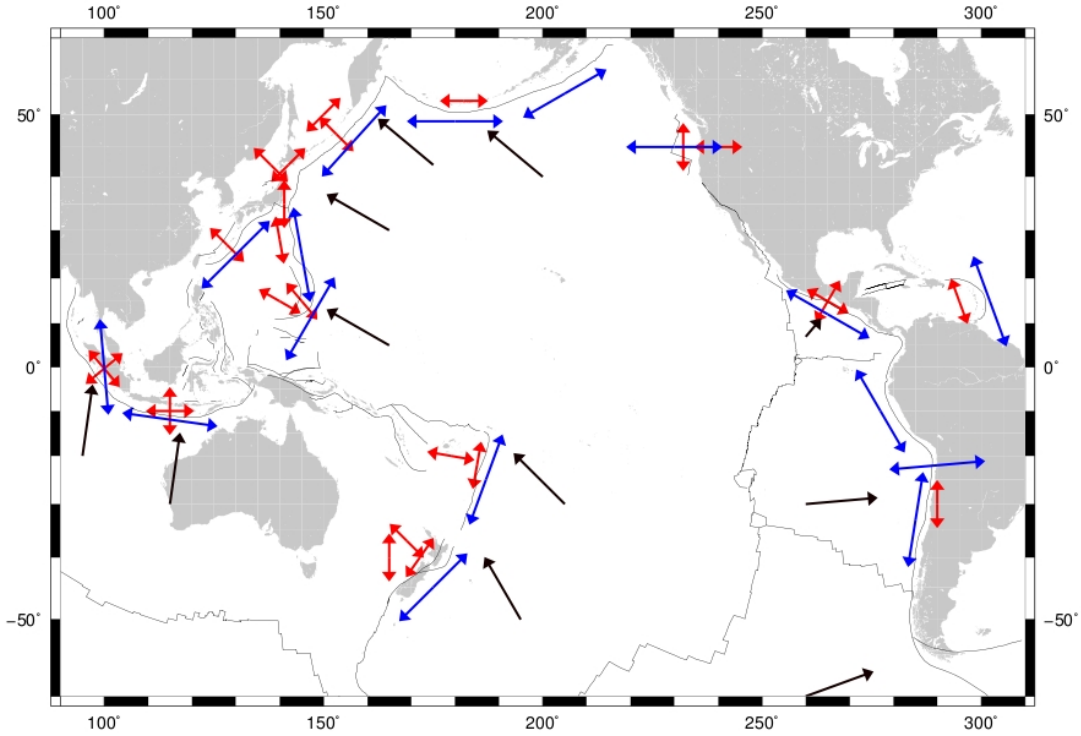

Figure 6.5: Map showing the variability in SWS measurements at subduction zones around the world. Blue represents sub-slab splitting measurements from core phases while red corresponds to splitting measurements from local phases due to anisotropy in the top of the subducting slab, mantle wedge and crust. Black arrows represent the direction of plate motion. Measurements after Long and Silver (2009). See Table 6.1.

6.3.4.1 Tonga

At the Tonga trench and within the backarc there is a complex pattern of SWS from local *S* events. Adjacent to the deformation front, trench-parallel directions are observed, which then rotate to trench-oblique, parallel to the subduction direction, at the Fiji platform. A similar pattern of splitting has been observed when analyzing SWS from *SKS* phases. The trench-parallel directions are attributed to along-arc mantle flow within

the mantle wedge, which is a result of slab rollback and an along-strike component of plate motion, while the trench-perpendicular fast directions observed at the Fiji Platform are due to subduction-induced backarc mantle flow (Fischer and Wiens, 1996; Fischer et al., 1998; Smith et al., 2001). *SKS* splitting measurements from the backarc sample much more of the mantle wedge than the sub-slab mantle, therefore only *SKS* measurements from the forearc can provide information on the amount and type of splitting occurring beneath the slab. Long and Silver (2008) propose that the sub-slab splitting has a trench-parallel fast direction with a delay time of 1.7 s +/- 0.7 s, corresponding to an anisotropic layer over a hundred km thick. .

6.3.4.2 New Zealand

Across North Island, near the Hikurangi subduction zone the observed SWS observations are not consistent. At the trench, teleseismic splitting measurements exhibit a trench-parallel fast direction with delay times of ~2.5 s (Greve et al., 2008). These observations have been contributed to trench-parallel mantle flow beneath the subducted slab, with a possible contribution of 0.5 s from trench-parallel fossil anisotropy within the subducting slab itself and 0.3 s from crustal anisotropy. Local SWS results agree with this, exhibiting trench-parallel fast directions with a max δt of 0.35 s (Morley et al., 2006). At the central volcanic zone (CVZ) the teleseismic results still indicate a trench-parallel fast direction but the delay time increases to 4.5 s (Greve et al., 2008). Analysis of the Fresnel zones suggests that the extra component of anisotropy is located within the mantle wedge. In contrast local *S* waves show a 90° rotation in fast direction from trench-parallel east of North Island to trench-perpendicular at the CVZ (Audoine et al., 2004; Morley et al., 2006). This was initially interpreted as trench-normal mantle flow within the upper mantle but is now believed to be a result of aligned melt bands which allow both trench-parallel and trench-perpendicular fast directions (Greve et al., 2008). On the western side of the CVZ the delay time from teleseismic splitting decreases, with no apparent splitting found within the backarc, on the western side of North Island, suggesting that mantle wedge dynamics terminate beneath the western side of the CVZ. This apparent isotropic region is possibly thought to be a result of local small-scale

mantle convection or vertical mantle flow resulting from the detachment of the lithosphere (Greve et al., 2008). Local SWS observations in the backarc suggest N-S fast polarization directions with delay times of ~0.22 s, which were attributed to a viscous blanket of material which is entrained by the motion of the Australian Plate (Morley et al., 2006), but the magnitude of the splitting is small enough to be accommodated in the crust (Greve et al., 2008).

6.3.4.3 Ryukyu

At the Ryukyu trench, trench-parallel fast directions are observed for teleseismic phases and generally also for local phases, with similar delay times of 0.25 - 2 s (Long and van der Hilst, 2005b; 2006). There is a larger variation in the local *S* observations in the high frequency band as 53 % of the results are within 20° of the trench direction compared to 66 % in the low frequency band. The similar magnitude of splitting and polarization directions for both local and teleseismic results suggest that the ray paths sample the same source of anisotropy. This is thought to be within the mantle wedge, within a 60-100 km thick layer with 10 % anisotropy, due to B-type olivine fabric (Long and van der Hilst, 2005b; 2006; Long et al., 2007). However, work by Kneller et al. (2008b) found that despite B-type olivine fabric within the forearc mantle explaining the local SWS, it is unable to explain the large magnitude teleseismic trench-parallel splitting measurements that sample the shallow tip of the forearc mantle. To account for this, additional crustal anisotropy or highly anisotropic material, such as foliated antigorite serpentinite within the cold tip of the forearc mantle, is required.

6.3.4.4 Japan

Within the forearc of the Marianas subduction zone the observed fast directions, based on local *S* observations, are oblique to the apparent plate motion with varying splitting times (Fouch and Fischer, 1998). Neither the slab-entrained flow model or fossil anisotropy can explain the observed directions. Instead they are thought to result from a combination of both. Within the backarc the splitting becomes parallel to apparent plate

motion due to slab-entrained flow (Fouch and Fischer, 1998). *SKS* splitting measurements from Wookey et al. (2005) indicate trench-parallel fast directions, with splitting times ranging from 0.5 to 1.0 s.

Splitting results from both local *S* and *sS* phases within the Izu-Bonin subduction system can be divided into two regions. In the south, NNW to SSE splitting is observed, with delay times becoming smaller further north, implying that anisotropy is weaker or becoming more complex (Anglin and Fouch, 2005). The anisotropy observed suggests a combination of convergence-parallel flow, trench-parallel shear along the boundary and inherent slab fabric. In the north, fast directions rotate to NNE -SSW, indicating that mantle flow is diverted behind the oceanward side of the Phillippine Sea Plate, south of the Phillippine-Eurasian Trench (Anglin and Fouch, 2005).

In central Japan both ScS phases and local *S* phases exhibit similar fast directions and similar delay times (Iidaka and Obara, 1995). On the west coast, N-S fast directions with large delay times are observed due to magma-filled cracks within the mantle wedge and not due to the alignment of olivine from convective flow (Iidaka and Obara, 1995). At the south coast, E-W fast directions with smaller delay times are found due to a shallow region of anisotropy which is a result of local deformation in the crust and shallower parts of the mantle (Iidaka and Obara, 1995).

Within NE Japan, observed fast directions from intermediate depth earthquakes show a clear separation between trench-normal direction in the backarc to trench-parallel in the forearc. Additionally, delay times within the backarc are slightly larger (~0.05s) than those in the forearc (Okada et al., 1995; Nakajima and Hasegawa, 2004; Nakajima et al., 2006; Huang et al., 2011). In the backarc, the trench-normal fast directions from the slab earthquakes are different to the trench-parallel fast directions recorded from shallow earthquakes (Huang et al., 2011). This suggests that there is anisotropy within the mantle wedge due to corner flow . However, the maximum delay time for the slab interface earthquakes is 0.3 s while for the shallow earthquakes it is 0.16 s, implying that only ~0.14 s of splitting is produced in the mantle wedge. The small amount of splitting

observed in the wedge may be a result of an isotropic or weak anisotropic zone in the middle of the mantle wedge. In contrast, within the forearc the observed fast directions for slab and crustal earthquakes both show dominant trench-parallel directions, with the maximum delay times for crustal earthquakes accounting for up to 80 % of the delay times recorded for the slab interface earthquakes (Huang et al., 2011). This suggests that within the forearc a large proportion of splitting is located within the crust. The remaining delay time of 0.1s is thought to be a result of either fossil anisotropy within the Pacific Plate or LPO of crystals and cracks in the upper part of the subducting slab. Both mechanisms are capable of producing trench-parallel fast directions and therefore contribute to observed splitting within the forearc (Huang et al., 2011). However, prior to the study by Huang et al. (2011) the rotation in fast direction was attributed to anisotropy within the mantle wedge. The trench-parallel fast directions, observed in the forearc, were thought to be a result of B-type olivine fabric and anisotropy within the slab (Nakajima et al., 2006).

6.3.4.5 Kamchatka

At the Kamchatka peninsula, *SKS* measurements exhibit trench-parallel fast directions above the Wadati Benioff Zone which then rotate to trench-perpendicular at the slab edges (Peyton et al., 2001). This has been interpreted as trench-parallel flow beneath the subducting slab with lateral flow around the slab through an opening created by the termination of subduction in the NW Pacific (Peyton et al., 2001). In contrast, local SWS parameters with delay times of 0.2 -0.6 s indicate a very complex spatial pattern of anisotropy which broadly implies a rotation in fast direction from trench-normal near the trench to trench-parallel within the backarc (Levin et al., 2004), opposite to the trend observed in NE Japan and Tonga (Fischer and Wiens, 1996; Fischer et al., 1998; Smith et al., 2001; Huang et al., 2011). The results were interpreted as 2D corner flow within the mantle wedge, which reaches no further inland than the volcanic arc (Levin et al., 2004).

6.3.4.6 Aleutian Islands

At the Aleutian-Alaska subduction zone, where the Pacific Plate subducts beneath North America, fast directions are approximately parallel to the volcanic arc, with splitting times of 0.1 s to 0.35 s, increasing with source depth due to anisotropy within the mantle wedge (Yang et al., 1995). The observed splitting is attributed to ~1 % SV anisotropy that results from the LPO of olivine by arc-normal shortening, which is accompanied by shearing or extension in the vertical or arc-parallel direction (Yang et al., 1995). SWS measurements by Long and Silver (2008) at three permanent stations, located 100 km above the wedge, yielded similar delay times (0.5 s to 1.0 s) and fast directions (trench-parallel) for both local and *SKS* SWS. This indicates that the sub-slab contribution to the observed splitting at the Aleutian subduction zone is very small, in the order of 0 -0.3s (Long and Silver, 2008).

6.3.4.7 Cascadia

Within the forearc of the active Cascadia subduction zone in the NW of the United States, local *S* and *SKS* waves exhibit different fast directions. *SKS* measurements from Currie et al. (2004) and Bostock and Cassidy (1995) are trench-normal with delay times of 1.0 to 1.5 s. This observed splitting is due to motion of the subducting Juan de Fuca Plate causing the LPO of olivine in the mantle below the subducting slab. Currie et al. (2004) assume most of the anisotropy is below the slab, with only a small contribution of splitting from the mantle wedge, as their observations are based on measurements close to the trench and therefore the raypaths mainly sample the sub-slab region. A study of local SWS in the forearc by Cassidy and Bostock (1996) found trench-parallel fast directions with delay times of up to 0.32 s for the deepest events. As the deepest events in the local study are located at 60 km depth, the ray paths do not sample very much of the mantle wedge and the anisotropy is attributed to the alignment of melt-filled cracks within the crust. In the backarc, the *SKS* fast directions remain trench-normal but further west, beneath the North American Craton SWS results exhibit significant variation, with a 90° periodicity. The observations were modeled as two layers of anisotropy, an upper 140 km layer, possibly reflecting fossil anisotropy, with a N-S fast direction and delay times of 1.4 s, and a lower 200 km layer with E - W fast directions and delay times of

2.0 s, produced by current mantle deformation (Currie et al., 2004). At the northern end of the subduction zone, above the Explorer Plate, the fast directions rotate northerly due to a change in mantle deformation and a transition from subduction to along-margin transform motion (Currie et al., 2004).

6.3.4.8 Caribbean

Pinero-Felicangeli and Kendall (2008) constrain SWS at the margins of the Caribbean Plate, which is sandwiched between the North America, South America, Cocos, and Nazca Plates, resulting in it being surrounded by a number of major shear zones and collisional belts. Teleseismic phases reveal fast directions which are parallel to the plate boundary and large delay times of 1.2 s - 2.1 s, with larger-magnitude splitting observed at the Caribbean-South America collisional front. Local *S* phases from up to 200 km event depth are trench-parallel and indicate a small amount of splitting of 0.1 - 0.3 s. The trench-parallel direction for the local SWS could be attributed to B-type olivine or aligned melt within the upper mantle wedge, but there is little depth dependency and the small magnitude of the splitting suggests that the anisotropy is within the crust (Pinero-Felicangeli and Kendall, 2008). The small magnitude of local SWS also implies that the majority of splitting seen in the *SKS* measurements is accrued beneath the top of the slab, from possible sub-slab flow, which is a result of slab rollback, or a change in the stress field generated by variation in the morphology or dip of the slab. The increase in delay time of *SKS* phases at the Caribbean-South American boundary is also observed by Russo et al. (1996) and Growdon et al. (2009) and has been associated with the South America Plate overriding its own detached slab at the eastern South American-Caribbean boundary causing extreme foliation and linearizion of the olivine.

6.3.4.9 Central America

Local SWS results exhibit both arc-parallel and arc-perpendicular directions in the forearc, arc and backarc, with the alteration in fast direction occurring over very short distances, less than 5 km (Abt et al., 2006; Abt et al., 2009). In order to account for the

range in anisotropy direction, a 3D model of crystallographic orientation was obtained for the mantle wedge. The best-fitting model indicates arc parallel flow down to at least 125 km depth beneath the backarc and arc, which may be a product of either toroidal flow around the edge of the slab in southern Costa Rica, slab rollback, along-strike components of plate motion or a combined effect of them all (Hoernle et al., 2008; Abt et al., 2009). *SKS* measurements consistently indicate trench-parallel fast directions with large delay times of up to 2.5 s, attributed to arc parallel flow beneath the slab or the deep backarc (Abt et al., 2006). The large splitting times for the *SKS* phases compared to the local *S* phases suggests that there is ~1.0-1.7 s of splitting beneath the subducting plate (Long and Silver, 2009).

6.3.4.10 South America

Along the Andean subduction zone, splitting from teleseismic phases indicate that fast directions are predominately trench-parallel due to the mantle flowing parallel around the northern and southern limits of the Nazca Plate. Localized areas of trench-normal direction have been recorded along the subduction zone and are believed to be due to the abrupt change in slab dip or a tear within the slab (Russo and Silver., 1994; Polet et al., 2000; Anderson et al., 2004). In contrast, teleseismic measurements by Bock at al. (1998) found fast directions that are predominately parallel to the absolute plate motion direction of the Nazca Plate (80°N). Only a 100 km wide area to the west of the active volcanic zone exhibited fast directions approximately parallel to the strike of the trench. These results were interpreted as mantle flow in the direction of apparent plate motion but when the flow encounters a steeply dipping part of the slab, west of the flat slab region, it is diverted to trench-parallel and remains in this direction over flat parts of the slab (Bock et al., 1998). Above the slab, fast directions are predominately N-S towards the coast, with delay times that increase with source depth, up to 0.3 s (Polet et al., 2000). The crustal component is calculated to be 0.1-0.15 s (Bock et al., 1998; Polet et al., 2000), with the remaining contribution coming from the mantle wedge due to east-west shortening of the South American Plate associated with the formation and evolution of the Andes (Polet et al., 2000). Moving further inland, the fast direction above the slab

alters from N-S with short delay times to E-W with bigger associated delay times. This is due to the transition between actively deforming Andean mantle in the west and a more stable and cooler Brazilian Craton in the east.

6.3.4.11 Sumatra and Java

A previous study by Hammond et al. (2010), using both local and *SKS* SWS observations beneath Sumatra and Java concluded that there are two main regions of anisotropy. The first is within the 40 km over-riding plate with horizontal, trench-parallel deformation. The second region is fossilized anisotropy within the subducting slab, producing N-S fast directions beneath Sumatra and E-W fast directions beneath Java. In addition to these two anisotropic layers, SWS observations within the forearc also suggest that a sub-slab layer of anisotropy may be present, producing trench-perpendicular fast directions for rays that traverse long distances within this region. The results of Hammond et al. (2010) imply that the mantle wedge is isotropic due to either 2D corner flow being of a similar magnitude to lateral flow from trench migration or that neither flow is strong enough for the development of a coherent LPO pattern.

Subduction Area	Local SWS	Teleseismic SWS	Reason For Observation	Source
Tonga	Forearc: Trench-parallel Backarc: Parallel to absolute plate motion	Φ: Forearc: Trench-parallel Backarc: Parallel to absolute plate motion	Local splitting at forearc is a result of slab rollback and an along strike component of plate motion. Backarc: Local splitting attributed to large scale deformation of mantle driven by coupling to overlying and subducting plates. Sub wedge splitting contributed to 1.7s of splitting.	Fischer and Wiens (1996) Fischer et al., (1998) Smith et al., (2001) Long and Silver (2008)
Hikurangi subduction Zone (New Zealand)	Forearc: Φ: Trench-parallel δt: 0.35 s CVZ: Φ: Trench-perpendicular Backarc:Φ: N-S, parallel apparent plate motion δt: 0.27 s	Forearc: Φ: Trench-parallel δt: 2.5 s CVZ: Φ: Trench-parallel δt: 4.5 s Backarc:Φ: No apparent splitting	Local *S*: Forearc: Crustal anisotropy. CVZ: trench-normal mantle flow in upper mantle or aligned melt band. Backarc: crust or flow aligned with plate motion *SKS*: Forearc: Trench-parallel flow beneath subducted slab with a possible contribution of trench-parallel fossil anisotropy within the slab. CVZ: Added contribution from aligned melt in mantle Backarc:local small scale mantle convections/vertical mantle flow	Audoine et al., (2004) Greve et al., (2008) Morley et al., (2006)
Sumatra/Java	Φ: Sumatra -Trench-	Φ: Sumatra - Oblique to	Local *S*: Splitting	Hammond et al.,

	parallel Java-Trench-parallel (shallow + deep earthquakes) and trench-perpendicular (intermediate depth earthquakes). δt : 0.1-0.4 s	the trench at mainland and trench-perpendicular at islands. Java - E-W δt : 0.8-2.0 s	within the overriding lithosphere. Mantle wedge is isotropic. *SKS*: Fossil anisotropy within the down going slab.	(2010) Long and Silver (2008)
Mariana	Forearc: Oblique to apparent plate motion. Backarc: Parallel to apparent plate motion.	Φ: Trench-parallel δt : 0.5-1.0 s	Observed anisotropy above slab is due to a combination of slab entrained model and fossil anisotropy.	Fouch and Fischer (1998) Wookey et al., (2005)
Izu-Bonin	S: NNW- SSE N: Rotate N-S to NE-SW	Φ: *SKS* Trench-parallel but back azimuthal variation sS: Similar to local *S*	Local *S* south: Combination of convergence parallel flow, trench-parallel shear and inherent slab fabric. Local *S* north: Mantle flow diverted.	Wirth and long (2010) Anglin and Fouch (2005)
Ryukyu	Φ: Trench-parallel δt :0.25 s - 2.0 s	Φ: Trench-parallel δt : :0.25 s - 1.2 s	Little splitting (0.2 s) below the slab. Splitting within the deep mantle forearc due to B-type olivine developing in 2D corner flow with additional splitting in cold tip forearc from crustal anisotropy of highly anisotropic foliated antigorite serpentinite.	Long and van der Hilst (2005b, 2006) Long et al., (2007) Kneller et al., (2008b)
Central Japan	W side volcanic front: N-S directions S coast: E-W	W side volcanic front: N-S directions S coast: E-W	Local and sS similar suggesting in W coast: magma filled cracks within mantle wedge. S coast: Local deformation in the crust and shallower	Iidaka and Obara (1995)

			parts of the mantle. Little subslab component.	
NE Japan	Forearc: Trench-parallel backarc: Trench-perpendicular		Forearc: Anisotropy predominantly within crust and a small amount of fossil anisotropy or LPO/ cracks in the slab. Backarc: 2D corner flow in mantle wedge but weak anisotropy.	Okada et al., (1995) Nakajima and Hasegawa (2004) Nakajima et al., (2006) Huang et al., (2011)
Kamchatka	Forearc: Trench-perpendicular Backarc: Trench-parallel δt : 0.2 -0.6 s	Φ: Trench-parallel δt : 1.0 s	*SKS*: Trench-parallel flow beneath subducting slab with lateral flow through opening where N corner of the subducted lithosphere is missing. local *S*: 2D corner flow extending to volcanic arc	Peyton et al., (2001) Levin et al., (2004)
Aleutian	Φ: Trench-parallel δt : 0.5-1.0 s	Φ: Nearly trench-parallel δt : 0.5-1.0 s	Anisotropy from mantle wedge due to olivine aligned from arc orthogonal shortening which is accompanied by shearing or extension in vertical or arc parallel direction. Little or no sub-slab splitting.	Yang et al., (1995) Long and Silver (2008)
Cascadia	Φ: Trench-parallel in forearc and trench-perpendicular in backarc. δt : 0.3 s	Φ: Trench-perpendicular δt : 1.0 - 1.5 s	*S* wave anisotropy: Alignment of melt filled crust within the mantle. *SKS* wave anisotropy: Lattice orientation of olivine with plate motion in the mantle below the slab.	Bostock and Cassidy (1995) Cassidy and Bostock (1996) Currie et al., (2004)

Caribbean	Φ: Trench-parallel δt : 0.1 - 0.3 s	Φ: Trench-parallel δt : 1.2 - 2.1 s	Local *S* phases anisotropy within the crust. ~1.0s anisotropy sub wedge from sub-slab flow resulting from slab rollback or a change in morphology or dip of the slab.	Pinero-Felicangeli and Kendall (2008) Russo et al., (1996) Growdon et al., (2009)
Central America	Φ: Trench-parallel and trench-perpendicular observed with changes over short distances (< 5 km) δt : 0.04 - 1.14 s, average 0.3 s.	Φ: Trench-parallel δt : 1.5 - 2.0 s	Local *S* : Along arc flow due to either slab rollback, the slab edge in Costa Rica, along strike component of plate motion or a combined effect of them all. *SKS*:Arc parallel anisotropy beneath the slab or deep backarc.	Abt et al., (2006) Hoernle et al., (2008) Abt et al., (2009)
South America	Φ: Trench-parallel (N-S) δt : Up to 0.3 s	Φ: Predominately trench-parallel but localized regions of trench-perpendicular and oblique δt : 2.0 - 2.5 s	*SKS* suggest mantle flowing round the N and S limits of the Nazca Plate with regions of trench-normal flow due to change in slab dip or a tear. Local *S* suggest that the majority within mantle wedge.	Russo and Silver (1994) Bock et al., (1998) Polet et al., (2000) Anderson et al., (2004)

Table 6.1: SWS measurements at subduction zones around the world.

6.3.5 Aims of this Study

The substantial variation in the recorded splitting measurements at subduction zones and the range of mechanisms to explain the observations show that subduction zones are very complicated environments. SWS from local shear waves exhibit variable fast directions (trench-parallel, trench-perpendicular and trench-oblique) and a large range of delay times (0.05-2 s). There is no one model which can explain all of the observed local

SWS measurements. Instead, anisotropy has been attributed to a wide range of mechanisms, e.g. SPO anisotropy in the crust and subducting slab from crack and fractures, SPO anisotropy in the mantle wedge from the alignment of melts and LPO anisotropy in the mantle wedge from 2D corner flow or trench-parallel flow. SWS results from teleseismic waves are more consistent, with the majority of subduction zones, where anisotropy occurs beneath the slab interface, exhibiting trench-parallel fast directions that are due to trench-parallel flow in the oceanic asthenosphere.

To determine where and what causes anisotropy in the Sumatra subduction zone, we will perform SWS analysis on *SKS* phases and local *S* phases from earthquakes at the slab interface, within the slab and along the Sumatran Fault. Earthquakes along the Sumatran Fault occur at shallow depths (< 20 km) so only travel through the upper part of the continental crust, allowing us to identify the crustal component of anisotropy. Local *S* phases from earthquakes at the slab interface and within the slab travel through the mantle wedge, crust and possibly the top of the subducting slab. Therefore, comparing the splitting measurements obtained from the events obtained at the slab interface and Sumatran Fault will allow us to identify the component of anisotropy from the mantle wedge (and possibly the top of the slab). Lastly, using the splitting results from the *SKS* phases and the local *S* phases, we will be able to determine the anisotropy occurring beneath the slab interface.

Chapter 7

Shear wave splitting (SWS) analysis on local *S* and *SKS* phases was carried out using data from both the Mentawai network and the central Sumatra network (Figure 3.2 and 3.4). The following chapter, which is a paper, will present and discuss the SWS results obtained in this study. The local and *SKS* SWS results are then discussed and compared to a previous study by Hammond et al. (2010) in Sumatra and other SWS studies at subduction zones around the world, to determine the cause of anisotropy beneath Sumatra. To aid our interpretation, forward modeling was used to model the splitting results we obtained.

Seismic Anisotropy in the Sumatra Subduction Zone

R. Collings[(1)] (rachel.collings@liverpool.ac.uk), S. Nippress [(1)], A.Rietbrock[(1)] , D. Lange[(2,4),] F. Tilmann[(2)], D. Natawidjaja[(3)] and B. Suwargadi[(3)]

[(1)] University of Liverpool, 4 Brownlow Street, Liverpool, L69 3GP, UK

[(2)]GFZ German Research Centre for Geosciences, Potsdam, Germany

[(3)]LabEarth, Indonesian Institute of Sciences (LIPI), Bandung, Indonesia

[(4)] Bullard Laboratories, Dept of Earth Science, University of Cambridge, Uk

In Review

7.1 Abstract

An important tool for understanding deformation occurring within a subduction zone is the measurement of seismic anisotropy, through observations of shear wave splitting (SWS). In Sumatra two temporary seismic networks were deployed between December 2007 and February 2009, covering the forearc between the forearc islands to the backarc. We use *SKS* and local SWS measurements to determine the type, amount and location of anisotropy. Local SWS measurements from the forearc islands exhibit trench-parallel

fast directions which can be attributed to shape preferred orientation of cracks/fractures in the overriding sediments. In the Sumatran Fault region the predominant fast direction is fault/trench-parallel, while in the backarc region it is trench-perpendicular. The trench-perpendicular measurements exhibit a positive correlation between delay time and ray path length in the mantle wedge, while the fault-parallel measurements are similar to the fault-parallel fast directions observed for two crustal events at the Sumatran Fault. This suggests that there are two layers of anisotropy, one due to entrained flow within the mantle wedge and a second layer within the overriding crust due to the shear strain caused by the Sumatran Fault. *SKS* splitting results show a NNW-SSE fast direction with delay times of 0.8-3.0 s. The fast directions are approximately parallel to the absolute plate motion of the subducting Indo-Australian Plate. The small delay times exhibited by the local SWS (0.05-0.45 s) in combination with the large *SKS* delay times suggests that the anisotropy generating the teleseismic SWS is dominated by entrained flow in the asthenosphere below the slab.

7.2 Introduction

Anisotropy is the directional dependence of seismic velocity within a material. When a shear wave propagates through an anisotropic medium it is split into two independent waves with polarizations perpendicular to each other, which travel at different velocities. The component that is polarized parallel to the direction of fast seismic velocity travels faster than the orthogonal component, causing shear wave splitting (SWS) (e.g. Savage, 1999). Two parameters are measured, the orientation of the fast shear wave and the delay time between the two arrivals. The fast direction corresponds to the anisotropic symmetry axis and the time lag between the two arrivals provides information on the product of the strength of anisotropy and the thickness of the anisotropic layer.

Since the early observations of SWS (Ando et al., 1983; Fukao, 1984), subduction zones have been among the most popular targets for SWS studies. An astonishing diversity in SWS patterns (e.g. Greve et al., 2008; Hammond et al., 2010; Long and van der Hilst, 2005) has been identified in different regions from both local *S* phases and teleseismic

phases such as *SKS*, including both trench-parallel and trench- perpendicular fast polarization directions (with some oblique directions as well) and widely variable delay time values. In fact, it is common for SWS observations to vary along a single subduction zone (e.g. Hammond et al., 2010). This variation in SWS observations reflects the complex structure of subduction zones with contributions to the SWS coming from various parts of the subducting system: the sub-slab mantle, the subducting slab, the mantle wedge and the overlying crust (Long and Silver, 2009).

It is widely accepted that seismic anisotropy generated in the upper mantle is dominated by lattice preferred orientation (LPO) in olivine (Savage, 1999). At these depths olivine is volumetrically abundant and has a significant single-crystal shear wave anisotropy of 18% (Mainprice, 2007). LPO measured in naturally deformed peridotite rocks (Christensen, 1984; Nicolas and Christensen, 1987) and in samples deformed in the laboratory (Zhang and Karato, 1995) suggests that the fast axis of olivine (a-axis) tends to align with the maximum shear direction or mantle flow direction (Babuška and Cara, 1991; Mainprice et al., 2000; Mainprice, 2007). These experimental observations and the fact that SWS fast polarization directions are shown to align with relative plate motion (e.g. Hall et al., 2000, Nippress et al., 2007) allowed seismologists to gain direct information about dynamic processes such as mantle flow. However, over the last decade a series of experiments (Katayama et al., 2004; Jung et al., 2006; and Katayama and Karato, 2006) have shown that the orientation of the fast axis of olivine does not always align with the maximum shear direction, but is dependent upon stress, temperature and water content. So there are now in fact 5 different types of olivine LPO: the original A-type plus B-, C-, D-, and E-types. In B-type anisotropy, which occurs at high differential stresses and hydrous conditions, the a-axis aligns orthogonal to the shear direction not parallel, as usual.

Seismic anisotropy can also develop from shape preferred orientation (SPO). SPO occurs when orientated cracks, faults, fractures, melt filled inclusions, compositional layering or lenses make an otherwise homogeneous medium anisotropic for wavelengths larger than the space interval (Backus, 1962). It is widely accepted that seismic

anisotropy in the crust is dominated by SPO (e.g. Crampin 1994). Crustal anisotropy develops predominantly in the upper 10-15 km of the crust, due to cracks and micro-cracks aligned with the direction of maximum stress (Crampin, 1994). However, in regions which contain large structural features, e.g. strike-slip faults, anisotropy is formed by fault-parallel aligned minerals and fractures that have developed from shearing along the plate boundary (Kaneshima, 1990; Gledhill and Stuart, 1996; Savage, 1999).

A global dataset of SWS observations (Long and Silver, 2008) using teleseismic *SKS* phases (delay times generally >1.0s) with contributions from mantle wedge anisotropy removed is dominated by trench-parallel fast directions. However, there are several regions that show trench-perpendicular fast polarization directions including the Juan de Fuca slab beneath Cascadia, the Middle America subduction zone beneath Mexico and in northern Chile. Long and Silver (2008) attribute the observed trench-parallel SWS observations to trench migration with a model where the slab is decoupled from the sub-slab mantle (due to shear heating of hot buoyant asthenosphere and subsequent entrainment of a thin asthenospheric layer decoupling the slab from the mantle), with a partial barrier to flow (at the top or bottom of the transition zone) which forces upper mantle material to move parallel to the trench. This trench-parallel sub-slab flow generates A-type olivine LPO that agrees with the *SKS* trench-parallel SWS measurements observed at most subduction zones around the world, bar the previously mentioned exceptions. Long and Silver (2008) also suggest that trench migration could cause trench-parallel flow within the mantle wedge, which would explain the trench-parallel splitting observations recorded from local shear waves in Tonga (Fischer and Wiens, 1996, Fischer et al., 1998) and Central America (Hoernle et al., 2008; Abt et al., 2009). However, Jung and Karato (2001) and Jung et al. (2009) report experimental data suggesting that the sub-slab mantle and the mantle wedge are dominated by B-type olivine fabric, which would imply that the observed trench-parallel fast directions beneath slabs and within mantle wedges are due not to trench-parallel flow but to entrained flow and 2D corner flow in the sub-slab region and mantle wedge, respectively.

Recently, alternative models have been proposed to explain these teleseismic SWS observations and suggest that the slab is anisotropic. Numerical models (Faccenda et al., 2008) invoke the hydration and serpentinization of trench-parallel faults that penetrate the lithospheric slab as a mechanism for generating trench-parallel teleseismic SWS. A last possibility is fossilized anisotropy in the down going-subducting slab (e.g. Hammond et al., 2010). As oceanic lithosphere is formed and moves over the asthenosphere, the fast axes of the anisotropic minerals (e.g. olivine) are aligned in the direction of plate motion (e.g. at the East Pacific Rise, Wolfe and Solomon, 1998; Harmon et al., 2004). These anisotropic characteristics can be frozen into the lithosphere, and may remain present in the subducted slab. However, it is unclear what portion of the slab is capable of retaining this fossilized deformation: the whole slab or just the central core, which is subject to the least amount of deformation as the slab subducts.

Recent studies (Hammond et al., 2010; Tono et al., 2009) have shown the importance of measuring SWS using both local and teleseismic arrivals in the same region to constrain the depth dependence of anisotropy. Using local earthquakes beneath Java-Sumatra, Hammond et al. (2010) report SWS observations that show trench-parallel fast directions, with 0.1–1.0 s (92% ≤0.6 s) delay times (Figure 7.1). SWS from *SKS* phases shows larger delay times (0.8–2.0 s), with fast polarization directions beneath Sumatra parallel (Figure 7.1) to the absolute plate motion (APM) and trench-parallel beneath Java (Figure 7.1). Hammond et al. (2010) explain the SWS from local events with anisotropy confined to the upper 40 km of the over-riding plate with horizontal, trench-parallel deformation and the larger delay times from *SKS* phases by significant fossilized anisotropy within the slab itself. The observed change in *SKS* fast polarization direction between Sumatra and Java correlates well with a significant change in plate age from >100 Ma in Java to <100 Ma beneath Sumatra and might indicate a fundamental change in mantle flow at ~100 Ma..

The substantial variation in the recorded splitting measurements at subduction zones and the range of mechanisms to explain the observations show that subduction zones are

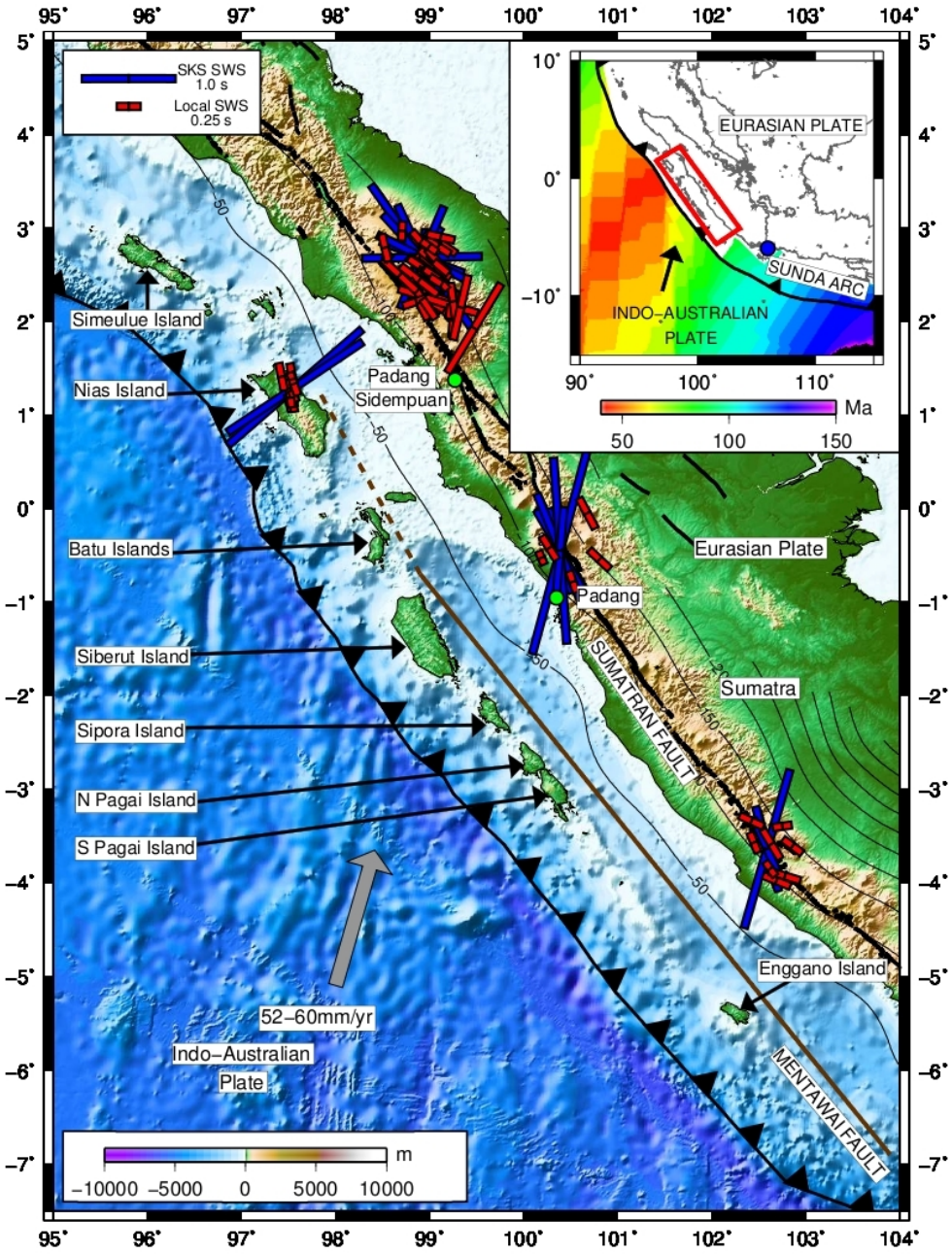

Figure 7.1: Map showing the West Sumatra subduction zone. The Indo-Australian Plate is moving toward the Eurasian Plate forming the Sunda Trench. The blue circle on the inset map of the Sunda Arc marks the position of the Sunda Strait and the red box is the location of the study area. The age of the incoming Indo-Australian Plate along the Sunda Arc (Müller et al., 1997) is indicated on the inset map. On the main map the location of the Mentawai Fault (Diament et al., 1992) (brown line) and the Sumatran Fault (Sieh and Natawidjaja, 2000) (black line) are shown. Black contours indicate the depth of the subducting slab (SLAB1.0, Hayes and Wald, 2009). The SWS observations of Hammond et al. (2010) are shown. Blue are SKS SWS measurements plotted at the station; while red are local SWS measurements plotted at the midpoint between event and station. The scale at the bottom left is bathymetry and topography.

complicated environments. In this study we use SWS observations on a dense temporal array from the Sumatran subduction zone to improve our understanding of the style and geometry of deformation within subduction zone setting.

7.3 Tectonic Setting

The subduction of the Indo-Australian Plate beneath the Eurasian Plate has formed the Sunda Arc which extends for 5,600 km from the Andaman Islands in the northwest to the Banda Arc in the southeast (Figure 7.1). The island of Sumatra is located on the overriding plate of the Sunda Arc between the Sunda Strait, in the south, and the Andaman Islands, in the north (Figure 7.1).

On the subducting Indo-Australian Plate lies the Wharton Fossil Ridge (Figure 2.1), a bathymetric feature that is left laterally offset by fossil transform faults, which is responsible for the variation in lithospheric age of the oceanic crust along the arc (Deplus et al., 1998). The age of the crust increases from 49 Ma below North Sumatra (where the Wharton Fossil Ridge subducts) to 134 Ma below Java (Figure 7.1), which is reflected in the dip, temperature and depth of the Wadati Benioff zone (Shapiro et al., 2008). Adjacent to the Wharton Fossil Ridge the subducting lithosphere is significantly more buoyant, warmer and subducting at a shallower angle (30°) than regions further north or south, where the lithosphere is less buoyant, cooler and dipping at 40°-50° (Shapiro et al., 2008). In addition to the changing temperature, age and dip of the subducting plate, along the Sunda Arc there is also a variation in the obliquity of the subduction (Figure 7.1). At the Sunda Strait the subduction angle changes from normal subduction beneath Java to oblique subduction underneath Sumatra (~40° at 2° N), with a convergence rate that decreases from 60 mm/yr at 6° S to 52 mm/yr at 2° N (Prawirodirdjo et al., 2000). A result of the oblique subduction is strain partitioning of the convergence into strike-slip motion and thrust motion. Strike-slip motion along the Sumatran margin is primarily accommodated by the Sumatran Fault, a large, highly segmented, strike-slip fault that extends for 1,900 km from the Sunda Strait to the Andaman sea across Sumatra, parallel and in close proximity to the volcanic arc (e.g

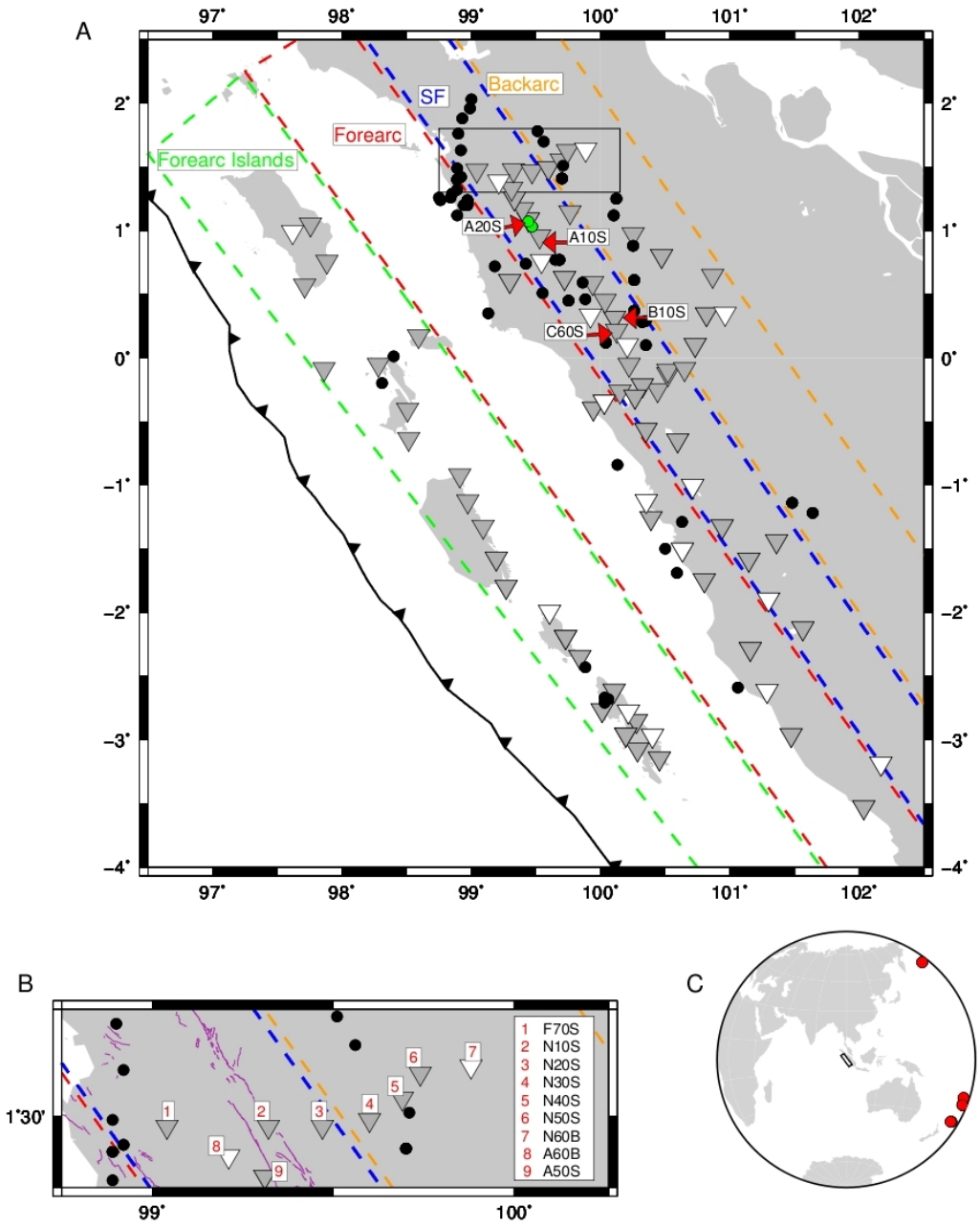

Figure 7.2: A: Map showing station locations. Dark grey triangles indicate 6TD instruments and white triangles show broadband instruments. The circles show the local events used in this study. Black circles show events at the slab interface, or within the slab and green circles show shallow events in the overriding crust. The study region is divided into 4 areas. The green dashed box is the forearc island region, red dashed box the forearc region, blue dashed box the Sumatran Fault region and the orange dashed box the backarc region. The black box indicates the location of the area shown in panel B. B: A zoomed in map of the stations in northern Sumatra. The Sumatran Fault trace is indicated by the purple lines. C: Map showing the location of the teleseismic events. The red circles are the locations of the teleseismic events and the black box is the study region.

Sieh and Natawidjaja, 2000).

7.4 Data and Method

Between December 2007 and February 2009 two seismic networks were installed in southern and central Sumatra (Figure 7.2), as well as the adjacent Mentawai, Nias, Batu and Siberut Islands, at two different time periods which overlapped by 6 months. The southern network, the Mentawai network, was installed in western Sumatra between 1° S and 4° S (Collings et al., 2011) and consisted of 18 CMG-6TD and 9 CMG-3T instruments sampling at 50 and 100 Hz, respectively. The network was decommissioned in October 2008. The second deployment was in central/northern Sumatra on the mainland, between Padang Sidempuan and Padang, as well as on Nias Island, Siberut Island and the Batu Islands (Lange et al., 2010). The dense northern network was installed between April 2008 and February 2009, and comprised of 52 three component stations with sampling rates of 50 and 100 Hz, including 7 broadband stations.

Prior to conducting the SWS analysis the seismic traces were band-passed filtered to improve the signal-to-noise ratio and increase the stability of the SWS measurements. *SKS* wave forms, originating from earthquakes at epicentral distances between 85° and 140°, were filtered between 0.05 and 0.3 Hz, while local *S* waves, arriving at incidence angles of 35° or less (i.e within the shear wave window (Evans, 1984)), were filtered between 0.1 and 3 Hz. The overlap in the filter bands between the *SKS* and local *S* waves minimizes the frequency dependent effects between the two data sets (Hammond et al., 2010). Locations for the local events were determined from a 3D velocity model in the Mentawai region (Collings et al., 2011) and a minimum 1D velocity model in the central/northern Sumatra region (Lange et al., 2010).

For local SWS analysis we used the program SHEBA (Teanby et al., 2004), which is based on the eigenvalue methodology of Silver and Chan (1991). For the teleseismic phases we used both SHEBA (Teanby et al., 2004) and SplitLab (Wüsterfeld et al., 2008). The advantage of using SplitLab is that SWS estimates are calculated using three

independent methods: eigenvalue (Silver and Chan, 1991), rotation and correlation (Bowman and Ando, 1987) and minimum transverse energy (Silver and Chan, 1991). Only *SKS* SWS measurements that produced stable and good quality results in both SplitLab and SHEBA (difference in $\Phi < 20°$ and $\delta t < 0.3$) were included in this study. In both SHEBA and SplitLab, automated SWS analysis is used. This enables the fast direction (Φ) and the splitting delay time (δt) to be calculated for a range of time windows within an initially manually-selected range, with the optimum Φ and δt values found using cluster analysis (Teanby et al., 2004). The resulting Φ and δt are not necessarily the results that produce the smallest error bars but are the results that are stable over various size of analysis windows.

7.5 Results

To assess the stability and quality of an SWS observation, a number of quality control tests were performed. If a shear wave has passed through an anisotropic medium it can be identified visually, prior to correction, by elliptical particle motion: For *SKS* waves significant energy on the transverse component is another indicator of horizontal anisotropy. After correction, in which both components have been rotated by Φ and one lagged by δt, the particle motion should become linear, the fast and slow waves should align and for *SKS* additionally the energy should be minimized on the corrected transverse component. If an observed SWS measurement did not exhibit this pattern it was rejected. Errors on the splitting parameters must also be as low as possible. The errors are estimated using the inverse F-Test which determines a confidence region for the SWS parameters (Silver and Chan, 1991). Any SWS observations with 1σ errors greater than 0.4 s in δt and 30° in Φ were discarded.

For *SKS* phases the polarization of the shear wave after the anisotropy correction (spol) was compared to the backazimuth. *SKS* phases should have been radially polarized during the *P* to *S* conversion at the core mantle boundary, so their spol and backazimuth should be similar; results in which they differed by more than 30° were rejected as this can indicate instability in the SWS measurement (Hammond et al., 2010).

In addition to these methods, the numerical criteria of Wüsterfeld and Bokelmann (2007) were implemented for the *SKS* phases. They use the difference in the fast directions and ratio of the delay times of the SWS measurements obtained using the rotation correlation and minimum transverse energy method, to determine the quality of the result. Based on synthetic data, a splitting measurement is defined as good if the delay time ratio between the two methods is between 0.7 and 1.2 s and the fast axis misfit is less than 15 °.

7.5.1 Teleseismic Results

A total of 20 *SKS* SWS observations from 4 events at 16 stations produced stable splitting results using both SHEBA and SplitLab (Figure 7.3, black SWS results, Table A4.1 and Figure A4.1 and A4.2). An additional 5 observations produced stable results in all 3 SWS techniques. However, the delay time ratios were not between 0.7 and 1.2 s and the misfits were >15° (Figure 7.3, light blue measurements, Table A4.2 and Figure A4.3 and A4.4). The good splitting measurements exhibit a consistent NNW to SSE fast direction, with an average fast direction of -10° (Figure 7.3). The average fast direction was calculated using a modified method of averaging directional data (Audoine et al., 2004) which was first described by Krumbein (1939) and applied to SWS fast directions by Kubo and Hiramatsu (1998). The bidirectional nature of fast directions means that directional statistics, instead of simple Gaussian statistics, must be used to calculate the mean. The delay times of the 20 good results are spread between 0.8 s and 3.0 s, with 60% of the measurements lying between 1.6 s and 2.4 s. The ray paths of the rays were calculated using the 2D velocity model of Collings et al. (2011) merged with PREM for depths greater than 200 km. The 2D tomographic model of Collings et al. (2011) was extrapolated to the NW beyond the area the model was developed for, and an additional inversion was run with events from both networks, to obtain an approximate 2D model for the forearc. The raypaths show that the rays travel a substantial distance beneath the slab-interface.

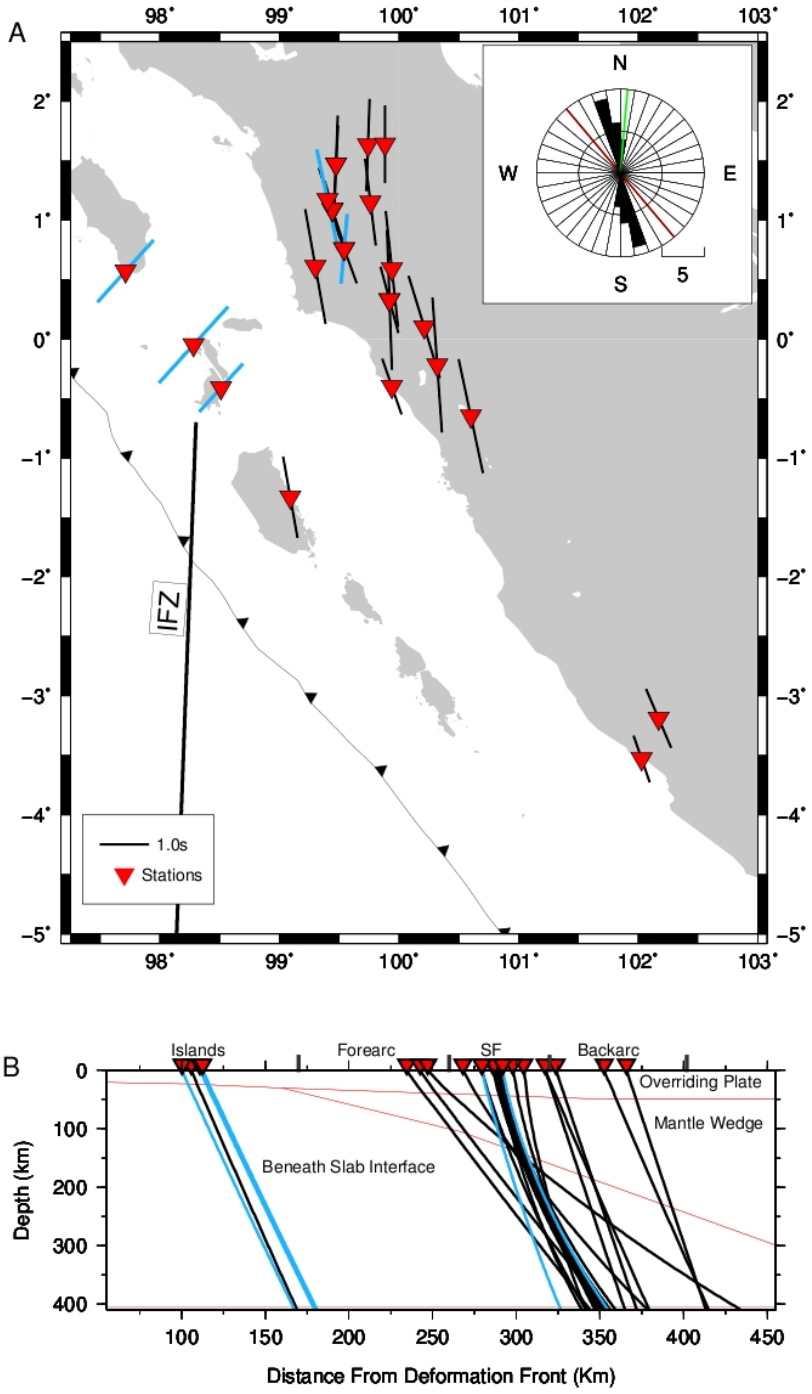

Figure 7.3: A: SKS SWS results using the minimum transverse energy method. Black measurements indicate good SWS results, while blue indicate stable SWS results but not classed as good. The measurements are plotted at the station. The position of the Investigator Fracture Zone (IFZ) is indicated. The rose diagram shows the orientation of the SWS fast directions. The orientation of the trench is indicated by the red line and the convergence direction is indicated by the green line. B: Profile perpendicular to the deformation front, showing the ray paths of teleseismic events together with the main structures of the margin from Collings et al. (2011).

7.5.2 Local Splitting Results

A total of 78 good local SWS measurements were obtained from 55 events at focal depths between 10 km and 200 km (Table A4.3 -A4.6, Figure A4.5 and A4.6). A good event was defined based on the criteria of Teanby et al. (2004), i.e. the shear phase was well defined and distinct; the fast and slow waves were similar and well matched after correction; particle motion was elliptical before correction and linear after correction; and the grid search produced a unique result. The fast directions (Figure 7.4A) are scattered but they indicate two predominant directions, NW-SE (trench-parallel) and ENE -WSW (trench-perpendicular). The delay times are spread between 0.05 s and 0.45 s. The results show a weak positive correlation between source depth and delay time for events deeper than 75 km depth (Figure 7.5C and 7.5D). This suggests that these rays sample a uniformly anisotropic structure in which the longer the ray path spends in the structure the greater the magnitude of the splitting.

Due to the observed spread in fast directions (Figure 7.4A), the local splitting results were analysed in four regions (forearc islands, forearc, Sumatran Fault and backarc, Figure 7.2A). The distance each ray spends in the mantle wedge and overlying crust was calculated using the 2D tomographic model of Collings et al. (2011). These distances were then plotted against observed delay times to identify trends (Figure 7.5).

7.5.2.1 Forearc Islands

The 6 splitting measurements obtained from stations on the forearc islands exhibit a coherent approximate trench-parallel fast direction (Figure 7.4B and Table A4.3), with an average direction of -59° (see section 7.5.1 for averaging technique) and a circular deviation of 0.03. The circular deviation is a measure of deviation from the average. If all the measurements are aligned the circular deviation is 0 and if they are poorly aligned it is 1. δt is spread between 0.1 and 0.31s. The rays travel for 20-25 km through accreted low velocity sediments and do not travel through the mantle wedge (Figure 7.5A and

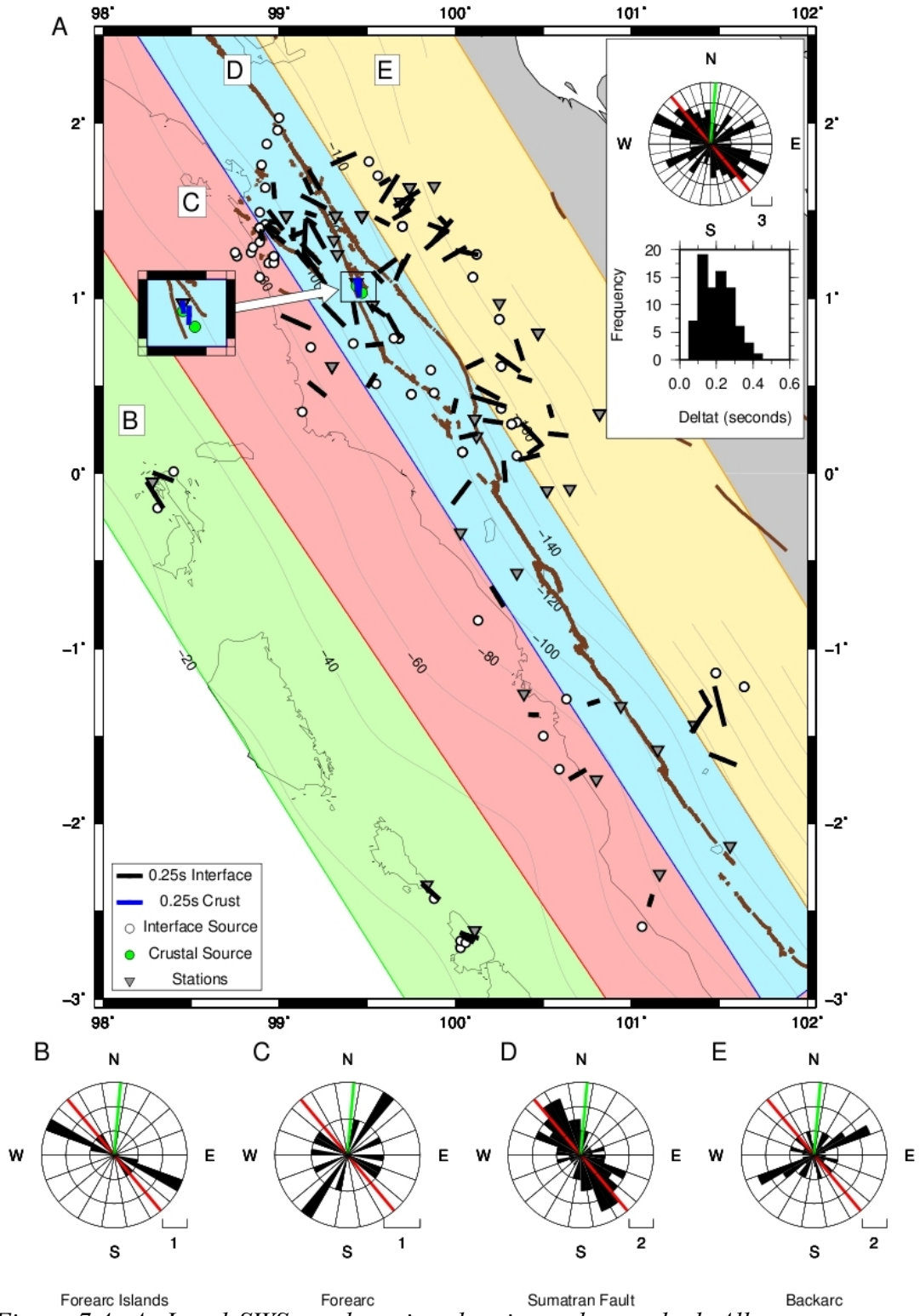

Figure 7.4: A: Local SWS results using the eigenvalue method. All measurements are plotted at the midpoint between the event location (white circles) and station (grey triangles). Brown lines represent the faults within the region. The forearc island region (green), forearc region (red), Sumatra Fault region (blue) and backarc region (orange) are coloured. Inlay shows a rose diagram with the SWS fast directions (in all rose diagrams the orientation of the trench is indicated by the red line and the convergence direction is indicated by the green line) and a histogram of delay times. Rose diagrams of SWS fast directions are shown for events located in the forearc island region (B), the forearc region (C), the Sumatran Fault region (D) and the backarc region (E).

7.5B).

7.5.2.2 Forearc

Only seven measurements were obtained in the forearc region, with two results showing trench-parallel fast directions, three results exhibiting approximately trench-perpendicular fast directions and two indicating trench-oblique fast directions (-88° and 16°) (Figure 7.4C, 7.5C and Table A4.4). The delay times vary between 0.08 s and 0.32 s. All rays travel ~30 km in the continental crust (Figure 7.5A) and do not show any correlation with δt (Figure 7.5C). However, in the mantle wedge there appears to be a weak positive correlation between distance traveled and δt.

7.5.2.3 Sumatran Fault

Although fast directions both perpendicular and parallel to the trench/Sumatran Fault are observed in the Sumatran Fault region (Table A4.5), the predominant fast direction is trench/fault-parallel (Figure 7.4D), which results in an average fast direction of -14°, with a circular deviation of 0.24. The delay times are between 0.06 s and 0.42 s. Splitting measurements from two events at the Sumatran Fault, located at ~ 13 km (therefore only traveling within the crust), exhibit fast directions that are approximately N-S with delay times of 0.10 to 0.17 s (Figure 7.4A, blue measurements). Though this is oblique to the general NW-SE trend of the fault and trench, in this region the Sumatran Fault trends in a more N-S direction, which is approximately parallel to the fast directions of the two crustal events. Only 2 SWS measurements were obtained from crustal events as the event had to occur beneath the station to ensure the angle of incidence was less than 35° and the data were often noisy, producing unstable splitting results. Events at the slab interface and within the slab travel between 35 km and 50 km in the crust (Figure 7.5A) and show no correlation with fast direction or delay time (Figure 7.5D). A positive correlation can be seen between distance traveled in the mantle wedge and delay time (Figure 7.5D). The relationship is particularly evident for the trench-perpendicular measurements.

7.5.2.4 Backarc

In the backarc both trench-parallel and trench-perpendicular fast directions are present (Table A4.6), but the predominant direction is trench-perpendicular (Figure 7.4A and 7.4E). The delay times vary between 0.09 and 0.34 s. The previous positive correlation observed in the forearc and Sumatran Fault region between distance traveled in the mantle wedge and δt is not as evident in the backarc region (Figure 7.5E). However, when separating the trench-parallel and trench-perpendicular results this relationship is more noticeable again for the trench-perpendicular measurements (Figure 7.5E, green measurements). The trench-parallel results remain scattered (Figure 7.5E, red measurements).

7.6 Discussion of Local *S* Splitting and Possible Mechanisms

The study of Hammond et al. (2010) concluded that the mantle wedge was nearly isotropic (0.3 % anisotropy) as no relationship between event depth and delay time was evident. Instead the observed SWS was attributed to anisotropy in the overriding plate, caused by a 40 km layer of vertically aligned cracks (Hammond et al., 2010). However, the amount of data and station coverage in the present study is greater and ray paths were calculated using local earthquake tomography (Collings et al., 2011), which allows a more in-depth analysis. A first order feature of the local SWS observations in this study (Figure 7.4) is the rotation in fast direction from a predominant trench-parallel direction close to the Sumatran Fault to a more trench-perpendicular direction further into the backarc. A transition from trench-parallel to trench-perpendicular splitting is also observed at several other subduction regions around the world such as NE Japan (Huang et al., 2011) and Tonga (Smith et al., 2001). The SWS observations show a positive relationship between length of ray path spent within the mantle wedge and delay time (Figure 7.5D and 7.5E), suggesting that anisotropy is present within the mantle wedge. In this study two splitting measurement from earthquakes along the Sumatran Fault (Figure 7.4 and Table A4.5, (YR JULDAY HHMM = 2008 248 1922 and 2008 339

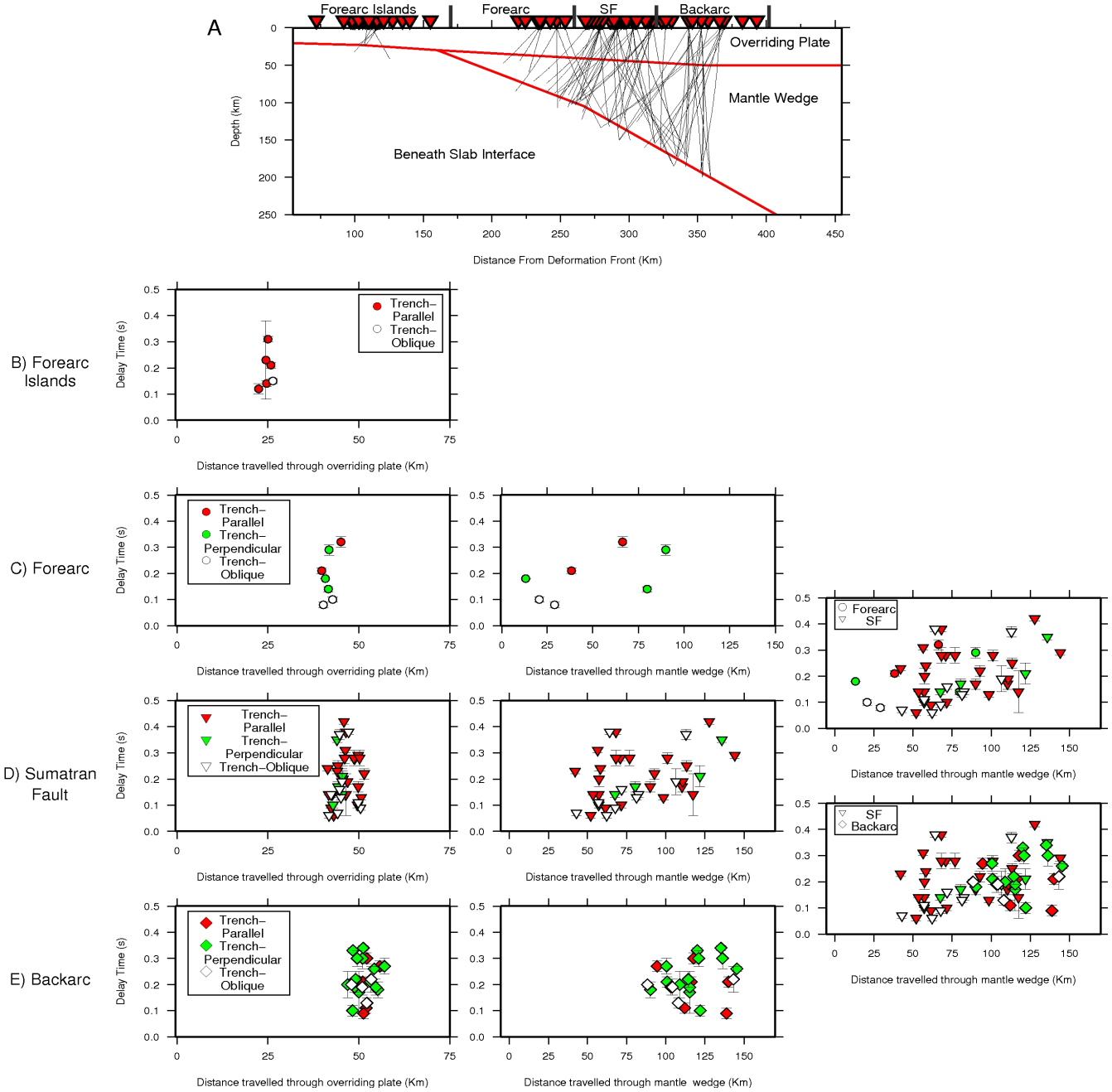

Figure 7.5: A) Ray paths of local events traced through local velocity model (from Collings et al., 2011). B) Distance each ray path has spent within the crust versus delay time for events in the forearc island region. In all plots red circles are fault/trench-parallel measurements, green circles are trench-perpendicular measurements and white circles are trench oblique measurements. C) Distance each ray path has spent within the crust (left) and mantle wedge (centre) versus delay time for events in the forearc region. Right hand graph is distance each ray path has spent within the mantle wedge versus delay time for events in the forearc and Sumatra Fault region. D) Distance each ray path has spent within the crust (left) and mantle wedge (centre) versus delay time for events in the Sumatran Fault region. Right hand graph is distance each ray path has spent within the mantle wedge versus delay time for events in the Sumatran Fault and backarc region. E) Distance each ray path has spent within the crust (left) and mantle wedge (centre) versus delay time for events in the backarc region.

714)) , at ~ 13 km depth, exhibit fast directions that are approximately parallel to the surface trace of the Sumatran Fault in that region, with delay times of 0.10-0.17 s, suggesting a crustal component of anisotropy within this region.

7.6.1 Forearc Islands

Previously, trench-parallel fast directions close to the subduction trench have been attributed to either B-type olivine fabric (Jung and Karato, 2001) or the effect of slab roll-back on mantle flow (Smith et al., 2001). It is clear from the ray paths of the events beneath the forearc islands (Figure 7.5A) that these rays do not travel through the mantle wedge and therefore the anisotropy must be located either within the overriding sediment or the subducting slab. The forearc islands are composed of low velocity sediments that were part of a former accretionary prism before being uplifted to form the forearc islands (Kopp et al., 2001; Collings et al., 2011). Anisotropy in the low velocity sediments beneath the forearc islands may therefore result from the alignment of trench-parallel cracks and minerals which could have occurred during uplift, when the former accretionary prism was subjected to a high amount of deformation. The hypocentre locations and local earthquake tomography in Collings et al. (2011) also show that beneath the forearc islands the subducting slab is hydrated and faulted which could also contribute to the observed local SWS. The trench-parallel fast directions at the forearc islands in Sumatra are similar to NE Japan (Huang et al., 2011), where trench-parallel splitting measurements in the forearc have recently been attributed to aligned cracks within the crust and either fossilized anisotropy (LPO orientation of crystals) or the alignment of cracks within the subducting slab.

7.6.2 Forearc, Sumatran Fault and Backarc Regions

7.6.2.1 Trench-Perpendicular Measurements

In the forearc, back arc and Sumatran Fault region a positive correlation is observed between ray path length in the mantle and delay time (Figure 7.5D and 7.5E, right hand

panel). This relationship is particularly evident for the trench-perpendicular splitting measurements in the Sumatran Fault and backarc regions (Figure 7.5 E, far right panel). The average delay time is 0.21s, which is small compared to Tonga and Ryukyu where a $\delta t > 1.0$ s has been observed for events at 75-100 km depth (Smith et al., 2001; Long and van der Hilst, 2006). In Sumatra only a small amount of splitting is suggested to occur within the mantle wedge itself, as the maximum delay time for a slab earthquake which exhibits approximately trench-perpendicular fast directions is 0.35 s. Long and Silver (2008) hypothesize that anisotropy in the mantle wedge beneath the forearc and arc is controlled by competing influences of two flow fields, 2D corner flow and 3D flow, whose relative importance is governed by the magnitude of the trench velocity normalized by the convergence velocity ($V_{norm}=|V_t|/V_c$).When $V_{norm} \leq \sim 0.2$, down dip motion dominates, resulting in 2D corner flow, when $V_{norm} \geq 0.6$ trench migration/advance dominates, resulting in a 3D flow field; between these two regimes small delay times are recorded as neither 2D or 3D flow dominates. At Sumatra, V_{norm} is calculated to be ~0.3 (Long and Silver, 2008) which suggests that the two flows are competing, resulting in an incoherent flow field which can change rapidly over short length scales and as a consequence causes only a small amount of splitting. This agrees with the SWS observations for the forearc region where various splitting directions are observed. Despite a positive correlation between delay time and length of ray path in the mantle wedge (Figure 7.5C), which implies that anisotropy is occurring within the mantle wedge, there is no predominant fast direction. Therefore neither 2D corner or 3D flow appears to dominate and the delay times are small. In the backarc region the predominant fast direction is trench-perpendicular (Figure 7.4E) and the trench-perpendicular SWS measurements from the Sumatra Fault and backarc region show a positive correlation between delay time and length of path in mantle wedge (Figure 7.5E, far right panel). This relationship is not as evident for the trench/fault-parallel and trench-oblique measurements but some correlation is still present. This suggests that the source of splitting for the trench-perpendicular measurements is in the mantle wedge due to corner flow, though the delay times imply that the anisotropy created is not strong. This is similar to SWS observations in NE Japan (Huang et al., 2011), where only 0.16 s of SWS is thought to occur in the mantle wedge due to the centre of the mantle wedge

being weakly anisotropic or isotropic. The predominant trench-perpendicular direction observed within the backarc region suggest that in this region the influence of trench migration on mantle flow is reduced; 2D corner flow should therefore dominate and result in trench-perpendicular fast directions (Long and Silver, 2008). We therefore attribute the observed trench-perpendicular fast directions in the backarc region and Sumatra Fault regions to 2D corner flow in the mantle wedge, which is induced by the viscous coupling between the subducting slab and the overlying mantle (Ribe, 1989). As the slab subducts, mantle wedge material is dragged down by viscous flow along the slab surface. The dragged down material is then passively replaced by hot and low viscosity mantle materials from deeper within the mantle wedge, resulting in an upward return flow. This generates seismic anisotropy which is dominated by the LPO of olivine, as the fast axis of olivine (a-axis) aligns with the mantle flow direction. Numerical modeling (Honda and Yoshida, 2005; Nakjima et al., 2006) has shown that the return flow is parallel to the maximum dip of the slab, and therefore at non-oblique subduction zones, parallel to the convergence direction. In Sumatra however, where oblique subduction is occurring, the return flow is oblique to the convergence direction but perpendicular to the strike of the trench.

7.6.2.2 Trench/ Sumatran Fault-Parallel SWS Observations

Within the Sumatran Fault region and isolated areas of the backarc, observed SWS fast directions are approximately parallel to the trench or to the Sumatran Fault. Trench-parallel fast directions previously have been attributed to trench-parallel flow within the mantle wedge resulting from trench migration (Smith et al., 2001, Long and Silver et al., 2008). As discussed above, the normalized trench migration / trench convergence value of 0.3 indicates that no coherent flow dominates in the mantle wedge, suggesting isolated regions of 3D flow could occur and create trench-parallel flow. Trench-parallel fast directions could also originate from B-type olivine fabric; this can develop within the mantle wedge when the water content and stress conditions are high (Jung and Karato, 2001). Despite these possible mechanisms we neglect anisotropy in the mantle as the cause of the trench-parallel fast directions for a number of reasons. Firstly, we do

not observe a positive correlation between delay time and distance traveled within the mantle wedge for trench-parallel measurements from the Sumatra Fault and backarc region (Figure 7.5, far right panel, red triangles). Secondly, in the vicinity of the Sumatran Fault and within the backarc region we would expect the influence of trench migration to diminish (Long and Silver, 2008). Finally, experimental results (Jung and Karato, 2001) and geodynamical modeling (Lassak et al., 2006) suggest that B-type olivine only develops in limited regions, specifically the forearc corner, and therefore should not be found in the Sumatran Fault and backarc regions. For the Mentawai region, the local earthquake tomography (Collings et al., 2011) does not indicate an elevated *Vp/Vs* ratio which is generally indicative of high water content within the mantle that could facilitate the development of B-type olivine LPO.

Another possible explanation for the trench-parallel fast directions is that they originate from anisotropy within the crust. Crustal anisotropy (Crampin, 1994) has previously been attributed to cracks that are aligned with the maximum compressive stress direction and can result in 1.5 % anisotropy in intact rocks and up to 10 % anisotropy in very fractured rocks. In Sumatra the maximum horizontal stress direction in the overriding Eurasian Plate is NE to SW (Mount and Suppe, 1992; Tingay et al., 2010), suggesting that it is not responsible for the observed trench/fault-parallel fast directions. In active fault zones regions, where cracks that have developed parallel to the maximum stress contain fluids at high pore pressures, a 90° flip in the fast polarization direction is observed (Zatsepin and Crampin, 1997; Crampin et al., 2002), which in Sumatra would result in fault-parallel fast directions. Despite this, we reject this mechanism as the cause of the trench-parallel observation, since the local earthquake tomography (Collings et al., 2011) and the minimum 1D model of the upper crust along the Sumatran Fault (Weller et al., 2012) display no evidence of significantly elevated *Vp/Vs* ratio in the continental crust, suggesting that no substantial fluids are present in the continental crust.

Anisotropy in regions which contain large structural features, e.g strike slip faults, has also been suggested to develop from preferential mineral alignment and orientated cracks and fractures (Kaneshima, 1990; Gledhill and Stuart, 1996; Savage, 1999). This is

true at the San Andreas Fault and Marlborough region of New Zealand, where many stations show fast directions consistently parallel to the strike of the faults, not the maximum compressive stress, and the anisotropy is attributed to mineral or fracture alignment caused by shearing along the plate boundary (Zhang and Schwartz, 1994; Balfour et al., 2005; Gledhill and Stuart, 1996; Savage et al., 2004). At the San Andreas Fault, in order to explain all of the SWS observations, the anisotropy created by vertically orientated fault-parallel cracks/fractures and mineral alignment in North California has to be confined to a narrow area around the fault; while in Southern California the anisotropic layer is either thinner or does not exist (Savage and Silver, 1993; Özalaybey and Savage, 1995). The situation at the San Andreas Fault is different to New Zealand, where rays recorded at most stations in South North Island and in North South Island exhibit fast directions that are nearly parallel to the strike of the major strike slip faults (Alpine Fault, Marlborough fault system, North Island dextral fault belt), suggesting that the strain is distributed over a large area and that the crust, lithospheric upper mantle and areas of the asthenospheric upper mantle are strongly coupled (Klosko et al., 1999; Audoine et al., 2000; Savage et al., 2004).

In Sumatra SWS measurements from 2 events originating on the Sumatran Fault, at a depth of ~13 km (Figure 7.4 and Table A4.5, (YR JULDAY HHMM = 2008 248 1922 and 2008 339 714)), exhibit fast directions approximately parallel to the surface trace of the Sumatran Fault in that region and delay times between 0.10 s-0.17 s, similar to delay times observed at the San Andreas Fault and the Marlborough region, New Zealand (Zhang and Schwartz, 1994; Liu et al., 2008; Balfour et al., 2005). This implies that a layer of anisotropy is located within the upper crust due to the shear strain exerted by the Sumatran Fault. Slab earthquakes recorded at stations within the backarc and Sumatran Fault region also exhibit trench/fault-parallel fast direction with larger delay times of up to 0.42 s, suggesting that deformation from simple shear extends deeper into the continental lithosphere and consequently could be masking any anisotropic signature from the 2D corner flow occurring below in the asthenosphere. A thick layer of anisotropy within the overriding plate agrees with the results of Hammond et al. (2010) who attribute anisotropy to a 40 km layer of vertically aligned cracks. As the local SWS

results do not exhibit a uniform fault-parallel direction throughout Sumatra, the shear strain is probably confined to a narrow region (~100 km) around the Sumatran Fault, which is similar to the SWS observations around the San Andreas Fault (Savage and Silver, 1993; Özalaybey and Savage, 1995). This can be seen clearly in the northern area of our study region, at stations F70S, N10S, N20S, N40S, N50S (Figure 7.2B). The two stations closest to the fault, N10S and N20S, as well as station F70S to the east where smaller strike-slip faults occur (Figure 7.2B), show approximate fault-parallel directions. Beyond this area, in the backarc, at stations N40S and N50S the fast direction rotates to a predominant trench-perpendicular direction. In the Sumatra Fault and backarc regions a positive correlation is apparent between ray path length in the mantle and delay time (Figure 7.5E, red trench-perpendicular measurements in far right panel), suggesting that anisotropy is located within the mantle wedge from 2D corner flow. We can not rule out a small component of crustal anisotropy from micro-crack alignment with the maximum stress direction (<0.1s), but it is unlikely to be the main cause of anisotropy.

The change in fast direction from fault-parallel to trench-perpendicular at stations N20S and N40S allows us to put some constraints on the location of anisotropy in this region (Alsina and Snieder, 1995). To investigate whether two stations sample the same region we calculate the Fresnel zone radius (Sheriff and Geldart, 1995).

$$Fresnel\ Zone\ Radius = \sqrt{\frac{VsZ}{2f}} \qquad (7.1)$$

where Vs is the shear velocity (average ~4 km/s) determined from the local earthquake tomography (Collings et al., 2011), Z is the depth and f is the dominant frequency 1.5 Hz. This equation is only valid if Z >> Vs/f and since Vs/f=2.5 km, we will only calculate the Fresnel zone radius for depths greater than 50 km.

Depth (km)	Fresnel Zone Radius (km)	Overlap (km)
50	8	no
75	10	yes
100	12	yes
150	14	yes

Table 7.1: Fresnel zone radius and overlap at different depths.

Stations N20S and N40S are ~26 km apart. The Fresnel zone radius calculations (Table 7.1) and the ray paths of two rays originating from the same event at 172 km depth suggest that the ray paths will overlap at depths greater than 75 km. We can therefore conclude that rays arriving at station N40S and N20S, originating from the same hypocentre location, will sample the same region of the mantle wedge below ~75 km depth but above this depth they sample different regions of the mantle wedge and crust. Therefore the observed change in SWS can be attributed to lateral variations in anisotropy in the continental lithosphere and the upper part of the mantle asthenosphere (i.e shallower than 75 km depth).

Attributing the observed fast directions at stations above or close to the Sumatran Fault to aligned fractures and bedding planes caused by the NW-SE trend of the Sumatran Fault would predict coherent fault-parallel fast directions at all stations on or close to the fault. Generally, nearby stations do show similar fault-parallel directions (e.g at stations N20S, A20S and F70S, Figure 7.2A), however there are exceptions. At stations A50S, A10S, C60S and B10S, which are situated above the Sumatran Fault, approximately trench/fault-perpendicular and trench/fault-oblique fast directions are observed. A possible explanation for these exceptions is that the Sumatran Fault is comprised of numerous segments separated by dilational and contractional stepovers, with abrupt changes in trend (Sieh and Natawidjaja, 2000). In addition to this, Weller et al. (2012) have found a complex set of faults bisecting the Sumatran Fault, which may also complicate the observed splitting. This suggests that the anisotropy induced by the structural fabric will not be consistently NW-SE throughout the lithosphere.

7.6.2.3 Two Layers of Anisotropy

From the discussion above, it appears that two layers of anisotropy are present, an upper layer in the continental lithosphere due to the structural fabric induced by Sumatran Fault and a lower layer in the asthenospheric mantle wedge due to 2D corner flow. When a wave traverses through two layers of anisotropy the signal is split twice, which can be identified by a $\pi/2$ periodicity in plots of δt and Φ versus source polarization (Yardley and Crampin, 1991; Silver and Savage, 1994). It has been pointed out that at high frequencies (~25 Hz) and if one only looks at the signal onset, information about the lower layer is lost (Yardley and Crampin, 1991). To ensure that information from the lower layer was not lost, prior to shear wave splitting analysis the local waves were bandpass filtered with corner frequencies of 0.1 Hz and 3 Hz (10 s and 0.33 s) (Section 7.4); therefore the observed delay times (average 0.2 s) were smaller than the typical period. Plots (Figure 7.6) of δt and Φ with respect to source polarization direction for stations within the Sumatran Fault and backarc region show a near $\pi/2$ periodicity, suggesting that two layers of anisotropy are present. Measurements that deviate from the apparent $\pi/2$ periodicity may be due to a dipping symmetry axis or laterally varying anisotropy that have not been included in the model (Savage and Silver, 1993; Silver and Savage, 1994). Unfortunately we do not have enough measurements to produce individual plots for each station, which may reduce the influence of laterally varying anisotropy in our models.

The plots of observed fast directions with respect to source polarization direction for the backarc and Sumatran Fault show a significant jump in the fast direction at a source polarization of ~60°-90° and 0°. Savage and Silver (1993) suggest that in order to obtain a significant 'jump' in the fast direction the splitting parameters of layer 1 and layer 2 must fit the following requirements: $\delta t_1 = \delta t_2$ and $30° < | \Phi_2 - \Phi_1 | < 60°$ or $120° < | \Phi_2 - \Phi_1 | < 150°$, with the 'jump' in fast direction versus source polarization and delay time versus source polarization occurring midway between the two fast/slow directions. Using the previously stated criteria we fit the observed periodicity using a trial and error method. Favorable models that produce a 'jump' in the fast direction from -90° to 90° at source

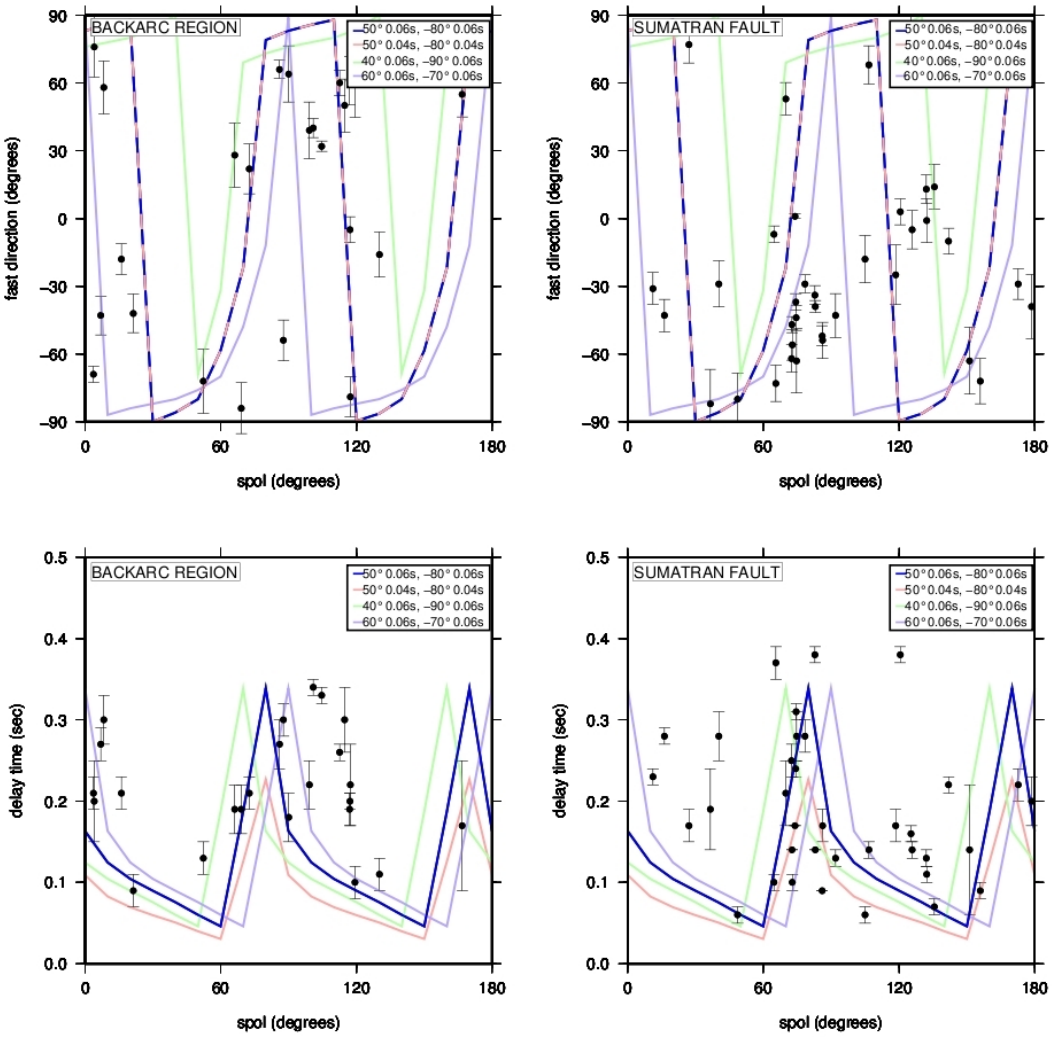

Figure 7.6: Comparisons of source polarization versus fast direction and delay times for stations within the Sumatran Fault and backarc regions. Plots suggest a π/2 periodicity with favorable models suggesting Φ_1 , δt_1 = 50°, 0.06 s and Φ_2 , δt_2 = -80°, 0.06 s (blue line). Models where Φ_1 , δt_1 = 50°, 0.04 s and Φ_2 , δt_2 = -80°, 0.04 s are shown by the red line. The green line is Φ_1 , δt_1 = 40°, 0.06 s and Φ_2 , δt_2 = -90°, 0.06 s and the purple line is Φ_1 , δt_1 = 60°, 0.06 s and Φ_2 , δt_2 = -70°, 0.06 s. Black circles are our observations.

polarizations of 0° and 60°-80° suggest a lower layer orientated NE-SW (050° +/- 10°) producing delay times of 0.06 s and an upper layer that has a similar delay time but with a fast axis orientated at -080°+/- 10° (Figure 7.6). If the delay time of these two layers is less than 0.06 s, the predicted delay times do not fit the observed delay times (Figure 7.6, red line), giving us a lower limit on the anisotropy values. The orientation of the lower

layer is approximately perpendicular to the strike of the trench (~140°), which is what is expected for 2D corner flow, and the small delay time agrees with the observations of Hammond et al. (2010), suggesting the mantle wedge is only weakly anisotropic. The upper layer fast axis orientation of -80° is oblique to the general trend of the Sumatran Fault (-40° to -50°) but as discussed earlier the fault is not a simple NW-SE trending structure. Instead, it consists of numerous segments separated by dilational and contractional stepovers with occasional abrupt changes in the trend of the fault. This may result in a variation in the orientation of the structural fabric induced in the overriding continental crust.

7.6.3 Forward Modeling

Synthetic SWS was modeled using the forward modeling software SynthSplit (Abt and Fischer, 2008). SynthSplit predicts SWS parameters using the particle motion perturbation method of Fischer et al. (2000) and has been tested with full synthetic waveform methods (Abt and Fischer, 2008). The forward modeling involves a large number of input parameters, including details of the incoming wave geometry, the characteristics of the anisotropic layer and several elastic parameters, with the number of input parameters increasing by five for each layer of anisotropy modeled. The model uses elastic parameters from studies of single crystals and assumes that each aggregate within a defined block of a model is perfectly aligned in the orientation specified. In reality the observed splitting times are considerably smaller than those predicted from the single crystal elastic coefficients, most likely due to the misalignment of a percentage of the crystals. To simulate this dilution of anisotropy, a dilution factor is inputed. The dilution factor can be calculated using the equation

$$Dilution factor\,(\%) = \frac{bulk\ S\ anisotropy\,(\%)}{single\ crystal\ anisotropy\,(\%)}\ x100 \qquad (7.2)$$

where a single olivine crystal *S* wave anisotropic strength is 18.1% (Kumazawa and Anderson, 1969) and the bulk *S* anisotropy is the strength of anisotropy within the layer.

The dilution factor is not the same as the percent of shear wave anisotropy, which is often referred to in published work, as there may be a variation in the percentage of

orientated grains within that layer and the percent of anisotropy depends on the direction of wave propagation (Abt and Fischer, 2008).

SynthSplit was used to model individual events at different stations. SynthSplit only allows one set of elastic parameters to be determined for each model, regardless of the number of layers. In the models that follow we use olivine-opx elastic coefficients throughout the model space, but at crustal depths, where olivine-opx elastic coefficients are generally not appropriate, they are only taken as a proxy for the more likely sources of crustal anisotropy, e,g stress induced cracks or deformation fabrics in crustal mineralogies (Abt and Fischer., 2008).

The local SWS observations were modeled using two layers of anisotropy. The upper layer is assumed to exhibit a fault-parallel fast direction from the transcurrent motion occurring along the Sumatran Fault so was modeled with the a-axis orientated NW to SE (-40°), which is the general trend of the Sumatran Fault. The lower layer of anisotropy, which originates from 2D corner flow within the mantle wedge, is modeled with the a-axis orientated approximately perpendicular to the trench (050°) and a dilution factor of 13% (equivalent to ~ 2 % bulk *S* anisotropy) . For all models a 70:30 composition of olivine to orthopyroxene was used and the synthetics were generated using a dominant period of 1.5s (~0.66Hz). Numerous models were run to test the sensitivity of theoretical SWS to orthorhombic and hexagonal symmetry. The predicted fast directions of the two symmetries are nearly identical and the delay time differences between the two are generally small, less than 0.12 s, suggesting that using either symmetry will result in approximately the same predicated SWS parameters. For the analysis we used models with hexagonal symmetry and focused on modeling stations which have the largest number of splitting observations (stations F70S, A20S, N20S and N40S (Figure 7.2)).

The modeling results and parameters used can be found in Figure 7.7 and Tables 7.2, 7.3, 7.4 and 7.5. At station N40S (Figure 7.2B , 7.7A and Table 7.2) in the backarc, the observed fast directions are generally trench-perpendicular (with the exception of event 4). The results are best modeled using an 150 km thick layer of anisotropy in the mantle

wedge with a weaker upper layer of anisotropy that has a dilution factor of 40 % with a thickness that varies from 1-50 km for event 4 . At station N20S (Figure 7.7B and Table 7.3), which is closer to Sumatran Fault, station A20S (Figure 7.7C and Table 7.4) on the Sumatran Fault and station F70S (Figure 7.7D and Table 7.5) west of the Sumatran Fault, the predominant fast direction is trench/fault-parallel. The modeling suggests that the lower layer of anisotropy decreases in thickness from 80 km beneath station N20S to 25 km beneath station F70S, implying that the strength of anisotropy in the mantle wedge decreases moving westwards from the backarc to the forearc. Anisotropy in the upper layer beneath stations N20S, A20S and F70S is stronger than in the lower layer, with a dilution factor and thickness of 50-60 % and 20-40 km, respectively, thus causing the observed trench/fault-parallel fast directions.

The forward modeling results show that the observed fast directions in the Sumatran Fault and backarc regions can be reproduced by two layers of anisotropy . At stations close to and beneath the Sumatran Fault (e.g F70S, A20S and N20S) the upper layer of anisotropy dominates, resulting in trench/fault-parallel fast directions; while in the backarc (e.g. station N40S) the anisotropy in the lower layer is stronger, causing trench perpendicular fast directions. These results support our conclusion that the observed splitting from the local *S* waves in the Sumatran Fault region and backarc is due to an upper layer of anisotropy which has formed from fault-parallel aligned fractures and minerals in the overriding plate, and a second lower layer of anisotropy, within the mantle wedge, due to corner flow (Figure 7.8).

Station N40S	**Upper Layer (Layer 1)**			**Lower Layer (Layer 2)**		
Event No.	Azimuth (°)	Dilution factor (%)	Thickness (km)	Azimuth (°)	Dilution factor (%)	Thickness (km)
1	-40	40	1	50	13	150
2	-40	40	1	50	13	150
3	-40	40	30	50	13	150
4	-40	40	50	50	13	150
5	-40	40	20	50	13	150
6	-40	40	30	50	13	150

Table 7.2: Forward modeling parameters for local SWS for station N40S.

Station N20S	**Upper Layer (Layer 1)**			**Lower Layer (Layer 2)**		
Event No.	Azimuth (°)	Dilution factor (%)	Thickness (km)	Azimuth (°)	Dilution factor (%)	Thickness (km)
1	-40	60	40	50	13	80
2	-40	60	30	50	13	80
3	-40	60	40	50	13	80
4	-40	60	30	50	13	80
5	-40	60	37	50	13	80
6	-40	60	40	50	13	80
7	-40	60	40	50	13	80

Table 7.3: Forward modeling parameters for local SWS for station N20S.

Station A20S	**Upper Layer (Layer 1)**			**Lower Layer (Layer 2)**		
Event No.	Azimuth (°)	Dilution factor (%)	Thickness (km)	Azimuth (°)	Dilution factor (%)	Thickness (km)
1	-40	50	30	50	13	25
2	-40	50	30	50	13	25
3	-40	50	30	50	13	25
4	-40	50	40	50	13	25
5	-40	50	40	50	13	25
6	-40	50	30	50	13	25

Table 7.4: Forward modeling parameters for local SWS for station A20S.

Station N20S	**Upper Layer (Layer 1)**			**Lower Layer (Layer 2)**		
Event No.	Azimuth (°)	Dilution factor (%)	Thickness (km)	Azimuth (°)	Dilution factor (%)	Thickness (km)
1	-40	60	20	50	13	25
2	-40	60	20	50	13	25
3	-40	60	30	50	13	25
4	-40	60	25	50	13	25
5	-40	60	20	50	13	25
6	-40	60	25	50	13	25
7	-40	60	25	50	13	25
	-40	60	20	50	13	25

Table 7.5: Forward modeling parameters for local SWS for station F70S.

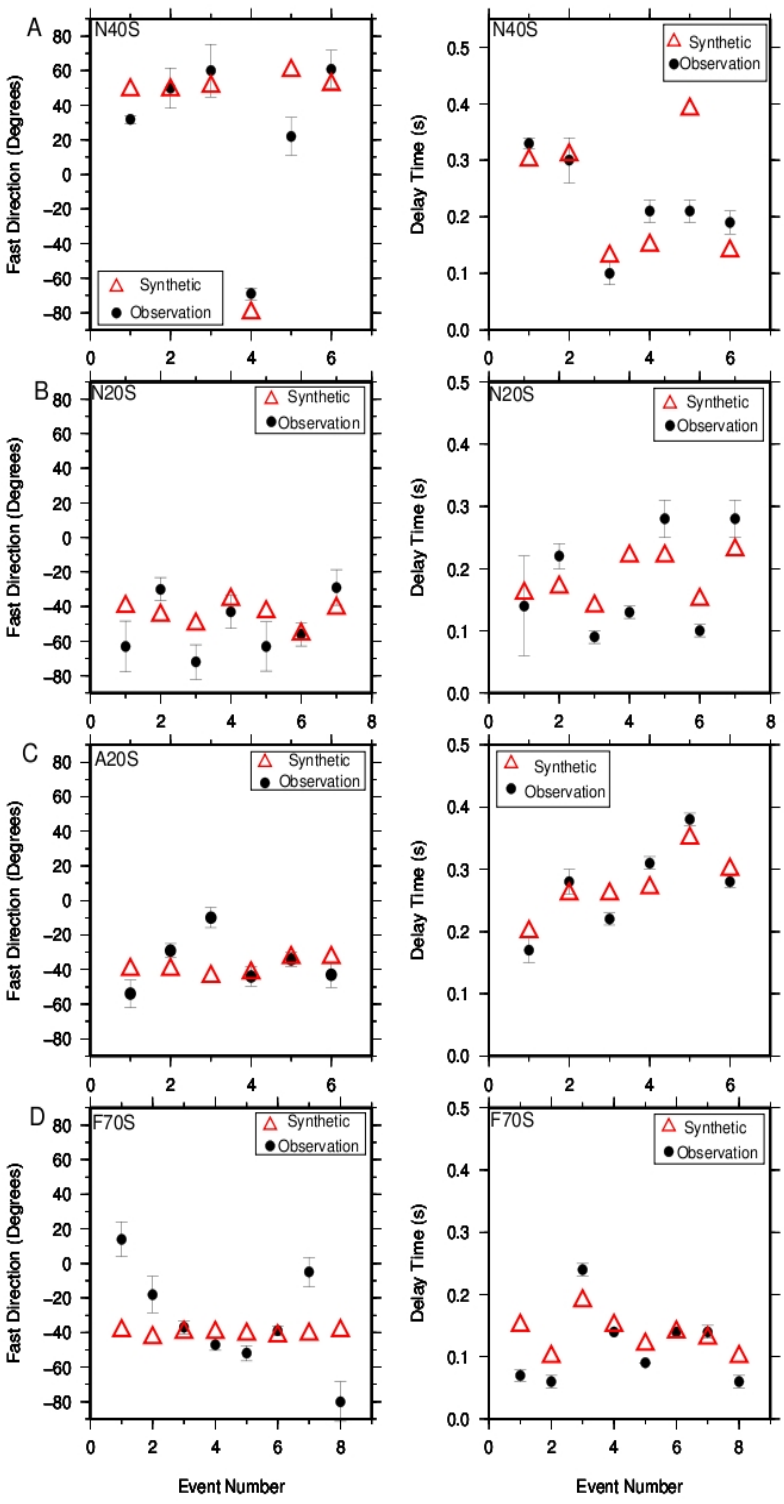

Figure 7.7: Comparison of predicted and observed local SWS. A) Station N40S in the backarc region. B) Station N20S in the backarc region. C) Station A20S in the Sumatran Fault region. D) Station F70S in the Sumatran Fault region. Black circles are observed splitting parameters. Red triangles are predicted SWS. Station locations are shown in Figure 7.2 and model parameters can be found in Table 7.2-7.5.

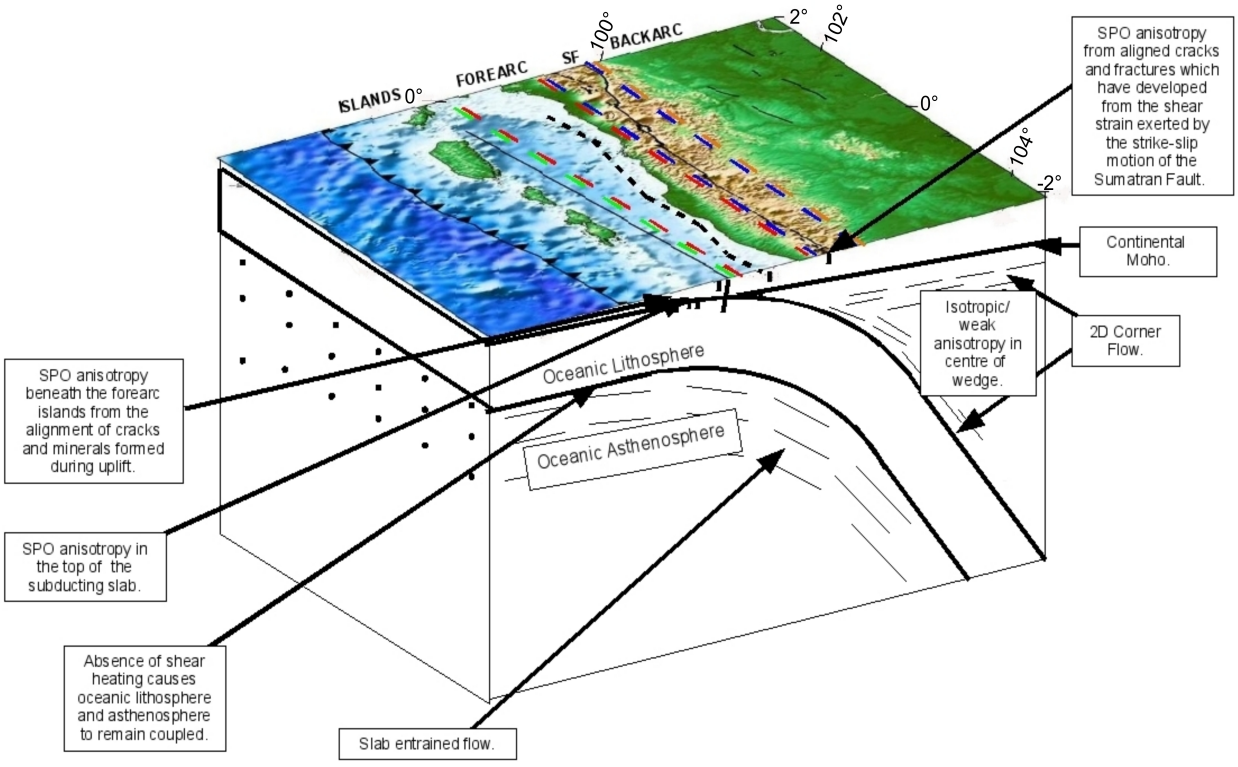

Figure 7.8: Figure illustrating the different types of anisotropy observed along the Sumatran Margin.

7.7 Teleseismic Splitting and Possible Mechanisms

Comparing the delay times of the *SKS* SWS measurements to the delay times of the local SWS measurements allows us to constrain where the anisotropy that generates the *SKS* SWS is located. Though the local SWS measurements and *SKS* SWS measurements were filtered using different frequency bands, the filter bands do overlap and this should minimize the frequency dependent effects between the two data sets. The maximum delay time observed from the local SWS observation is 0.42 s, whereas the delay times of the *SKS* SWS measurements are between 0.8 s and 3.0 s (Figure 7.3). As the local SWS results show only a small amount of splitting, the anisotropy that causes the observed *SKS* SWS must come from beneath the slab interface.

Long and Silver's (2008) global study of SWS concluded that sub-wedge splitting is dominated by trench-parallel directions with only a few exceptions (e.g Cascadia; Currie et al., 2004). Generally, teleseismic SWS measurements reported here exhibit a fast direction which is approximately parallel to the motion of the subducting Indo-Australian Plate (Figure 7.3) and does not fit the global trend observed by Long and Silver (2008). The predominantly APM (Apparent Plate Motion) parallel fast direction agrees with Hammond et al. (2010) (Figure 7.1) who attribute their *SKS* SWS observations to fossilized anisotropy within the subducting slab. However, the forward modeling approach of Hammond et al. (2010) uses a steeply dipping (> 45°) slab, but local seismicity (Lange et al., 2010; Collings et al., 2011) clearly indicates a shallower dipping slab for the region (~35° until 100 km depth), which cause the rays to travel predominately in the oceanic asthenosphere, not within the lithosphere of the subducting slab. Additionally, the thickness of the lithosphere in their model is estimated to be 100 km beneath both Sumatra and Java, which ignores the significant difference in slab age between these two regions (49 Ma below North Sumatra, where the Wharton Fossil Ridge subducts, to 134 Ma beneath Java, Figure 2.1) and is unrealistically large for central Sumatra where the lithospheric thickness is ~70 km. So although fossilized anisotropy within the subducting slab may contribute to the splitting, another source is likely to be present.

Preferentially-orientated hydrated faults and cracks within the uppermost slab have been shown to cause strong SWS with trench-parallel fast directions (Faccenda et al., 2008; Healy et al., 2009). Previous bathymetry, seismic reflection, gravity and magnetic surveys (Deplus, 1998; Graindorge et al., 2008) in the Sunda Arc have found that the subducting Indo-Australian Plate south of Sumatra has N-S trending faults, approximately parallel to the convergence direction, while at Java, trench-parallel (~E-W) normal faults are present on the oceanic crust adjacent to the trench (Masson et al., 1990), reflecting the observed rotation in the fast direction of the *SKS* measurements. Despite this, previous modeling results by Hammond et al. (2010) show that a thin anisotropic layer at the top of the slab cannot fit their observations as the rays only spend a small amount of time within this layer, which results in the magnitude of the splitting

being considerably smaller than the observed δt (0.8-2.0 s, Figure 7.1) for the *SKS* measurements.

The alignment of the *SKS* fast directions with the direction of motion of the Indo-Australian Plate suggests that anisotropy is caused by entrained flow of the asthenosphere beneath the subducting slab. This was first suggested by Savage (1999) who concluded that when a subducting slab is moving over relatively stable asthenosphere, the a-axis and therefore the fast directions are orientated parallel to the direction of plate motion. However, due to the number of trench-parallel observations being recorded from teleseismic phases, this model was neglected for most subduction zones (Long and Silver, 2008). Numerical modeling of entrained asthenospheric flow by Morgan et al. (2007) suggests that the lower side of the slab entrains a layer of asthenosphere, whose thickness depends upon the subduction rate, density contrast and viscosity of the asthenosphere. When the asthenosphere has a 200 km thick upper layer that has a higher temperature and is more depleted than the underlying mantle (formed by buoyant upwelling plumes), a thin sheet (10-30 km thick) of asthenosphere is entrained by the subducting slab and a large scale return flow away from the trench occurs. The thickness of the entrained sheet increases as the subduction rate increases and will be thicker beneath the forearc than beneath the backarc. However, when there is no strong density and viscosity contrast in the upper asthenosphere layer, the asthenosphere is easily dragged down by the slab, resulting in a thick layer (up to 200 km) of asthenosphere being entrained by the slab (Morgan et al., 2007). As the asthenosphere is dragged down beneath the slab, simple shear causes the LPO of minerals (predominantly olivine), with the a-axis dipping approximately at the same angle as the slab and pointing along the convergence direction. This would result in a significant layer of anisotropy beneath the subducting slab.

Trench-parallel directions exhibited by teleseismic phases at the majority of subduction zones around the world are attributed to trench-parallel flow induced by trench migration and requires decoupling between the slab and asthenosphere, a partial barrier to flow at depths and a distant barrier to horizontal flow (Long and Silver, 2008). It is possible that

these requirements are not being fulfilled in some subduction zones, including Sumatra and Cascadia. Long and Silver (2009) hypothesize that for Cascadia, where the teleseismic SWS observations exhibit trench-perpendicular splitting (Currie et al., 2004) despite trench migration occurring, the mechanism for decoupling is not working properly. They propose that the decoupling between the slab and asthenosphere occurs due to a thin entrained layer of hot asthenosphere (Morgan et al., 2007), which requires an upper asthenosphere that is physically distinct from its surroundings. However, unlike Morgan et al. (2007) this physically distinct layer is not attributed to buoyant mantle upwelling; instead it is thought to be a result of shear heating (Long and Silver, 2009). Shear heating occurs when mantle material beneath newly-formed lithosphere is subjected to shear deformation by the motion of the overlying oceanic plate as it moves away from the ridge. Beneath Cascadia it is thought that the young lithosphere (5-10 Ma) there has not reached the amount of strain needed for the shear heating mechanism to produce the very low viscosities needed for decoupling the motion of the slab from the surrounding asthenosphere, allowing a thick layer of asthenosphere to be easily entrained by the slab (Morgan et al., 2007). If this hypothesis is true, one would expect to observe APM parallel fast directions at other subduction zones where young lithosphere is subducting and a transition in fast direction from APM-parallel to trench-parallel in subduction zones where there is an along-strike increase in the age of the subducting crust. Beneath northern Sumatra (where the Wharton Fossil Ridge subducts) and Java there is such an along-strike crustal age variation from 49 Ma in North Sumatra to 134 Ma in Java (Figure 7.1). Although the plate is still significantly older than in Cascadia, one would expect the coupling between the asthenosphere and overlying lithosphere to be stronger beneath northern Sumatra than beneath Java as the amount of shear strain that has been induced will be smaller. The reduced strain beneath Sumatra may therefore not have reached the amount needed for the shear heating mechanism to reach a steady state, allowing the entrainment of the sub-slab asthenosphere. A similar observation of *SKS* SWS fast directions parallel to plate convergence direction has been made in central Chile, where the plate age is 30 Ma (Nippress et al., 2011).

Another important difference between Java and Sumatra is the transition from normal

subduction to oblique subduction (Figure 7.1). Could the change in geometry be responsible for the trench-parallel flow observed beneath Java and trench-oblique flow seen beneath Sumatra? The slab between Java and Sumatra appears continuous (Syracuse and Abers, 2006) and despite the change in subduction angle both regions are undergoing similar magnitudes of trench advance (Lallemand et al., 2008), suggesting that lateral flow should be able to develop beneath Java and Sumatra. This, along with the observation of trench-parallel splitting from sub-slab anisotropy at other oblique subduction zones (e.g New Zealand, Marson-Pidgeon et al., 1999), leads us to reject the transition from normal to oblique subduction as the cause of the variation in *SKS* Φ between Java and Sumatra.

Trench-perpendicular fast directions are observed at 3 stations situated on Batu and Nias Island (blue lines, Figure 7.3), similar to the *SKS* measurements observed at Nias Island by Hammond et al. (2010) (Figure 7.1). Though the measurements were not classed as good because the delay time ratio of the splitting parameters obtained using the rotation correlation method and minimum transverse energy method were not between 0.7 and 1.2 and the misfit between the fast directions were greater than 15°, the results were stable in the three different SWS analysis techniques and therefore should not be automatically rejected. A possible explanation for the small area of trench-perpendicular fast directions is that in this region of the subduction zone the Investigator Fracture Zone is subducting beneath the Eurasian plate, which may complicate the anisotropy.

From the above discussion we suggest that the observed teleseismic SWS is likely to be dominated by LPO sub-slab anisotropy that has developed due to a thick layer of asthenosphere being entrained by the subducting slab (Figure 7.8). A possible mechanism for entrained flow and not trench-parallel flow is that despite trench advance occurring, the shear heating mechanism that is thought to be responsible for decoupling at most subduction zones has not yet produced a low viscosity layer, such that the subducting lithosphere and underlying asthenosphere remain coupled. As the fossil spreading direction is almost parallel to the absolute plate motion it is possible that fossilized anisotropy in the oceanic lithosphere also contributes to the observed splitting,

but the thickness of the lithosphere is far too small to be able to account for the observed splitting delay times.

7.7.1 Forward Modeling

Similar to the local SWS observations, SynthSplit (Abt and Fischer, 2008) was used to forward model the teleseismic SWS observations. For all models a single layer was used to represent the sub-slab anisotropic layer, a 70:30 composition of olivine to orthopyroxene was used and the synthetics were generated using a period of 6.5 s (~0.15 Hz), a typical frequency of the *SKS* waves. We performed numerous sensitivity tests comparing theoretical and observed SWS for each of the input parameters provided by SynthSplit. In particular, we tested the orientation (azimuth) and dip (20°-60°) of the a-axis, symmetry, thickness and dilution factor. Predicted fast directions for hexagonal and orthorhombic symmetries are typically nearly identical (Figure 7.9A). The delay time between the two symmetries varies with backazimuth but generally the differences are small, less than 0.25 s (Figure 7.9A).

The fast directions were modeled using a-axes orientated at different azimuths and dip. When the a-axis is orientated parallel to the trench (-040º) the predicted fast directions clearly do not fit the observed SWS observations (Figure 7.9B). The observed fast directions are best modeled by a layer that has its a-axis aligned in the direction of plate motion (~002°) and dipping steeply at 40°-60°, steeper than the dip of the plate (~35°).

In order to model the observed delay times, the dilution factor and thickness of the layers were varied. For a-axis dips of 40° and 60°, models were run with layers 100 km, 150 km and 200 km thick and dilution factors of 50% and 75% (Figure 7.9C, 7.9D and 7.9E). We noted a trade-off between the layer thickness and the dilution factor as a thicker layer and higher dilution factor will result in larger delay times. A layer whose a-axis is dipping at 60° with either a thick layer (>200 km when a dilution factor of 50% is used) or a high dilution factor (> 75% with a 150 km thick layer) fits the observed delay times for backazimuths of 100°-120° but is unable to fit the observed delay times for

backazimuths of ~37°. However, if the a-axis is dipping at 40°, a layer 150 km thick with a dilution factor of 50%-75% can model all the observed delay times reasonably well. The actual anisotropic strength is likely to be smaller, as we have not included the splitting accrued in the slab, mantle wedge and crust, which will contribute to the observed delay times.

The forward modeling shows that the *SKS* SWS fast direction/delay time dependency on backazimuth can be modeled using a thick (150 -200 km) layer of strong anisotropy (~9% bulk *S* anisotropy) that has its a-axis aligned with the convergence direction (~002°). Furthermore, the forward modeling results suggest that the fast direction dependency on backazimuth is best modeled using an a-axis which is dipping steeply at 40°-60°. However, the forward modeling of the delay time dependency on backazimuth suggests that an a-axis dip of 60° is unable to fit all the observations. The delay times are best modeled using an a-axis dip of ~40°. A dip of 40° is similar to the dip of the subducting slab (~35°) at 40 -100 km, depth (Collings et al., 2011). However, theses values are likely to be poorly constrained due to the simplicity of the forward modeling. For example, it has been assumed that all of the rays arrive at an incidence angle of 10° and the a-axis dip is constant. Despite this, the modeling results suggest that the observed teleseismic SWS is from the LPO sub-slab anisotropy that has developed due to a thick layer of asthenosphere being entrained by the subducting slab (Figure 7.8)

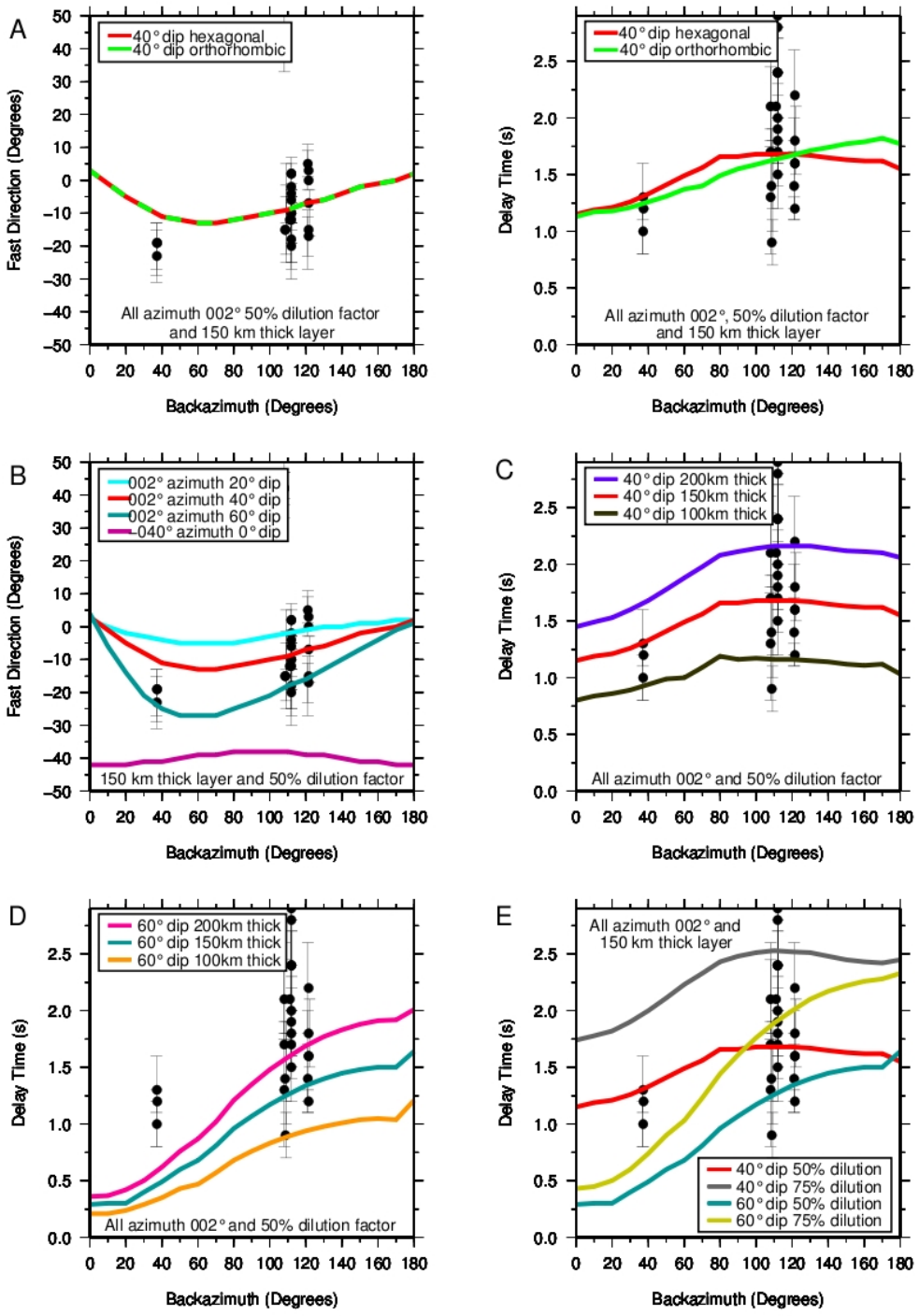

Figure 7.9: Comparison of predicted and observed teleseismic SWS (black circles). Unless otherwise stated the parameters used in the forward modeling are: 150 km thick layer, 50 % dilution factor, a-axis azimuth 002° and dip 40°, assuming hexagonal symmetry. A) Effect of symmetry axis on predicted SWS. B) Sensitivity of predicted SWS to a-axis dip. C) Sensitivity of predicted SWS to layer thickness with an a-axis dipping at 40°. D) Sensitivity of predicted SWS to layer thickness with an a-axis dipping at 60°. E) Sensitivity of predicted SWS to dilution factor and a-axis dip.

7.8 Conclusions

Using local seismic data from two temporary seismic networks in the Sumatra subduction zone we have used SWS observations to improve our understanding of the style and geometry of deformation that occurs. Our main findings are as follows (Figure 7.8):

- Beneath the forearc islands, which are located 75-150 km from the deformation front, a layer of SPO anisotropy is located within the low velocity sediments due to the trench-parallel alignment of cracks and fractures that were formed when the sediments were uplifted.

- In the Sumatran Fault region the predominant fast direction of local earthquake SWS is trench/fault-parallel. The trench/fault-parallel fast direction is attributed to a layer of anisotropy in the continental lithosphere. The anisotropy is formed by fault-parallel aligned minerals and fractures that have developed from the shear strain exerted by the strike-slip motion of the Sumatran Fault. In order to explain all of the measurements within the backarc, the anisotropic layer has to be confined to a ~100 km region around the fault.

- In the backarc region the predominant fast direction of local earthquake SWS is trench-perpendicular. The observed SWS is attributed to LPO anisotropy in the mantle wedge due to 2D corner flow. The small delay times suggest that the centre of the mantle wedge is either isotropic or contains weak anisotropy.

- *SKS* SWS is primarily sensitive to the sub-slab anisotropy structure and indicates that beneath the slab interface a thick layer (150 km-200 km) of LPO anisotropy has developed due to the asthenosphere being entrained by the subducting slab. The a-axis of the olivine crystals are aligned parallel to the APM direction of the Indo-Australian Plate and are at a similar dip (~40°) to the dip of the subducting slab (35°). A possible mechanism for the oceanic lithosphere and asthenosphere

to remain coupled is that the shear heating mechanism has not yet heated up the boundary layer below the slab sufficiently to allow a very low viscosity channel to form and cause decoupling between the subducting plate and the asthenosphere.

7.9 Acknowledgments

The project was funded by NERC (NE/D002575/1 and NE/F012209/1). We thank the SeisUK facility in Leicester (loans 828 and 858) and the University of Liverpool for the provision of instruments. We also thank the Earth Observatory Singapore for funding part of the fieldwork and letting us co-occupy sites of the SuGAr GPS array. We acknowledge the support of colleagues at Geotek-LIPI and the whole field crew which made this experiment possible. We gratefully acknowledge the cooperation of many Sumatran landowners for allowing us to install the seismic stations on their property. Furthermore we thank the captain and crew of the Andalas and the field crews for their excellent work under difficult conditions.

Chapter 8

The Structure and Seismological Processes Occurring within the Sumatra Subduction Zone

In this study we have used data from two local networks, Mentawai and Central Sumatra, installed between December 2007 and February 2009, from 4°S to 2°N, reaching from the forearc islands to the backarc, to constrain the geometry of the subduction zone, the state of stress in the slab and the upper plate, as well as the underlying subduction zone processes. Using a high quality data set of events from the Mentawai network a 1D minimum velocity model was derived. Subsequently, we inverted for 2D and 3D *Vp* and *Vp/Vs* models of the region and accurate hypocentre locations. Focal mechanisms were obtained using the first motion polarity of the *P* wave arrival and the take-off angles and azimuths computed in the final 3D velocity model. Additionally, SWS analysis for local and teleseismic *S* wave arrivals was performed to determine the type and amount of anisotropy beneath the slab interface, within the mantle wedge and within the continental crust.

In the following chapter the main findings of this study are bought together to produce a comprehensive image of the subduction zone and the processes occurring within it.

8.1 The Forearc

The Sumatra forearc contains forearc islands, which are a unique feature of the subduction zone. The forearc islands are part of the inner wedge in the dynamic Coulomb Wedge model, where the inner wedge overlies the velocity weakening part of the subduction interface and the outer wedge overlies the velocity strengthening part of the subduction interface (Wang and Hu, 2006). They are composed of low velocity sediments (4.5-5.8 km/s) (Figure 5.8 and 5.9) that contain free water within their pores

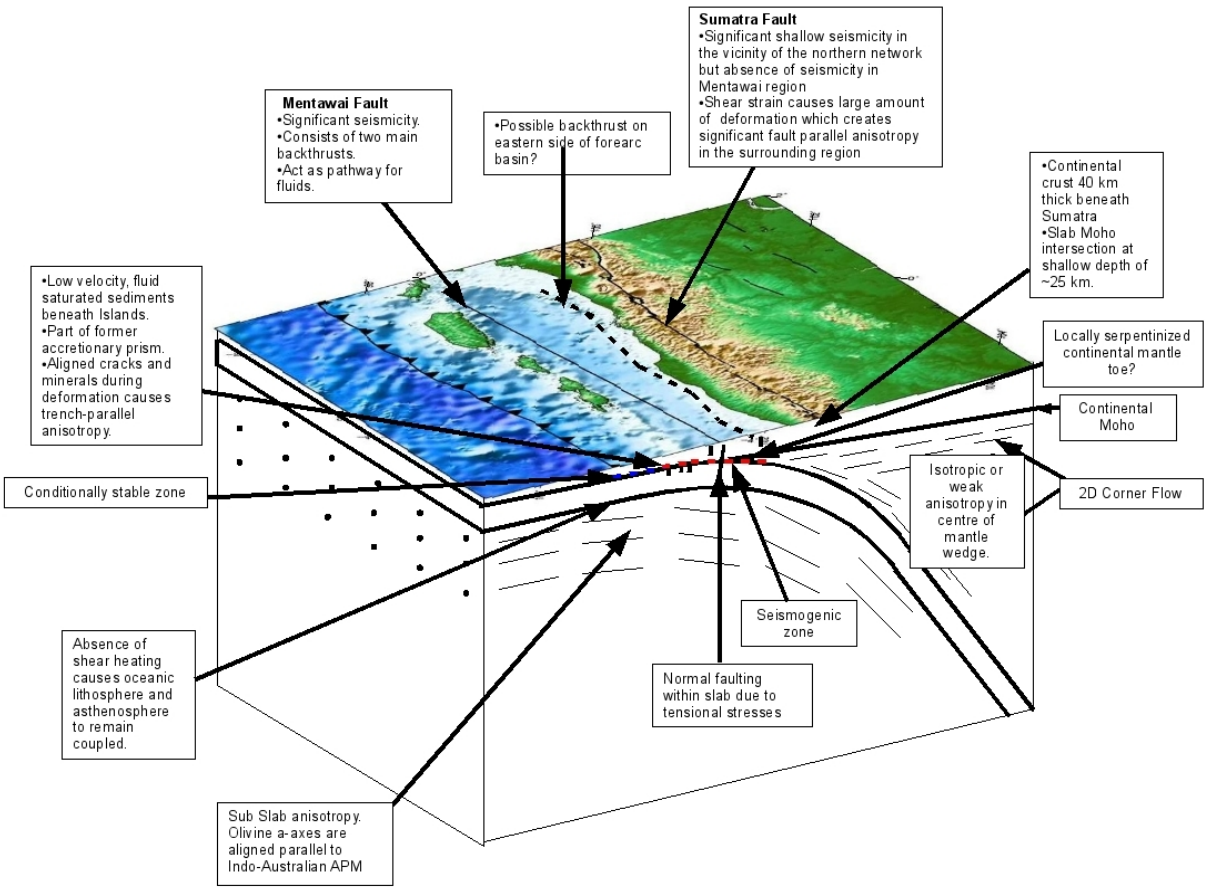

Figure 8.1: The structure and seismogenic processes occurring within the Sumatra subduction zone; inferred from the tomography, seismicity distribution, focal mechanisms and SWS results.

which is expelled during compaction (Figure 8.1). The sediments were previously part of a former accretionary prism which was later consolidated and uplifted (Kopp et al., 2001, (Figure 5.12 and 8.1)). No high velocity regions are imaged beneath the forearc islands in the Mentawai region (Figure 5.8 and 5.9), suggesting that no ophiolites are present and that their uplift was not aided by underplating of sliced oceanic crust, which has previously been suggested (Samuel et al., 1997; Singh et al., 2008). During uplift, the forearc islands underwent a significant amount of deformation, creating aligned cracks and fractures which causes SPO anisotropy.

The forearc basins (Figure 8.1), landward of the forearc islands, are underlain by a 25

km thick continental crust, that increases to a thickness of 30 km beneath mainland Sumatra. The significant amount of seismic activity that occurs within the continental crust in the Mentawai segment suggests a substantial amount of deformation is occurring within the overriding plate. Hypocentre locations from the earthquakes recorded in the Mentawai network suggest that two faults exist within the forearc, the Mentawai Fault on the western side of the forearc basin between the forearc islands and the forearc basin, and a second backthrust on the eastern side of the forearc basin (Figure 8.1).

The Mentawai Fault, on the western side of the forearc basin (Figure 8.1), exhibits seismicity from 5 to 25 km depth within the centre of the study region and is dispersed over two backthrusts, a main backthrust and a frontal backthrust. The high *Vp/Vs* imaged at the fault implies that the backthrust could act as a pathway for fluids released within the slab. A recent study by Kumar et al. (2010) has postulated that expelled aqueous fluid from the down-going plate migrates upwards through the fracture conduit at the Mentawai Fault, instead of forming serpentinization at the downdip region. This would result in a wide seismogenic zone, agreeing with our observations (see section 8.4).

A backthrust, similar to the Mentawai Fault, has been imaged in the northern Sumatra segment of the Sumatra Megathrust (Chauhan et al., 2009), suggesting that backthrusts are a persistent feature along the Sumatran margin. In the northern Sumatra segment the backthrust is divided into a main and frontal backthrust (Chauhan et al., 2009), similar to the observations made by Singh et al., (2009) for the Mentawai Fault in our study region. Chauhan et al. (2009) suggest that the frontal backthrust in the northern segment is the continental backstop on which the thick, highly compacted, accreted sediments, lying to the SW, deform. Due to the similarities between the backthrusts in the northern Sumatra segment and the Mentawai segment it is therefore feasible that the frontal backthrust also acts as the continental backstop within the Mentawai segment (Figure 5.9, 5.12 and 8.1). In addition to this, in the northern Sumatra segment, sharp bathymetry lineaments lie at the SW of the Aceh basin, where the frontal backthrust arrives at the seafloor, implying that the backthrust is active within this segment and consequently could be uplifting the forearc islands, though the slip occurring may be co-seismic or aseismic. Within our

study area we unfortunately do not have high resolution bathymetry available, but the presence of significant seismicity where the Mentawai Fault is thought to be located (Figure 5.8, 5.9. and 5.11) does indicate that the backthrust is also active in the central/southern Mentawai segment. A recent study in the northern Mentawai segment has also concluded that two clusters of activity occurred on the Mentawai Fault in 2005 and 2009 (Wiseman et al., 2011b). However, from our results we are unable to determine whether, during a large event, co-seismic slip could occur along the backthrust, or if the backthrust itself is a plausible source for a large destructive earthquake, which would be an additional tsunami hazard. During the 2004 rupture it has been suggested that a secondary source of tsunami generation may have existed (Smith et al., 2005) and co-seismic slip along the backthrust may have been a geologically viable source for this (Chauhan et al., 2009).

In contrast to the central network (Lange et al., 2010), no seismicity was recorded on the Sumatran Fault from the Mentawai network. However, SWS analysis on traces from central network stations on and around the Sumatran Fault indicate that there is a layer of anisotropy in the continental lithosphere causing trench/fault-parallel splitting (Figure 7.4). The anisotropy has formed from fault-parallel aligned fractures and minerals that have developed from the shear strain exerted by the strike-slip motion of the Sumatran Fault.

8.2 The Continental Mantle

Beneath Sumatra the continental Moho lies at a depth of 30 to 40 km, shallowing beneath the forearc to intersect the slab at 25 km depth, ~140 km from the deformation front (Figure 8.1). From the seismicity distribution, tomography and anisotropy results we can determine information about the thermal structure of the mantle wedge, in particular the cold forearc and hot volcanic arc.

The forearc mantle overlying the decoupled zone between the wedge and slab is cold and isolated from 2D corner flow, consequently causing the thermal regime of the

mantle wedge to be controlled by the subducting slab. These low temperature conditions provide a stable environment for the formation of serpentinite in the forearc, providing there is fluid present. The point on the slab interface where decoupling to partial coupling between the overlying mantle wedge and slab occurs, is thought to coincide with the downdip limit of large megathrust earthquakes (Kneller et al., 2005). In the Mentawai region of Sumatra the downdip limit of large thrust earthquakes corresponds to approximately 50 km depth (beneath the eastern side of the forearc basin), suggesting that the wedge/slab interface above this depth is decoupled and this is where the cold forearc is located (Kneller et al., 2005) (Figure 8.2). In Sumatra, like all other subduction zones, the presence of a cold forearc corner causes surface heat flow observations to decrease from ~100 mW/m^2 at the trench to values of ~50 mW/m^2 above the decoupled region (Wada et al., 2008; Hippchen and Hyndman, 2008). However, despite the cold forearc conditions providing a stable environment for serpentinization, in Sumatra no

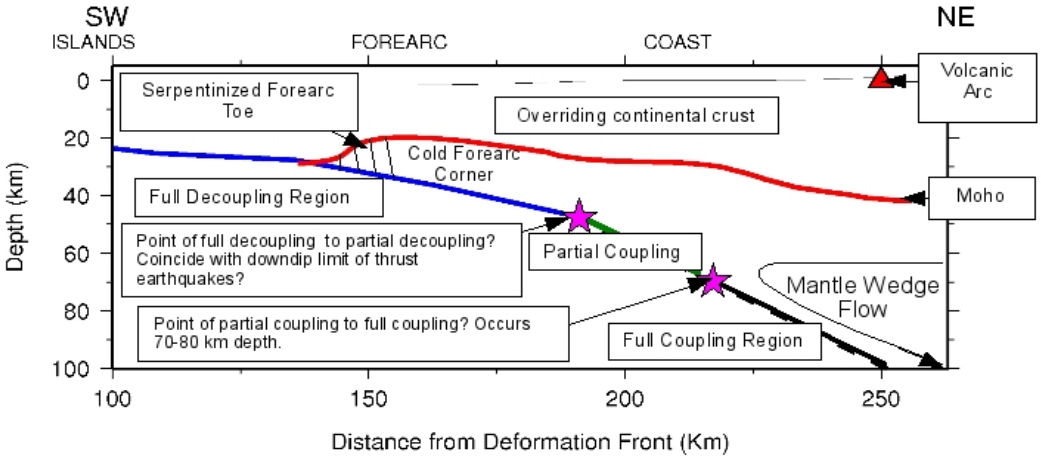

Figure 8.2: Thermal structure of the Sumatra subduction zone

widespread serpentinization is observed as we do not observe any large regions of the mantle wedge that have a low *Vp* and high *Vp/Vs* (Figure 5.8, 5.9, 8.1 and 8.2). Only a small localized region with a low *Vp* (~7.70 km/s)and high *Vp/Vs* (> 1.85) is observed at the toe of the wedge (Figure 5.8 and 5.12), suggesting either that fluids are not released or, if they are, that they do not infiltrate the mantle wedge. If fluids are released from the

down-going plate they may migrate through a fracture conduit at the Mentawai Fault, instead of causing serpentinization (Kumar et al., 2010), resulting in a wide seismogenic zone.

Beneath 50 km depth partial decoupling occurs, with full coupling between the wedge and interface taking place beneath 70-80 km depth, below and downdip of the volcanic arc (Wada and Wang, 2009). Within the fully coupled region, the coupling between the wedge and slab causes hot material from greater depths to replace the colder material that travels downdip with the slab, creating a corner flow within the wedge that controls the thermal regime. The introduction of corner flow within the wedge results in an increase in the surface heat flow (Wada et al., 2008). Thermal models of the Sumatra subduction zone and surface heat flow measurements suggest that the introduction of corner flow causes an increase in heat flow from ~50 mW/m^2, 150 km from the deformation front, to ~100 mW/m^2, 275 km from the deformation front (Hippchen and Hyndman, 2008). Without the introduction of corner flow the observed surface heat flow would continue to decrease as the distance from the deformation front increases (Wada et al., 2008). Corner flow in the mantle wedge also allows A-type olivine fabric to develop. The a-axes of the olivine minerals are aligned in the direction of mantle flow, thus producing trench-perpendicular splitting (Figure 8.1). For events in the backarc and Sumatran Fault regions, we observe trench-perpendicular splitting directions that exhibit a positive correlation between delay time and ray path length in the mantle wedge (Figure 7.5), suggesting that 2D corner flow can be found ~225-250 km from the deformation front, where the slab lies at a depth > 100 km. In this region full coupling between the plate interface and mantle wedge is taking place. Closer to the deformation front, within the forearc region, only a small number of splitting measurements are obtained and there is no predominant fast direction. The hypocentres of three events arriving at the forearc station are within the partially coupled region between the subducting interface and mantle wedge and therefore 2D corner flow may not be present (Kneller et al., 2005; Wada et al., 2008; Wada and Wang, 2009). Additionally, the small number of splitting measurements and lack of coherent fast direction in the forearc may be due to competition between 2D corner flow and 3D flow generated from trench

migration/advance (Long and Silver, 2008). This results in a non-coherent flow field which can change rapidly over short length scales and as a consequence causes only a small amount of splitting,

8.3 The Subducting Oceanic Plate

The seismicity and tomography has allowed us to image the Wadati Benioff zone within the Mentawai segment of the Sumatra subduction zone. The subducting slab lies at a depth of 20 km beneath the forearc islands, dipping at 13°, to reach a depth of 30 km beneath the western side of the forearc islands (Figure 5.12 and 8.1). This is similar to the results of a seismic reflection study by Singh et al. (2011a) who imaged the slab dipping at 12°, ~110 km from the deformation front (~ 20 km depth), within the Mentawai region. The aftershocks of the Sumatra-Andaman earthquake also indicate that the subducting slab dips at a shallow angle (< 10°) close to the trench, before increasing to between 15°-20° at larger depths, similar to the observations in our study region (Engdahl et al., 2007). This suggests that for shallow depths above ~30 km, the subduction angle of the plate is similar along the whole of the Sumatran margin. The seismicity distribution and high *Vp/Vs* ratio of 1.75-1.90 (Figure 5.8 and 5.9) indicates that in the Mentawai segment of the subduction zone the upper part of the subducting slab (0- 25 km depth) is hydrated and faulted.

Beneath a depth of 30 km (~150 km from the deformation front) the slab is no longer hydrated and faulted (Figure 5.8 and 5.9), and its dip increases to ~35°, resulting in the slab lying at a depth of 60 km below the coast of Sumatra (Figure 8.1). A previous study in Sumatra has suggested that in the northern Sumatra segment of the megathrust, where the age of the crust is 55 Ma to 60 Ma (Müller et al., 1997), the slab dips at ~30° below 40-50 km depth; while beneath Andaman and Java, where the plate age is older (100 Ma, Müller et al., 1997) the slab dip is steeper, 40° to 50° (Shapiro et al., 2008) at the same depth. In the Mentawai region the age of the plate is ~60 Ma. If the thermal parameters (i.e. temperature) primarily control the dip of the subducting plate along the Sumatra megathrust at depths > 40-50 km, we would assume the dip of the plate in our study

region would be closer to the dip observed within the northern Sumatra segment than the dip observed within the Java/Andaman segments, which is what we found.

A thick layer of anisotropy (> 150 km) can be found in the oceanic asthenosphere of the subducting slab. The a-axes of the predominant mineral, olivine, are orientated in the direction of plate convergence (002°), dipping at an angle of ~40°, due to entrained flow. This implies that the asthenosphere is still strongly coupled to the subducting slab and has not become decoupled as suggested for the majority of subduction zones around the world to account for the trench-parallel fast directions.

8.4 The Seismogenic Zone

The 2007 aftershocks recorded within our study indicate that seismicity begins at approximately 20 km depth along the subduction interface, continuing almost uninterrupted, until 50 km depth. This, along with the co-seismic slip of the 2007 and 2010 ruptures, as well as the tomography, allows us to put constraints on the updip and downdip limits of the seismogenic zone within the Mentawai region, which is important for assessing seismic hazard.

Prior to the 2010 earthquake, based on the 2007 Bengkulu aftershock distribution, as well as the extent of the Bengkulu and Nias megathrust ruptures, the updip limit of the seismogenic zone was thought to coincide with the slope break of the forearc morphology (approximately 500-1000 m bathymetry contour) (Tilmann et al. 2010), which marks the transition from outer wedge to inner wedge (Wang and Hu, 2006) (Figure 8.3 A). This is similar to what has previously been observed at many subduction zones around the world, including Java (Krabbenhoeft et al., 2010). The outer wedge actively deforms, building up the updip velocity-strengthening part of the subduction fault (seaward portion of the accretionary prism) while the inner wedge is less deformed, overlying the velocity-weakening part of the subduction fault, with the slope break representing the transition in physical properties and plate coupling. This usually coincides with the point the temperature on the thrust fault reaches 100°C - 150°C (e.g.

Oleskevich et al.,1999) which allows stable sliding smectite clays to dehydrate, producing illite chlorite that exhibits stick slip or velocity-weakening behaviour. However, the rupture area of the 2010 earthquake and its aftershock locations, as well as the discovery of an historical event in North Sumatra in 1907 within the shallow part of the Simeulue-Nias segment (Kanamori et al., 2010), suggest that for the Sumatra margin this conclusion may need to to be revised.

The 2010 event nucleated just southwest of a cluster of 2007 aftershocks and propagated to the NW, updip to the trench, beneath the outer wedge, in a region that was previously almost asesmic during the temporary experiment; only a handful of events were located there and the depths of all but one of them, though poorly constrained, indicate hypocentres well within the down-going plate. The 2010 Mentawai event appears to follow the model of Bilek and Lay (2002) which proposes that rupture initiates within a frictionally unstable region of the interface before propagating updip, into the

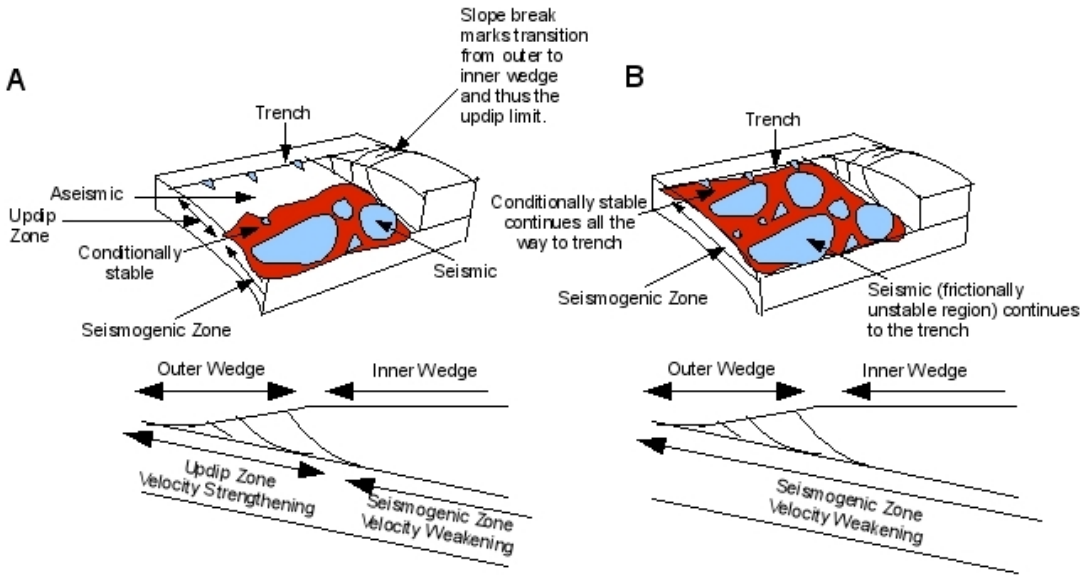

Figure 8.3: Updip limit of the seismogenic zone. A) The previously assumed Coulomb Wedge model of Wang and Hu (2006) in which the updip limit of rupture coincides within the slope break that marks the transition from outer to inner wedge. B) The model currently thought to apply in Sumatra. Conditionally stable behaviour extends to the trench with patches of frictionally stable behaviour within it, suggesting that the updip limit extends to trench and is not marked by the slope break.

conditionally stable zone where no rupture can nucleate. However, the presence of aftershocks nucleating within the suggested conditionally stable zone, at depths shallow enough to be on the plate interface, suggests that small patches of the plate interface exhibit frictionally unstable behaviour all the way to the trench (Figure 8.3 B) (Bilek et al., 2011).

The unusual case of the 2010 tsunami earthquake rupturing directly updip of a previous megathrust rupture, (Konca et al., 2008; Lay et al., 2011; Newman et al., 2011), and with comparable peak and average slip values (Lay et al., 2011; Newman et al., 2011), raises the question whether the margin usually breaks in this mode, or whether great megathrust earthquakes more commonly break the whole width from the trench to the downdip end of the seismogenic zone. Although no definitive answer is possible, there does appear to be evidence for the separate rupture of the deep frictionally unstable interface and conditionally stable shallow interface in the Simeulue-Nias segment of the margin. A historical event in north Sumatra in 1907 has recently been shown to have occurred within the shallow part of the Simeulue-Nias segment (Kanamori et al., 2010), notably within an area that has also experienced significant afterslip after the 2005 megathrust earthquake (Hsu et al., 2006). The updip ends of the 2005 Nias earthquake and 2007 Bengkulu earthquake, as well as their aftershocks, appear to be correlated with the forearc morphology as predicted by dynamic Coulomb Wedge theory (Wang and Hu, 2006), suggesting that at least the boundary between the great earthquake rupture and the tsunami earthquake is not specific to the current sequence but a long-standing feature of the margin. Therefore the separate rupture of the conditionally stable shallow plate interface in tsunami earthquakes and the deep frictionally unstable part in great megathrust earthquakes is not unprecedented, and the potential for tsunami earthquakes, either following a great megathrust rupture or in the interseismic period, probably exists for a large part of the Sunda Margin. We also can not rule out the rupture initiating in the known frictionally unstable region and then subsequently propagating all the way to the trench, as in the southern part of 2004 rupture, which in the Padang region would have the potential to cause a M_w 8.5 earthquake.

At subduction zones the downdip limit of the locked fault zone is thought to correspond to either a thermal (Oleskevich et al., 1999) or a compositional control (Hyndman et al., 1997). If the plate interface does not reach temperatures of 350°C-450°C before its intersection with the continental Moho, the downdip limit is thought to occur there due to the presence of aseismic hydrous minerals (serpentinite) in the overlying mantle that allow stable sliding. If the critical temperatures are reached before the Moho/subduction thrust intersection, aseismic slip occurs due to the stable sliding of quartzo-feldspathic rocks. In the Mentawai segment, based on the 7.5 km/s contour, the subduction interface intersects the continental Moho ~140 km from the trench at a shallow depth of ~25 km . The hypocentre of the M_w 7.9 event on the 12 September 2007 and the slip models of both the M_w 8.4 and M_w 7.9 2007 events (Figure 8.1) as well as geodetic data indicate that the seismogenic zone extends beyond this point until at least ~185 km from the trench (Chlieh et al., 2008; Konca et al., 2008). This agrees with the seismicity distribution we obtained, as seismicity is present almost continuously along the subduction interface until ~50 km depth, 180 km from the trench but beyond this, it is diffuse and not observed beyond 225 km from the trench. Therefore, the Moho inferred from the velocity model is shallower than the observed downdip limit of the seismogenic zone. This contradicts the hypothesis that the continental Moho-slab interface intersection is the downdip limit, if the critical temperature is not already reached at shallower depths. This appears to be a coherent feature of the Sunda Margin, as Dessa et al. (2009) and Klingelhoefer et al. (2010) suggest that the deeper part of the 2004 rupture also occurred on the interface between the forearc mantle and down-going plate.

The thermal models of Hippchen and Hyndman (2008) for the Batu Islands, where the plate age is ~44 Ma, indicate that the 350°C to 450°C isotherms are reached 156 to 230 km from the trench, respectively. The plate age at the Mentawai segment is ~ 60 Ma (Sdrolias and Müller, 2006), which would move the thermal limits ~ 20 km landward to 176 and 250 km respectively (Hippchen and Hyndman, 2008) where the subducting slab is beneath the continental Moho. This indicates that the subducting plate is too cool to allow stable sliding of quartzo-feldspathic rocks (Blanpied et al., 1991, 1995) above the Moho/subduction thrust intersection. The inferred downdip limit for the seismogenic

zone from our seismicity distribution and from the slip models of the 2007 events lies between the 350°C and 450°C isotherms, which is well below the temperature needed for ductile flow of mafic rocks and crust (Hippchen and Hyndman, 2008).

A potential explanation for the downdip zone to be deeper than the Moho intersection is that the forearc mantle is not serpentinized. In this study we generally do not observe a lower *Vp* and high *Vp/Vs* in the mantle wedge (Figure 5.8 and 5.9) suggesting no widespread serpentinization but we do observe a small amount at the toe of the mantle wedge, adjacent to the subduction interface. The region of very localized serpentinization coincides with the gap in aftershock activity on the subduction interface (~150 km from the deformation front). Despite the absence of aftershock activity, this region of the interface did experience co-seismic slip during the M_w 8.4 and M_w 7.9 event. It has previously been proposed by DeShon et al. (2006) that in Costa Rica, where the mantle wedge is serpentinized, rupture during a large earthquake may not initiate along the subduction interface where there is serpentinization but is still able to propagate along it. This may be similar to our findings for the Mentawai region as the 2007 events ruptured along the region of partial serpentinization but due to the possible weaker coupling in this region, aftershocks were unable to initiate.

A possible cause for the absence of serpentinization in the mantle wedge is that the mechanism of fluid release has a specific temperature range and as a result there are gaps where there is no slab dehydration (Dessa et al., 2009). In our study region of Sumatra, the age of the subducting Indo-Australian Plate is ~ 60 Ma (Sdrolias and Müller, 2006) causing peak crustal dehydration to occur at ~72 km depth, at the top of the subducting slab (Wada and Wang, 2009). As a result we would not anticipate the degree of serpentinization observed in the Cascadia subduction zone, where crustal dehydration occurs at a shallower depth of ~40 km (Wada and Wang, 2009). A higher degree of volcanism would instead occur, which is what is observed (Wada and Wang, 2009). Alternatively, the fluids released from the subducting slab may not react with the forearc lithospheric mantle as they do not infiltrate it; they instead could be drained trenchwards along the hydrofractured main thrust zone (Seno, 2005). It has been suggested the

Mentawai Fault may act as fracture conduit for fluids expelled from the down-going plate (Kumar et al., 2010), which may explain the high *Vp/Vs* ratio imaged at the fault in the tomography models.

8.5 Where will the Next Large Earthquake Occur?

A common question that is asked in assessing ruptures along a subduction megathrust is where will the next earthquake occur? There are two main opposing models to explain rupture initiation. The first model, the asperity model, assumes that high moment release (asperities) occurs because of the frictional properties of the plate interface (Lay and Kanamori, 1981). This results in the rupture segmentation remaining the same for several earthquake cycles. Alternatively, the second model assumes that time-dependent stress heterogeneities (filling of seismic gaps) are the dominant factor controlling the extent of great earthquakes, implying that rupture regions will vary with each earthquake cycle (Shaw, 2000).

In Sumatra we generally do not observe any correlation between forearc basins/negative gravity anomalies and regions of peak co-seismic slip, but a relationship between strongly coupled patches of the megathrust and seismic asperities is observed (Chlieh et al., 2008). Despite this being a different association than was previously suggested by Wells et al. (2003) and Song and Simons (2003), it still suggests that asperities are due to frictional properties of the plate interface, therefore implying that the observed segmentation will persist for several earthquake cycles.

From the apparent correlation between the co-seismic slip distribution of past events in different earthquake cycles, as well as the relationship between co-seismic slip and areas of high coupling, two regions that act as a permanent barrier to rupture propagation can be identified within the Mentawai segment.

The first long-term barrier is at the northern end of the Mentawai segment (Figure 1.1 and 2.2), roughly at the equator, beneath the Batu Islands and coincides with a gravity

high, low coupling area and a narrow locked zone (Chlieh et al., 2008). This barrier stopped the northern rupture of 1797 event and the southern ruptures of the1861 and 2005 events. The region itself does not experience any earthquakes greater than $M_w > 8$ (e.g. M_w 7.7 in 1935, Rivera et al., 2004). Previous geophysical surveys have identified that in this region the Investigator Fracture Zone on the Indo-Australian Plate subducts beneath the overriding Eurasian Plate, which could act as a barrier to rupture propagation (Newcomb and McCann, 1987). Various mechanisms have previously been suggested for the cause of this barrier, for example, the increasing roughness of the plate, creating regions of velocity weakening material with very high fracture energy (amount of energy needed to maintain an ongoing rupture propagation on a fault) (Llenos and McGuire, 2007) and patches of seismogenic strengthening material existing in the previously assumed velocity-weakening part of the megathrust (Llenos and McGuire, 2007).

The second permanent barrier is at the southern end of the Mentawai segment (Figure 1.1), near Enggano Island within a weakly coupled region (Chlieh et al.,2008) that does not experience any earthquakes greater than $M_w > 8$. Within this region we are unable to assign the low coupling to the subduction of a fracture zone. Singh et al. (2011b) have found evidence for a subducted seamount, which could entrain fluid-rich sediments at the subduction interface and damage the overriding plate, therefore reducing the interface coupling. However, the width of this seamount, 40 km, is not large enough to account for the whole of the low coupling area between 4°S and 6°S. Therefore the cause of this area of low coupling remains enigmatic.

The recent earthquake cycle in the Mentawai segment began with an M_w 8.4 event on 12 September 2007 (Figure 2.2). This rupture initiated in the southern region of the Mentawai segment, close to the weakly coupled area of the megathrust at Enggano Island, and propagated north to North Pagai Island. An M_w 7.9 earthquake occurred 12 hours later, near the northern end of the M_w 8.4 asperity, rupturing the downdip region of the seismogenic zone (Figure 2.2). The 2007 ruptures ceased within a highly coupled region of the plate interface, suggesting that their termination was controlled by

variations in shear stress along the margin and not the properties of the plate interface (Konca et al., 2008). In our seismicity distribution we find a NW-SE trending group of aftershocks immediately updip of the peak slip region in the northern asperity of the first earthquake on the 12 September 2007 (M_w 8.4) (Figure 5.11). Updip of the second earthquake (M_W 7.9), aftershock activity is more intense and extends to the forearc islands. However, the majority of aftershocks, including the M_w 7.2 event on 25 February 2008, are found further along strike, NW of North Pagai Island, between the main co-seismic rupture asperities of the M_w 8.4 and M_w 7.9 events and the secondary (northwestern) asperity of the M_w 7.9 event, located at 2° S (Figure 5.11). This region appears not to have ruptured during the two events but experiences a large proportion of the aftershocks we recorded in our network. The 25 October 2010 M_w 7.7 (5.13) event initiated just southwest of a 2007 aftershock cluster, on the southwest side of South Pagai Island, and propagated updip to the trench, implying that the aftershocks near the hypocentre had concentrated the stress within this region (Figure 5.13). Following this pattern, we anticipate that the next large rupture initiation will be at roughly 1-2°S, just north of our recorded aftershock distribution (Figure 5.11), as the aftershocks will have concentrated the stress within this region as well. The rupture would then propagate north to the weakly coupled patch of the megathrust at the Batu Islands (Figure 5.1), within the previous rupture area of the 1797 earthquake, where it has been well-documented that an earthquake is overdue (e.g Chlieh et al., 2008). Despite the shallow part of the interface rupturing separately to the frictionally unstable part in the current earthquake cycle of the Mentawai segment, a 200 km wide rupture could potentially take place along the interface in this region, causing a devastating earthquake and tsunami.

Chapter 9

Conclusions

Using local seismic data from two temporary seismic networks we have imaged the structure of the Mentawai region, within the Mentawai Segment of the Sumatra subduction zone (Figure 1.2 and 2.1) by inverting for 2D and 3D velocity models and accurately relocating aftershocks of the 12 September 2007 M_w 8.4 and M_w 7.9 earthquakes. In addition to this we have used shear wave splitting (SWS) observations to determine seismic anisotropy within the region and thus increase our understanding of the style and geometry of deformation occurring. Our main conclusions are:

- The forearc islands are underlain by upto 20km thick, low *Vp* (< 5.8 km/s) and high *Vp/Vs* (>2) material, probably fluid-saturated sediments which were part of a former accretionary prism. A layer of SPO anisotropy is located within the low velocity sediments due to the alignment of cracks and fractures that were formed when the sediments were uplifted.

- Clustered seismic activity is found for distances of ~75-180 km from the trench and to a depth of ~50 km, but sparse activity associated with the slab can be traced down to depths of 100 km. However, no significant local seismicity is located below the downdip end of the M_w 8.4 Bengkulu earthquake on 12 September 2007.

- Underneath the Mentawai Islands the plate interface lies at ~20 km depth, with the seismicity distribution and high *Vp/Vs* ratio (1.75-1.90) suggesting it is faulted and hydrated. Further landward at ~30 km depth we found a cluster of normal faulting events below the plate interface, which are thought to initiate from tensional stresses within the slab.

•Beneath the slab interface a thick layer (150-200 km) of sub-slab LPO anisotropy had developed due to the asthenosphere being entrained by the subducting slab. The a-axes of the olivine crystals are aligned parallel to the APM of the Indo-Australian Plate and at ~40°. A possible mechanisms for the oceanic lithosphere and asthenosphere to have remained coupled, unlike the majority of subduction zones around the world, is that the shear heating mechanism has not yet heated up the boundary layer below the slab sufficiently to allow a very low viscosity channel to form and cause decoupling between the subducting plate and the asthenosphere.

•The continental Moho is less than 30 km deep at the point of intersection with the subduction thrust. Lower *P* wave velocities of around 7.5 to 7.7 km/s and high *Vp/Vs* ratios of 1.8 to 1.9 in the toe of the mantle wedge indicate a modest degree of mantle serpentinization. At the subduction interface, adjacent to the region of modest serpentinization, there are no aftershocks despite this region rupturing during the 2007 events, suggesting that there is weaker coupling in this area.

•In the backarc region the predominant fast direction of the local SWS measurements is trench-perpendicular. The trench-perpendicular fast directions show a positive correlation between delay time and ray path distance in the mantle wedge. This suggests that anisotropy is due to 2D corner flow in the mantle wedge. However, the small delay times suggest that the centre of the mantle wedge is either isotropic or contains weak anisotropy.

•Two clusters of activity are found within the ~25 to 30 km thick overriding crust. The location of the first cluster confirms that the Mentawai Fault is active and may act as a path way for fluid migration. Focal mechanisms suggest that the Mentawai Fault may accommodate backthrust movement. The second cluster on the eastern side of the forearc basin exhibits thrust motion and could be interpreted as a second backthrust, assuming a fault is aligned with the NE dipping seismicity cluster.

•No seismicity was recorded on the Sumatran Fault from the Mentawai network. However, the central network, which extended further into the arc/backarc, recorded a significant amount of activity. SWS analysis on these traces suggests that along the Sumatran Fault there is a layer of anisotropy in the continental lithosphere that masks the SWS from the mantle wedge below. The anisotropy has formed from fault parallel aligned fractures and minerals that have developed from the shear strain exerted by the strike-slip motion of the Sumatran Fault. In order to explain all of the measurements within the forearc and backarc the anisotropic layer in the continental lithosphere has to be confined to a ~100 km region around the fault.

•The M_w 7.7 Mentawai earthquake on 25 October 2010 initiated at the southeastern limit of the aftershock region of the 2007 events. It propagated northwest and updip, all the way to the trench, in a zone that was nearly aseismic during the temporary seismic experiment two years before. Shallow aftershocks of the 2010 event suggest that patches of frictionally unstable behaviour can occur all the way to the trench.

• The co-seismic slip of the 2007 events, as well as the aftershock distribution, suggests that the down-dip limit to rupture propagation is 175-200 km from the trench at ~50 km depth. Therefore the downdip limit of the seismogenic zone is not the intersection of the megathrust with the continental Moho. Instead, it is beneath the forearc mantle and is attributed to a change in the physical properties of the plate interface.

• Despite the shallow part of the interface rupturing separately to the frictionally unstable part in the current earthquake cycle of the Mentawai segment, a 200 km wide rupture could potentially take place along the interface and therefore should be taken into consideration when determining hazard models for this region.

9.1 Future Work

In addition to *Vp* and *Vp/Vs t*omography, attenuation tomography would further our

understanding of the Sumatra subduction zone. Seismic attenuation is particularly useful in identifying spatial variations in temperature, as well as volatile and melt content and therefore could provide additional information on the location of fluids within the forearc.

Many studies have shown that SWS is frequency dependent. Measurements made in high frequency bands (> 2 Hz) are sensitive to small scale heterogeneities and are generally biased towards the upper layers of anisotropy, while low to mid frequency measurements (0.1-0.2 Hz) tend to smooth out small scale heterogeneities and contain information about the lower layers of anisotropy. Due to two layers of anisotropy being present in the Sumatran Fault region and back arc region, frequency-dependency splitting may help to constrain the magnitude and location of anisotropy in the crust and mantle wedge.

From the SWS results and forward modeling it appears that there are two regions of LPO anisotropy, the first is in the mantle wedge and the second is in the asthenosphere of the subducting slab. Geodynamic modeling using the characteristics of the Sumatra subduction zone (i.e. convergence direction/amount, trench advance, slab dip) could be used to identify if these regions are able to produce anisotropy . This can be done by using a thermo-viscous modeling algorithm (MILAMIN, Dabrowski et al., 2008) to model the temperature, velocity and strain rate field which can be inputed into D-Rex (Kaminski et al., 2004) to predict LPO anisotropy and thus the magnitude of the anisotropy and orientation of the a-axes. However, in Sumatra, due to the oblique subduction, a 2D model is not adequate to model the subduction zone and a 3D model is required.

A.1

Waveforms

Examples of *P* picks and *S* picks of different weights. Each pick was assigned a weight (0-4) which reflected the uncertainty in where to place it. Picks with weighting 0, were clear to determine (error +/- 0.05 s), while picks weighted 4 were very difficult to determine (error +/- 0.5 s). See Table 3.3 for further information on the uncertainity defined to each weight.

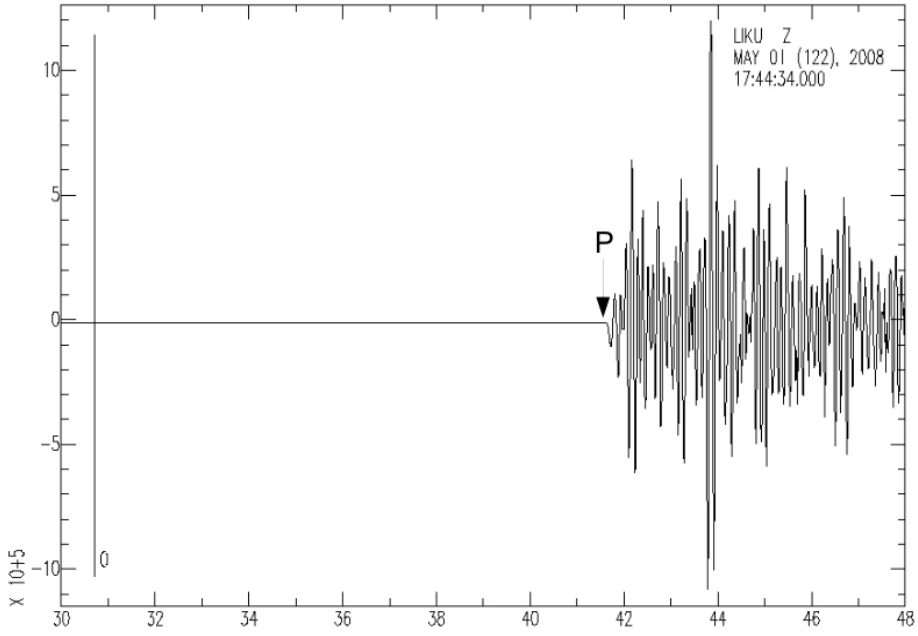

Figure A1.1: P Pick Weight 0

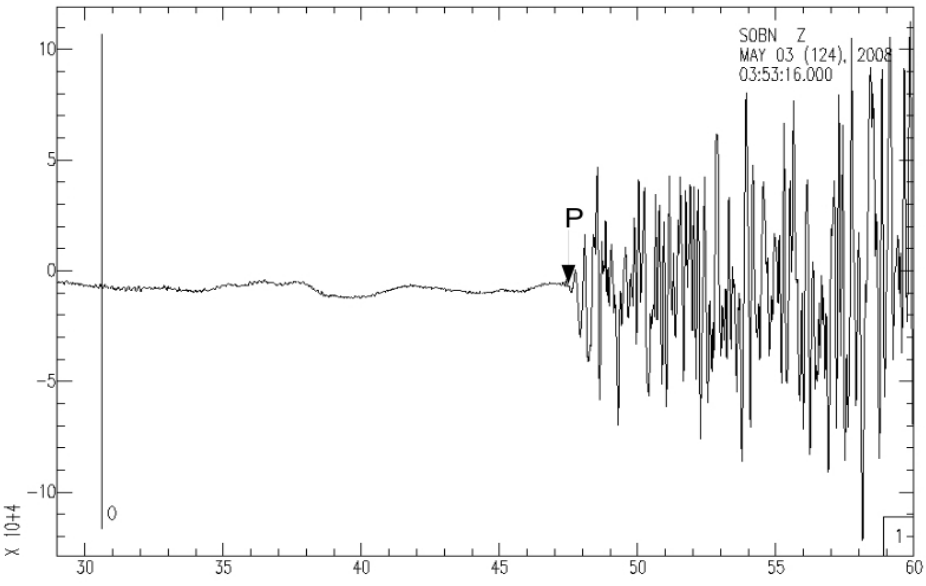

Figure A1.2: P Pick Weight 1

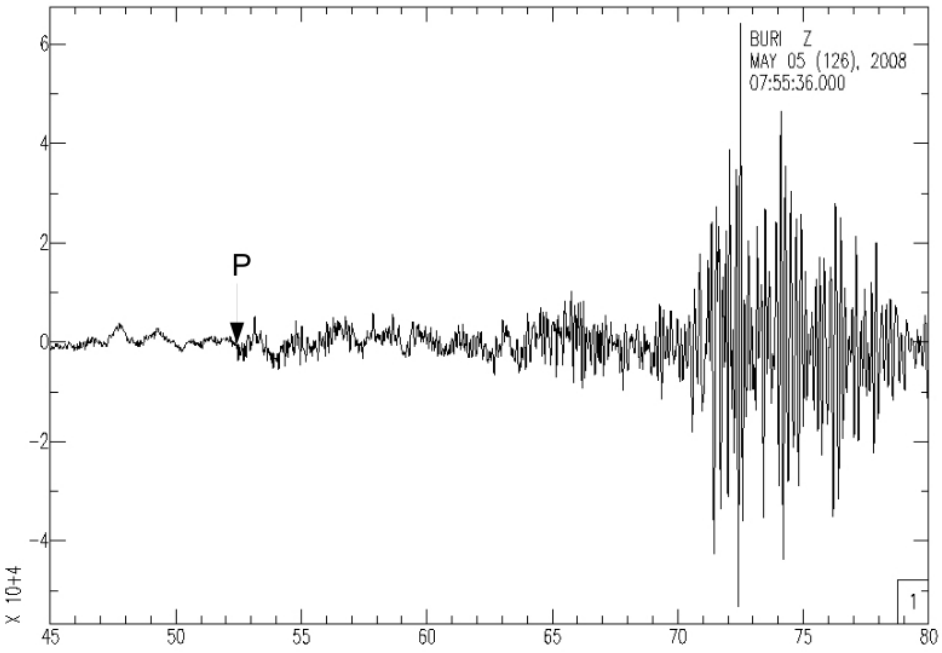

Figure A1.3: P Pick Weight 2

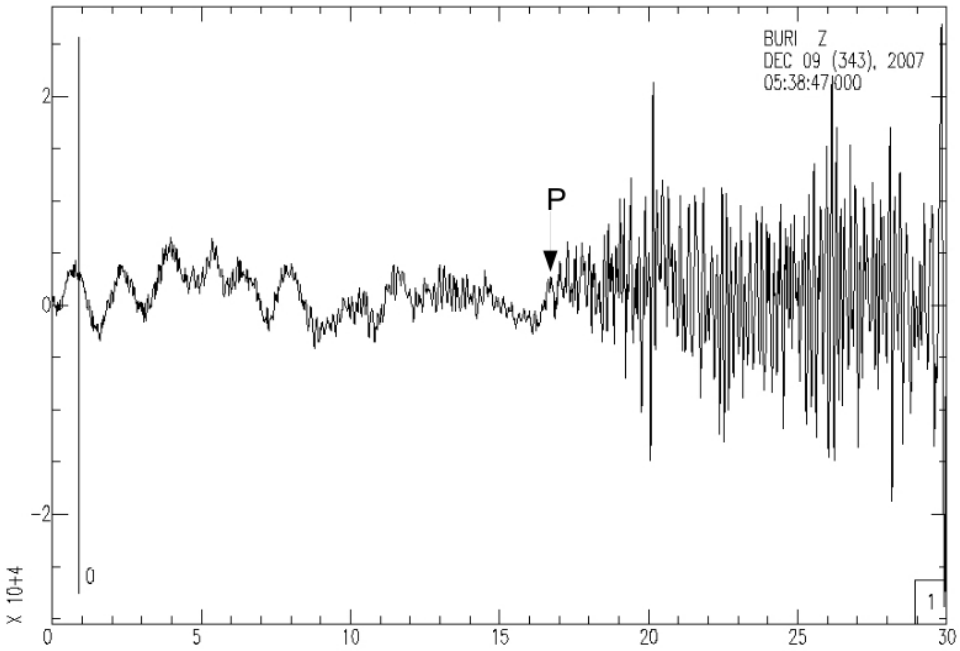

Figure A1.4: P Pick Weight 3

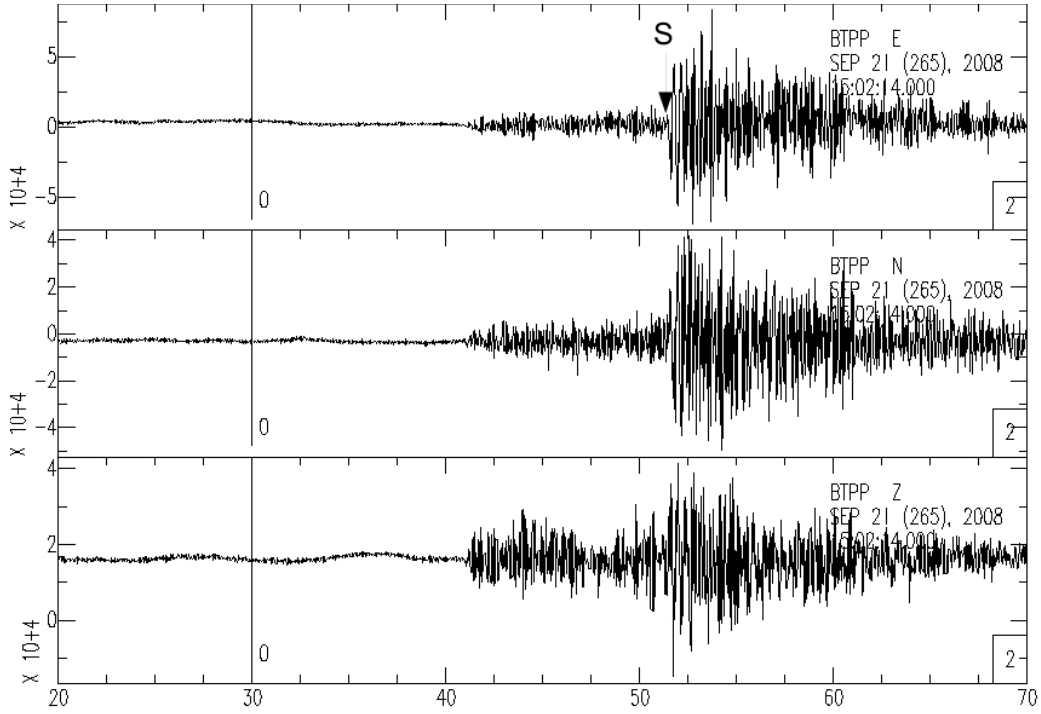

Figure A1.5: S Pick Weight 0

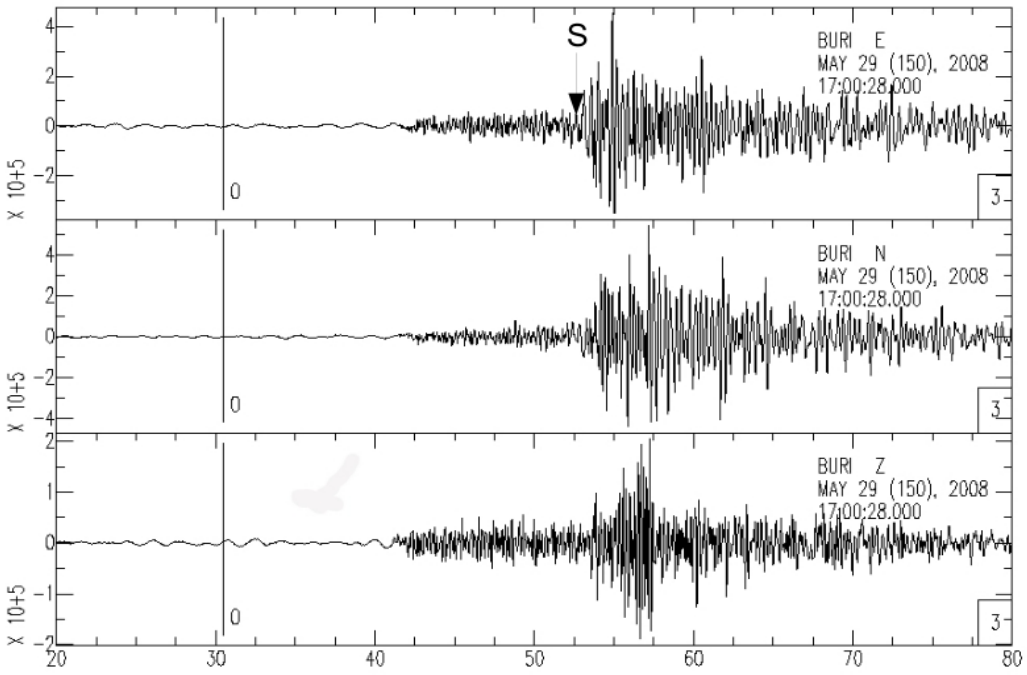

Figure A1.6: S Pick Weight 1

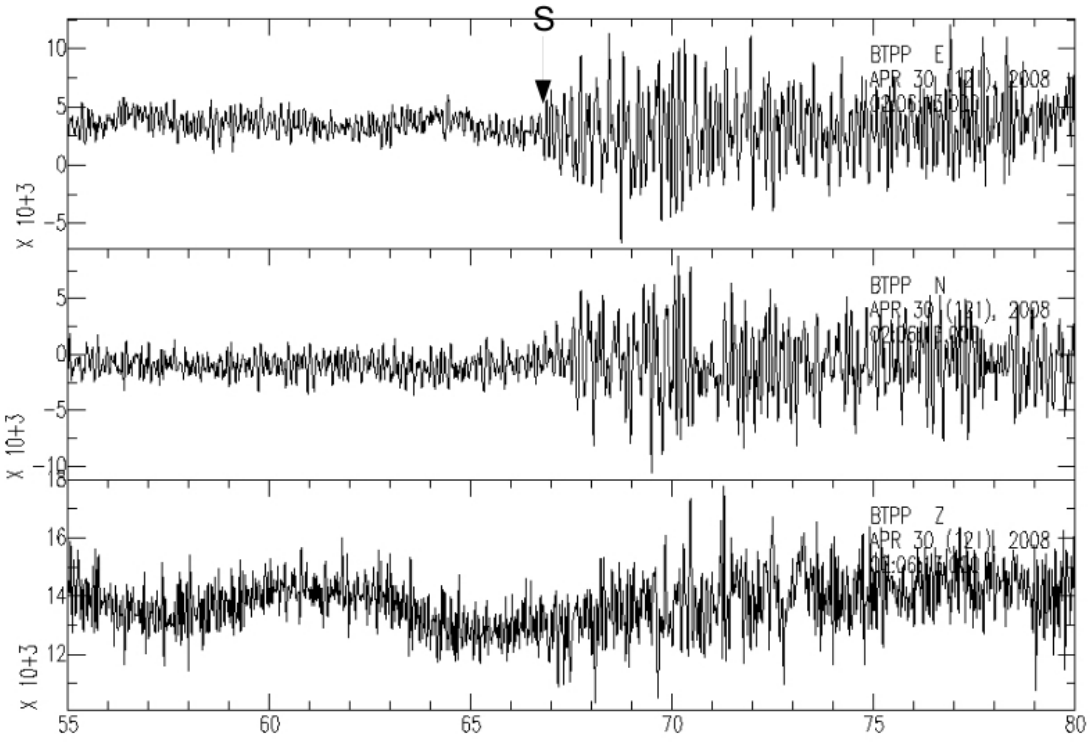

Figure A1.7: S Pick Weight 2

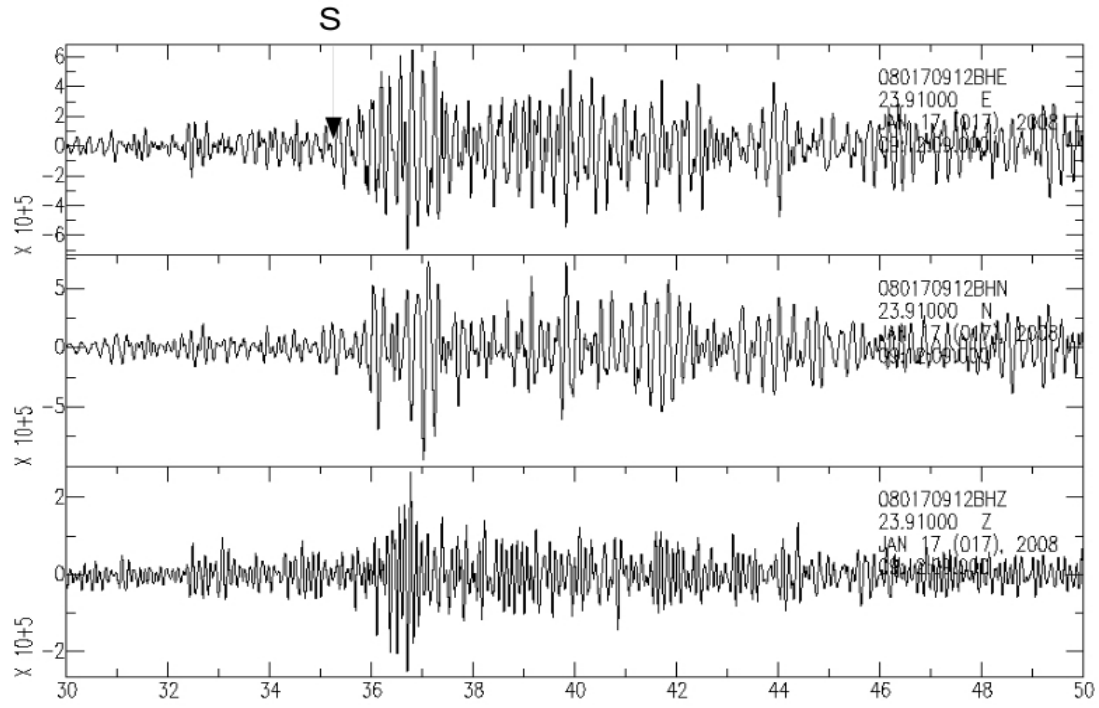

Figure A1.8: S Pick Weight 3

A.2

Tomography

This appendix contains supporting figures and tables for the 1D, 2D and 3D velocity models described in Chapter 5. Also included are examples of the FocMec solutions in Table 5.1 and the Kopp et al. (2001) *P* velocity model of the forearc.

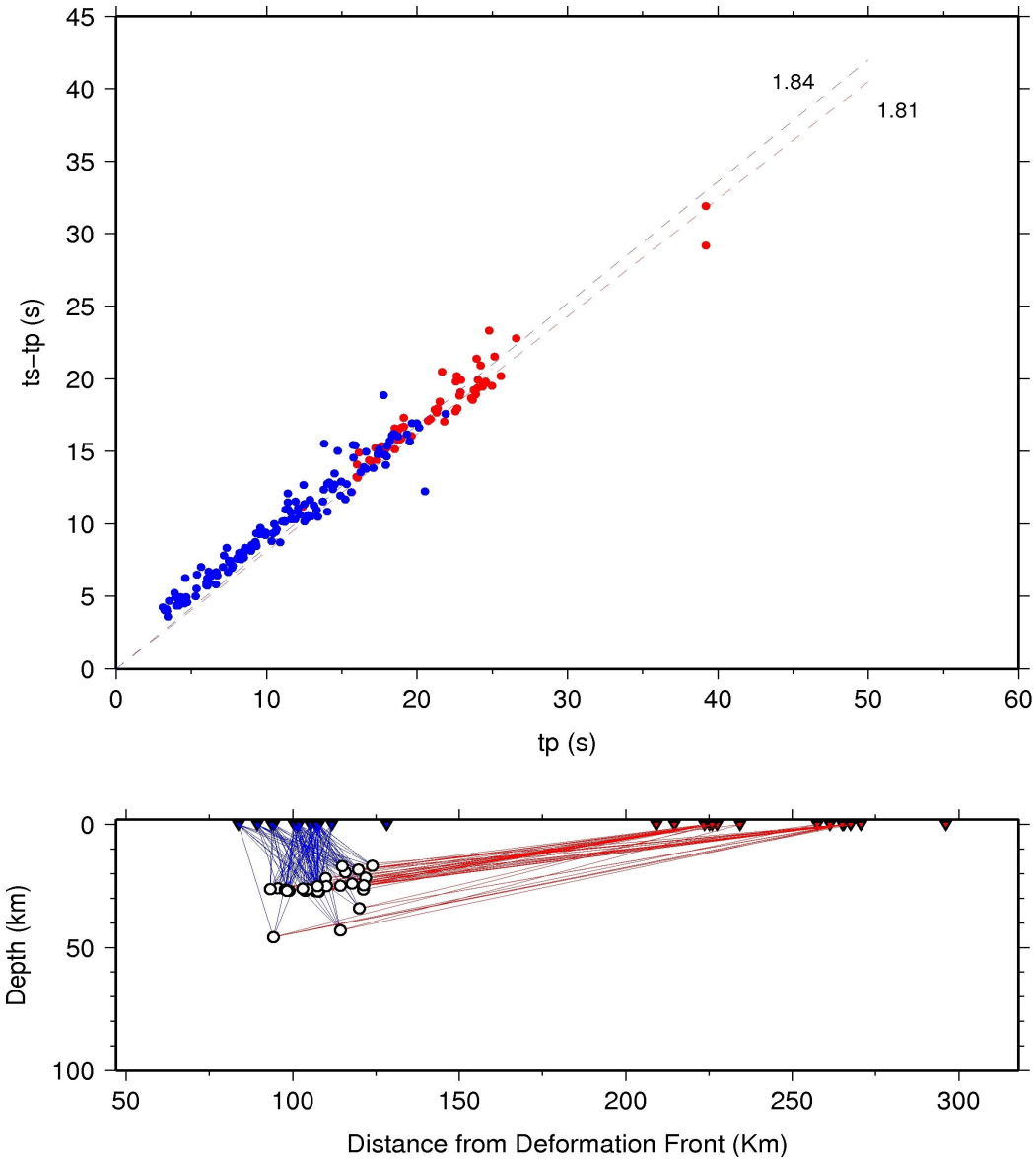

Figure A2.1: Top: Wadati diagrams of events beneath the Mentawai Islands. tp= *Travel time between the epicentre and seismic station for the P waves and* ts= *Travel time between the epicentre and seismic station for the S waves. Bottom: Ray paths. Raypaths traveling to the Mentawai Islands stations are shown in blue, while ray paths traveling to Sumatra mainland stations are shown in red.*

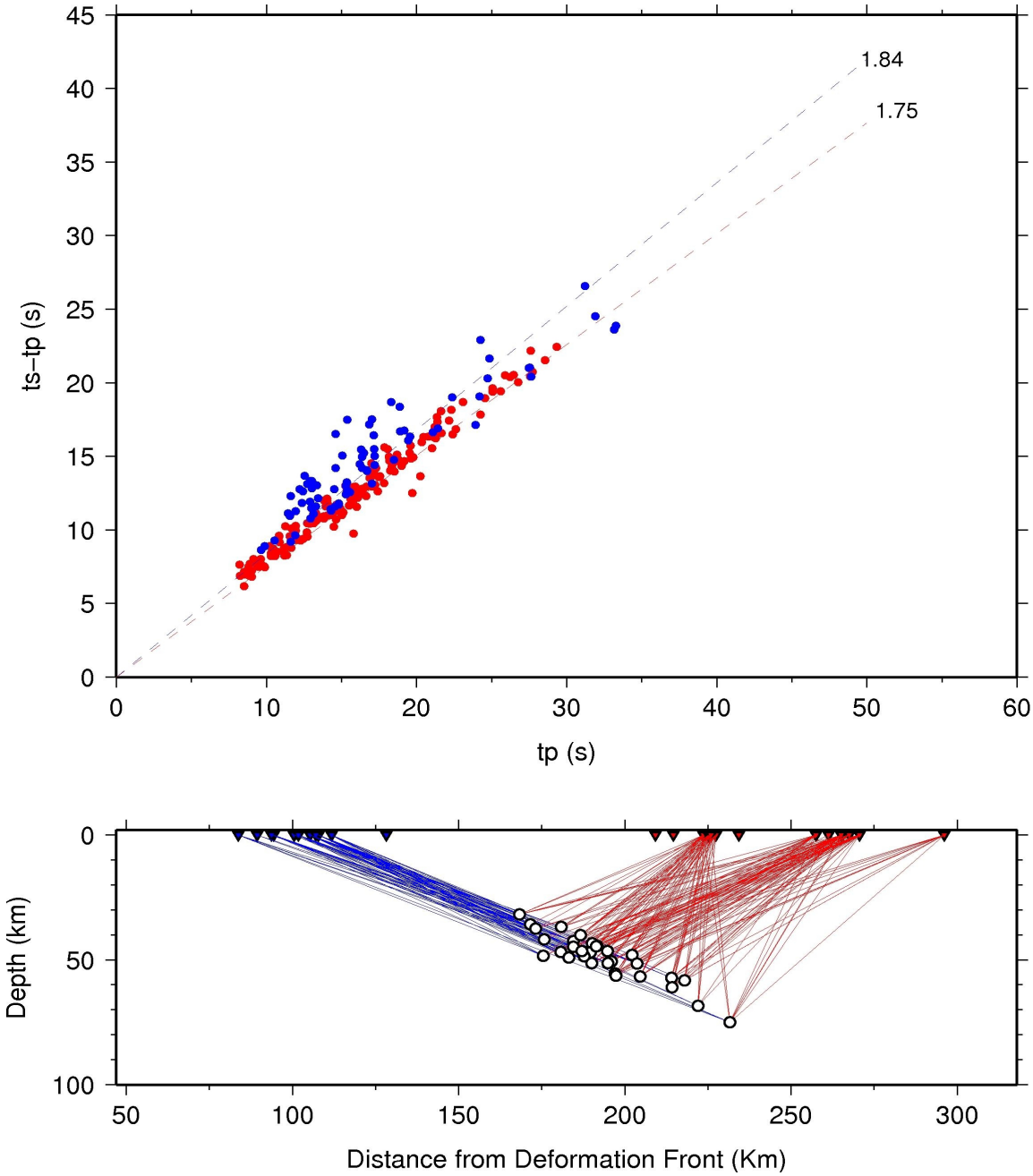

Figure A2.2: Wadati diagrams of events beneath mainland Sumatra. tp= *Travel time between the epicentre and seismic station for the P waves and* ts= *Travel time between the epicentre and seismic station for the S waves. Bottom: Ray paths. Raypaths traveling to the Mentawai Islands stations are shown in blue, while ray paths traveling to Sumatra mainland stations are shown in red.*

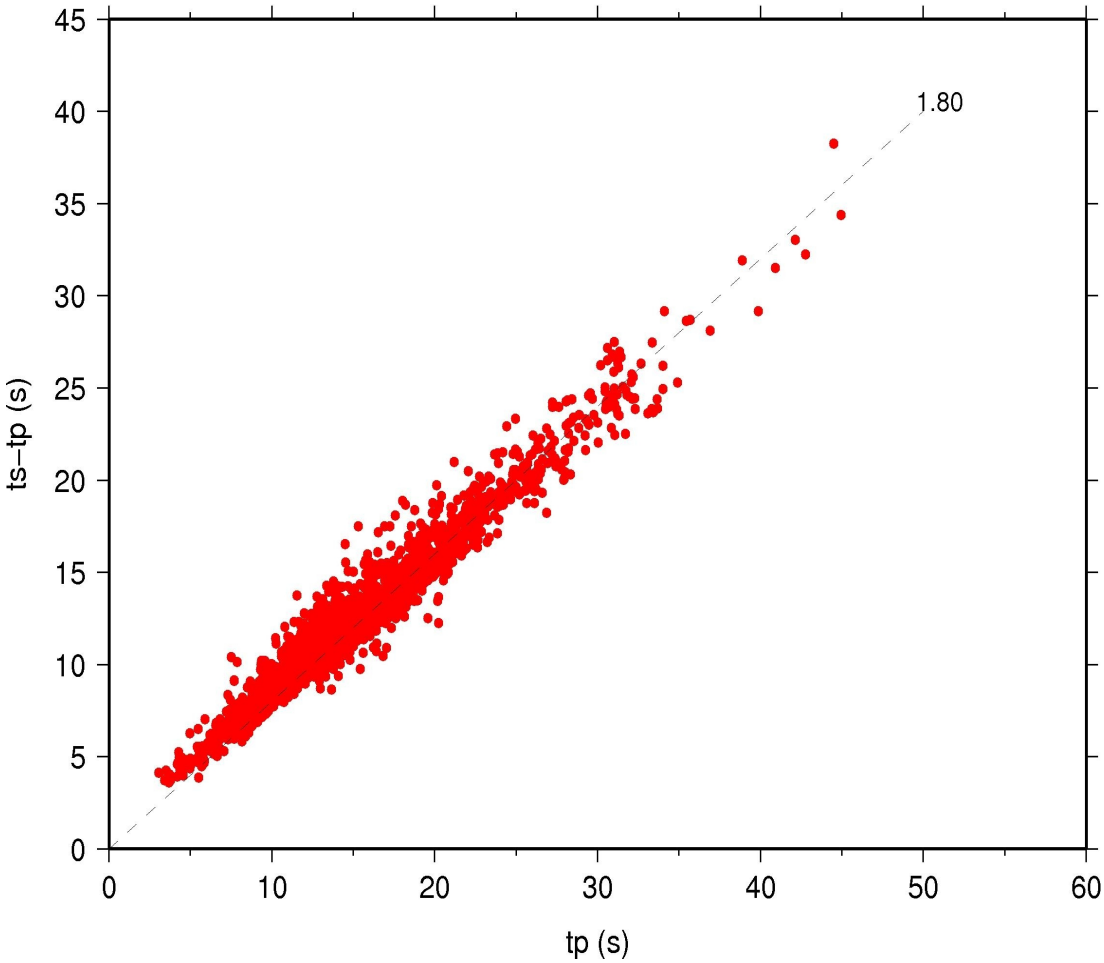

Figure A2.3: Wadati diagram. tp= *Travel time between the epicentre and seismic station for the P waves and* ts= *Travel time between the epicentre and seismic station for the S waves.*

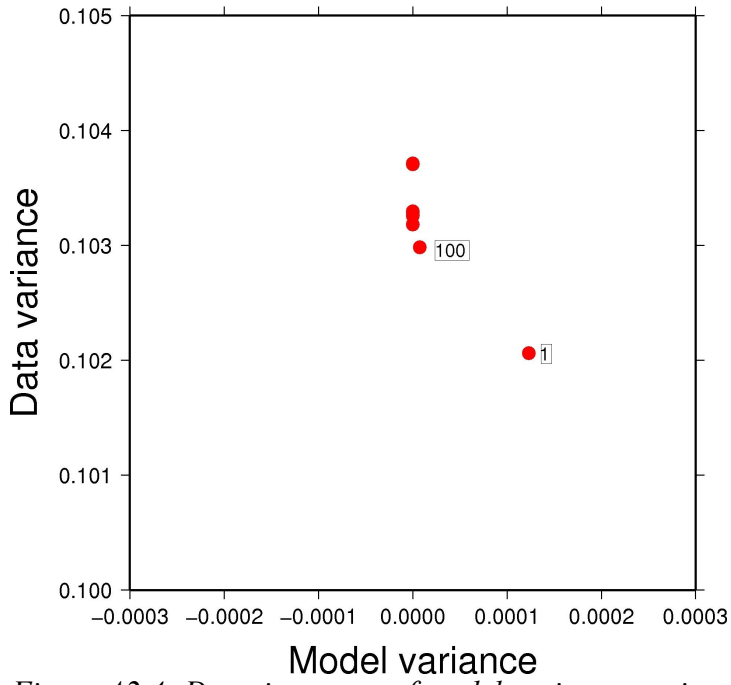

Figure A2.4: Damping curve of model variance against data variance for the 1D velocity model. A damping value of 100 was chosen.

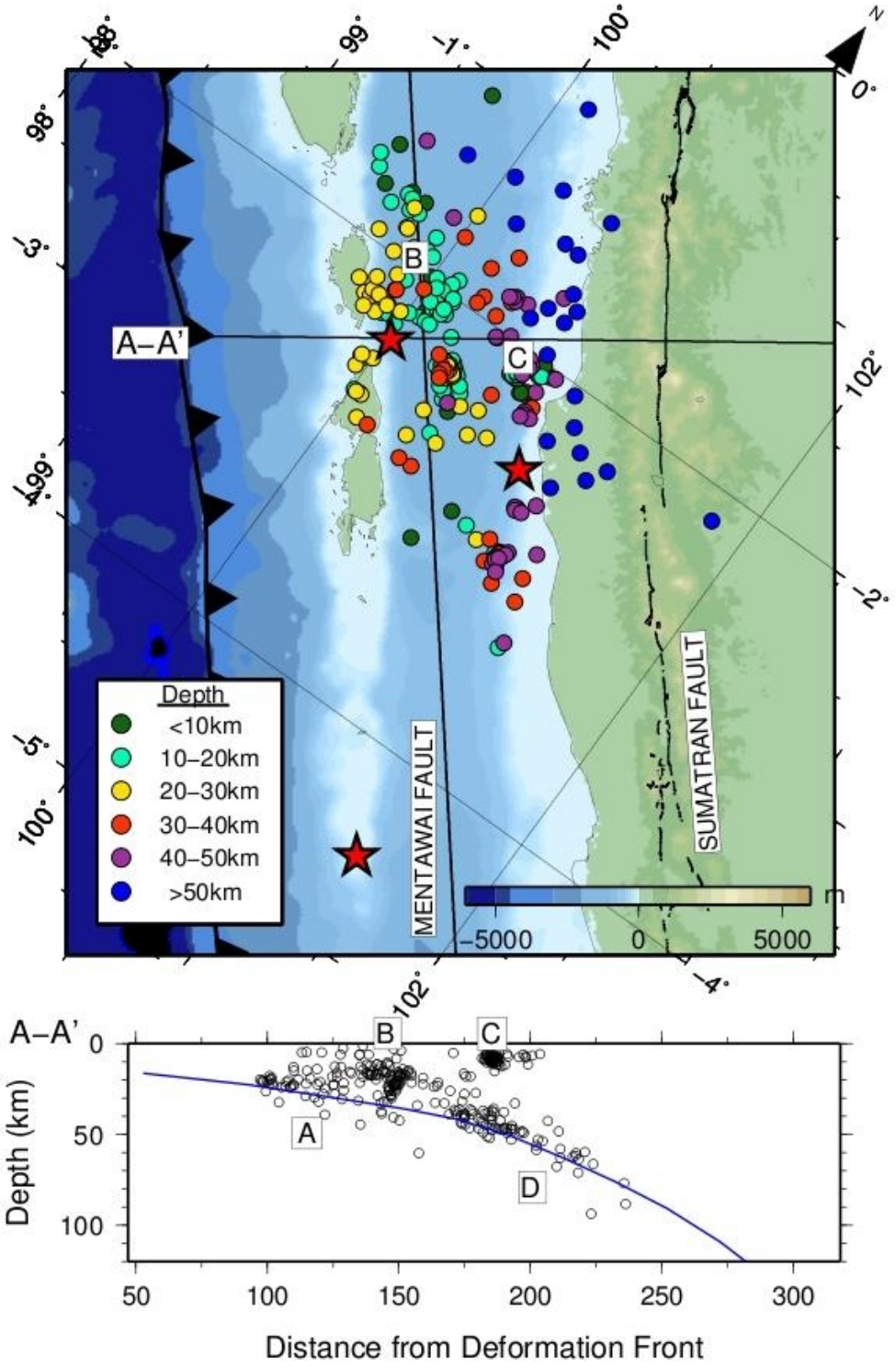

Figure A2.5: Top: Hypocentre location of 312 earthquakes used in the simultaneous inversion for accurate hypocentres, 1D velocity models and station corrections, The events have been located using the 1D minimum Vp and Vs model (Figure 5.3). Red stars are the location of the large megathrust earthquakes (Mw 8.4 and Mw 7.9 on the 12 September 2007 and Mw 7.2 on the 25 February 2008). Bottom: Cross section along line A-A'. A=Plate interface beneath the Islands, B=Mentawai Fault Region, C=Backthrust on the eastern side of the forearc basin, D=Plate interface beneath the forearc basin.

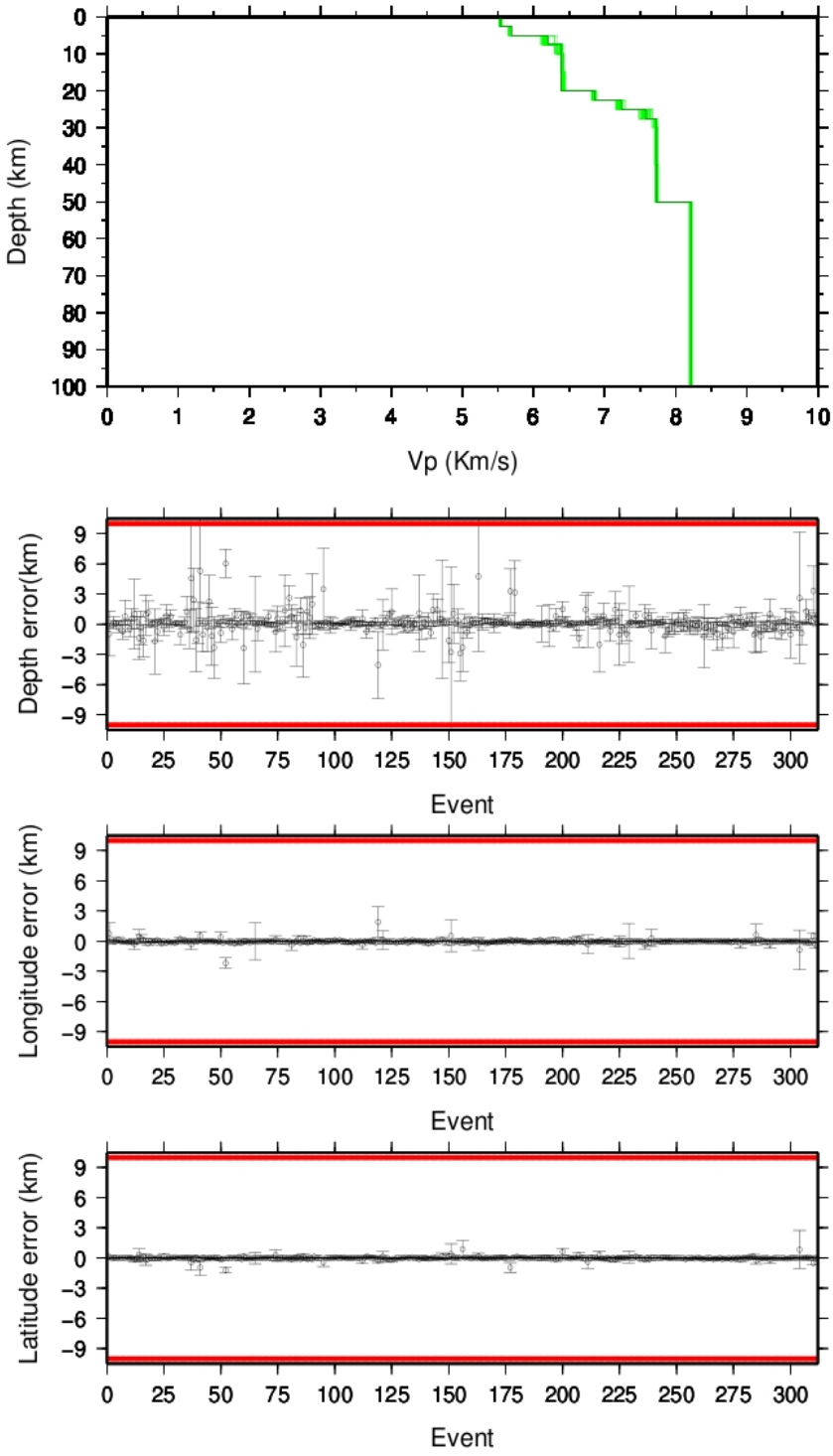

Figure A2.6: Bottom: The average error and std in latitude, longitude and depth for each event. The error is the difference between the final hypocentre location from the 1D minimum model and the hypocentre location after the event has been randomly moved up to 10 km in latitude, longitude and depth and a joint inversion is performed using the previously determined 1D Vp model as the starting model. Top: The resulting 1D Vp models following the joint inversion. The previously determined 1D Vp minimum model is shown in black.

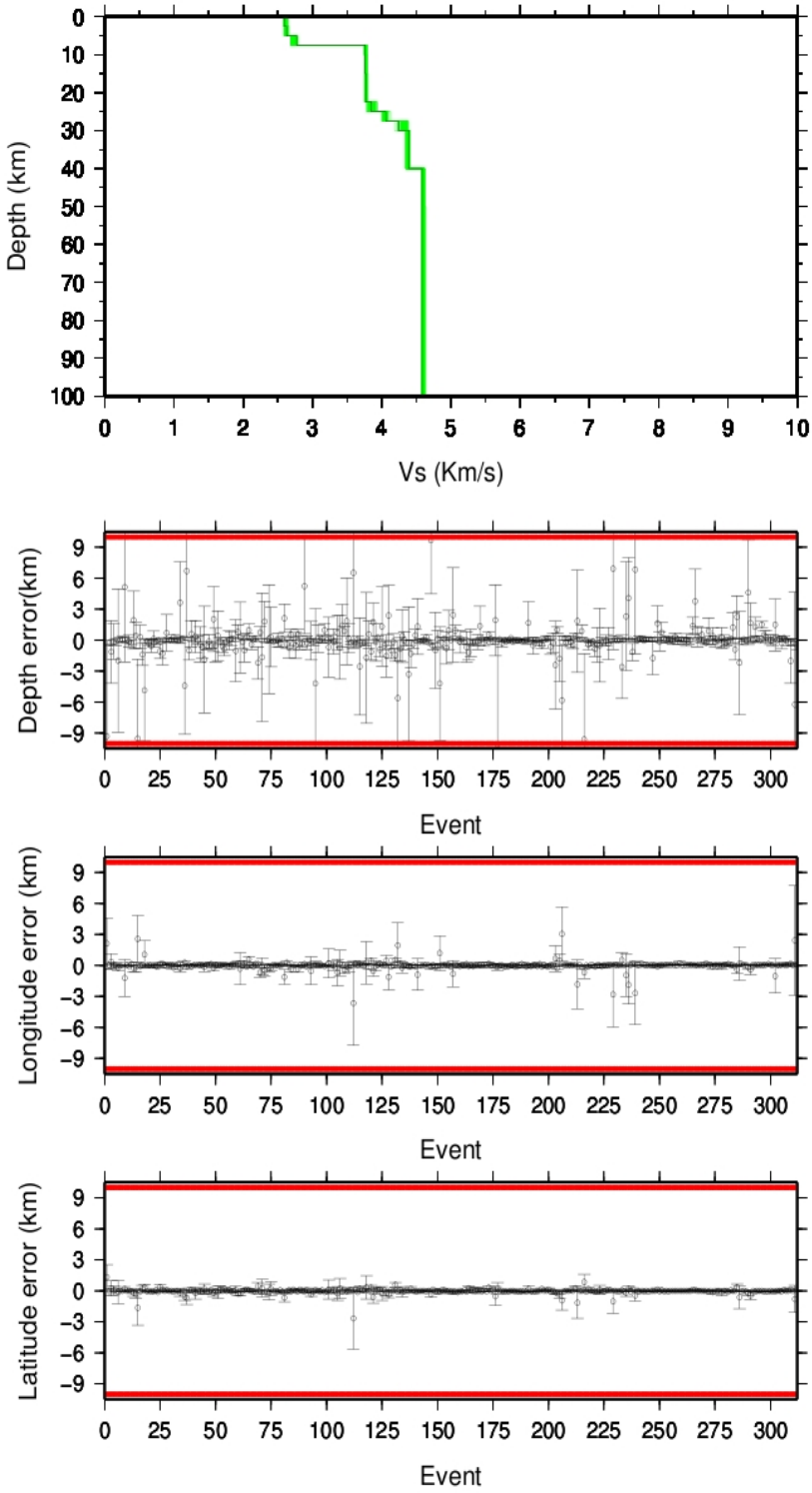

Figure A2.7: Bottom: The average error and std in latitude, longitude and depth for each event. The error is the difference between the final hypocentre location from the 1D minimum model and the hypocentre location after the event has been randomly moved up to 10 km in latitude, longitude and depth and a joint inversion is performed using the previously determined 1D Vp and Vs models as the starting models. Top: The resulting 1D Vs models following the joint inversion. The previously determined 1D Vs minimum model is shown in black.

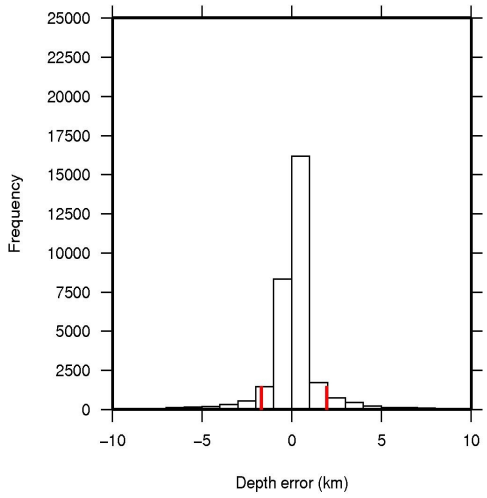

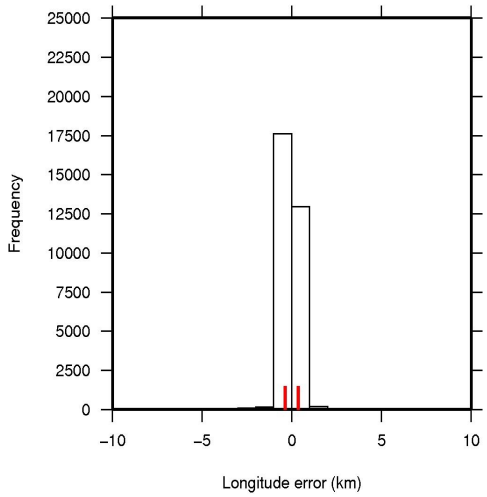

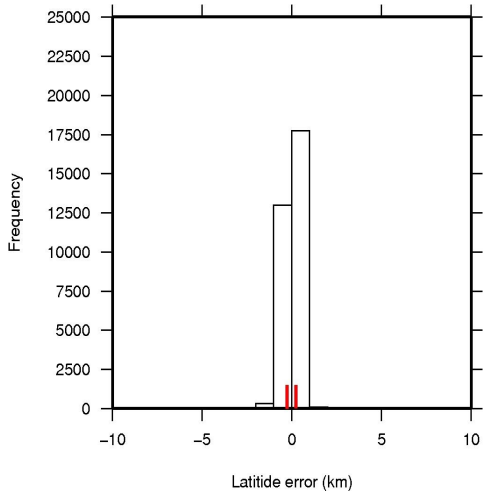

Figure A2.8: Histogram of errors in latitude, longitude and depth between the final hypocentre locations and the hypocentre locations after they have been randomly moved up to 10 km in latitude, longitude and depth and a joint inversion for Vp model being performed. One standard deviation is indicated by the red bars.

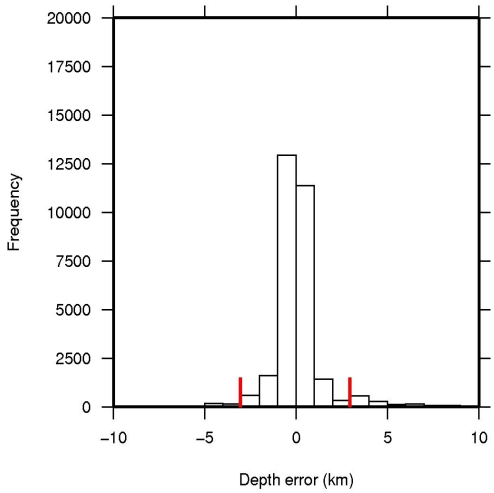

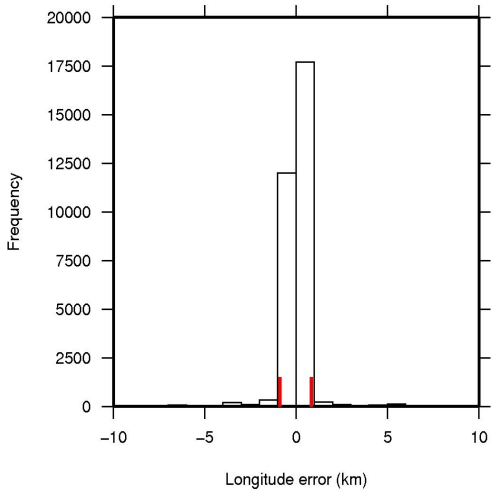

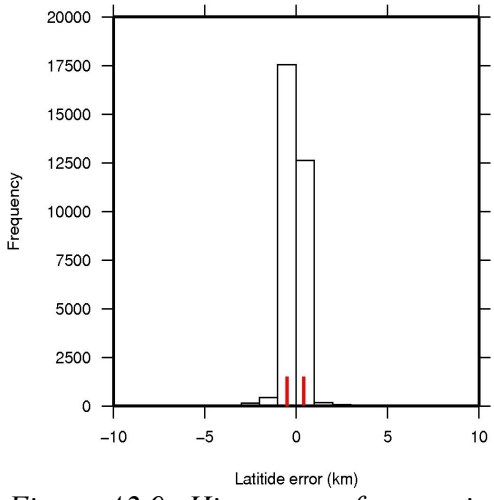

Figure A2.9: Histogram of errors in latitude, longitude and depth between the final hypocentre locations and the hypocentre locations after they have been randomly moved up to 10 km in latitude, longitude and depth and a joint inversion for Vs model being performed. One standard deviation is indicated by the red bars.

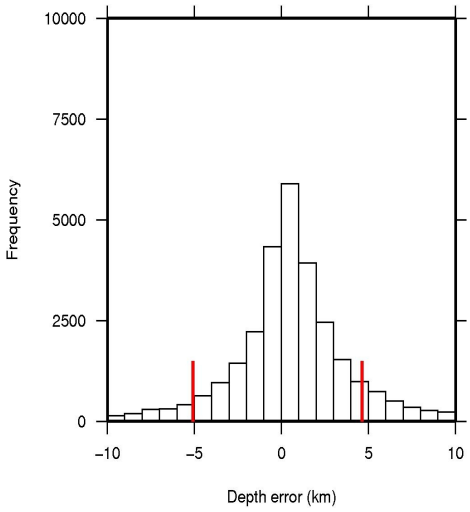

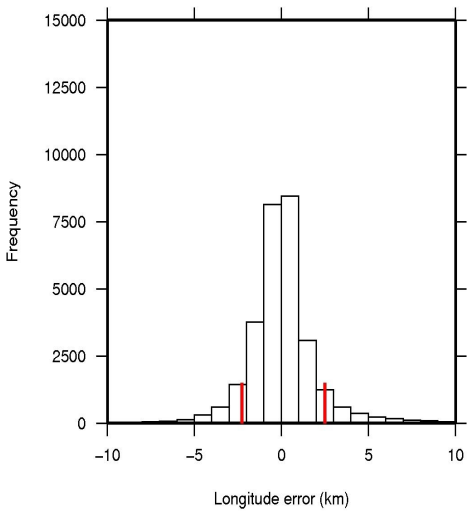

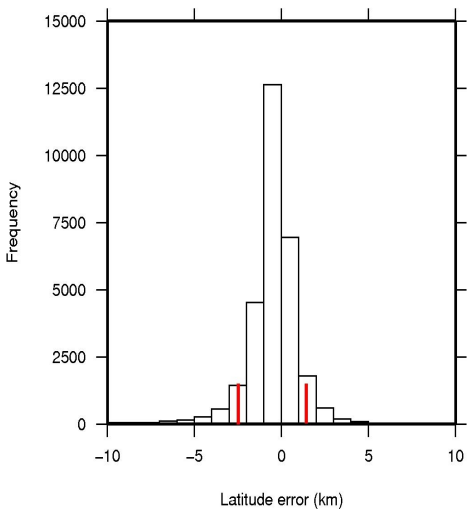

Figure A2.10: Histogram of errors in Latitude, longitude and depth between the final hypocentre locations and the hypocentre locations after the bootstrap method has been applied and a 1D inversion is carried out to determine the Vp model . One standard deviation is indicated by the red bars.

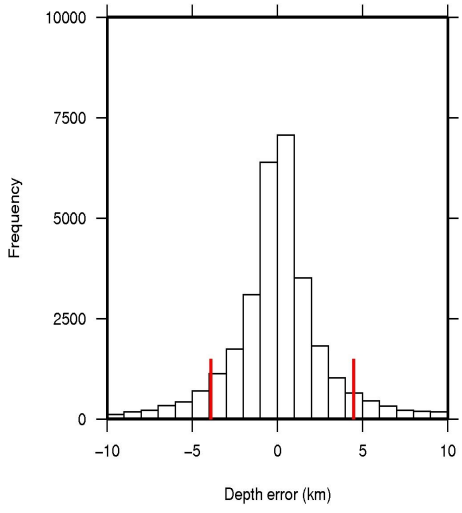

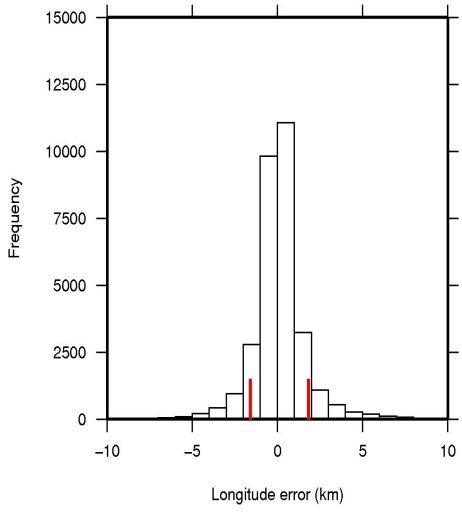

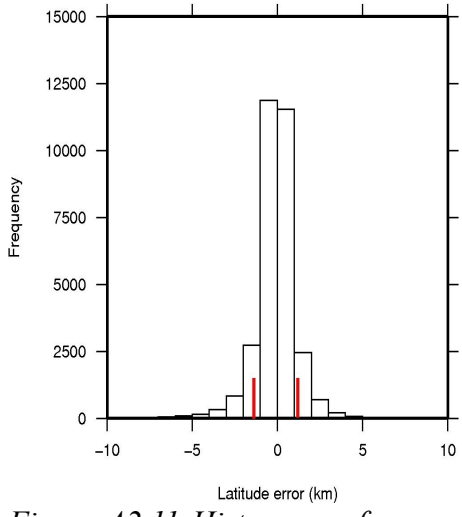

Figure A2.11 Histogram of errors in Latitude, longitude and depth between the final hypocentre locations and the hypocentre locations after the bootstrap method has been applied and a 1D inversion is carried out to determine the Vs model . One standard deviation is indicated by the red bars.

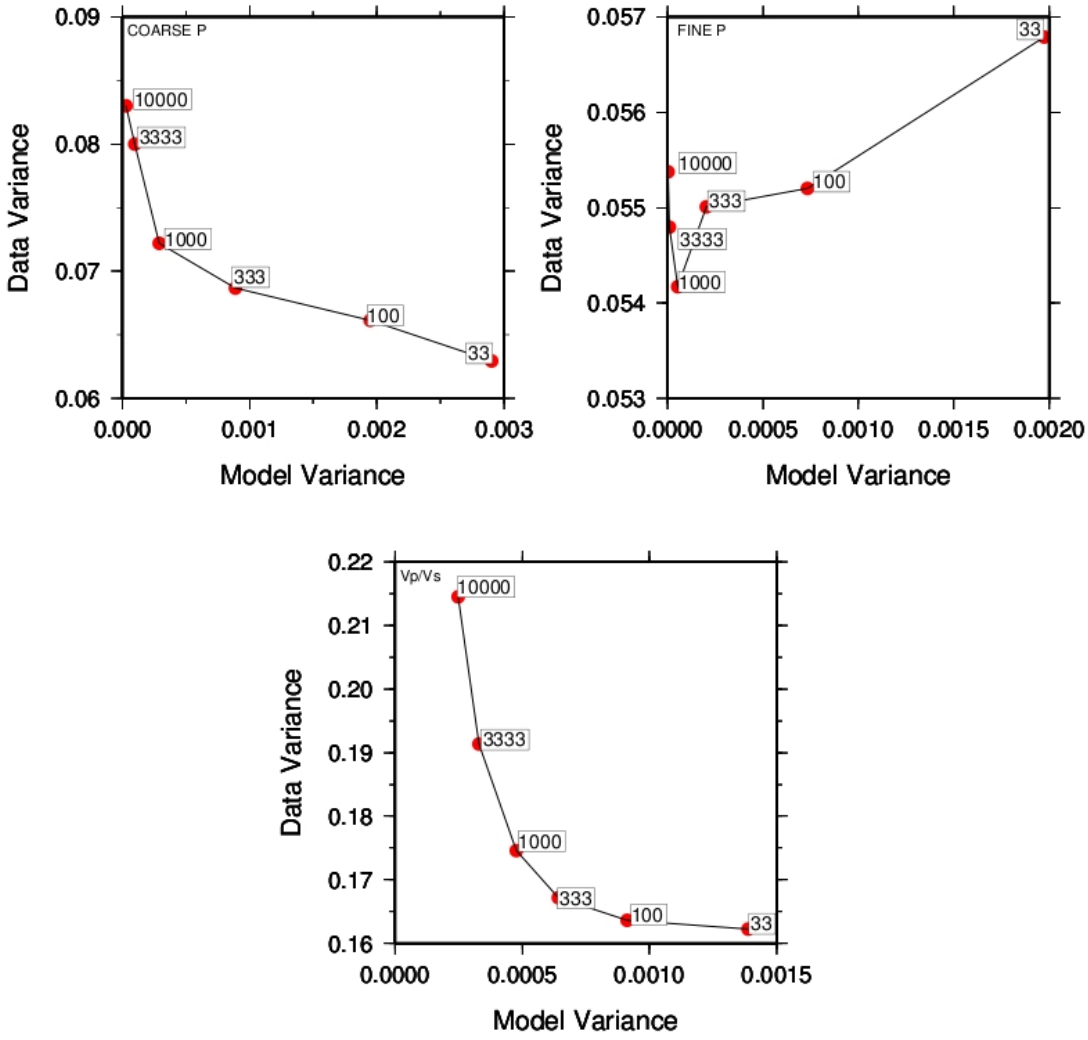

Figure A2.12: Damping curves for the 2D tomography.

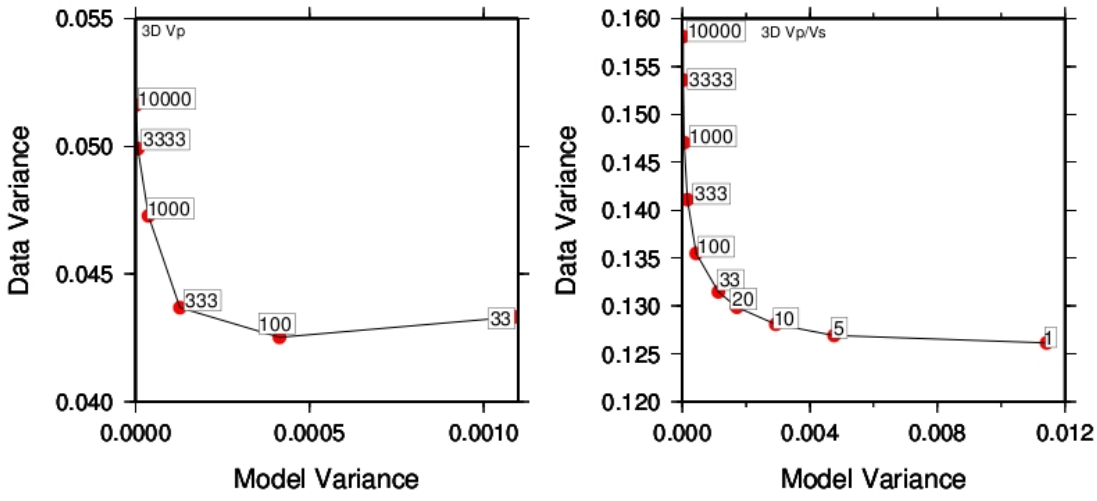

Figure A2.13: Damping Curves for the 3D inversion.

Model	Chosen Damping Value
Coarse 2D *Vp*	1000
Fine 2D *Vp*	1000
Fine 2D *Vp/Vs*	100
3D *Vp*	100
3D *Vp/Vs*	33

Table A2.1: Chosen damping value for each model.

Station	P Wave Station correction	S Wave Station Correction
SWLT	-0.06	0
BTPP	-0.04	-0.02
DPBR	0.01	0
PKNN	0.03	0.01
PDRK	-0.01	0
LUNG	0.03	0
RTMD	0	0
LAIS	0	0
LIKU	0.01	0.01
MLKN	0	0
TIKU	0	0
MAKA	-0.11	-0.04
BURI	0.08	0.01
BSAT	0	-0.03
SLBU	0.06	0.02
MLKP	0.05	0.02
SOBN	0	0
DSAO	0	0
SMYA	-0.01	0.03
PSKI	0	0
JSLT	0.03	0
UBTU	0.02	0
SDRM	-0.02	0
SRBN	0	0
ATTB	-0.01	0
SKAP	0	0
PRKB	-0.04	0.01
PPNG	-0.01	0.01
NGNG	0	0

Table A2.2: P wave and S wave corrections for the final 3D Vp and Vp/Vs model.

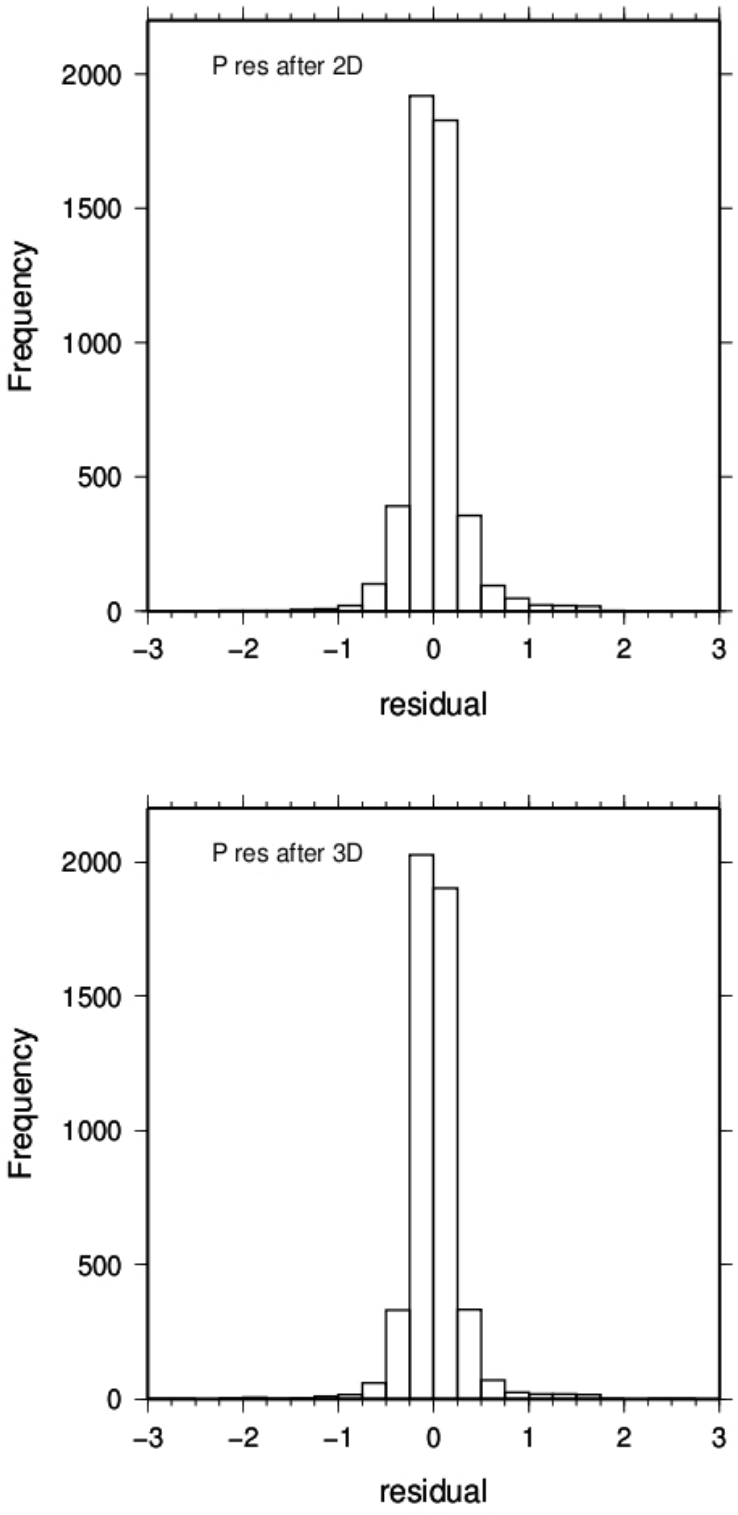

Figure A2.14: Histogram of P residuals. Top: Residuals after inversion for the 2D Vp and Vp/Vs model Bottom: Residuals after inversion for the 3D Vp and Vp/Vs model.

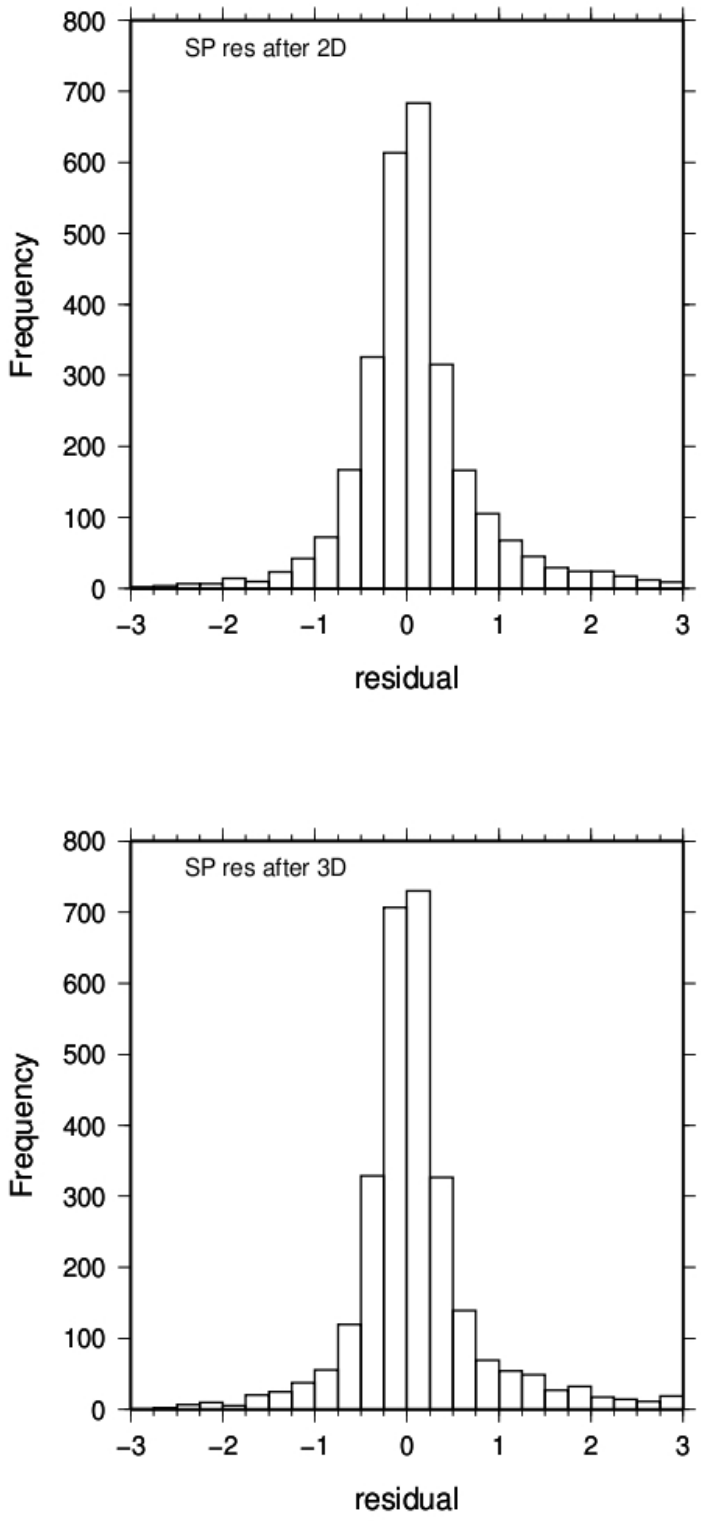

Figure A2.15: Histogram of S-P residuals. Top: Residuals after inversion for the 2D Vp and Vp/Vs model Bottom: Residuals after inversion for the 3D Vp and Vp/Vs model.

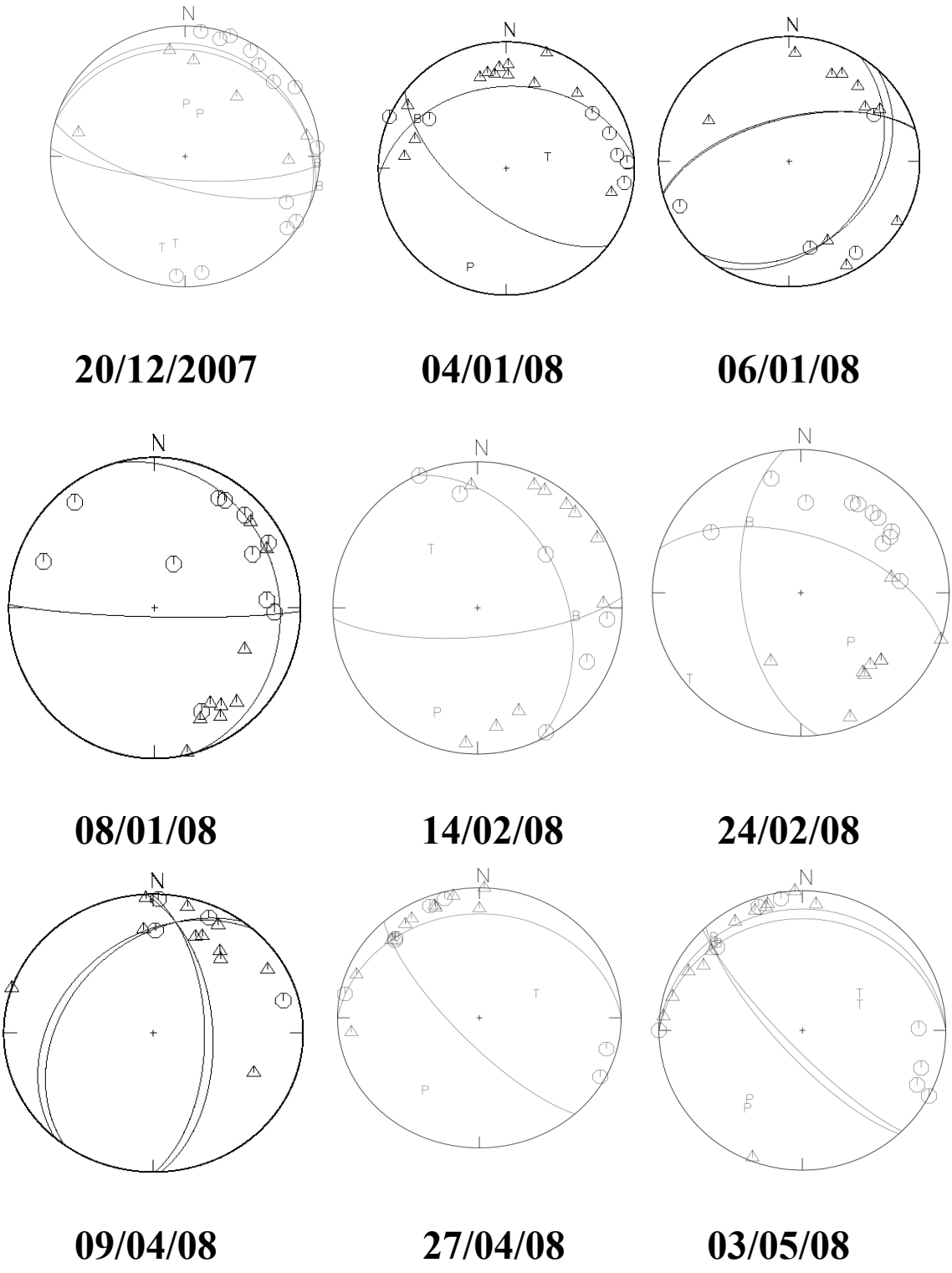

Figure A2.16: Examples of FocMec soultions for events in Table 5.1.

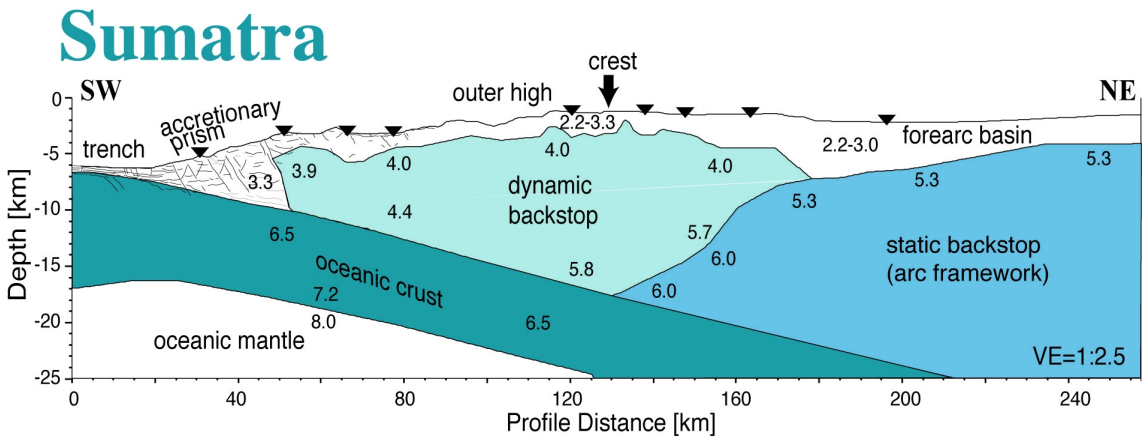

Figure A2.17: Velocity model of the forearc by Kopp et al., (2001). See Figure 2.1 for the location of the model.

A.3

Event Catalogue

Event catalogue for 538 earthquakes that had ≥ 6 *P* picks and ≥ 4 *S* picks. Events were located using the 3D *Vp* and *Vp/Vs* velocity models. RMS is a measure of the error in the event location. It is the root mean square travel time residual.

Date (YY/MM/DD)	Time(HH:MM:SS.SS)	Latitude	Longitude	Depth (km)	No. Picks	RMS (s)
07/12/09	07:23:59.76	-2.3280	100.3955	14	16	0.11
07/12/10	06:54:24.85	-2.8373	101.0586	22	21	0.15
07/12/10	08:54:36.47	-2.8480	101.0786	13	20	0.3
07/12/10	09:01:11.38	-2.8583	101.0587	20	12	0.17
07/12/10	11:55:59.41	-2.3193	100.2866	30	14	0.12
07/12/11	13:01:02.33	-1.8053	99.9087	0	16	0.51
07/12/12	14:04:01.97	-2.2940	100.3381	13	20	0.21
07/12/13	19:07:40.85	-2.8562	101.0330	5	18	0.26
07/12/14	19:42:19.83	-1.8733	99.7325	27	16	0.12
07/12/15	02:19:04.40	-2.8205	101.0627	5	24	0.2
07/12/16	09:13:58.00	-3.5268	100.4638	24	26	1.01
07/12/16	18:13:33.86	-1.5007	99.3168	1	20	1.03
07/12/17	22:54:49.38	-3.0648	100.0090	28	30	0.3
07/12/18	12:18:49.74	-2.2122	100.5371	1	25	0.14
07/12/18	17:34:21.58	-2.4720	100.3680	13	15	0.13
07/12/19	09:08:34.75	-2.2985	100.3723	14	18	0.27
07/12/19	18:56:00.73	-2.3352	100.3103	32	25	0.1
07/12/20	01:09:40.53	-2.3058	100.5610	36	22	0.16
07/12/20	03:10:31.93	-2.3347	100.3403	31	35	0.12
07/12/20	07:42:54.76	-3.5762	100.5150	28	27	0.67
07/12/20	11:25:05.10	-2.2110	100.0579	22	18	0.17
07/12/22	10:43:08.40	-2.9223	100.0870	18	17	0.12
07/12/22	10:46:16.28	-2.9235	100.0874	17	18	0.1
07/12/22	12:04:41.34	-3.2473	100.1453	21	26	0.16
07/12/22	15:24:00.93	-1.5293	100.1740	60	20	0.13
07/12/22	15:53:53.42	-3.3877	100.6664	35	23	0.24
07/12/22	16:40:19.94	-2.3295	100.3144	26	20	0.13
07/12/22	20:42:46.64	-2.1405	100.6180	8	35	0.09
07/12/22	20:46:21.51	-2.1410	100.6130	6	22	0.15
07/12/22	23:42:32.89	-1.9232	100.0930	17	19	0.25
07/12/23	01:47:31.38	-3.2365	100.1345	22	35	0.19
07/12/23	03:29:42.07	-2.1382	100.6135	5	32	0.1
07/12/23	03:43:24.64	-3.2612	100.1013	19	24	0.47
07/12/23	04:31:34.42	-3.2373	100.1494	19	16	0.1
07/12/23	07:43:43.26	-2.1217	100.6082	7	18	0.16
07/12/23	08:27:34.98	-2.3820	100.4268	18	24	0.44
07/12/23	09:34:06.49	-3.2780	100.4710	26	26	0.21
07/12/23	14:16:56.56	-2.3443	100.2679	10	29	0.26
07/12/23	15:48:45.97	-3.6368	99.9395	13	24	0.6
07/12/23	16:56:14.01	-2.3422	100.2774	38	21	0.09
07/12/24	03:13:04.70	-2.4687	100.3693	19	30	0.25
07/12/24	04:01:21.76	-1.7515	100.0008	36	26	0.19
07/12/24	07:34:01.94	-2.0147	99.9885	6	26	0.17

Date (YY/MM/DD)	Time(HH:MM:SS.SS)	Latitude	Longitude	Depth (Km)	No. Picks	RMS (s)
07/12/24	19:53:53.43	-3.4012	100.2573	20	20	0.46
07/12/24	21:47:29.04	-2.9040	100.9239	25	21	0.17
07/12/25	19:02:30.64	-2.3400	100.9678	7	20	0.36
07/12/26	00:10:12.87	-2.3472	100.3151	36	18	0.09
07/12/26	17:28:14.48	-3.3105	100.1024	24	24	0.88
07/12/27	05:58:25.98	-2.9268	100.1054	19	24	0.17
07/12/27	06:18:05.40	-3.1782	100.1992	19	27	0.13
07/12/27	12:52:39.68	-2.2007	100.0532	19	17	0.21
07/12/27	13:23:10.50	-2.3617	100.3561	21	15	0.2
07/12/27	15:04:34.72	-2.1422	100.0886	18	27	0.27
07/12/27	16:09:35.49	-5.4933	101.0781	53	16	0.46
07/12/27	21:02:30.44	-1.7295	99.6875	12	14	0.22
07/12/27	21:51:11.68	-1.9410	100.2448	39	35	0.12
07/12/28	04:04:52.08	-3.6010	100.1424	20	15	0.33
07/12/28	16:22:41.14	-2.0428	100.1417	21	34	0.3
07/12/28	18:07:31.66	-3.3808	100.3002	18	21	0.34
07/12/31	03:20:35.86	-2.9012	100.2543	24	15	0.18
07/12/31	08:51:19.19	-2.3337	100.3652	22	23	0.18
07/12/31	09:49:34.15	-2.1027	100.6243	9	24	0.15
08/01/01	03:25:11.94	-3.7823	100.6539	27	24	0.56
08/01/01	21:24:35.61	-2.0542	100.7489	7	18	0.08
08/01/02	03:56:24.29	-2.9030	101.0616	24	24	0.41
08/01/03	00:31:06.74	-2.3560	100.4025	18	16	0.16
08/01/03	09:35:51.87	-1.9940	99.3927	22	25	0.2
08/01/03	13:43:51.32	-5.1242	101.1228	45	14	0.41
08/01/03	14:03:10.41	-1.6315	99.5529	17	23	0.7
08/01/03	18:27:39.87	-2.7703	100.1242	20	23	0.11
08/01/04	04:50:09.89	-2.1623	100.7617	6	16	0.1
08/01/04	07:29:20.13	-2.8900	100.8300	28	35	0.27
08/01/04	13:25:54.20	-1.4412	99.1347	11	20	0.15
08/01/04	15:48:30.59	-2.3355	100.3144	26	35	0.19
08/01/05	00:20:05.33	-2.1318	100.6153	9	29	0.15
08/01/05	13:23:28.39	-2.1323	100.6102	10	34	0.14
08/01/05	13:45:51.13	-2.1417	100.6114	4	20	0.07
08/01/05	13:51:24.03	-2.1358	100.6124	5	21	0.15
08/01/05	15:28:33.13	-2.7117	100.3423	29	19	0.09
08/01/05	17:10:45.11	-2.0418	100.1227	22	20	0.26
08/01/06	03:38:16.22	-2.1902	100.0482	14	29	0.2
08/01/06	15:19:17.82	-2.1218	100.5888	1	20	0.21
08/01/06	17:20:35.78	-2.1368	100.6182	8	23	0.14
08/01/06	18:20:38.99	-2.2168	100.0726	20	23	0.14
08/01/06	19:04:23.39	-3.3975	100.7934	28	14	0.21
08/01/07	14:20:49.07	-3.1808	100.1935	17	17	0.1
08/01/07	16:43:00.71	-1.5905	99.9738	22	22	0.23
08/01/08	01:13:30.06	-2.2475	99.8833	24	30	0.11
08/01/09	00:31:30.05	-2.3782	100.3381	36	29	0.14
08/01/09	07:05:36.74	-2.2390	99.9347	32	14	0.12
08/01/09	12:39:55.86	-3.1458	101.7401	2	24	0.64
08/01/09	17:46:05.37	-2.1330	100.6107	4	22	0.16

Date (YY/MM/DD)	Time(HH:MM:SS.SS)	Latitude	Longitude	Depth (km)	No. Picks	RMS (s)
08/01/10	14:29:15.06	-1.8427	100.4575	40	16	0.38
08/01/10	17:58:15.34	-2.2387	99.9253	31	15	0.09
08/01/10	18:32:03.54	-1.8070	100.1791	36	30	0.18
08/01/10	19:30:30.98	-2.8900	100.0502	22	27	0.1
08/01/10	22:14:02.54	-2.9300	100.0668	26	26	0.23
08/01/11	05:33:54.31	-2.1400	100.6207	8	23	0.14
08/01/11	16:59:49.22	-2.0700	100.4230	35	27	0.13
08/01/12	01:21:36.36	-2.9797	101.0861	31	27	0.23
08/01/12	03:02:03.54	-3.2558	101.3262	15	23	0.53
08/01/12	12:31:21.07	-2.2960	100.2737	26	21	0.23
08/01/12	15:02:14.96	-2.1143	99.3442	24	18	0.15
08/01/12	18:41:31.67	-2.4630	100.4124	42	21	0.11
08/01/12	09:33:21.51	-2.1362	100.6112	3	18	0.08
08/01/13	13:42:51.35	-2.0782	100.7732	44	20	0.15
08/01/13	18:37:39.77	-2.8465	101.0492	42	16	0.24
08/01/13	19:47:21.21	-2.1227	100.0405	24	16	0.1
08/01/13	14:49:08.96	-1.9392	99.8025	29	20	0.07
08/01/14	15:39:40.07	-2.9650	101.0916	24	20	0.28
08/01/14	19:43:35.03	-2.4292	100.3618	24	18	0.12
08/01/15	01:10:45.05	-2.9260	100.0761	18	18	0.08
08/01/17	09:12:09.36	-2.9382	101.2148	32	31	0.21
08/01/17	17:25:18.47	-2.9443	101.0743	18	35	0.42
08/01/17	22:42:30.08	-2.2145	99.3885	24	28	0.21
08/01/17	01:07:00.97	-3.1238	100.1559	16	15	0.14
08/01/18	12:24:36.55	-2.1655	100.5832	4	17	0.25
08/01/18	14:45:40.36	-2.1370	100.0264	24	24	0.09
08/01/19	16:02:07.57	-3.2720	101.2650	11	30	0.54
08/01/19	18:08:55.56	-3.4303	100.3805	25	19	1.09
08/01/19	22:09:56.01	-3.1247	100.1568	17	23	0.17
08/01/19	03:46:14.54	-3.1357	100.1527	16	23	0.23
08/01/20	09:41:44.98	-3.5632	101.2653	34	15	0.34
08/01/20	19:13:09.03	-2.3485	100.2917	38	27	0.07
08/01/20	03:16:45.60	-3.3350	100.8560	22	17	0.3
08/01/21	19:09:28.51	-2.3850	99.8757	21	28	0.09
08/01/21	23:03:11.94	-1.7902	99.7451	19	17	0.17
08/01/21	01:15:52.14	-2.3305	100.3417	27	24	0.14
08/01/22	03:38:18.84	-3.0618	100.6663	1	15	0.61
08/01/22	05:48:23.73	-2.3187	100.2793	30	22	0.22
08/01/22	07:18:19.19	-2.5698	100.0312	25	15	0.37
08/01/22	20:48:55.71	-3.2092	100.2094	28	22	0.2
08/01/22	19:23:34.36	-2.9800	101.0343	32	25	0.43
08/01/23	02:14:39.60	-3.1088	100.1889	15	15	0.05
08/01/24	10:57:56.71	-1.8315	99.8400	26	14	0.19
08/01/24	20:41:27.42	-2.3337	100.2770	34	26	0.09
08/01/24	00:16:10.99	-2.2008	100.7293	6	19	0.1
08/01/25	04:35:06.72	-2.3303	100.3298	31	27	0.08
08/01/25	08:12:37.08	-3.2568	100.1180	19	18	0.35
08/01/25	17:09:25.47	-1.6752	100.2768	39	17	0.19
08/01/25	21:55:38.45	-2.3083	100.3052	25	25	0.23
08/01/25	07:04:32.54	-2.1937	100.7177	3	26	0.17

Date (YY/MM/DD)	Time(HH:MM:SS.SS)	Latitude	Longitude	Depth (km)	No. Picks	RMS (s)
08/01/26	18:26:40.10	-2.1988	100.7143	3	14	0.08
08/01/26	20:51:23.97	-3.1307	100.1381	18	26	0.28
08/01/26	21:19:14.26	-2.1365	100.6143	7	32	0.12
08/01/26	22:56:48.31	-2.3372	100.3016	28	24	0.15
08/01/28	12:43:32.29	-2.8263	100.2322	17	14	0.2
08/01/28	15:25:29.62	-2.9812	101.0574	23	26	0.23
08/01/28	20:51:47.25	-1.8383	99.8390	25	22	0.27
08/01/28	21:53:10.49	-2.3625	100.3446	32	37	0.12
08/01/29	08:40:44.77	-2.5455	100.3973	13	16	0.14
08/01/29	18:25:48.99	-2.9648	99.9590	14	16	0.73
08/01/29	22:25:13.58	-2.3507	100.3341	32	22	0.05
08/01/30	17:22:05.97	-1.4017	99.7616	64	35	0.22
08/01/30	22:25:52.82	-2.3423	100.2873	30	27	0.13
08/01/31	06:32:44.29	-2.1533	100.0715	25	20	0.11
08/02/01	06:50:35.99	-2.8423	100.2452	22	13	0.28
08/02/01	16:58:26.61	-3.3705	100.3163	23	17	0.36
08/02/02	05:38:46.74	-2.6195	101.0700	48	19	0.12
08/02/03	03:28:17.73	-2.3335	100.3299	31	27	0.11
08/02/03	09:57:25.23	-2.1113	100.6089	8	14	0.06
08/02/04	01:45:21.22	-2.4795	100.1917	10	14	0.17
08/02/04	02:42:20.56	-2.2268	99.8020	24	14	0.07
08/02/04	12:36:06.72	-1.8033	100.6542	54	20	0.39
08/02/04	16:36:29.28	-3.5267	100.2392	35	16	0.12
08/02/04	19:45:18.94	-2.2922	99.8651	22	28	0.13
08/02/04	21:16:19.01	-3.4005	101.4730	11	28	0.28
08/02/04	22:52:51.45	-2.9043	101.0491	20	24	0.36
08/02/05	03:04:56.56	-3.5783	100.6558	24	21	0.71
08/02/05	11:37:53.52	-1.0780	100.5318	6	18	0.87
08/02/05	13:39:48.40	-2.0237	100.0550	14	19	0.21
08/02/06	04:43:20.47	-3.6882	100.5419	46	18	0.23
08/02/06	17:48:31.42	-1.9712	99.6137	24	27	0.12
08/02/07	14:36:07.55	-1.7840	100.5608	63	16	0.18
08/02/08	03:26:54.10	-2.3232	100.2824	29	18	0.1
08/02/08	09:25:29.81	-2.5193	100.5891	23	25	0.23
08/02/08	23:07:26.84	-2.1165	100.6221	9	23	0.18
08/02/09	02:59:19.14	-2.3090	99.8515	21	17	0.09
08/02/11	00:32:00.32	-2.8202	100.3541	21	25	0.49
08/02/11	19:57:03.54	-2.2973	100.7558	47	28	0.18
08/02/11	20:05:10.70	-2.9633	101.0958	28	24	0.25
08/02/11	20:40:36.28	-2.3175	100.3297	24	28	0.23
08/02/12	01:29:41.37	-3.0385	101.1359	21	30	0.3
08/02/12	18:50:38.45	-3.2720	100.1472	25	16	0.32
08/02/14	00:35:54.75	-3.2118	100.1765	18	23	0.23
08/02/14	02:03:30.77	-2.1677	100.0703	25	25	0.13
08/02/14	03:44:02.89	-2.1570	100.0693	20	24	0.17
08/02/14	09:08:15.85	-2.3198	100.3089	26	29	0.2
08/02/14	12:17:31.09	-2.9432	101.0695	29	32	0.21
08/02/14	23:05:49.34	-3.3077	100.2143	23	25	0.24
08/02/15	06:01:54.59	-2.1520	100.0742	26	24	0.08
08/02/15	09:08:26.91	-2.3607	100.3194	36	19	0.04

Date (YY/MM/DD)	Time(HH:MM:SS.SS)	Latitude	Longitude	Depth (km)	No. Picks	RMS (s)
08/02/15	09:32:41.91	-2.3330	100.3349	25	19	0.2
08/02/15	21:26:20.81	-3.1713	100.6783	15	18	0.32
08/02/16	02:02:25.71	-3.5395	101.5481	15	29	0.65
08/02/16	16:40:25.76	-1.9790	100.3630	36	19	0.12
08/02/19	04:13:52.44	-1.9912	97.2007	39	17	0.08
08/02/19	06:29:53.82	-3.3500	100.7852	24	27	0.24
08/02/19	15:06:51.75	-2.4313	100.5581	28	16	0.33
08/02/19	17:01:32.18	-2.4547	99.7707	21	28	0.14
08/02/19	17:15:02.15	-2.2072	100.6973	2	20	0.17
08/02/19	17:26:37.17	-2.4450	99.7899	21	31	0.12
08/02/19	21:30:00.24	-2.2058	100.7011	7	23	0.17
08/02/20	00:19:04.20	-2.4558	99.7960	20	30	0.09
08/02/20	05:38:56.70	-2.4692	100.6727	25	30	0.24
08/02/20	17:06:55.68	-2.5688	100.3360	26	32	0.15
08/02/21	05:42:12.35	-2.4113	99.7755	21	26	0.11
08/02/22	03:29:05.93	-2.3848	99.8063	19	18	0.23
08/02/22	04:49:11.28	-2.2738	101.1236	63	20	0.21
08/02/22	06:44:44.08	-1.7883	99.7298	28	27	0.17
08/02/22	10:43:51.29	-1.7195	99.4688	12	21	0.29
08/02/22	12:34:02.51	-2.9030	101.0683	36	17	0.21
08/02/23	02:09:01.72	-2.4900	99.8030	20	30	0.13
08/02/23	07:17:10.62	-2.5908	99.8163	20	30	0.27
08/02/23	07:34:53.50	-1.9800	100.2355	40	18	0.15
08/02/23	09:17:25.73	-2.0905	100.6390	44	37	0.18
08/02/23	09:26:21.08	-2.0622	100.6309	47	19	0.19
08/02/23	13:07:27.00	-2.5857	99.8120	20	33	0.13
08/02/23	18:16:05.44	-2.5605	99.8558	18	19	0.23
08/02/23	18:52:35.43	-2.5728	99.8585	19	30	0.14
08/02/23	19:56:56.35	-2.5657	99.8690	19	16	0.12
08/02/23	20:40:29.57	-2.5540	99.8582	17	15	0.17
08/02/24	02:20:56.90	-2.6240	99.8262	19	25	0.11
08/02/24	04:36:31.85	-3.7863	101.8560	24	28	0.64
08/02/24	07:04:31.73	-2.6508	99.7697	16	21	0.65
08/02/24	08:53:38.22	-2.4467	99.8212	20	33	0.15
08/02/24	11:10:05.05	-2.1718	99.8747	29	21	0.2
08/02/24	12:10:49.88	-2.5593	99.8488	19	34	0.13
08/02/24	12:14:27.28	-2.5625	99.8465	18	22	0.12
08/02/24	14:40:31.10	-2.5468	99.8277	19	34	0.15
08/02/24	14:46:21.93	-2.5512	99.8242	19	28	0.19
08/02/24	14:52:23.50	-2.5775	99.9023	18	21	0.15
08/02/24	14:57:31.25	-2.5865	99.8623	19	27	0.15
08/02/24	15:39:49.38	-2.5435	99.9073	16	14	0.07
08/02/24	16:12:55.11	-2.4987	99.8955	19	23	0.15
08/02/24	17:54:27.34	-2.5160	99.7655	20	21	0.08
08/02/24	18:00:29.27	-2.5337	99.8618	18	25	0.19
08/02/25	02:08:26.10	-2.3773	100.3051	40	31	0.08
08/02/25	07:23:33.47	-2.4475	99.8415	20	14	0.17
08/02/25	07:33:03.17	-2.5752	99.9377	18	25	0.12
08/02/25	08:46:26.63	-2.7018	99.9682	17	23	0.22
08/02/25	08:54:00.49	-2.7103	99.8340	19	29	0.22

Date (YY/MM/DD)	Time(HH:MM:SS.SS)	Latitude	Longitude	Depth (km)	No. Picks	RMS (s)
08/02/25	10:12:29.00	-2.6782	100.0480	19	21	0.08
08/02/25	10:13:44.68	-2.7743	100.1204	19	17	0.13
08/02/25	10:17:30.93	-2.5432	99.9200	16	18	0.23
08/02/25	10:38:46.43	-2.4582	99.7878	21	33	0.16
08/02/25	11:06:00.50	-2.5348	99.9460	17	15	0.16
08/02/25	13:33:50.25	-2.4520	99.7894	20	25	0.15
08/02/25	14:14:26.07	-2.4380	99.8134	21	32	0.12
08/02/25	15:08:19.56	-2.6902	99.8642	18	21	0.15
08/02/25	15:24:31.08	-3.0338	99.9970	20	15	0.26
08/02/25	18:06:04.25	-2.4665	99.7914	20	26	0.24
08/02/25	18:27:36.05	-2.5225	99.9192	18	16	0.11
08/02/25	18:53:17.35	-1.7898	99.5237	8	23	0.3
08/02/25	19:17:08.61	-2.4588	99.8581	19	21	0.11
08/02/25	19:53:29.05	-1.4805	100.5282	67	18	0.12
08/02/25	20:30:49.89	-2.8638	100.0255	18	28	0.11
08/02/25	21:02:18.89	-2.3930	99.7255	20	26	0.16
08/02/25	21:29:03.41	-2.6530	99.8204	20	22	0.09
08/02/25	21:45:04.48	-2.3200	99.7782	22	27	0.1
08/02/25	22:44:34.09	-2.4278	99.5932	16	29	0.2
08/02/25	23:05:13.31	-2.4027	99.6856	20	18	0.22
08/02/26	00:33:48.70	-2.5205	99.9339	17	18	0.12
08/02/26	00:58:35.58	-2.0970	99.8602	25	24	0.14
08/02/26	03:57:24.27	-2.6873	99.9884	18	24	0.13
08/02/26	04:42:24.53	-2.4988	99.5327	24	29	0.38
08/02/26	05:29:12.99	-2.6938	99.8503	19	32	0.12
08/02/26	07:27:17.58	-2.6717	100.0512	19	27	0.12
08/02/26	08:11:56.61	-2.2913	99.8624	22	23	0.26
08/02/27	02:39:37.25	-2.6752	100.0490	19	17	0.13
08/02/27	10:25:14.99	-2.5047	99.9832	21	31	0.18
08/02/27	11:20:44.19	-2.4855	99.7383	20	19	0.08
08/02/27	21:03:28.03	-2.7207	99.8824	22	25	0.09
08/02/28	00:49:24.42	-2.2242	100.0988	19	21	0.17
08/02/28	06:53:47.95	-3.4493	100.3739	26	16	0.19
08/02/28	11:15:38.26	-2.1838	100.7068	8	24	0.24
08/02/28	18:06:23.39	-2.0850	101.9252	15	20	0.47
08/02/29	06:36:41.07	-1.4983	99.5968	35	33	0.08
08/02/29	09:17:31.73	-2.2062	100.0685	19	27	0.35
08/02/29	17:54:42.88	-2.9038	100.0948	17	23	0.17
08/02/29	18:13:16.09	-1.8428	100.3848	41	17	0.09
08/03/01	02:48:58.10	-3.1107	101.2450	23	28	0.36
08/03/01	10:32:54.92	-2.0652	100.9141	62	30	0.19
08/03/01	10:44:31.86	-1.9890	100.0792	24	16	0.1
08/03/01	22:25:03.39	-2.7207	99.8726	23	35	0.17
08/03/01	22:56:56.91	-2.7182	99.8774	22	29	0.18
08/03/02	01:05:55.60	-1.9375	100.7053	4	23	0.18
08/03/02	02:22:09.65	-1.8153	99.6060	21	18	0.11
08/03/02	11:23:51.40	-2.0448	100.1342	6	17	0.46
08/03/02	18:43:05.39	-1.7655	99.5477	17	17	0.71
08/03/03	02:37:28.16	-2.2585	99.7457	23	28	0.12
08/03/03	03:08:27.05	-2.2657	99.8311	19	17	0.49

Date (YY/MM/DD)	Time(HH:MM:SS.SS)	Latitude	Longitude	Depth (km)	No. Picks	RMS (s)
08/03/03	03:53:50.68	-2.2458	99.7941	23	31	0.16
08/03/03	07:00:40.08	-2.3203	99.7592	22	30	0.12
08/03/03	10:06:34.36	-4.6717	100.5506	57	16	0.16
08/03/03	14:24:48.31	-2.2545	100.6121	0	17	0.1
08/03/03	16:53:57.21	-1.8557	100.3740	39	16	0.23
08/03/03	18:40:48.64	-2.3012	100.3238	18	20	0.25
08/03/03	21:11:09.88	-5.6503	101.2681	65	6	0.42
08/03/04	20:29:20.27	-1.7895	101.4427	2	18	0.51
08/03/05	01:37:06.25	-2.1285	100.0998	24	22	0.11
08/03/05	13:26:35.11	-2.2255	99.8112	23	33	0.11
08/03/05	16:10:02.77	-2.7445	99.6511	23	17	0.23
08/03/05	18:55:22.58	-2.2227	99.7902	24	33	0.14
08/03/05	20:33:49.75	-2.7050	99.8765	22	28	0.12
08/03/06	03:36:14.26	-2.2682	99.7170	23	34	0.14
08/03/06	21:54:32.18	-2.1708	99.8640	25	23	0.08
08/03/07	05:00:09.59	-2.6783	100.0473	18	19	0.11
08/03/07	14:54:53.40	-1.7187	99.7118	14	25	0.35
08/03/07	16:48:27.35	-3.1295	100.2043	15	14	0.04
08/03/08	03:30:03.19	-2.0587	101.0293	6	14	0.13
08/03/08	21:33:24.85	-2.7623	100.4455	1	16	0.31
08/03/09	09:16:22.27	-2.6688	99.7920	20	36	0.25
08/03/09	23:04:13.19	-2.6398	100.4036	22	27	0.31
08/03/10	15:57:30.51	-2.4043	100.3267	25	20	0.17
08/03/10	19:56:19.15	-2.5238	99.7881	20	30	0.08
08/03/10	20:32:42.99	-1.9633	100.6981	42	14	0.29
08/03/12	05:10:52.69	-1.8382	100.3732	43	23	0.2
08/03/12	18:44:43.72	-2.5188	99.7836	20	27	0.14
08/03/13	06:55:43.59	-2.1055	99.8178	26	32	0.13
08/03/13	20:53:17.61	-4.9555	101.2415	33	17	0.24
08/03/13	21:56:26.61	-2.5963	99.6183	27	25	0.12
08/03/13	22:00:13.71	-2.3745	99.9817	8	33	0.2
08/03/13	22:27:51.51	-1.8620	100.3740	40	13	0.06
08/03/15	00:15:08.68	-1.2643	100.2920	73	23	0.13
08/03/16	03:38:44.97	-2.4622	99.8984	20	20	0.12
08/03/16	08:41:00.03	-2.3295	100.3145	30	31	0.13
08/03/16	13:01:26.36	-2.8527	100.0659	17	20	0.16
08/03/16	16:27:05.04	-2.9013	101.0727	23	27	0.47
08/03/16	23:05:28.07	-2.8682	101.0029	19	34	0.52
08/03/17	06:57:31.07	-2.0728	100.6987	5	20	0.2
08/03/17	20:43:44.09	-2.0547	100.0539	23	18	0.15
08/03/18	04:39:50.71	-3.5462	100.9640	26	23	0.25
08/03/18	12:21:12.58	-3.3008	100.3298	22	24	0.73
08/03/19	11:19:52.61	-2.6942	100.9958	45	25	0.12
08/03/19	11:35:54.15	-2.6932	100.9861	44	23	0.18
08/03/20	01:44:21.66	-2.1372	100.1041	21	18	0.25
08/03/20	14:46:41.32	-2.0153	102.2172	10	26	0.5
08/03/20	15:57:08.74	-2.7543	100.2138	29	34	0.13
08/03/20	18:53:47.99	-2.9882	99.4699	9	23	0.77
08/03/20	20:03:40.57	-2.8270	99.6748	44	16	0.3
08/03/21	16:11:09.44	-2.0903	99.9897	29	25	0.16

Date (YY/MM/DD)	Time(HH:MM:SS.SS)	Latitude	Longitude	Depth (km)	No. Picks	RMS (s)
08/03/21	20:57:21.20	-2.1093	100.0743	24	27	0.16
08/03/21	23:32:41.63	-2.3192	100.2674	32	33	0.17
08/03/22	14:43:08.80	-1.6293	99.9727	35	25	0.17
08/03/23	03:52:20.53	-1.8918	99.7331	26	29	0.13
08/03/24	05:36:23.53	-3.0585	101.2549	30	24	0.27
08/03/24	06:24:38.36	-2.7028	100.9858	43	26	0.19
08/03/24	19:22:44.77	-2.2922	100.7480	41	34	0.22
08/03/24	21:28:51.35	-2.3372	100.2876	34	29	0.14
08/03/25	03:22:16.05	-2.6920	99.9792	18	37	0.14
08/03/25	20:43:46.13	-1.7342	99.5976	19	17	0.27
08/03/26	20:42:39.23	-4.8808	100.4430	36	18	0.33
08/03/27	01:28:10.56	-2.1097	100.1520	14	21	0.26
08/03/27	07:18:57.14	-1.9155	99.9101	16	17	0.1
08/03/28	00:30:39.20	-2.1087	100.6210	9	30	0.2
08/03/28	16:57:49.66	-3.2878	100.3110	28	25	0.47
08/03/28	20:14:05.39	-2.1118	100.6206	8	25	0.07
08/03/28	21:50:58.05	-2.3637	101.2024	66	22	0.09
08/03/29	10:37:05.23	-2.6787	99.9548	18	21	0.07
08/03/29	10:41:39.15	-2.2633	100.7038	0	17	0.18
08/03/29	23:47:22.44	-2.1617	99.7592	24	14	0.07
08/03/31	02:44:37.65	-2.3128	100.3225	19	16	0.26
08/03/31	13:30:57.29	-2.9062	101.0841	26	27	0.4
08/03/31	15:47:50.52	-2.9193	101.0836	27	29	0.36
08/03/31	16:00:22.20	-2.8898	101.0858	28	21	0.2
08/03/31	16:37:58.91	-2.9253	101.0793	31	29	0.25
08/03/31	17:07:10.72	-0.9088	99.5837	6	33	0.52
08/03/31	20:26:40.76	-3.1242	100.1582	18	22	0.19
08/03/31	21:15:55.97	-3.1373	100.1495	17	20	0.18
08/03/31	22:58:52.11	-3.1205	100.1647	16	15	0.14
08/04/02	08:48:49.28	-4.3595	102.6475	14	16	0.55
08/04/02	19:09:01.42	-0.3193	99.0332	11	30	0.59
08/04/03	08:51:56.92	-1.5162	100.0817	32	14	0.35
08/04/04	13:35:05.52	-2.0863	100.6424	47	22	0.19
08/04/04	18:39:49.78	-2.2072	100.5449	1	22	0.2
08/04/05	03:15:26.56	-2.4842	101.0876	59	21	0.13
08/04/05	15:21:37.88	-1.9960	100.0947	10	16	0.27
08/04/09	14:47:48.89	-2.4883	100.4513	11	15	0.16
08/04/09	03:38:30.77	-3.7620	100.7310	35	19	0.41
08/04/09	14:47:49.12	-2.5058	100.4429	9	20	0.23
08/04/09	21:21:46.40	-1.2937	100.0141	53	26	0.28
08/04/10	15:47:43.01	-2.2800	100.6770	6	19	0.09
08/04/10	17:01:48.81	-2.6268	99.8468	18	17	0.18
08/04/11	22:05:30.00	-3.3917	100.8595	17	14	0.56
08/04/12	21:36:14.37	-2.1413	100.6387	41	25	0.23
08/04/13	00:06:01.84	-2.0515	100.7226	7	24	0.26
08/04/14	10:21:49.53	-1.7957	99.7024	19	30	0.22
08/04/16	04:34:22.13	-2.8235	100.4537	31	21	0.11
08/04/17	16:53:36.73	-1.6062	99.4012	7	20	0.28
08/04/18	02:01:09.24	-1.9198	99.3969	21	25	0.19
08/04/18	14:32:57.33	-2.0862	100.6889	2	20	0.14

Date (YY/MM/DD)	Time(HH:MM:SS.SS)	Latitude	Longitude	Depth (km)	No. Picks	RMS (s)
08/04/18	20:51:18.09	-2.9387	100.0419	17	16	0.45
08/04/19	20:47:34.28	-2.3403	100.8035	53	25	0.15
08/04/20	05:20:47.60	-1.6407	99.4780	4	20	0.33
08/04/20	11:21:09.73	-2.8702	100.7475	5	22	0.52
08/04/20	19:27:51.09	-1.0483	99.5516	42	21	0.21
08/04/22	01:46:03.06	-2.1908	99.4527	25	21	0.19
08/04/22	08:02:25.40	-1.8425	100.4086	47	22	0.19
08/04/23	00:12:59.20	-1.5223	99.1387	14	18	0.23
08/04/23	04:29:52.79	-1.5785	99.3742	10	17	0.33
08/04/24	05:07:48.14	-1.6595	100.5985	59	29	0.26
08/04/24	13:18:06.41	-2.3548	100.3409	31	28	0.09
08/04/24	13:33:42.25	-1.7585	99.6113	20	17	0.16
08/04/26	02:21:51.82	-0.8293	100.1475	100	34	0.31
08/04/27	05:44:57.67	-1.5492	99.8420	23	14	0.44
08/04/27	08:08:45.77	-1.8752	99.7042	29	18	0.37
08/04/27	10:44:50.33	-2.3330	99.9141	22	23	0.11
08/04/27	13:16:12.87	-1.6207	99.1685	36	14	0.42
08/04/28	09:36:33.45	-2.0883	100.6986	4	30	0.16
08/04/28	10:56:27.68	-3.7625	100.2140	48	15	0.76
08/04/29	14:04:39.09	-1.4987	99.1331	14	16	0.33
08/04/30	05:31:15.47	-2.6730	100.4946	32	18	0.08
08/04/30	16:15:25.11	-3.2873	100.2424	24	24	0.4
08/05/01	17:44:55.29	-2.9860	101.0906	18	28	0.47
08/05/03	18:49:12.36	-0.3775	99.4562	76	20	0.68
08/05/04	04:41:29.81	-2.3108	100.9087	42	22	0.37
08/05/04	19:50:42.33	-3.2955	100.2266	23	24	0.19
08/05/04	22:20:36.06	-2.3270	100.3584	20	25	0.23
08/05/04	23:12:43.64	-2.1293	100.6351	15	29	0.17
08/05/05	09:52:42.57	-2.2883	100.7297	44	30	0.19
08/05/05	20:06:12.25	-2.2667	99.3371	30	23	0.2
08/05/06	07:21:15.07	-2.0858	100.6323	12	26	0.25
08/05/08	15:21:11.92	-1.0092	99.5940	29	24	0.29
08/05/10	22:51:19.91	-2.0827	100.4106	37	26	0.14
08/05/12	05:36:04.60	-2.3417	100.3423	29	18	0.14
08/05/14	11:21:04.90	-2.2708	100.3268	7	26	0.34
08/05/14	11:47:41.67	-2.0817	100.7127	7	23	0.15
08/05/14	21:25:18.18	-2.5300	99.7521	24	17	0.1
08/05/14	21:44:10.32	-2.5457	99.7129	22	24	0.15
08/05/15	11:27:03.03	-2.5837	99.8299	21	22	0.16
08/05/15	11:37:55.75	-2.5742	99.8428	21	22	0.15
08/05/16	00:46:35.44	-3.8325	99.9119	34	17	0.18
08/05/17	20:56:09.41	-1.9793	100.0283	11	20	0.35
08/05/18	10:58:32.76	-3.0860	100.1106	21	19	0.23
08/05/20	17:08:01.03	-3.2462	101.3231	17	26	0.27
08/05/20	17:53:34.95	-2.1307	99.4954	23	20	0.17
08/05/21	06:51:59.49	-2.0650	100.6095	10	20	0.1
08/05/22	14:11:35.57	-3.2622	100.1772	19	21	0.45
08/05/23	20:51:19.72	-1.9575	99.8890	26	18	0.16
08/05/24	03:15:55.18	-2.2395	99.4419	24	21	0.22
08/05/24	21:04:17.58	-2.1785	100.7328	51	20	0.09

Date (YY/MM/DD)	Time(HH:MM:SS.SS)	Latitude	Longitude	Depth (km)	No. Picks	RMS (s)
08/05/26	03:09:11.94	-2.1825	101.0016	63	20	0.13
08/05/26	15:55:02.55	-1.8932	100.4863	49	19	0.18
08/05/27	17:04:24.06	-2.5105	99.6371	26	17	0.17
08/05/28	04:53:37.08	-1.7070	99.9139	47	27	0.15
08/05/29	17:00:56.03	-2.6903	99.9270	20	23	0.12
08/06/02	20:11:47.07	-1.9710	100.6610	45	23	0.39
08/06/06	00:11:59.07	-2.1185	100.1167	17	22	0.14
08/06/06	23:11:55.78	-2.6680	99.9933	16	15	0.16
08/06/10	05:27:06.73	-1.5507	99.4725	5	22	0.3
08/06/12	19:09:16.51	-2.0158	100.4632	43	23	0.12
08/06/13	12:35:22.04	-2.3683	99.9906	5	19	0.34
08/06/14	07:16:39.19	-2.3242	100.3152	29	24	0.18
08/06/16	00:29:09.66	-2.1310	100.1012	25	20	0.11
08/06/17	16:02:23.69	-3.0637	100.0327	23	22	0.22
08/06/20	12:24:55.46	-2.2053	98.4791	36	22	0.11
08/06/20	20:47:07.00	-2.3027	100.7436	46	26	0.19
08/06/21	03:36:38.51	-2.1395	98.5453	27	22	0.56
08/06/21	15:54:03.35	-0.4128	98.5525	28	14	0.2
08/06/23	03:45:19.50	-2.2130	100.2271	21	17	0.19
08/06/23	11:28:40.74	-5.8382	100.6402	55	7	0.17
08/06/30	00:56:19.28	-2.2725	101.2549	76	28	0.14
08/07/07	00:32:54.91	-2.2902	100.7882	51	21	0.12
08/07/08	20:39:36.10	-2.2692	99.3768	29	18	0.17
08/07/09	23:21:55.92	-2.1305	100.6005	1	22	0.25
08/07/09	23:30:44.00	-2.1402	100.6190	7	18	0.07
08/07/10	01:00:46.58	-2.1543	100.6109	7	23	0.12
08/07/10	01:34:29.76	-2.1553	100.6275	7	18	0.12
08/07/10	03:53:56.40	-2.1438	100.6216	9	25	0.11
08/07/10	04:42:43.05	-2.1422	100.6089	9	22	0.1
08/07/10	10:05:55.88	-1.8608	100.3970	44	23	0.2
08/07/10	12:38:23.27	-2.1432	100.6238	10	23	0.1
08/07/10	14:24:13.73	-2.1615	100.6136	8	21	0.11
08/07/10	17:13:22.08	-2.1673	100.6155	10	26	0.12
08/07/10	18:48:03.57	-2.1565	100.6138	8	21	0.1
08/07/10	20:51:01.82	-2.1478	100.6190	10	20	0.06
08/07/11	02:03:53.24	-2.1595	100.6184	7	18	0.09
08/07/12	20:37:47.94	-2.1173	100.6607	10	20	0.2
08/07/13	04:12:25.41	-2.1457	100.6259	9	26	0.09
08/07/13	04:19:29.42	-2.1470	100.6315	10	19	0.17
08/07/13	04:53:35.64	-2.1612	100.6182	8	21	0.14
08/07/13	12:35:32.51	-2.1578	100.6115	8	25	0.13
08/07/14	01:09:26.64	-2.1193	100.6510	5	21	0.2
08/07/14	01:36:12.85	-2.1445	100.6212	5	17	0.09
08/07/15	02:28:21.27	-2.1460	100.6264	9	23	0.07
08/07/15	03:08:00.03	-2.1467	100.6114	9	21	0.16
08/07/16	01:15:32.95	-2.1533	100.6148	9	26	0.11
08/07/17	05:50:44.98	-2.1582	100.6272	8	22	0.17
08/07/17	15:19:01.91	-2.1428	100.6318	9	21	0.11
08/07/18	19:48:21.23	-2.1623	100.6133	7	14	0.08
08/07/20	04:35:34.28	-2.4672	99.9603	22	21	0.49

Date (YY/MM/DD)	Time(HH:MM:SS.SS)	Latitude	Longitude	Depth (km)	No. Picks	RMS (s)
08/07/28	07:10:02.60	-1.2155	99.6647	22	26	0.29
08/07/28	07:46:15.20	-1.8743	100.3676	39	23	0.16
08/07/29	09:28:22.15	-2.1455	100.6360	8	20	0.11
08/07/29	12:00:44.25	-2.0948	100.6363	10	14	0.18
08/07/31	16:41:17.38	-2.8185	100.4003	35	18	0.09
08/08/03	08:56:30.21	-2.1420	100.6214	7	21	0.12
08/08/05	00:49:27.21	-2.1467	100.6247	10	18	0.05
08/08/05	18:18:41.88	-2.3017	100.3031	26	20	0.17
08/08/16	08:02:26.06	-2.1523	100.6185	5	16	0.08
08/08/16	11:07:35.41	-2.1607	100.6145	11	20	0.09
08/08/25	01:32:47.85	-1.8535	100.3743	44	22	0.18
08/08/25	23:14:34.13	-2.4237	100.3410	18	18	0.19
08/08/26	17:19:38.41	-2.1212	100.6425	8	20	0.27
08/08/27	07:45:24.53	-2.2032	99.6992	24	16	0.12
08/08/27	10:54:32.89	-2.0143	99.7475	26	24	0.2
08/08/27	20:36:32.33	-1.4773	100.4350	66	20	0.17
08/08/29	12:42:29.32	-2.1377	100.6194	10	23	0.13
08/09/04	02:03:27.02	-2.6930	101.0291	43	20	0.18
08/09/05	21:26:36.82	-1.6962	99.6587	30	22	0.26
08/09/06	14:17:20.82	-1.7712	99.6706	12	22	0.15
08/09/07	16:48:36.51	-2.1470	100.6220	6	17	0.13
08/09/07	17:48:24.30	-2.1497	100.6199	10	22	0.15
08/09/08	07:33:55.33	-1.7037	100.5800	52	19	0.14
08/09/08	10:43:27.30	-2.3200	100.3134	30	20	0.31
08/09/11	13:32:22.60	-2.3388	100.3472	21	19	0.25
08/09/12	21:59:07.17	-2.1475	100.5966	8	25	0.09
08/09/13	02:08:02.70	-2.1483	100.5882	8	23	0.06
08/09/13	20:15:53.29	-2.1515	100.5911	9	17	0.06
08/09/14	17:45:47.46	-2.3122	100.7386	44	17	0.16
08/09/14	20:24:25.56	-2.1465	100.6194	10	20	0.1
08/09/15	04:22:04.13	-2.7952	101.1987	44	22	0.3
08/09/15	12:47:34.48	-2.1322	100.6236	7	18	0.15
08/09/15	15:50:06.34	-2.1535	100.6176	8	16	0.07
08/09/16	04:34:54.46	-2.1452	100.6333	8	21	0.15
08/09/17	11:33:00.79	-1.8505	100.3516	44	21	0.18
08/09/19	07:37:54.57	-2.2292	99.9689	28	19	0.16
08/09/20	13:54:41.86	-2.1427	100.6333	11	20	0.12
08/09/20	17:44:08.20	-1.1043	99.7148	0	21	0.59
08/09/20	21:51:19.22	-2.1555	100.6013	6	17	0.1
08/09/20	22:34:01.93	-1.7045	100.6692	73	24	0.23
08/09/21	15:02:41.37	-2.0317	100.6946	8	17	0.07
08/09/23	00:12:53.79	-2.1423	100.6100	10	19	0.17
08/09/25	20:33:07.82	-2.2452	99.8802	30	20	0.18
08/10/01	00:33:52.20	-2.2572	100.7855	38	21	0.22
08/10/01	16:50:46.57	-2.0710	100.0548	23	16	0.07
08/10/02	13:02:58.33	-2.4375	100.4731	25	19	0.2

A.4

Shear Wave Splitting Results

This appendix contains the shear wave splitting results (25 SKS and 78 local) shown in Chapter 7. Also included are figures illustrating how a SWS result was analysed.

YR	JD	HHMM	LAT (°) (Source)	LON (°) (Source)	LAT (°) (Sta)	LON (°) (Sta)	Depth (km)	Baz (°)	Spol (°)	Sheba Φ (°)	Sheba Φ error (°)	Sheba δt (s)	Sheba δt error (s)	Φ RC (°)	δt RC (s)	Φ SC (°)	δt SC (s)	Φ EV (°)	δt EV (s)	STA
2008	82	2124	52.18	-178.72	-3.19	102.17	132	37	19	-38	4.25	1.38	0.07	-36.86	1.36	-31<-23<-17	1.1<1.3<1.6	-34.9	1.4	ATTB
2008	82	2124	52.18	-178.72	-3.53	102.03	132	37	40	-16	6	1.05	0.08	-13.86	1.04	-29<-19<-13	0.8<1.0<1.3	-14.9	1	LAIS
2008	82	2124	52.18	-178.72	-0.4	99.94	132	37	21	-35	12	1.2	0.13	-22.52	1.16	-27<-19<-13	0.8<1.0<1.4	-14.5	1.2	TIKU
2008	293	510	-21.82	-173.56	1.09	99.44	43.3	112	105	-22	9.75	1.9	0.22	-22.06	1.9	-29<-18<-13	1.5<1.8<2.2	-26	1.8	A20S
2008	296	1256	-18.4	-174.98	1.09	99.44	244	109	109	-11	14.75	0.9	0.22	-18.45	0.85	-29<-15<-7	0.7<0.9<1.1	-19.5	0.8	A20S
2008	344	624	-31.03	-176.54	1.09	99.44	18.8	121	128	0	4.5	1.02	0.04	-27.53	1.17	-23<-15<-11	1.0<1.2<1.3	-20.5	1.2	A20S
2008	293	510	-21.82	-173.56	0.59	99.94	43.3	112	102	-16	7	2.17	0.26	-15.07	2.14	-15<-6<-5	2.0<2.4<2.8	-14.1	2.2	B30S
2008	293	510	-21.82	-173.56	-0.22	100.32	43.3	112	101	-13	3.75	2.58	0.21	-12.1	2.62	-13<-4<-3	2.4<2.8<3.2	-14.1	2.6	C20S
2008	293	510	-21.82	-173.56	-0.65	100.6	43.3	112	113	-13	7.25	2.35	0.21	-18.13	2.26	-25<-12<-5	1.8<2.4<2.9	-10.1	2.4	F03S
2008	293	510	-21.82	-173.56	0.61	99.3	43.3	112	96	-24	4.5	2.1	0.14	-22.08	2.14	-19<-10<-7	2.0<2.4<2.8	-22.1	2.1	F50S
2008	293	510	-21.82	-173.56	1.47	99.47	43.3	112	113	4	6.25	2.13	0.34	3.93	2.16	-7<2<7	1.5<2.0<2.7	1.9	2	N20S
2008	344	624	-31.03	-174.98	1.47	99.47	18.8	121	118	2	2.75	1.63	0.09	2.46	1.57	-3<3<9	1.4<1.6<2.0	-4.5	1.5	N20S
2008	293	510	-21.82	-173.56	1.63	99.74	43.3	112	111	1	2.75	1.92	0.15	-2.02	1.71	-3<2<5	1.6<1.9<2.3	2	1.9	N50S
2008	293	510	-21.82	-173.56	-1.33	99.09	43.3	112	111	-10	5.5	1.72	0.17	-13	1.62	-19<-10<-7	1.4<1.7<2.0	-10.2	1.7	Z20S
2008	293	510	-21.82	-173.56	0.33	99.92	29	112	110	-4	7.25	2.82	0.36	-4	2.8	-13<-2<1	2.2<2.9<3.4	-4.1	2.8	B15B
2008	296	1256	-18.4	-174.98	0.33	99.92	233	109	110	-12	10.5	1.56	0.2	-18.49	1.44	-29<-15<-17	1.0<1.4<1.8	-15.5	1.4	B15B
2008	293	510	-21.82	-173.56	0.76	99.54	29	112	111	-24	16.5	1.5	0.28	-24.07	1.44	-35<-20<-11	1.2<1.5<1.8	-18.1	1.5	B50B
2008	344	624	-31.03	-174.98	1.15	99.76	19	122	134	4	5.5	1.9	0.1	-0.5	1.89	-17<-7<-3	1.5<1.8<2.1	-4.5	1.8	L60S
2008	344	624	-31.03	-174.98	0.1	100.21	18	121	110	-25	17	2.16	0.3	-21.56	2.12	-27<-17<-9	1.8<2.2<2.6	-26.6	2.1	C45B
2008	344	624	-31.03	-174.98	1.64	99.88	18	122	109	-14	10.5	1.38	0.22	-12.46	1.4	-13<0<5	1.2<1.6<1.9	-14.5	1.4	N60B

Table A4.1: Good SKS SWS measurements. JD= Julian day, Baz=Backazimuth, spol=source polarization, Sheba= Eigenvalue method using Sheba, RC=rotation

correlation method using SplitLab, SC=Silver and Chan (1991) minimum transverse energy method using Splitlab and EV=eigenvalue method using SplitLab.

YR	JD	HHMM	LAT (°) (Source)	LON (°) (Source)	LAT (°) (Sta)	LON (°) (Sta)	Depth (km)	Baz (°)	Spol (°)	Sheba Φ (°)	Sheba Φ error (°)	Sheba δt (s)	Sheba δt error (s)	Φ RC (°)	δt RC (s)	Φ SC (°)	δt SC (s)	Φ EV (°)	δt EV (s)	STA
2008	293	510	-21.82	-173.56	0.33	99.4	43	112	96	-28	9.5	1.85	0.24	-28.06	1.84	-25<-12<-5	1.6<2.1<2.7	-28.1	1.8	A30S
2008	296	1256	-18.4	-174.98	0.33	98.51	244	108	125	77	23	0.72	0.34	76	0.74	33<42<56	0.8<1.3<1.9	58	0.9	Y20S
2008	344	624	-31.03	-174.98	0.76	99.54	15	121	113	-4	6.25	1.2	0.16	-15	0.96	-1<5<11	1.1<1.4<1.7	-2.5	1.2	B50B
2008	296	1256	-18.4	-174.98	0.33	97.71	244	108	127	58	8.5	1.3	0.28	65	1.14	39<42<48	1.8<2.1<2.6	60	1.2	X10S
2008	296	1256	-18.4	-174.98	0.33	98.28	244	108	114	45	2.75	1.95	0.13	51	1.64	37<42<48	1.8<2.1<2.6	50	1.9	Y40S

Table A4.2: Additional 5 stable SKS SWS measurements. For abbreviations see table A4.1

YEAR	JULDAY	HHMM	LAT (°) (Source)	LON (°) (Source)	LAT (°) (Station)	LON (°) (Station)	Depth (km)	EPI Dist (°)	BAZ (°)	Spol (°)	Φ (°)	Φ error (°)	δt (s)	δt error (s)	STA
2009	43	2137	-0.2	98.32	-0.05	98.28	24.7	0.15	168.19	108.58	-32	6.25	0.31	0.01	Y40S
2008	267	732	0.01	98.4	-0.05	98.28	31.9	0.13	63.17	52.33	-68	5.75	0.21	0.01	Y40S
2008	56	723	-2.43	99.88	-2.35	99.84	19.85	0.09	150.57	20.76	-48	24	0.23	0.15	DSAO
2008	57	727	-271	100.03	-2.61	100.11	18.83	0.12	218.22	14.76	-61	4.5	0.12	0.02	SMYA
2008	58	239	-2.67	100.03	-2.61	100.11	18.87	0.1	234.48	10.96	-67	2.5	0.14	0.01	SMYA
2008	67	500	-2.68	100.06	-2.61	100.11	18.39	0.09	214.33	359.34	-78	2.75	0.15	0.01	SMYA

Table A4.3: Local SWS measurements from the forearc island region

YEAR	JULDAY	HHMM	LAT (°) (Source)	LON (°) (Source)	LAT (°) (Station)	LON (°) (Station)	Depth (km)	EPI Dist (°)	BAZ (°)	Spol (°)	Φ (°)	Φ error (°)	δt (s)	δt error (s)	STA
2008	178	456	1.12	98.89	0.61	99.3	101.8	0.65	321.99	328.01	-66	9.5	0.32	0.02	F50S
2008	183	1544	0.45	99.75	0.61	99.3	135.9	0.47	109.3	156.5	31	10.25	0.14	0.01	F50S
2008	269	6	0.35	99.13	0.61	99.3	83.7	0.3	212.44	21.68	-51	3	0.21	0.01	F50S
2009	26	522	0.12	100.04	-0.34	100.03	126.8	0.47	1.23	176.54	37	10.5	0.29	0.02	S04S
2008	252	733	-1.69	100.59	-1.75	100.8	52.01	0.21	285.53	156.74	60	1.25	0.18	0	LIKU
2008	56	1953	-1.5	100.5	-1.26	100.39	67.36	0.26	154.08	62.43	-88	7.5	0.08	0.01	SWLT
2008	33	538	-2.59	101.06	-2.29	100.16	48.07	0.31	197.54	45.76	16	10.25	0.1	0.01	LUNG

Table A4.4:Local SWS measurements from the forearc region

YEAR	JULDAY	HHMM	LAT (°) (Source)	LON (°) (Source)	LAT (°) (Station)	LON (°) (Station)	Depth (km)	EPI Dist (°)	BAZ (°)	Spol (°)	Φ (°)	Φ error (°)	δt (s)	δt error (s)	STA
2008	137	2045	1.4	98.89	1.33	99.31	103.2	0.42	279.24	106.74	68	8.5	0.14	0.01	A50S
2008	137	2045	1.4	98.89	1.47	99.04	103.2	0.17	244.4	48.61	-80	11.5	0.06	0.01	F70S
2008	146	1002	1.22	98.97	1.47	99.32	102.8	0.43	234.9	120.52	3	5.75	0.38	0.01	N10S
2008	146	1216	1.24	98.97	1.09	99.44	102.5	0.49	287.74	82.87	-34	4.25	0.38	0.01	A20S
2008	152	1026	0.72	99.18	1.09	99.44	92.2	0.45	215.42	74.58	-44	5.5	0.31	0.01	A20S
2008	157	523	1.76	98.9	1.47	99.04	132.5	0.32	339.97	125.89	-5	8.5	0.14	0.01	F70S
2008	159	617	0.61	100.26	0.31	100.11	190.2	0.33	26.8	72.55	-62	6	0.25	0.02	B10S
2008	159	617	0.61	100.26	0.21	100.12	190.2	0.42	18.74	65.58	-73	8	0.37	0.02	C60S
2008	159	1124	1.42	98.92	1.09	99.44	101.9	0.61	302.5	16.34	-43	7.25	0.28	0.01	A20S
2008	163	1333	0.46	99.88	0.31	100.11	127.1	0.26	301.88	132.14	13	6.25	0.13	0.01	B10S
2008	165	1335	1.2	98.94	1.25	99.33	93.6	0.39	262.64	358.61	-39	14.25	0.2	0.03	A40S
2008	174	2217	1.26	98.84	1.47	99.32	87.5	0.53	246.16	132.25	-1	9.75	0.11	0.01	N10S
2008	185	2243	1.29	98.85	1.47	99.04	103.2	0.27	228.16	83	-39	2.75	0.14	0	F70S
2008	195	757	2.03	99	1.25	99.33	134.1	0.84	337	118.4	-25	13.25	0.17	0.02	A40S
2008	207	1738	0.51	99.55	0.96	99.53	126.1	0.44	177.73	125.34	84	10.5	0.16	0.01	A10S
2008	236	716	1.41	99.7	0.96	99.53	172.7	0.48	20.24	69.93	53	7.25	0.21	0.04	A10S
2008	296	1957	0.77	99.68	1.09	99.44	150.5	0.4	142.62	86.18	-54	8	0.17	0.02	A20S
2009	26	522	0.12	100.04	0.31	100.11	126.8	0.2	200.61	207.03	77	8.25	0.17	0.01	B10S
2009	35	817	0.28	100.32	0.21	100.11	155.4	0.21	100.58	36.5	-82	15.25	0.19	0.05	B10S
2008	232	1933	0.74	99.42	1.09	99.44	113	0.35	183.89	141.96	-10	5.75	0.22	0.01	A20S
2008	240	1558	0.59	99.86	1.09	99.44	147.1	0.65	139.68	78.42	-29	4	0.28	0.02	A20S
2008	290	1141	1.2	98.97	1.47	99.04	105.4	0.28	195.26	85.95	-52	4.5	0.09	0	F70S
2008	359	837	-0.84	100.13	-0.57	100.35	76.5	0.35	219.26	11.16	-31	7	0.23	0.01	F50S
2008	172	1823	1.32	98.89	1.47	99.04	90.5	0.21	225.13	72.69	-47	3.5	0.14	0	F70S
2008	200	247	-1.29	100.63	-1.33	100.94	94.6	0.31	276.96	184.78	72	6.5	0.1	0.01	BTPP
2008	241	2239	-1.22	101.64	-1.44	101.36	174.9	0.35	52.05	41.6	-14	7.25	0.42	0.01	PDRK
2008	241	2239	-1.22	101.64	-1.58	101.15	174.9	0.61	53.82	177.57	35	8	0.35	0.01	PKNN
2008	262	649	-1.14	101.48	-2.13	101.56	157.1	0.98	355.08	335.11	-68	11.5	29	0.01	DPBR
2008	262	649	-1.14	101.48	-1.44	101.36	157.1	0.32	21.73	91.55	-29	3.25	0.19	0.01	PDRK
2008	159	1124	1.42	98.92	1.47	99.04	101.9	0.13	247.08	74.38	-37	3.75	0.24	0.01	F70S
2008	292	1101	1.24	98.76	1.47	99.04	81.3	0.36	230.14	102.01	-18	10.5	0.06	0.01	F70S
2009	12	21	1.26	98.75	1.47	99.04	76	0.37	234.14	135.6	14	10	0.07	0.01	F70S
2008	248	1922	1.03	99.47	1.09	99.44	9.8	0.06	156.56	73.97	1	1	0.17	0	A20S
2008	339	714	1.07	99.44	1.09	99.44	12.8	0.02	169.6	64.75	-7	3.75	0.1	0.01	A20S
2008	137	2045	1.4	98.99	1.47	99.47	103.2	0.58	263.46	72.78	-56	6.75	0.1	0.01	N20S
2008	146	1216	1.24	98.97	1.47	99.47	102.5	0.54	245.73	40.27	-29	102.5	0.28	0.03	N20S
2008	226	1927	1.88	98.93	1.47	99.47	119.4	0.68	307.32	352.8	-30	6.75	0.22	0.02	N20S
2008	236	716	1.41	99.7	1.47	99.47	172.7	0.23	102.83	331.27	-63	14.75	0.14	0.08	N20S
2008	284	1550	1.63	98.92	1.47	99.47	109.4	0.57	286.82	74.68	-63	14.25	0.28	0.02	N20S
2009	51	1044	0.77	99.65	1.47	99.47	130.9	0.71	165.03	91.96	-43	9.75	0.13	0.01	N20S
2009	51	1140	1.49	98.89	1.47	99.47	97.3	0.58	272.03	336.02	-72	10	0.09	0.01	N20S

Table A4.5: Local SWS measurements from the Sumatran Fault region

YEAR	JULDAY	HHMM	LAT (°) (Source)	LON (°) (Source)	LAT (°) (Station)	LON (°) (Station)	Depth (km)	EPI Dist (°)	BAZ (°)	Spol (°)	Φ (°)	Φ error (°)	δt (s)	δt error (s)	STA
2008	146	2057	0.37	100.26	-0.09	100.65	166.7	0.59	319.29	166.86	55	10	0.17	0.08	S20S
2008	146	2057	0.37	100.26	0.34	100.82	166.7	0.56	272.3	130.3	-16	10	0.11	0.02	S40S
2008	159	617	0.61	100.26	0.8	100.47	190.2	0.29	228.23	16.03	-18	6.75	0.21	0.02	L30S
2008	183	1544	0.45	99.75	0.8	100.47	135.9	0.81	244.1	90.05	64	12.5	0.18	0.03	L30S
2008	226	1637	1.12	100.1	1.55	99.69	199.6	0.59	136.21	114.88	50	11.75	0.3	0.04	N40S
2008	226	1637	1.12	100.1	1.63	99.74	199.6	0.62	144.3	100.85	40	4.25	0.34	0.01	N50S
2008	223	1804	1.7	99.56	1.55	99.69	175.2	0.2	317.89	104.72	32	2.25	0.33	0.01	N40S
2008	236	716	1.41	99.7	1.55	99.69	172.7	0.14	178.96	117.09	61	10.75	0.19	0.02	N40S
2008	236	716	1.41	99.7	1.63	99.74	172.7	0.22	192.25	99.27	39	12.5	0.22	0.03	N50S
2008	296	1957	0.77	99.68	1.55	99.69	150.5	0.78	180.7	72.63	22	11	0.21	0.02	N40S
2008	296	1957	0.77	99.68	1.63	99.74	150.5	0.86	183.89	66.24	28	142.5	0.19	0.03	N50S
2008	313	2223	0.1	100.35	0.34	100.82	160.6	0.53	242.87	69.16	-84	11.25	0.19	0.03	S40R
2008	318	547	1.78	99.51	1.55	99.69	167.8	0.3	321.43	119.45	60	15.25	0.1	0.02	N40S
2009	4	1713	0.29	100.35	0.97	100.25	162.2	0.68	171.59	87.77	-54	9	0.3	0.02	L40S
2009	26	522	0.12	100.04	-0.1	100.52	126.8	0.53	294.78	117.11	-5	5.75	0.2	0.01	S10S
2009	26	522	0.12	100.04	0.34	100.82	126.8	0.81	254.4	7.01	-43	8.5	0.27	0.02	S40S
2009	27	2244	0.88	100.25	1.63	99.74	190.5	0.9	145.56	112.64	60	5.5	0.26	0.01	N50S
2009	35	817	0.28	100.32	0.8	100.47	155.4	0.55	196.38	52.34	-72	14.25	0.13	0.02	L30S
2009	35	817	0.28	100.32	-0.1	100.52	155.4	0.42	331.41	183.98	76	13.5	0.2	0.05	S10S
2009	27	2244	0.88	100.25	1.64	99.88	190.5	0.84	153.85	297.37	-79	8.75	0.22	0.05	N60B
2008	216	927	1.51	99.71	1.63	99.74	186.9	0.12	198.8	188.36	58	11.75	0.3	0.03	N50S
2008	234	2013	196	98.99	1.63	99.74	126.1	0.82	293.96	85.95	66	4	0.27	0.03	N50S
2008	332	1234	1.25	100.12	1.55	99.69	206.6	0.52	124.9	3.78	-69	3.5	0.21	0.02	N40S
2008	332	1234	1.25	100.12	1.63	99.74	206.6	0.53	134.53	21.32	-42	8.5	0.09	0.02	N50S

Table A4.6: Local SWS measurements from the backarc region

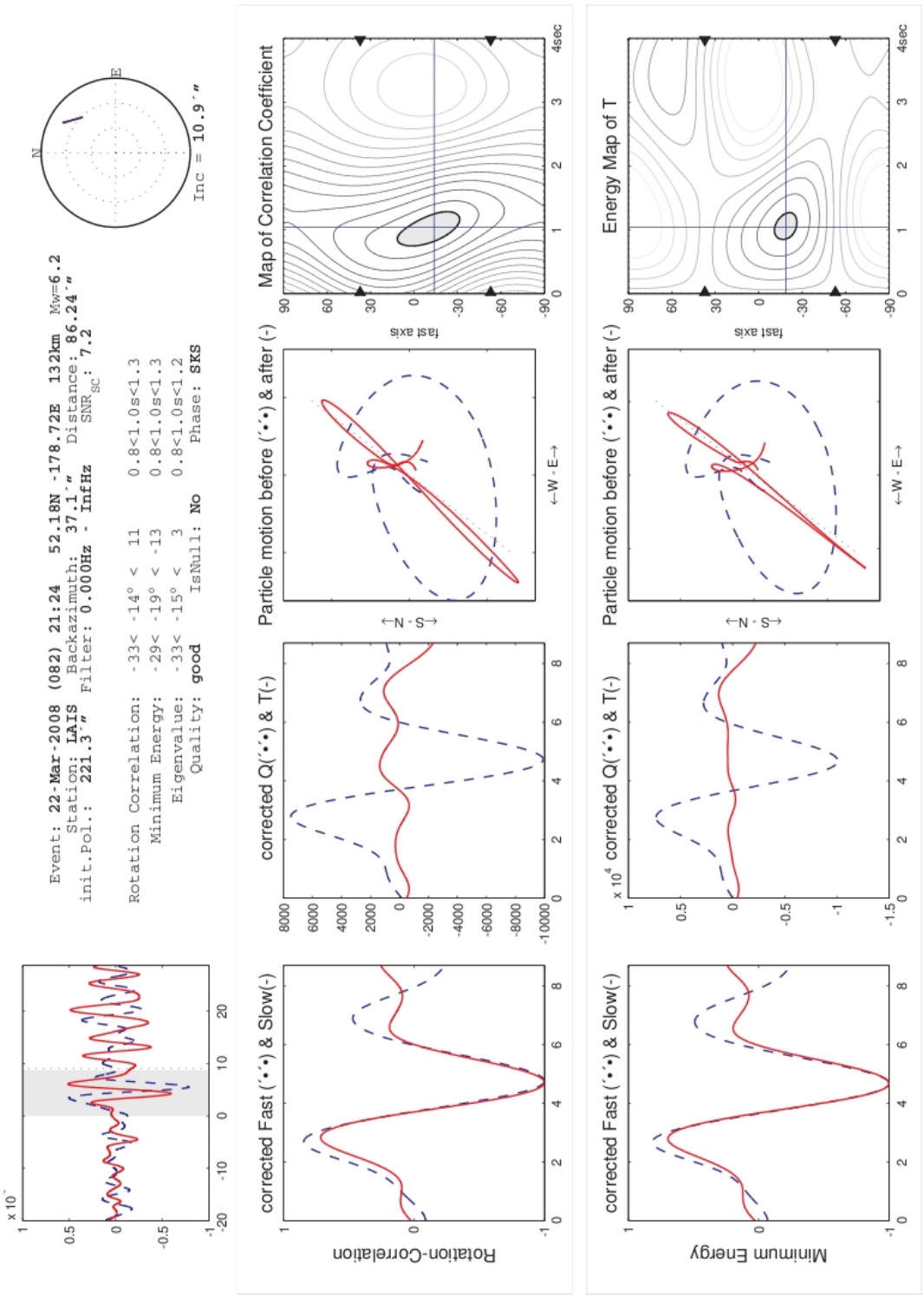

Figure A4.1: SKS SWS result for station LAIS. Example of SplitLab (Wüsterfeld et al., 2008) method of shear wave splitting. After correction, in which both components have been rotated by Φ and one lagged by δt, the energy has been minimized on the corrected transverse component and the particle motion is linear.

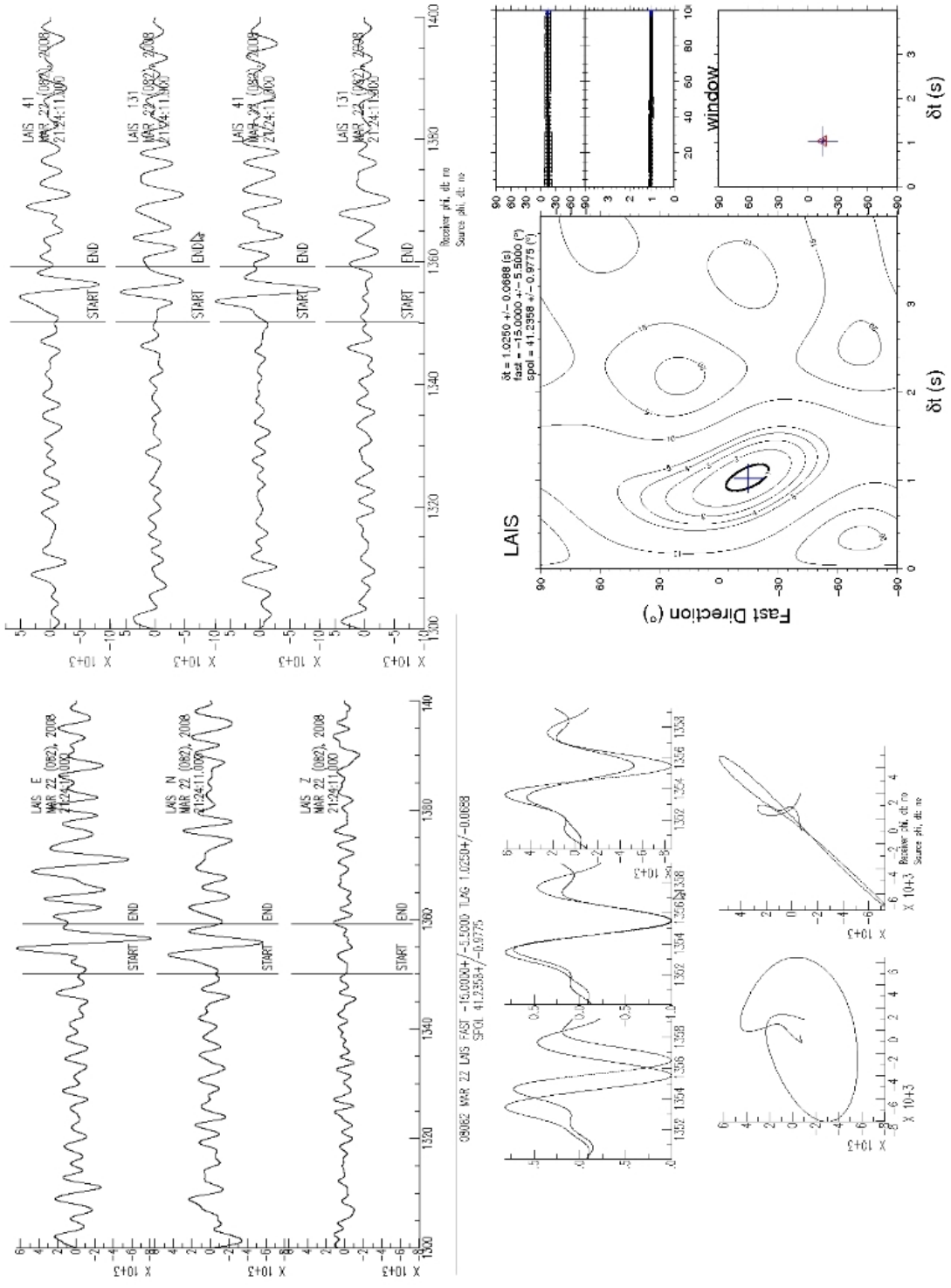

Figure A4.2: SKS SWS result for station LAIS. Example of the Teanby et al., (2004) (Sheba) method of shear wave splitting. After correction, in which both components have been rotated by Φ and one lagged by δt, the energy has been minimized on the corrected transverse component and the particle motion is linear.

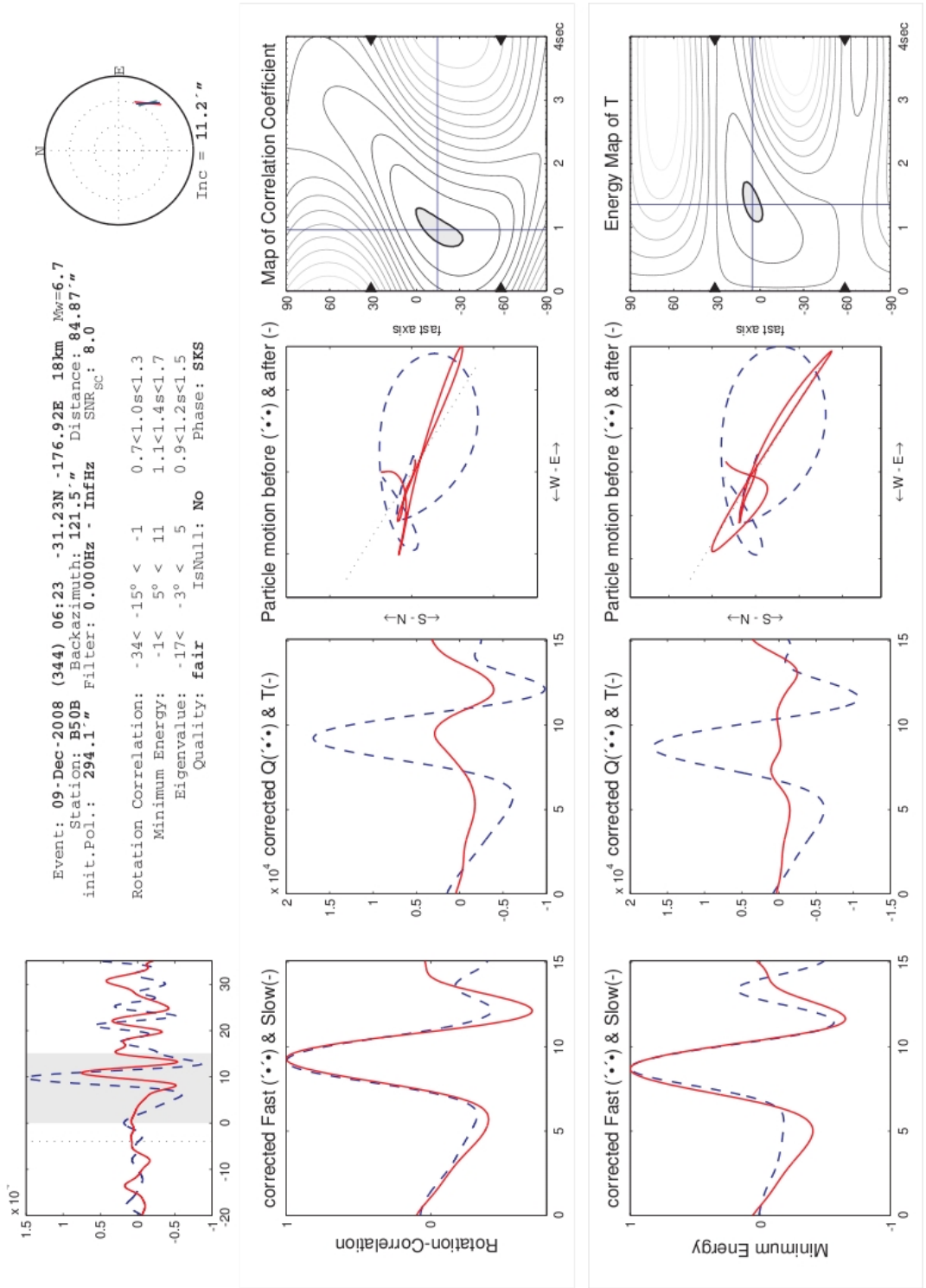

Figure A4.3: SKS SWS result for station B50B. Example of SplitLab (Wüsterfeld et al., 2008) method of shear wave splitting. After correction, in which both components have been rotated by Φ and one lagged by δt, the energy has been minimized on the corrected transverse component and the particle motion is linear.

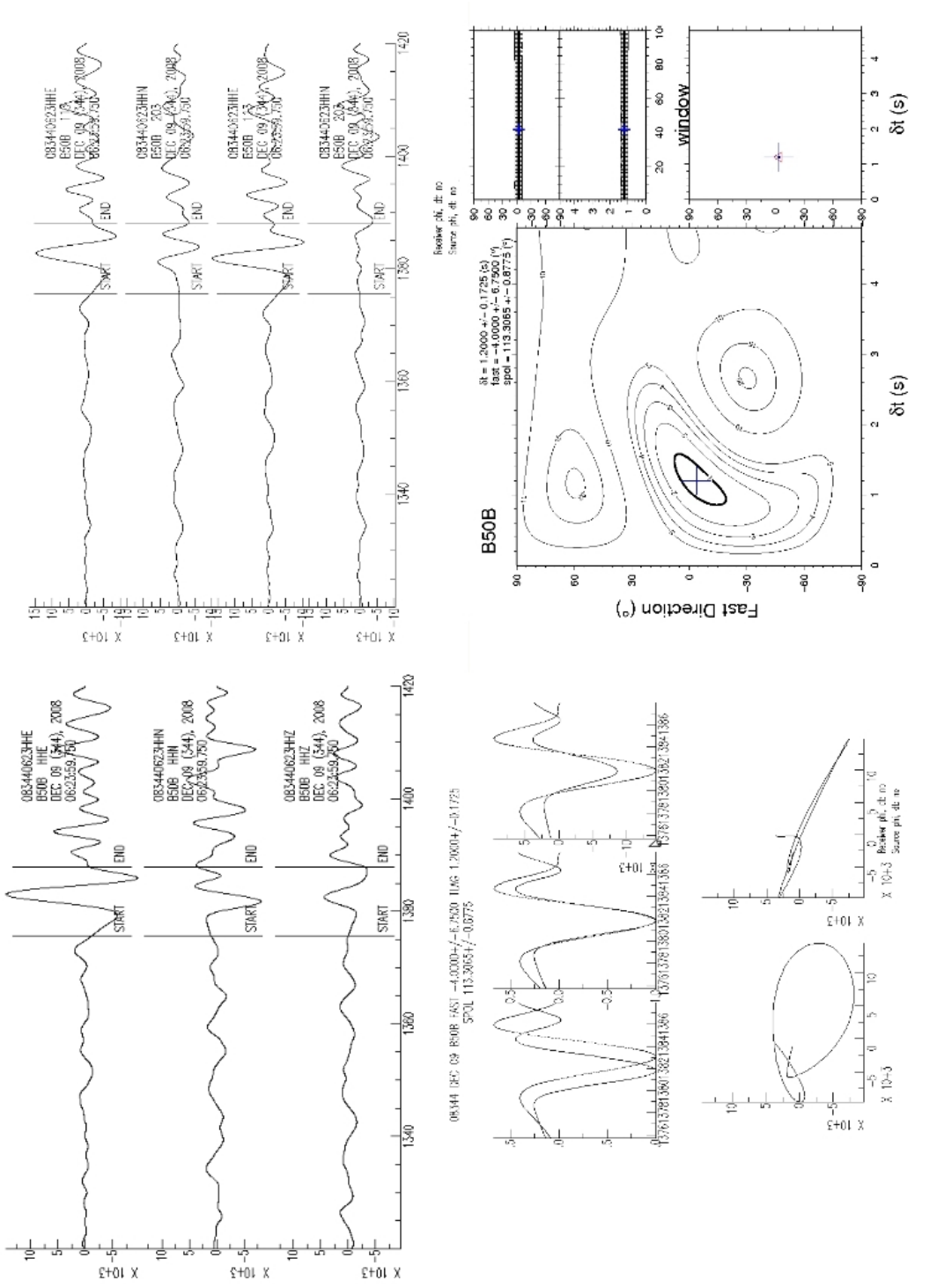

Figure A4.4: SKS SWS result for station B50B. Example of the Teanby et al., (2004) (Sheba) method of shear wave splitting. After correction, in which both components have been rotated by Φ and one lagged by δt, the energy has been minimized on the corrected transverse component and the particle motion is linear.

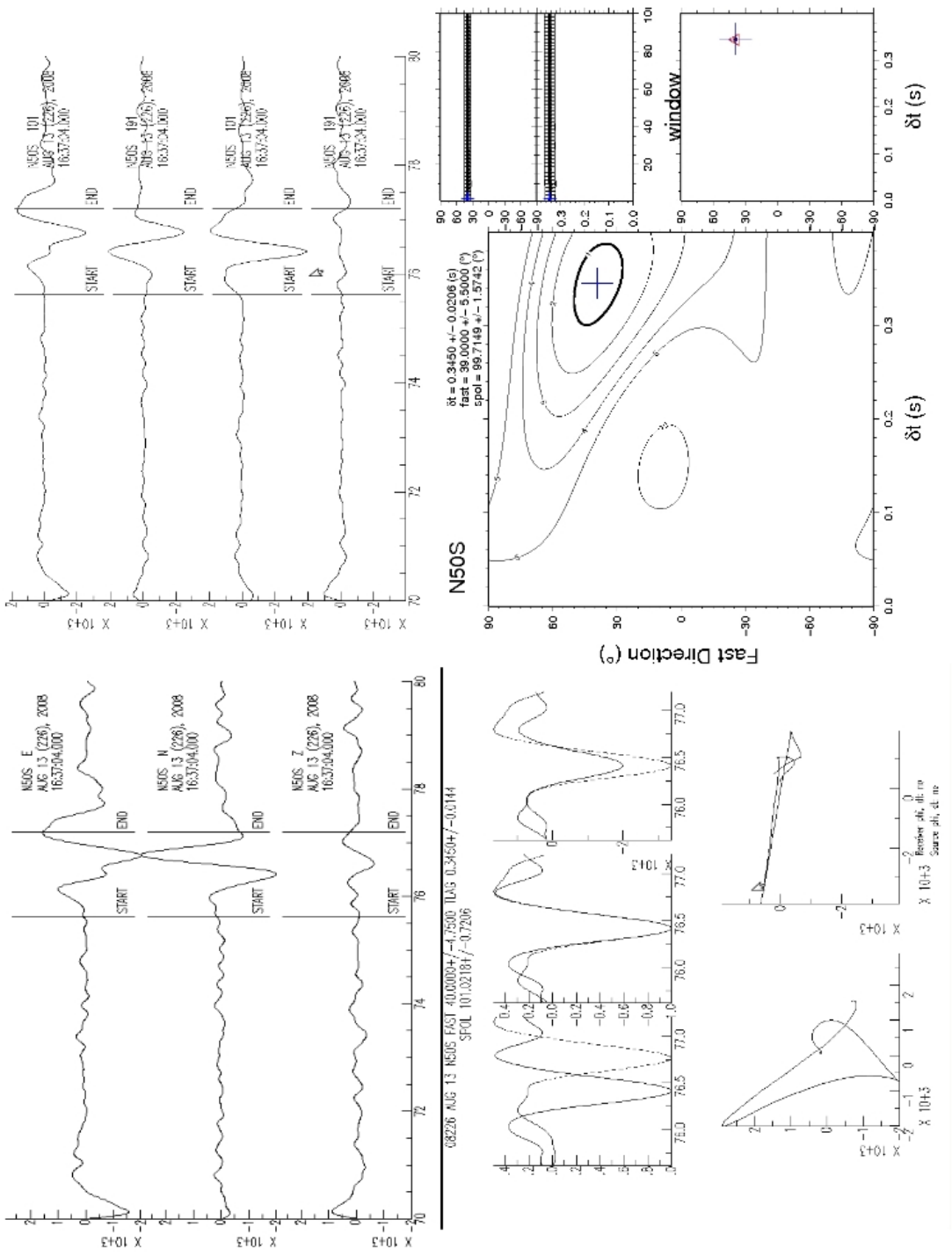

Figure A4.5: Local SWS result for station N50S using the Teanby et al., (2004) (Sheba) method of shear wave splitting. After correction, in which both components have been rotated by Φ and one lagged by δt, the energy has been minimized on the corrected transverse component and the particle motion is linear.

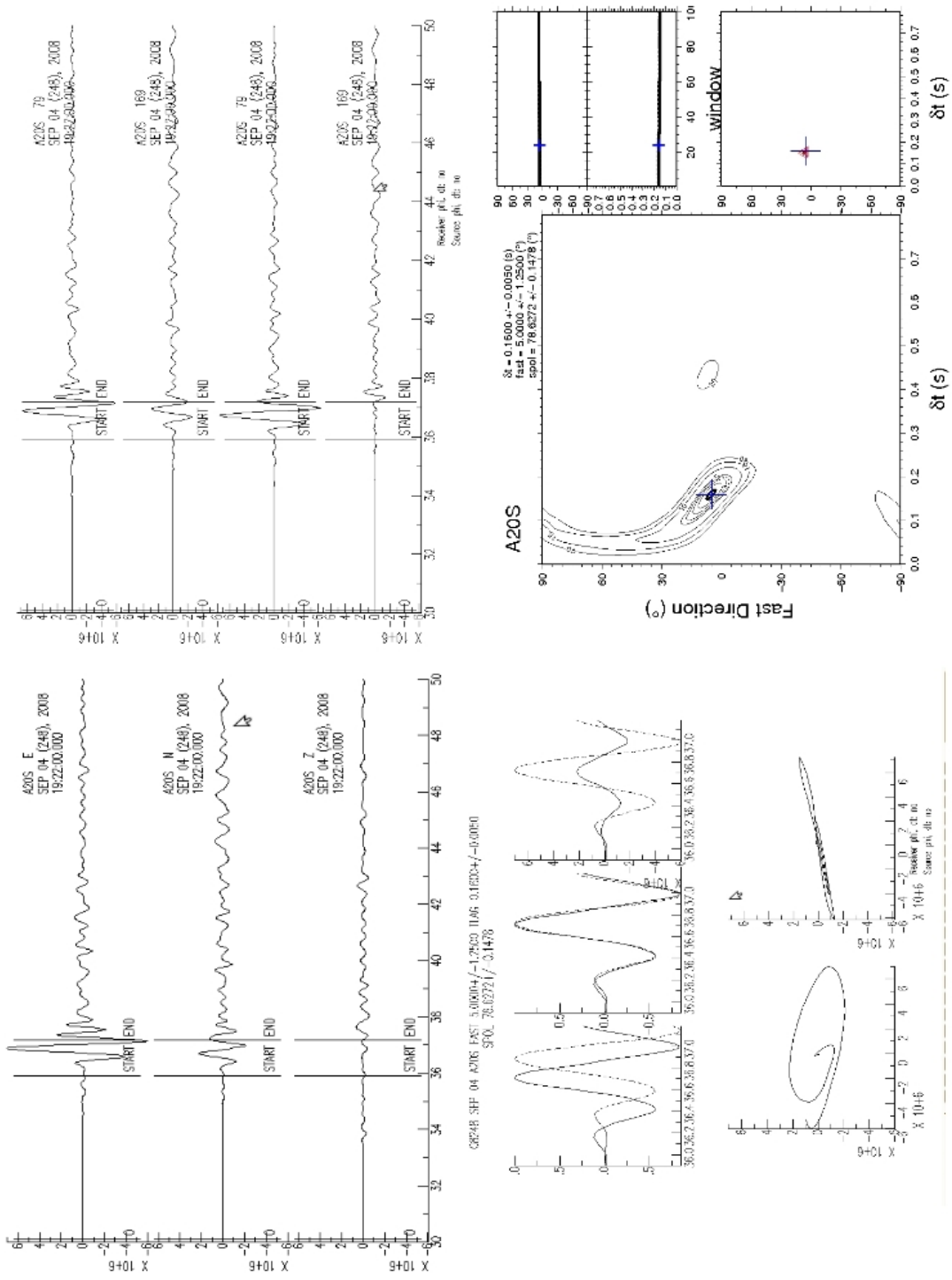

Figure A4.6: Local SWS result for station A20S using the Teanby et al., (2004) (Sheba) method of shear wave splitting. After correction, in which both components have been rotated by Φ and one lagged by δt, the energy has been minimized on the corrected transverse component and the particle motion is linear.

References

Abercrombie, R. E., M. Antolik, and G. Ekstrom (2003), The June 2000 M-w 7.9 earthquakes south of Sumatra: Deformation in the India-Australia Plate, Journal of Geophysical Research-Solid Earth, 108(B1), 2018-2033.

Abt, D. L., K. M. Fischer, L. Martin, G. A. Abers, J. M Protti, V. Gonzalez, and W. Strauch (2006), Shear-wave splitting in the central American subduction zone: implications for flow and melt in the mantle wedge, EOS. Tran. Am. Geophys. Un., 87(52), Fall Meet Suppl., Abstract T22C-05.

Abt, D. L., and K. M. Fischer (2008), Resolving three-dimensional anisotropic structure with shear wave splitting tomography, Geophysical Journal International, 173(3), 859-886.

Abt, D. L., K. M. Fischer, G. A. Abers, W. Strauch, J. M. Protti, and V. Gonzalez (2009), Shear wave anisotropy beneath Nicaragua and Costa Rica: Implications for flow in the mantle wedge, Geochemistry Geophysics Geosystems, 10(O05S15), doi:10.1029/2009GC002375.

Aki, K., and W. H. K. Lee (1976), Determination of 3 - dimensional velocity anomalies under a seismic array using 1st-*P* arrival times from local earthquakes. 1. A homogeneous initial model, Journal of Geophysical Research-Solid Earth, 81(23), 4381-4399.

Aki, K., A. Christofferson and E. S Husebye (1977), Determination of the three-dimensional seismic structure of the lithosphere, Journal of Geophysical Research-Solid Earth, 82, 277-296.

Alsina, D., and R. Snieder (1995), Small-scale sub-lithospheric continental mantle deformation: constraints from *SKS* splitting observations, Geophysics Journal International, 123, 431-448.

Ammon, C. J., C. Ji, H. K. Thio, D. Robinson, S. Ni, V. Hjorleifsdottir, H. Kanamori, T. Lay, S. Das, D. Helmberger, G. Ichinose, J. Polet, and D. Wald (2005), Rupture process of the 2004 Sumatra-Andaman earthquake, Science, 308(5725), 1133-1139.

Anderson, M. L., G. Zandt, E. Triep, M. Fouch, and S. Beck (2004), Anisotropy and mantle flow in the Chile-Argentina subduction zone from shear wave splitting analysis, Geophysical Research Letters, 31(23), L3608, doi:10.1029/2004GL020906.

Ando, M., Y. Ishikawa, and F. Yamazaki (1983), Shear Wave Polarization in the upper mantle beneath Honshu, Japan, Journal of Geophysical Research-Solid Earth, 88(7), 5850-5864.

Anglin, D. K., and M. J. Fouch (2005), Seismic Anisotropy in the Izu-Bonin subduction system, Geophysics Research Letters, 32, doi:10.1029/2005GL022714.

Audoine, E., M. K. Savage, and K. Gledhill (2000), Seismic anisotropy from local earthquakes in the transition region from a subduction to a strike-slip plate boundary, New Zealand, Journal of Geophysical Research-Solid Earth, 105(B4), 8013-8033.

Audoine, E., M. K. Savage, and K. Gledhill (2004), Anisotropic structure under a back-arc spreading region, the Taupo Volcanic Zone, New Zealand, Journal of Geophysical Research-Solid Earth, 109(B11), B11305, doi:10.1029/2003JB002932.

Babuška, V., and M. Cara (1991), Seismic anisotropy in the Earth, Springer, ISBN 978-0-7923-1321-2.

Backus, G. E. (1962), Long-wave elastic anisotropy produced by horizontal layering, Journal of Geophysical Research, 67(11), 4427-4440.

Balfour, N. J., M. K. Savage, and J. Townend (2005), Stress and crustal anisotropy in Marlborough, New Zealand: evidence for low fault strength and structure-controlled anisotropy, Geophysical Journal International, 163(3), 1073-1086.

Beaudry, D., (1983), Depositional history and structural evolution of a sedimentary basin in a modern forearc setting, western Sunda Arc, Indonesia, Ph. D thesis. 154 pp., Univ. of Calif., Scripps Inst. of Oceanogr., San Diego.

Bellier, O., and M. Sebrier (1994), Relationship between tectonism and volcanism along the great Sumatran Fault Zone deduced by spot image analyses, Tectonophysics, 233(3-4), 215-231.

Bellier, O., and M. Sebrier (1995), Is the slip rate variation on the great Sumatran Fault accommodated by fore-arc stretching, Geophysical Research Letters, 22(15), 1969-1972.

Bilek, S. L., and T. Lay (2002), Tsunami earthquakes possibly widespread manifestations of frictional conditional stability, Geophysical Research Letters, 29(14), 1673-1676, doi:10.1029/2002GL015215.

Bilek, S. L. (2010), The role of subduction erosion on seismicity, Geology, 38(5), 479-480.

Bilek, S. L., E. R. Engdahl, H. R. DeShon, and M. E Hariri (2011), The 25 October 2010 Sumatra tsunami earthquake: Slip in a slow patch, Geophysical Research Letters, 38, L14306, doi:10.1029/2011GL047864.

Blanpied, M. L., D. A. Lockner, and J. D. Byerlee (1991), Fault stability inferred from granite sliding experiments at hydrothermal conditions, Geophysical Research Letters, 18(4), 609-612.

Blanpied, M. L., D. A. Lockner, and J. D. Byerlee (1995), Frictional slip of granite at hydrothermal conditions, Journal of Geophysical Research-Solid Earth, 100(B7), 13045-13064.

Bock, G., R. Kind, A. Rudloff, and G. Asch (1998), Shear wave anisotropy in the upper mantle beneath the Nazca plate in northern Chile, Journal of Geophysical Research-Solid Earth, 103(B10), 24333-24345.

Booth, D. C., and S. Crampin (1985), Shear-wave polarizations on a curved wave-front at an isotropic free-surface, Geophysical Journal of the Royal Astronomical Society, 83(1), 31-45.

Bostock, M. G., and J. F. Cassidy (1995), Variation in *SKS* splitting across western Canada, Geophysical Research Letters, 22(1), 5-8.

Bowman, J. R., and M. Ando (1987), Shear-wave splitting in the upper mantle wedge above the Tonga subduction zone, Geophysical Journal of the Royal Astronomical Society, 88(1), 25-41.

Briggs, R. W., K. Sieh, A. J. Meltzner, D. Natawidjaja, J. Galetzka, B. Suwargadi, Y.-J. Hsu, M. Simons, N. Hananto, I. Suprihanto, D. Prayudi, J.-P. Avouac, L. Prawirodirdjo and Y. Bock(2006), Deformation and slip along the Sunda Megathrust in the great 2005 Nias-Simeulue earthquake, Science, 311(5769), 1897-1901.

Buttles, J., and P. Olson (1998), A laboratory model of subduction zone anisotropy, Earth and Planetary Science Letters, 164(1-2), 245-262.

Carlson, R. L., and D. J. Miller (2003), Mantle wedge water contents estimated from seismic velocities in partially serpentinized peridotites, Geophysical Research Letters, 30(5),1250-1253.

Cassidy, J. F., and M. G. Bostock (1996), Shear-wave splitting above the subducting Juan deFuca plate, Geophysical Research Letters, 23(9), 941-944.

Chauhan, A. P. S., S. C. Singh, N. D. Hananto, H. Carton, F. Klingelhoefer, J. X. Dessa, H. Permana, N. J. White, D. Graindorge, and O. B. S. S. T. Sumatra (2009), Seismic imaging of forearc backthrusts at northern Sumatra subduction zone, Geophysical Journal International, 179(3), 1772-1780.

Chevrot, S. (2000), Multichannel analysis of shear wave splitting, Journal of Geophysical Research-Solid Earth, 105(B9), 21579-21590.

Chlieh, M., J. P. Avouac, K. Sieh, D. H. Natawidjaja, and J. Galetzka (2008), Heterogeneous coupling of the Sumatran megathrust constrained by geodetic and paleogeodetic measurements, Journal of Geophysical Research-Solid Earth, 113(B5), B05305, doi:10.1029/2007JB0004981.

Christensen, N. I. (1984), The magnitude, symmetry and origin of upper mantle anisotropy based on fabric analyses of ultramafic tectonites, Geophysical Journal of the Royal Astronomical Society, 76(1), 89-111.

Clift, P. and P. Vannucchi (2004), Controls on tectonic accretion versus erosion in subduction zones: implications for the origin and recycling of the continental crust, Review of Geophysics., 42, RG2001 , doi:10.1029/2003RG000127.

Collings, R., D. Lange, F. Tilmann, A. Rietbrock, D. H. Natawidjaja, B. Suwargadi, M. Miller and J. Saul (2012), Structure and seismogenic properties of the Mentawai segment of the Sumatra subduction zone revealed by local earthquake travel time tomography., Journal of Geophysical Research,117, B01312, doi:10.1029/2011JB008469.

Crampin, S., and J. H. Lovell (1991), A decade of shear-wave splitting in the earths crust - what does it mean - what use can we make it - and what should we do next, Geophysical Journal International, 107(3), 387-407.

Crampin, S. (1994), The fracture criticality of crustal rocks, Geophysical Journal International, 118(2), 428-438.

Crampin, S., T. Volti, S. Chastin, A. Gudmundsson, and R. Stefansson (2002), Indication of high pore-fluid pressures in a seismically-active fault zone, Geophysical Journal International, 151(2), F1-F5, doi:10.1046/j.1365-246X.2002.01830.x.

Cross, T. A., and R. H. Pilger (1982), Controls of subduction geometry, location of magmatic arcs, and tectonics of arc and back-arc regions, Geological Society of America Bulletin, 93(6), 545-562.

Currie, C. A., R. D. Hyndman, K. Wang, and V. Kostoglodov (2002), Thermal models of the Mexico subduction zone: Implications for the megathrust seismogenic zone, Journal of Geophysical Research-Solid Earth, 107, 2370, doi:10.1029/2001JB000886.

Currie, C. A., J. F. Cassidy, R. D. Hyndman, and M. G. Bostock (2004), Shear wave anisotropy beneath the Cascadia subduction zone and western North American craton, Geophysical Journal International, 157(1), 341-353.

Dabrowski, M., M. Krotkiewski, and D. W. Schmid (2008), MILAMIN: MATLAB-based finite element method solver for large problems, Geochemistry Geophysics Geosystems, 9, Q04030, doi:10.1029/2007GC001719.

Deplus, C., M. Diament, H. Hébert, G. Bertrand, S. Dominguez, J. Dubois, J. Malod, P. Patriat, B. Pontoise, and J. J. Sibilla (1998), Direct evidence of active deformation in the eastern Indian oceanic plate, Geology, 26(2), 131-134.

DeShon, H. R., and S. Y. Schwartz (2004), Evidence for serpentinization of the forearc mantle wedge along the Nicoya Peninsula, Costa Rica, Geophysical Research Letters, 31, L21611, 4pp, doi:10.1029/2004GL021179.

DeShon, H. R., E. R. Engdahl, C. H. Thurber, and M. Brudzinski (2005), Constraining the boundary between the Sunda and Andaman subduction systems: Evidence from the 2002 M-w 7.3 Northern Sumatra earthquake and aftershock relocations of the 2004 and 2005 great earthquakes, Geophysical Research Letters, 32, L24307, 5pp, doi:10.1029/2005GL024188.

DeShon, H. R., S. Y. Schwartz, A. V. Newman, V. Gonzalez, M. Protti, L. R. M. Dorman, T. H. Dixon, D. E. Sampson, and E. R. Flueh (2006), Seismogenic zone structure beneath the Nicoya Peninsula, Costa Rica, from three-dimensional local earthquake *P*- and *S*-wave tomography, Geophysical Journal International, 164(1), 109-124.

Dessa, J. X., F. Klingelhoefer, D. Graindorge, C. Andre, H. Permana, M. A. Gutscher, A. Chauhan, S. C. Singh, and S.-O. S. Team (2009), Megathrust earthquakes can nucleate in the forearc mantle: Evidence from the 2004 Sumatra event, Geology, 37(7), 659-662.

Diament, M., H. Harjono, K. Karta, C. Deplus, M. Gerard, O. Lassal, A. Martin, and J. Malod (1992), Mentawai Fault zone off Sumatra - A new key to the geodynamics of western Indonesia, Geology, 20(3), 259-262.

Eberhart-Phillips, D. (1986), Three-dimensional velocity structure in northern California Coast Ranges from inversion of local earthquake arrival times, Bulletin of the Seismological Society of America, 76(4), 1025-1052.

Eberhart-Phillips, D. (1993), Local earthquake tomography: earthquake source regions in seismic tomography: Theory and practice edited by H. M. Iyer and K. Hirahara, pp 613-643, Cahpman and Hall, London.

Eberhart-Phillips, D and A. J. Michael (1998), Seismotectonics of the Loma Prieta, California, region determined from three-dimensional *Vp*, *Vp/Vs* and seismicity, Journal of Geophysical Research-Solid Earth, 103, 21,099-21,120.

Eberhart-Phillips, D., M. Reyners, M. Chadwick, and J. M. Chiu (2005), Crustal heterogeneity and subduction processes: 3-D *Vp*, *Vp/Vs* and Q in the southern North Island, New Zealand, Geophysical Journal International, 162(1), 270-288.

Engdahl, E. R., R. van der Hilst, and R. Buland (1998), Global teleseismic earthquake relocation with improved travel times and procedures for depth determination, Bulletin of the Seismological Society of America, 88(3), 722-743.

Engdahl, E. R., A. Villasenor, H. R. DeShon, and C. H. Thurber (2007), Teleseismic relocation and assessment of seismicity (1918-2005) in the region of the 2004 M(w) 9.0 Sumatra-Andaman and 2005 M(w) 8.6 Nias Island great earthquakes, Bulletin of the Seismological Society of America, 97(1), S43-S61.

Evans, R. (1984), Effects of the free-surface on shear wavetrains, Geophysical Journal of the Royal Astronomical Society, 76(1), 165-172.

Evans, J, D. Eberhart-Phillips, and C. H. Thurber (1994), User's manual for SIMULPS12 for imaging *Vp* and *Vp/Vs*: a derivative of the "thurber" tomographic inversion SIMUL3 for local earthquakes and explosions, USGS - Open-file report, 94-431, 101.

Faccenda, M., L. Burlini, T. V. Gerya, and D. Mainprice (2008), Fault-induced seismic anisotropy by hydration in subducting oceanic plates, Nature, 455, 1097-1100.

Fischer, K. M., and D. A. Wiens (1996), The depth distribution of mantle anisotropy beneath the Tonga subduction zone, Earth and Planetary Science Letters, 142(1-2), 253-260, doi: 10.1016/0012-821X(86)00084-2.

Fischer, K. M., M. J. Fouch, D. A. Wiens, and M. S. Boettcher (1998), Anisotropy and flow in Pacific subduction zone back-arcs, Pure and Applied Geophysics, 151(2-4), 463-475.

Fischer, K. M., E. M. Parmentier, A. R. Stine, and E. R. Wolf (2000), Modeling anisotropy and plate-driven flow in the Tonga subduction zone back arc, Journal of Geophysical Research-Solid Earth, 105(B7), 16181-16191.

Fouch, M. J., and K. M. Fischer (1998), Shear wave anisotropy in the Mariana subduction zone, Geophysical Research Letters, 25(8), 1221-1224.

Franke, D., M. Schnabel, S. Ladage, D. R. Tappin, S. Neben, Y. S. Djajadihardja, C. Mueller, H. Kopp, and C. Gaedicke (2008), The great Sumatra-Andaman earthquakes - Imaging the boundary between the ruptures of the great 2004 and 2005 earthquakes, Earth and Planetary Science Letters, 269(1-2), 118-130.

Fukao, Y. (1984), Evidence from core-reflected shear-waves for anisotropy in the Earth's mantle, Nature, 309(5970), 695-698.

Gahalaut, V. K., and J. K. Catherine (2006), Rupture characteristics of 28 March 2005 Sumatra earthquake from GPS measurements and its implication for tsunami generation, Earth and Planetary Science Letters, 249(1-2), 39-46.

Genrich, J. F., Y. Bock, R. McCaffrey, L. Prawirodirdjo, C. W. Stevens, S. S. O. Puntodewo, C. Subarya, and S. Wdowinski (2000), Distribution of slip at the northern Sumatran fault system, Journal of Geophysical Research-Solid Earth, 105(B12), 28327-28341.

Gledhill, K. R and G. Stuart (1996), Seismic anisotropy in the fore-arc region of the Hikurangi subduction zone, New Zealand, Physics of the Earth and Planetary Interiors, 95, 211-225.

Graeber, F. M., and G. Asch (1999), Three-dimensional models of *P* wave velocity and *P*-to-*S* velocity ratio in the southern central Andes by simultaneous inversion of local earthquake data, Journal of Geophysical Research-Solid Earth, 104(B9), 20237-20256.

Graindorge, D., F. Klingelhoefer, J.-C. Sibuet , L. McNeill, T. J. Henstock, S. Dean, M.-A. Gutscher, J. X. Dessa, H. Permana, S. C. Singh, H. Leau, N. White, H. Carton, J. A. Malod, C. Rangin, K. G. Aryawan, A. K. Chaubey, A. Chauhan, D. R. Galih, C. J. Greenroyd, A. Laesanpura, J. Prihantono, G. Royle, and U. Shankar (2008), Impact of lower plate structure on upper plate deformation at the NW Sumatran convergent margin from seafloor morphology. Earth and Planetary Science Letters, 275 (3-4), 201-210.

Greve, S. M., M. K. Savage, and S. D. Hofmann (2008), Strong variations in seismic anisotropy across the Hikurangi subduction zone, North Island, New Zealand, Tectonophysics, 462(1-4), 7-21.

Grevemeyer, I., and V. M. Tiwari (2006), Overriding plate controls spatial distribution of megathrust earthquakes in the Sunda-Andaman subduction zone, Earth and Planetary Science Letters, 251, 199-208.

Growdon, M. A., G. L. Pavlis, F. Niu, F. L. Vernon, and H. Rendon (2009), Constraints on mantle flow at the Caribbean-South American plate boundary inferred from shear wave splitting, Journal of Geophysical Research-Solid Earth, 114, B02303, doi:10.1029/2008JB005887.

Gulick, S. P. S., J. A. Austin, Jr., L. C. McNeill, N. L. B. Bangs, K. M. Martin, T. J. Henstock, J. M. Bull, S. Dean, Y. S. Djajadihardja, and H. Permana (2011), Updip rupture of the 2004 Sumatra earthquake extended by thick indurated sediments, Nature Geoscience, 4(7), 453-456.

Gunawan, A., F. Tilmann, D. Lange, R. Collings, A. Rietbrock, D. Natawidjaja, S. Widiyantoro (2011), Moho depth estimation beneath Sumatra and Mentawai Islands using receiver function recorded with a temporary array, Geophysical Research Abstracts, 13, EGU2011-8072.

Haberland, C., A. Rietbrock, D. Lange, K. Bataille, and T. Dahm (2009), Structure of the seismogenic zone of the south-central Chilean margin revealed by local earthquake traveltime tomography, Journal of Geophysical Research-Solid Earth, 114, B01317, doi:10.1029/2008JB005802.

Hall, C. E., K. M. Fischer, E. M. Parmentier, and D. K. Blackman (2000), The influence of plate motions on three-dimensional back arc mantle flow and shear wave splitting, Journal of Geophysical Research-Solid Earth, 105(B12), 28009-28033.

Hamilton, W., (1977), Subduction in the Indonesian region. In Talwani, M., and Pitman, W. C, III (Eds.), Island arcs, deep sea trenches, and back-arc basins, Am. Geophys. Union, Washington, 15-32.

Hammond, J. O. S., J. Wookey, S. Kaneshima, H. Inoue, T. Yamashina, and P. Harjadi (2010), Systematic variation in anisotropy beneath the mantle wedge in the Java-Sumatra subduction system from shear-wave splitting, Physics of the Earth and Planetary Interiors, 178(3-4), 189-201, doi:10.1016/j.pepi.2009.10.003.

Harmon, N., D. W. Forsyth, K. M. Fischer, and S. C. Webb (2004), Variations in shear-wave splitting in young Pacific seafloor, Geophysical Research Letters, 31(15), L15609, doi:10.1029/2004GL020495.

Haslinger, F., E. Kissling, J. Ansorge, D. Hatzfeld, E. Papadimitriou, V. Karakostas, K. Makropoulos, H. G. Kahle, and Y. Peter (1999), 3D crustal structure from local earthquake tomography around the Gulf of Arta (Ionian region, NW Greece), Tectonophysics, 304(3), 201-218.

Hayes, G. P., and D. J. Wald (2009), Developing framework to constrain the geometry of the seismic rupture plane of the subduction interface a prior - a probabilistic approach, Geophysical Journal International, 176, 951-964.

Healy, D., S. M. Reddy, N. E. Timms, E. M. Gray, and A. V. Brovarone (2009), Trench-parallel fast axes of seismic anisotropy due to fluid-filled cracks in subducting slabs, Earth and Planetary Science Letters, 283(1-4), 75-86.

Hekinian, R. (1974), Petrology of igneous rocks from leg 22 in the northeastern Indian Ocean, Deep Sea Drilling Projects and Reports, 22, doi:10.2973/dsdp.proc.22.117.1974.

Henstock, T. J, L. C. McNeil, and D. R. Tappin (2006), Seafloor morphology of the Sumatran subduction zone: Surface rupture during megathrust earthquakes? Geology, 34(6), 458-488.

Hino, R., S. Ito, H. Shiobara, H. Shimamura, T. Sato, T. Kanazawa, J. Kasahara, and A. Hasegawa (2000), Aftershock distribution of the 1994 Sanriku-oki earthquake (M_w7.7) revealed by ocean bottom seismographic observation, Journal of Geophysical. Research-Solid Earth., 105, B9, 21697-21710, doi:10.1029/2000JB900174.

Hippchen, S., and R. D. Hyndman (2008), Thermal and structural models of the Sumatra subduction zone: Implications for the megathrust seismogenic zone, Journal of Geophysical Research-Solid Earth, 113(B12), B12103, doi:10.1029/2008JB005698.

Hoernle, K., D. L. Abt, K. M. Fischerm, H. Nichols, F. Hauff, G. A. Abers, P. van den Bogaardm, K. Heydolph, G. Alvarado, M. Protti, and W. Strauch (2008), Geochemical and geophysical evidence for arc-parallel flow in the mantle wedge beneath Costa Rica and Nicaragua, Nature, 451(7182), 1094-1098.

Honda, S., and T. Yoshida (2005), Effects of oblique subduction on the 3-D pattern of small-scale convection within the mantle wedge, Geophysical Research Letters, 32(13).

Hsu, Y. J., M. Simons, J. P. Avouac, J. Galetzka, K. Sieh, M. Chlieh, D. Natawidjaja, L. Prawirodirdjo, and Y. Bock (2006), Frictional afterslip following the 2005 Nias-Simeulue earthquake, Sumatra, Science, 312, 1921-1926.

Huang, Z., D. Zhao, and L. Wang (2011), Shear wave anisotropy in the crust, mantle wedge, and subducting Pacific slab under northeast Japan, Geochemistry Geophysics Geosystems, 12, Q01002, pp17, doi:10.1029/2010GC003343.

Husen, S., E. Kissling, E. R. Flueh, and G. Asch (1999), Accurate hypocentre determination in the seismogenic zone of the subducting Nazca plate in north Chile using a combined on-/offshore network, Journal of Geophysical International, 138, 687-701.

Husen, S., E. Kissling, and E. R. Flueh (2000), Local earthquake tomography of shallow subduction in north Chile: A combined onshore and offshore study, Journal of Geophysical Research-Solid Earth, 105(B12), 28183-28198.

Hyndman, R. D., and K. Wang (1995), The rupture zone of Cascadia great earthquakes from current deformation and the thermal regime, Journal of Geophysical. Research-Solid Earth., 100, B11, 22133-22154, doi:10.1029/95JB01970.

Hyndman, R. D., M. Yamano, and D. A. Oleskevich (1997), The seismogenic zone of subduction thrust faults, Island Arc, 6(3), 244-260.

Hyndman, R. D., and S. M. Peacock (2003), Serpentinization of the forearc mantle, Earth and Planetary Science Letters, 212(3-4), 417-432.

Iidaka, T., and K. Obara (1995), Shear-wave polarization anisotropy in the mantle wedge above the subducting Pacific Plate, Tectonophysics, 249(1-2), 53-68.

Iidaka, T., and F. L. Niu (1998), Evidence for an anisotropic lower mantle beneath eastern Asia: Comparison of shear-wave splitting data of *SKS* and *P660s*, Geophysical Research Letters, 25(5), 675-678.

Jung, H., and S. Karato (2001), Water-induced fabric transitions in olivine, Science, 293(5534), 1460-1463.

Jung, H., I. Katayama, Z. Jiang, T. Hiraga, and S. Karato (2006), Effect of water and stress on the lattice-preferred orientation of olivine, Tectonophysics, 421(1-2), 1-22.

Jung, H., W. Mo, and H. W. Green (2009), Upper mantle seismic anisotropy resulting from pressure-induced slip transition in olivine, Nature Geoscience, 2(1), 73-77.

Kaminski, E., N. M. Ribe, and J. T. Browaeys (2004), D-Rex, a program for calculation of seismic anisotropy due to crystal lattice preferred orientation in the convective upper mantle, Geophysical Journal International, 158(2), 744-752.

Kanamori, H. (1972), Mechanism of tsunami earthquakes, Physics of the Earth and Planetary Interiors, 6, 346-359.

Kanamori, H., L. Rivera, and W. H. K. Lee (2010), Historical seismograms for unraveling a mysterious earthquake: The 1907 Sumatra Earthquake, Geophysical Journal International, 183(1), 358-374.

Kaneshima, S. (1990), Origin of crustal anisotropy - shear-wave splitting studies in Japan, Journal of Geophysical Research-Solid Earth, 95(B7), 11121-11133.

Karato, S., and P. Wu (1993), Rheology of the upper mantle - a synthesis, Science, 260(5109), 771-778.

Karig, D. E., S. Suparka, G. F. Moore, P. E. Hehanussa (1978), Structure and Cenozoic evolution of the Sundra Arc in the central Sumatran Region, AAPG Memoirs, 29, 223-237.

Karig, D. E., S. Suparka, G. F Moore, and P. E Hehanussa (1979), Cenozoic evolution if the Sunda Arc in the central Sumatra region, in J. Watkins and L. Montadert eds., Geological and Geophysical Investigations of Continental Slopes and Rises, Am. Asssoc, Petroleum Geologists Mem. 29, 223-237.

Karig, D. E., M. B. Lawrence, G. F. Moore, and J. R. Curray (1980), Structural framework of the fore-arc basin, NW Sumatra, Journal of Geology Society London, 137, 1-15.

Katayama, I., H. Jung, and S. I. Karato (2004), New type of olivine fabric from deformation experiments at modest water content and low stress, Geology, 32(12), 1045-1048.

Katayama, I., and S. I. Karato (2006), Effect of temperature on the B- to C-type olivine fabric transition and implication for flow pattern in subduction zones, Physics of the Earth and Planetary Interiors, 157(1-2), 33-45.

Kawakatsu, H. (1986), Downdip tensional earthquakes beneath the Tonga Arc - A double seismic zone, Journal of Geophysical Research-Solid Earth and Planets, 91(B6), 6432-6440.

Kendall, J. M. (1994), Teleseismic arrivals at midocean ridge - effects of mantle melt and anisotropy, Geophysical Research Letters, 21(4), 301-304.

Kendall, J. M. (2000), Seismic anisotropy in the boundary layers of the Earth's mantle, invited chapter for Earth's Deep Interior: Mineral Physics and Tomography from the Atomic to the Global Scale, eds. S. Karato, L. Stixruse, R.C. Liebermann, T. G. Masters and A. M. Forte, Geophysical Monograph Series 117, AGU, 149-175.

Kieckhefer, R. M., G. G. Shor, J. R. Curray, W. Sugiarta, and F. Hehuwat (1980), Seismic refraction studies of the Sunda Trench and fore-arc basin, Journal of Geophysical Research, 85(NB2), 863-889.

Kissling, E. (1988), Geotomography with local earthquake data, Reviews of Geophysics, 26(4), 659-698.

Kissling, E., W. L. Ellsworth, D. Eberhart-Phillips, and U. Kradolfer (1994), Initial reference models in local earthquake tomography, Journal of Geophysical Research-Solid Earth, 99(B10), 19635-19646.

Kissling, E., S. Solarino, and M. Cattaneo (1995), Improved seismic velocity reference model from local earthquake data in northwestern Italy, Terra Nova, 7(5), 528-534.

Klingelhoefer, F., M. A. Gutscher, S. Ladage, J. X. Dessa, D. Graindorge, D. Franke, C. Andre, H. Permana, T. Yudistira, and A. Chauhan (2010), Limits of the seismogenic zone in the epicentral region of the 26 December 2004 great Sumatra-Andaman earthquake: Results from seismic refraction and wide-angle reflection surveys and thermal modeling, Journal of Geophysical Research-Solid Earth, 115, B01304, pp23, doi10.1029/2009JB006569.

Klosko, E. R., F. T. Wu, H. J. Anderson, D. Eberhart-Phillips, T. V. McEvilly, E. Audoine, M. K. Savage and K. R. Gledhill (1999), Upper mantle anisotropy in the New Zealand Region, Geophysical Research Letters, 26(10), 1497-1500

Kneller, E. A., P. E. van Keken, S. Karato, and J. Park (2005), B-type olivine fabric in the mantle wedge: Insights from high-resolution non-Newtonian subduction zone models, Earth and Planetary Science Letters, 237(3-4), 781-797.

Kneller, E. A., and P. E. van Keken (2008), Effect of three-dimensional slab geometry on deformation in the mantle wedge: Implications for shear wave anisotropy, Geochemistry Geophysics Geosystems, 9, Q01003, 21pp, doi:10.1029/2007GC001677.

Kneller, E. A., M. D. Long, and P. E. van Keken (2008b), Olivine fabric transitions and shear wave anisotropy in the Ryukyu subduction system, Earth and Planetary Science Letters, 268, 268-282.

Konca, A. O., V. Hjorleifsdottir, T. R A. Dong, J. P. Avouac, D. V. Helmberger, C. Ji, K. Sieh, R. Briggs and A. Meltzner (2007), Rupture kinematics of the 2005 Mw 8.6 Nias-Simeulue earthquake from the joint inversion of seismic and geodetic data, Bulletin of the Seismological Society of America, 97, 307-322.

Konca, A. O., J.-P. Avouac, A. Sladen, A. J. Meltzner, K. Sieh, P. Fang, Z. Li, J. Galetzka, J. Genrich, M. Chlieh, D. H. Natawidjaja, Y. Bock, E. J. Fielding, C. Ji and D. V. Helmberger (2008), Partial rupture of a locked patch of the Sumatra megathrust during the 2007 earthquake sequence, Nature, 456(7222), 631-635.

Kopp, H., E. R. Flueh, D. Klaeschen, J. Bialas, and C. Reichert (2001), Crustal structure of the central Sunda margin at the onset of oblique subduction, Geophysical Journal International, 147(2), 449-474.

Kopp, H., W. Weinrebe, S. Ladage, U. Barckhausen, D. Klaeschen, E. R. Flueh, C. Gaedicke, Y. Djajadihardja, I. Grevemeyer, A. Krabbenhoeft, C. Papenberg, M. Zillmer (2008), Lower slope morphology of the Sumatra trench system, Basin research., 20(4), 519–529, doi:10.1111/j.1365-2117.2008.00381.x.

Krabbenhoeft, A., R. W. Weinrebe, H. Kopp, E. R. Flueh, S. Ladage, C. Papenberg, L. Planert, and Y. Djajadihardja (2010), Bathymetry of the Indonesian Sunda margin-relating morphological features of the upper plate slopes to the location and extent of the seismogenic zone, Natural Hazards and Earth System Sciences, 10(9), 1899-1911.

Krumbein, W. C. (1939), Preferred orientation of pebbles in sedimentary deposits, Journal of Geology, 47(7), 673-706.

Kubo, A., and Y. Hiramatsu (1998), On presence of seismic anisotropy in the asthenosphere beneath continents and its dependence on plate velocity: Significance of reference frame selection, Pure and Applied Geophysics, 151(2-4), 281-303.

Kumar, R. T. R., T. K. Maji, and R. R. Nair (2010), Assessment of flexural analysis applied to the Sumatra-Java subduction zone, Journal of Earth System Science, 119(5), 717-730.

Kumazawa, M., and O. L. Anderson (1969), Elastic moduli, pressure derivatives, and temperature derivatives of single-crystal olivine and single-crystal forsterite, Journal of Geophysical Research-Solid Earth, 74(25), 5691-5972.

Lallemand, S., A. Heuret, C. Faccenna, and F. Funiciello (2008), Subduction dynamics as revealed by trench migration, Tectonics, 27, TC3014, doi:10.1029/2007TC002212.

Lange, D., F. Tilmann, A. Rietbrock, R. Collings, D. H. Natawidjaja, B. W. Suwargadi, P. Barton, T. Henstock, and T. Ryberg (2010), The fine structure of the subducted Investigator Fracture Zone in western Sumatra as seen by local seismicity, Earth and Planetary Science Letters, 298(1-2), 47-56, doi:10.1016/j.espl.2010.07.020.

Langer, H., R. Raffaele, A. Scaltrito, and L. Scarfi (2007), Estimation of an optimum velocity model in the Calabro-Peloritan mountains-assessment of the variance of model parameters and variability of earthquake locations, Geophysical Journal International, 170(3), 1151-1164.

Lasitha, S., M. Radhakrishna, and T. D. Sanu (2006), Seismically active deformation in the Sumatra-Java trench-arc region: geodynamic implications, Current Science, 90(5), 690-696.

Lassak, T. M., M. J. Fouch, C. E. Hall, and E. Kaminski (2006), Seismic characterization of mantle flow in subduction systems: Can we resolve a hydrated mantle wedge?, Earth and Planetary Science Letters, 243(3-4), 632-649.

Lay, T., and H. Kanamori (1981), An asperity model of large earthquake sequences, Maurice Ewing Ser. 4, 579-592.

Lay, T., L. Astiz, H. Kanamori, and D. H. Christensen (1989), Temporal variations of large interplate earthquakes in coupled subduction zones, Physics of the Earth and Planetary Interiors, 54(3-4), 258-312.

Lay, T., and T. C. Wallace (1995), Modern global seismology, Academic Press, Orlando.

Lay, T., H. Kanamori, C. J. Ammon, M. Nettles, S. N. Ward, R. C. Aster, S. L. Beck, M. R. Brudzinski, R. Butler, H. R. DeShon, G. Ekstrom, K. Satake, and S. Sipkin (2005), The great Sumatra-Andaman earthquake of 26 December 2004, Science, 308(5725), 1127-1135.

Lay, T., C. J. Ammon, H. Kanamori, Y. Yamazaki, K. F. Cheung, and A. R. Hutko (2011), The 25 October 2010 Mentawai tsunami earthquake (M(w) 7.8) and the tsunami hazard presented by shallow megathrust ruptures, Geophysical Research Letters, 38, L06301, 5pp, doi:10.1029/2010GL046552.

Le Meur, E., J. Virieux, and P. Podvin (1997), Seismic tomography of the Gulf of Corinth: a comparison of methods, Ann. Geofis., 40, 1-24.

Levin, V., D. Droznin, J. Park, and E. Gordeev (2004), Detailed mapping of seismic anisotropy with local shear waves in southeastern Kamchatka, Geophysical Journal International, 158(3), 1009-1023.

Liu, Y., H. Zhang, C. Thurber, and S. Roecker (2008), Shear wave anisotropy in the crust around the San Andreas Fault near Parkfield: spatial and temporal analysis, Geophysical Journal International, 172(3), 957-970.

Llenos, A. L., and J. J. McGuire (2007), Influence of fore-arc structure on the extent of great subduction zone earthquakes, Journal of Geophysical Research-Solid Earth, 112, B09301, 31pp, doi:10.1029/2007JB004944.

Long, M. D., and R. D. van der Hilst (2005), Estimating shear-wave splitting parameters from broadband recordings in Japan: A comparison of three methods, Bulletin of the Seismological Society of America, 95(4), 1346-1358.

Long, M. D., and R. D. van der Hilst (2005b), Upper mantle anisotropy beneath Japan from shear wave splitting, Physics of the Earth and Planetary Interiors, 151(3-4), 206-222.

Long, M. D., and R. D. van der Hilst (2006), Shear wave splitting from local events beneath the Ryukyu arc: Trench-parallel anisotropy in the mantle wedge, Physics of the Earth and Planetary Interiors, 155(3-4), 300-312.

Long, M. D., B. H. Hager, M. V. de Hoop, and R. D. van der Hilst (2007), Two-dimensional modeling of subduction zone anisotropy with application to southwestern Japan, Geophysical Journal International, 170(2), 839-856.

Long, M. D., and P. G. Silver (2008), The subduction zone flow field from seismic anisotropy: A global view, Science, 319(5861), 315-318.

Long, M. D., and P. G. Silver (2009), Shear wave splitting and mantle anisotropy: measurements, interpretations, and new directions, Survey Geophysics, 30, 407-461, doi:10.1007/s10712-009-9075-1.

Long, M. D., and P. G. Silver (2009), Mantle flow in subduction systems: The subslab flow field and implications for mantle dynamics, Journal of Geophysical Research-Solid Earth, 114, doi:10.1029/2008JB006200.

Lorito, S., F. Romano, A. Piatanesi, and E. Boschi (2008), Source process of the September 12, 2007, M(W) 8.4 southern Sumatra earthquake from tsunami tide gauge record inversion, Geophysical Research Letters, 35(2), L02310, 6pp, doi:10.1029/2007GL032661.

MacPherson, K. A., D. Hidayat, S. Goh (2010), Receiver function structure beneath a broad-band seismic station in South Sumatra, AGU, Fall Meeting 2010, abstract#S13A-1979.

Mainprice, D. (1997), Modeling the anisotropic seismic properties of partially molten rocks found at mid-ocean ridges, Tectonophysics, 279, 161-179.

Mainprice, D., G. Barruol, and W. B. Ismail, (2000), The seismic anisotropy of the Earth's mantle: From single crystal to polycrystal. In Karato, S.-I, A. M Forte, R. C Liberman, G. Masters and L. Stixrude (Ed) Earth's deep interior, Mineral physics and tomography from the atomic to the global scale, AGU, Washington D.C, USA.

Mainprice, D. (2007), Seismic anisotropy of the deep Earth from a mineral and rock physics perspective, In Schubert G (Ed) Treatise in Geophysics, 2, 437-492, Oxford, UK.

Malod, J. A., B. M. Kemal (1996), The Sumatra Margin: Oblique subduction and lateral displacement of the accretionary prism, Geological Society, London, Special Publications, 106, 19-28.

Marson-Pidgeon, K., M. K. Savage, K. Gledhill, and G. Stuart (1999), Seismic anisotropy beneath the lower half of the North Island, New Zealand, Journal of Geophysical Research-Solid Earth, 104(B9), 20277-20286.

Masson, D. G., L. M. Parson, J. Milsom, G. Nichols, N. Sikumbang, B. Dwiyanto, and H. Kallagher (1990), Subduction of seamounts at the Java trench - a view with long range sidescan sonar, Tectonophysics, 185(1-2), 51-65.

McCaffrey, R. (1991), Slip vectors and stretching of the Sumatran Fore-Arc Basin, Geology, 19(9), 881-884.

McCaffrey, R. (1992), Oblique plate convergence, slip vectors, and forearc deformation, Journal of Geophysical Research-Solid Earth, 97, B6, 8095-8915.

McCaffrey, R. (1993), On the role of the upper plate in great subduction zone earthquakes, Journal of Geophysical Research-Solid Earth, 98(B7), 11953-11966.

McCaffrey, R., P. C. Zwick, Y. Bock, L. Prawirodirdjo, J. F. Genrich, C. W. Stevens, S. S. O. Puntodewo, and C. Subarya (2000), Strain partitioning during oblique plate convergence in northern Sumatra: Geodetic and seismologic constraints and numerical modeling, Journal of Geophysical Research-Solid Earth, 105(B12), 28363-28376.

McCloskey, J., D. Lange, F. Tilmann, S. S. Nalbant, A. F. Bell, D. H. Natawidjaja, and A. Rietbrock (2010), The September 2009 Padang earthquake, Nature Geoscience, 3(2), 70-71.

Meade, C., and R. Jeanloz (1991), Deep focus earthquakes and recycling of water into the earths mantle, Science, 252(5002), 68-72.

Menke, W. (1984), Geophysical Data Analysis: Discrete Inverse Theory, Academic Press, Orlando.

Menke, W. (1989), Geophysical Data Analysis: Discrete Inverse Theory, Academic Press,

Miura, S., S. Kodaira, A. Nakanishi, T. Tsuru, N. Takahashi, N. Hirata, and Y. Kaneda (2003), Structural characteristics controlling the seismicity of southern Japan Trench fore-arc region, revealed by ocean bottom seismographic data, Tectonophysics, 363(1-2), 79-102.

Morgan, J. P., J. Hasenclever, M. Hort, L. Ruepke, and E. M. Parmentier (2007), On subducting slab entrainment of buoyant asthenosphere, Terra Nova, 19(3), 167-173.

Morley, A. M., G. W. Stuart, J. M. Kendall, and M. Reyners (2006), Mantle wedge anisotropy in the Hikurangi subduction zone, central North Island, New Zealand, Geophysical Research Letters, 33, L05301, doi:10.1029/2005GL024569.

Mount, V. S., and J. Suppe (1992), Present-day stress orientations adjacent to active strike-slip faults, Journal of Geophysical Research-Solid Earth, Journal of Geophysical Research-Solid Earth, 97(B8), 11995-12013.

Muzli, M., J. Saul, G. Asch, R. Wang, and F. Tilmann (2011), Co-seismic displacement of the 2010, M_w 7.8 Mentawai earthquake obtained from strong motion data, Geophysical Research Abstracts, 13, EGU2011-10653-2.

Müller, R. D., W. R. Roest, J. Y. Royer, L. M. Gahagan, and J. G. Sclater (1997), Digital isochrons of the world's ocean floor, Journal of Geophysical Research-Solid Earth, 102(B2), 3211-3214.

Nakajima, J., and A. Hasegawa (2004), Shear-wave polarization anisotropy and subduction-induced flow in the mantle wedge of northeastern Japan, Earth and Planetary Science Letters, 225(3-4), 365-377.

Nakajima, J., J. Shimizu, S. Hori, and A. Hasegawa (2006), Shear-wave splitting beneath the southwestern Kurile arc and northeastern Japan arc: A new insight into mantle return flow, Geophysical Research Letters, 33(5), L05305, 4pp, doi:10.1029/2005GL025053.

Nalbant, S. S., S. Steacy, K. Sieh, D. Natawidjaja, and J. McCloskey (2005), Earthquake risk on the Sunda trench, Nature, 435(7043), 756-757.

Natawidjaja, D. H., K. Sieh, M. Chlieh, J. Galetzka, B. W. Suwargadi, H. Cheng, R. L. Edwards, J. P. Avouac, and S. N. Ward (2006), Source parameters of the great Sumatran megathrust earthquakes of 1797 and 1833 inferred from coral microatolls, Journal of Geophysical Research-Solid Earth, 111(B6), 37, B06403, 37pp, doi:10.1029/2005JB004025.

Newcomb, K. R., and W. R. McCann (1987), Seismic history and seismotectonics of the Sunda Arc, Journal of Geophysical Research-Solid Earth and Planets, 92(B1), 421-439.

Newman, A. V., G. Hayes, Y. Wei, and J. Convers (2011), The 25 October 2010 Mentawai tsunami earthquake, from real-time discriminants, finite-fault rupture, and tsunami excitation, Geophysical Research Letters, 38, L05302, doi:10.1029/1010GL046498.

Nicolas, A., and N. I. Christensen (1987), Formation of anisotropy in upper mantle peridotites - A review, In: Composition, structure and dynamics of lithosphere-asthenosphere system, eds L. E. Fuch and C. Froidevaux, Geodynamics, series 16, AGU, Washington D.C.

Nippress, S. E. J., N. J. Kusznir, and J. M. Kendall (2004), Modeling of lower mantle seismic anisotropy beneath subduction zones, Geophysical Research Letters, 31, L19612, doi:10.1029/2004GL020701.

Nippress, S. E. J., and A. Rietbrock (2007), Seismogenic zone high permeability in the Central Andes inferred from the relocations of micro-earthquakes, Earth and Planetary Science Letters, 263, 235-245.

Nippress, S. E. J., A. Rietbrock, and A. E. Heath (2010), Optimized automatic pickers: application to the ANCORP data set, Geophysical Journal International, 181(2), 911-925.

Nippress, S. E. J., S. Hicks, A. Rietbrock, M, Whipple, R. Collings, and C. Haberland (2011), Sub-slab mantle anisotropy beneath south-central Chile, AGU Fall Meet. Suppl, Abstract DI41A-2068.

Niu, F. L., and A. M. Perez (2004), Seismic anisotropy in the lower mantle: A comparison of waveform splitting of *SKS* and *SKKS*, Geophysical Research Letters, 31, L24612, doi:10.1029/2004GL021196.

Okada, T., T. Matsuzawa, and A. Hasegawa (1995), Shear-wave polarization anisotropy beneath the northeastern part of Honshu, Japan, Geophysical Journal International, 123(3), 781-797.

Oleskevich, D. A., R. D. Hyndman, and K. Wang (1999), The updip and downdip limits to great subduction earthquakes: Thermal and structural models of Cascadia, south Alaska, SW Japan, and Chile, Journal of Geophysical Research-Solid Earth, 104(B7), 14965-14991.

Ozalaybey, S., and M. K. Savage (1995), Shear-wave splitting beneath western United-States in relation to plate tectonics, Journal of Geophysical Research-Solid Earth, 100(B9), 18135-18149.

Pacheco, J. F., and L. R. Sykes (1992), Seismic moment catalog of large shallow earthquakes, 1900 TO 1989, Bulletin of the Seismological Society of America, 82(3), 1306-1349.

Pacheco, J. F., L. R. Sykes, and C. H. Scholz (1993), Nature of seismic coupling along simple plate boundaries of the subduction type, Journal of Geophysical Research, 98, 14133-14159.

Park, J., and V. Levin (2002), Geophysics - seismic anisotropy: Tracing plate dynamics in the mantle, Science, 296(5567), 485-489.

Peacock, S. M. (1990), Fluid processes in subduction zones, Science, 248(4953), 329-337.

Peyton, V., V. Levin, J. Park, M. Brandon, J. Lees, E. Gordeev, and A. Ozerov (2001), Mantle flow at a slab edge: Seismic anisotropy in the Kamchatka region, Geophysical Research Letters, 28(2), 379-382.

Pinero-Feliciangeli, L. T., and J. M. Kendall (2008), Sub-slab mantle flow parallel to the Caribbean plate boundaries: Inferences from *SKS* splitting, Tectonophysics, 462(1-4), 22-34.

Polet, J., P. G. Silver, S. Beck, T. Wallace, G. Zandt, S. Ruppert, R. Kind, and A. Rudloff (2000), Shear wave anisotropy beneath the Andes from the BANJO, SEDA, and PISCO experiments, Journal of Geophysical Research-Solid Earth, 105(B3), 6287-6304.

Prawirodirdjo, L., Y . Bock, R. McCaffrey, J. Genrich, E. Calais, C. Stevens, S. S. O. Puntodewo, C. Subarya, J. Rais, P. Zwick, and Fauzi (1997), Geodetic observations of interseismic strain segmentation at the Sumatra subduction zone, Geophysical Research Letters, 24(21), 2601-2604.

Prawirodirdjo, L., Y. Bock, J. F. Genrich, S. S. O. Puntodewo, J. Rais, C. Subarya, and S. Sutisna (2000), One century of tectonic deformation along the Sumatran fault from triangulation and Global Positioning System surveys, Journal of Geophysical Research-Solid Earth, 105(B12), 28343-28361.

Ranero, C. R., J. P. Morgan, K. McIntosh, and C. Reichert (2003), Bending-related faulting and mantle serpentinization at the Middle America trench, Nature, 425(6956), 367-373.

Restivo, A., and G. Helffrich (2006), Core-mantle boundary structure investigated using *SKS* and *SKKS* polarization anomalies, Geophysical Journal International, 165(1), 288-302.

Reyners, M., D. Eberhart-Phillips, and G. Stuart (1998), A three-dimensional image of the shallow subduction: crustal structure of the Raukumara peninsula, New Zealand, Geophysics Journal International, 137, 873-890.

Ribe, N. M. (1989), Seismic anisotropy and mantle flow, Journal of Geophysical Research-Solid Earth and Planets, 94(B4), 4213-4223.

Rietbrock, A. and F. Scherbaum (1998), The GIANT analysis system, Seismology Research Letters, 69 (1), 40–45.

Rietbrock, A., and F. Waldhauser (2004), A narrowly spaced double-seismic zone in the subducting Nazca plate, Geophysical Research Letters, 31(10), 608-611.

Rivera, L., K. Sieh, D. Helmberger, and D. Natawidjaja (2002), A comparative study of the Sumatran subduction-zone earthquakes of 1935 and 1984, Bulletin of the Seismological Society of America, 92(5), 1721-1736.

Ruff, L., and H. Kanamori (1983), Seismic coupling and uncoupling at subduction zones, Tectonophysics, 99, 99-117.

Ruff, L. (1996), Large earthquakes in subduction zones: Segment interaction and recurrence time in subduction: Top to Bottom, pp 91-105*,* eds G. E. Bebout, D. W. Scholl, S. H. Kirby, and P. Platt, Geophysical Monograph 96, AGU.

Russo, R. M., and P. G. Silver (1994), Trench parallel flow beneath the Nazca Plate from seismic anisotropy, Science, 263(5150), 1105-1111.

Russo, R. M., P. G. Silver, M. Franke, W. B. Ambeh, and D. E. James (1996), Shear-wave splitting in northeast Venezuela, Trinidad, and the eastern Caribbean, Physics of the Earth and Planetary Interiors, 95(3-4), 251-275.

Samuel, M. A., Harbury, N. A., Bakri, A., Banner, F. T. and L. Hartono (1997), A new stratigraphy for the islands of the Sumatran Arc, Indonesia. J. SE Asian Earth Sci. 15, 339–380.

Satake, K., Y. Nishimura, P. Putra, E. Yulianto, M. Sugimoto, A. Koresawa, M. H. Pradono, and Pariatmono (20011), Tsunami field survey for the Mentawai, Indonesia earthquake of October 25, 2010 Report to UNESCO Jakarta Office.

Savage, J. C. (1969), Mechanics of deep-focus faulting, Tectonophysics, 8(2), 115-127.

Savage, M. K., and P. G. Silver (1993), Mantle deformation and tectonics - constraints from seismic anisotropy in the western United States, Physics of the Earth and Planetary Interiors, 78(3-4), 207-227.

Savage, M. K. (1999), Seismic anisotropy and mantle deformation: What have we learned from shear wave splitting?, Reviews of Geophysics, 37(1), 65-106.

Savage, M. K., K. M. Fischer, and C. E. Hall (2004), Strain modeling, seismic anisotropy and coupling at strike-slip boundaries: Applications in New Zealand and the San Andreas fault, Vertical coupling and decoupling in the lithosphere, J. Grocott, B. Tikoff, K. J. W. McCaffrey, and G. Taylor (Ed), Geological Society of London, Special Publications, 227, 9-40.

Scholz, C. H., M. Wyss, and S. W. Smith (1969), Seismic and aseismic slip on the San Andreas Fault, Journal of Geophysical Research, 4(8), 2049-2069, doi:10.1029/JB074j008p02049.

Sdrolias, M., and R. D. Muller (2006), Controls on back-arc basin formation, Geochemistry Geophysics Geosystems, 7, Q04016, 40pp, doi:10.1029/2005GC001090.

Seno, T. (2005), Variation of downdip limit of the seismogenic zone near the Japanese islands: Implications for the serpentinization mechanism of the forearc mantle wedge, Earth and Planetary Science Letters, 231(3-4), 249-262.

Seno, T., D. P. Zhao, Y. Kobayashi, and M. Nakamura (2001), Dehydration of serpentinized slab mantle: Seismic evidence from southwest Japan, Earth Planets and Space, 53(9), 861-871.

Shapiro, N. M., M. H. Ritzwoller, and E. R. Engdahl (2008), Structural context of the great Sumatra-Andaman Islands earthquake, Geophysical Research Letters, 35(5), L05301, 5pp, doi:10.1029/2008GL033381.

Shaw, B. E. (2000), The edges of large earthquakes and the epicenters of future earthquakes: Stress-induced correlations in elastodynamic fault models, Pure and Applied Geophysics, 157(11-12), 2149-2164.

Shearer, P. M, (1999), Introduction to Seismology, Cambridge University Press.

Shelly, D. R, G. C. Beroza, H. Zhang, C. H. Thurber, and S. Ide (2006), High resolution subduction zone seismicity and velocity structure beneath Ibaraki Prefecture, Japan, Journal of Geophysical Research-Solid Earth, 111, doi:10.1029/2005JB004081.

Sheriff, R. E., and L. P. Geldart (1995), Exploration seismology, Cambridge University Press.

Sieh, K., and D. Natawidjaja (2000), Neotectonics of the Sumatran fault, Indonesia, Journal of Geophysical Research-Solid Earth, 105(B12), 28295-28326.

Silver, P. G., and W. W. Chan (1991), Shear-wave splitting and subcontinental mantle deformation, Journal of Geophysical Research-Solid Earth, 96(B10), 16429-16454.

Silver, P. G., and M. K. Savage (1994), The interpretation of shear-wave splitting parameters in the presence of 2 anisotropic layers, Geophysical Journal International, 119(3), 949-963.

Simoes, M., J. P. Avouac, R. Cattin, and P. Henry (2004), The Sumatra subduction zone: A case for a locked fault zone extending into the mantle, Journal of Geophysical Research-Solid Earth, 109(B10), B10402, doi:10.1029/2003JB002958.

Singh, S. C., H. Carton, P. Tapponnier, N. D. Hananto, A. P. S. Chauhan, D. Hartoyo, M. Bayly, S. Moeljopranoto, T. Bunting, P. Christie, H. Lubis, and J. Martin (2008), Seismic evidence for broken oceanic crust in the 2004 Sumatra earthquake epicentral region, Nature Geoscience, 1(11), 777-781.

Singh, S. C., N. D. Hananto, A. P. S. Chauhan, H. Permana, M. Denolle, A. Hendriyana, and D. Natawidjaja (2009), Evidence of active backthrusting at the NE Margin of Mentawai Islands, SW Sumatra, Geophysical Journal International, 180(2), 703–714, doi:10.1038/ngeo336.

Singh, S. C., N. D. Hananto, and A. P. S. Chauhan (2011), Enhanced reflectivity of backthrusts in the recent great Sumatran earthquake rupture zones, Geophysical Research Letters, 38, L04302, 5pp, doi:10.1029/2010GL046227.

Singh, S. C., N. Hananto, M. Mukti, H. Permana, Y. Djajadihardja, and H. Harjono (2011a), Seismic images of the megathrust rupture during the 25th October 2010 Pagai earthquake, SW Sumatra: Frontal rupture and large tsunami, Geophysical Research Letters, 38, L16313, 6pp, doi:10.1029/2011GL048935.

Singh, S. C., N. Hananto, M. Mukti, D. P. Robinson, S. Das, A. Chauhan, H. Carton, B. Gratacos, S. Midnet, Y. Djajadihardja, and H. Harjona (2011b), Aseismic zone and earthquake segmentation associated with a deep subducted seamount in Sumatra, Nature Geoscience, 4(5), 308-311.

Smith, G. P., D. A. Wiens, K. M. Fischer, L. M. Dorman, S. C. Webb, and J. A. Hildebrand (2001), A complex pattern of mantle flow in the Lau backarc, Science, 292(5517), 713-716.

Smith, W. H. F., R. Scharro, V. V. Titov, D. Arcas, and B. K. Arbic (2005), Satellite altimeters measure tsunamis, Oceanography, 18(2).

Snoke, J. A., J. W. Munsey, A. C. Teague, and G. A. Bollinger (1984), A program for focal mechanism determination by combined use of polarity and SV-*P* amplitude ratio data, Earthquake Notes, 55(3), 15-20.

Song, T. R. A., and M. Simons (2003), Large trench-parallel gravity variations predict seismogenic behavior in subduction zones, Science, 301(5633), 630-633.

Spakman, W., and G. Nolet (1988), Imaging algorithms, accuracy and resolution in delay time tomography, in Mathematical Geophysics, edited by N. Vlarr et al., pp 155-187, D. Reidel, Norwell, Mass.

Stern, R. J. (2002), Subduction zones, Reviews of Geophysics, 40(4), 1012-1049, doi:10.1029/2001RG00108.

Subarya, C., M. Chlieh, L. Prawirodirdjo, J.-P. Avouac, Y. Bock, K. Sieh, A. J. Meltzner, D. H. Natawidjaja, and R. McCaffrey (2006), Plate-boundary deformation associated with the great Sumatra-Andaman earthquake, Nature, 440(7080), 46-51.

Syracuse, E. M., and G. A. Abers (2006), Global compilation of variations in slab depth beneath arc volcanoes and implications, Geochemistry Geophysics Geosystems, 7, Q05017, 18pp, doi:10.1029/2005GC001045.

Teanby, N. A., J. M. Kendall, and M. Van der Baan (2004), Automation of shear-wave splitting measurements using cluster analysis, Bulletin of the Seismological Society of America, 94(2), 453-463.

Thurber, C. H. (1983), Earthquakes locations and 3-dimensional crustal structure in the the Coyote lake area, Journal of Geophysical Research-Solid Earth, 88(NB10), 8226-8236.

Thurber, C. H. (1992), Hypocentre velocity structure coupling in local earthquake tomography, Physics of the Earth and Planetary Interiors, 75(1-3), 55-62.

Thurber, C. H. (1993), Local earthquake tomography: velocities and *Vp/Vs*-theory in seismic tomography: Theory and practice edited by H. M. Iyer and K. Hirahara, pp 563-583, Cahpman and Hall, London.

Thurber, C. H., and S. R. Atre (1993), 3-dimensional *VP/VS* variations along the Loma-Prietra rupture zone, Bulletin of the Seismological Society of America, 83(3), 717-736.

Thurber, C., and D. Eberhart-Phillips (1999), Local earthquake tomography with flexible gridding, Computers & Geosciences, 25(7), 809-818.

Tichelaar, B. W, and L. J. Ruff (1991), Seismic coupling along the Chilean subduction zone, Journal of Geophysical Research-Solid Earth, 96, 11997-12022.

Tichelaar, B. W., and L. J. Ruff (1993), Depth of seismic coupling along subduction zones, Journal of Geophysical Research-Solid Earth, 98(B2), 2017-2037.

Tilmann, F. J., T. J. Craig, I. Grevemeyer, B. Suwargadi, H. Kopp, and E. Flueh (2010), The updip seismic/aseismic transition of the Sumatra megathrust illuminated by aftershocks of the 2004 Aceh-Andaman and 2005 Nias events, Geophysical Journal International, 181(3), 1261-1274.

Tingay, M., C. Morley, R. King, R. Hillis, D. Coblentz, and R. Hall (2010), Present-day stress field of Southeast Asia, Tectonophysics, 482(1-4), 92-104.

Tono, Y., Y. Fukao, T. Kunugi, and S. Tsuboi (2009), Seismic anisotropy of the Pacific slab and mantle wedge beneath the Japanese islands, Journal of Geophysical Research-Solid Earth, 114, B07307, 16pp, doi:10.1029/2009JB006290.

Toomey, D. R., and G. R. Foulger (1989) Tomographic inversion of local earthquake data from the Hengill-Grensdalur central volcano complex, Iceland, Journal of Geophysical Research-Solid Earth and Planets, 94(B12), 17497-17510.

Um, J., and C. Thurber (1987), A fast algorithm for 2-point seismic ray tracing, Bulletin of the Seismological Society of America, 77(3), 972-986.

Vauchez, A., A. Tommasi, G. Barruol, and J. Maumus (2000), Upper mantle deformation and seismic anisotropy in continental rifts, Physics and Chemistry of the Earth Part a-Solid Earth and Geodesy, 25(2), 111-117.

Vecsey, L., J. Plomerova, and V. Babuska (2008), Shear-wave splitting measurements - Problems and solutions, Tectonophysics, 462(1-4), 178-196.

Vinnik, L. P., R. Kind, G. L. Kosarev, and L. I. Makeyeva (1989), Azimuthal anisotropy in the lithosphere from observations of long-period *S*-waves, Geophysical Journal International, 99(3), 549-559.

Wada, I., K. Wang, J. He, and R. D. Hyndman (2008), Weakening of the subduction interface and its effects on surface heat flow, slab dehydration, and mantle wedge serpentinization, Journal of Geophysical Research-Solid Earth, 113, B04402, 15pp, doi:10.1029/2007JB005190.

Wada, I., and K. Wang (2009), Common depth of slab-mantle decoupling: Reconciling diversity and uniformity of subduction zones, Geochemistry Geophysics Geosystems, 10, Q100009, 36pp, doi:10.1029/2009GC002570.

Walker, K. T., A. A. Nyblade, S. L. Klemperer, G. H. R. Bokelmann, and T. J. Owens (2004), On the relationship between extension and anisotropy: Constraints from shear wave splitting across the East African Plateau, Journal of Geophysical Research-Solid Earth, 109, B08302, doi:10.1029/2003JB002866.

Walker, K. T., M. Ishii, and P. M. Shearer (2005), Rupture details of the 28 March 2005 Sumatra Mw 8.6 earthquake imaged with teleseismic *P* waves, Geophysical Research Letters, 32, L24303, doi:10.1029/2005GL024395.

Wang, K., and Y. Hu (2006), Accretionary prisms in subduction earthquake cycles: The theory of dynamic Coulomb wedge, Journal of Geophysical Research-Solid Earth, 111(B6), B06410, 16pp, doi:10.1029/2005JB004094.

Weller, O., D. Lange, F. Tilmann, D. Natawidjaja, A. Rietbrock, R. Collings, and L. Gregory (2012), The structure of the Sumatran Fault revealed by local seismicity, Geophysics Research Letters, doi:10.1029/2011GL050440.

Wells, R. E., R. J. Blakely, Y. Sugiyama, D. W. Scholl, and P. A. Dinterman (2003), Basin-centered asperities in great subduction zone earthquakes: A link between slip, subsidence, and subduction erosion?, Journal of Geophysical Research-Solid Earth, 108(B10), 2507, doi:10.1029/2002JB002072.

Wirth, E., and M. D. Long (2010), Frequency-dependent shear wave splitting beneath the Japan and Izu-Bonin subduction zones, Physics of the Earth and Planetary Interiors, 181, 141-154.

Wiseman, K., and R. Buergmann (2011), Stress and seismicity changes on the Sunda Megathrust preceding the 2007 M(w) 8.4 earthquake, Bulletin of the Seismological Society of America, 101(1), 313-326.

Wiseman, K., P. Banerjee, K. Sieh, R. Burgmann, and D. H. Natawidjaja (2011b), Another potential source of destructive earthquakes and tsunami offshore of Sumatra, Geophysical Research Letters, 38, L10311, doi:10.1029/2011GL047226.

Wolfe, C. J., and S. C. Solomon (1998), Shear-wave splitting and implications for mantle flow beneath the MELT region of the East Pacific Rise, Science, 280(5367), 1230-1232.

Wookey, J., J. M. Kendall, and G. Barruol (2002), Mid-mantle deformation inferred from seismic anisotropy, Nature, 415(6873), 777-780.

Wookey, J., J. M. Kendall, and G. Rumpker (2005), Lowermost mantle anisotropy beneath the north Pacific from differential *S*-*ScS* splitting, Geophysical Journal International, 169, 829-838.

Wüstefeld, A., and G. Bokelmann (2007), Null detection in shear-wave splitting measurements, Bulletin of the Seismological Society of America, 97(4), 1204-1211.

Wüstefeld, A., G. Bokelmann, C. Zaroli, and G. Barruol (2008), SplitLab: A shear-wave splitting environment in Matlab, Computers & Geosciences, 34(5), 515-528.

Yang, X., K. M. Fischer, and G. A. Abers (1995), Seismic anisotropy beneath the Shumagin Islands segment of the Aleutian-Alaska subduction zone, Journal of Geophysical Research, 100(B9), 18165-18177, doi:10.1029/95JB01425.

Yardley, G. S., and S. Crampin (1991), Extensive-dilatance anisotropy - Relative information in *VSPS* and reflection surveys, Geophysical Prospecting, 39(3), 337-355.

Zatsepin, S. V., and S. Crampin (1997), Modeling the compliance of crustal rock .I. Response of shear-wave splitting to differential stress, Geophysical Journal International, 129(3), 477-494.

Zhang, S. Q., and S. Karato (1995), Lattice preferred orientation of olivine aggregates deformed in simple shear, Nature, 375(6534), 774-777.

Zhang, Z., and S. Y. Schwartz (1994), Seismic anisotropy in the shallow crust of the Loma-Prieta segment of the San-Andreas fault system, Journal of Geophysical Research-Solid Earth, 99(B5), 9651-9661.

Zhao, D. P., A. Hasegawa, and S. Horiuchi (1992), Tomographic imaging of *P* and *S* wave velocity structure beneath northwestern Japan, Journal of Geophysical Research-Solid Earth, 97,19909-19928.

Zhao, D. P., K. L. Wang, G. C. Rogers, and S. M. Peacock (2001), Tomographic image of low *P* velocity anomalies above slab in northern Cascadia subduction zone, Earth Planets and Space, 53(4), 285-293.

Acknowledgments

My main supervisor Professor Andreas Rietbrock is thanked for providing help and guidance throughout the duration of the PhD, without his patience and support I would have not have been able to submit this thesis. Additionally, thanks must also go to Frederik Tilmann and Dietrich Lange who assisted with the data acquisition, pre-processing and gave useful comments and assistance throughout. Recognition must also go to Stuart Nippress who assisted in the shear wave splitting analysis and provided valuable comments. Useful comments and corrections were also given by Julia Collings and Alex Davis. Lastly, this project would not have been possible without the hard work and dedication of everyone involved in the field work. I gratefully acknowledge the cooperation of many Sumatran landowners for allowing us to install the seismic stations on their property. Furthermore I thank the captain and crew of the Andalas and the field crews for their excellent work under difficult conditions.